Domenico Cimini
Frank S. Marzano
Guido Visconti
(Editors)

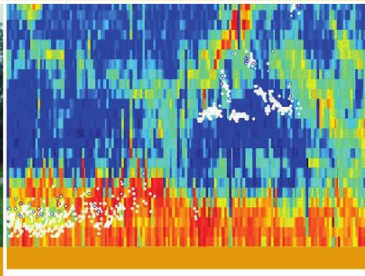

Integrated Ground-Base

Applications for Climate, Meteorology, and Civil Protection

Integrated Ground-Based Observing Systems

Domenico Cimini · Frank S. Marzano ·
Guido Visconti
Editors

Integrated Ground-Based Observing Systems

Applications for Climate, Meteorology, and Civil Protection

Springer

Editors
Dr. Domenico Cimini
Istituto di Metodologie per l'Analisi Ambientale
Consiglio Nazionale delle Ricerche
C.da S. Loja
85050 Tito Scalo, Potenza
Italy
cimini@imaa.cnr.it

Prof. Guido Visconti
Universita L'Aquila
Dipto. Fisica
INFN Unit
Via Vetoio 10
67010 L'Aquila
Italy
guido.visconti@aquila.infn.it

Prof. Frank S. Marzano
Università di Roma
Dipto. Ingegneria Elettronica
Via Eudossiana 18
00184 Roma
Italy
marzano@die.uniroma1.it

ISBN 978-3-642-12967-4 e-ISBN 978-3-642-12968-1
DOI 10.1007/978-3-642-12968-1
Springer Heidelberg Dordrecht London New York

Library of Congress Control Number: 2010930910

Cover design: deblik, Berlin

Printed on acid-free paper

Springer is part of Springer Science+Business Media (www.springer.com)

Preface

This volume presents a collection of selected articles based on presentations at the seventh edition of the International Summer School on Atmospheric and Oceanic Sciences (ISSAOS), annually organized by the University of L'Aquila, Italy. This seventh edition, held during September 4–7, 2007 in the amazing venue of the medieval Castle of the city of L'Aquila, focused on "Integrated Ground-Based Observing System Applications for Climate, Meteorology, and Civil Protection."

The goal of ISSAOS 2007 was to bring together experts and young researchers in ground-based remote sensing to discuss the need for integrated systems and their contribution to a variety of applications, including weather forecast, meteorology, climatology, natural hazard monitoring, and transportation support.

Important questions related to weather, climate, etc., cannot be answered without a broad view of the atmospheric processes and their mutual links. Ground-based remote sensing provides useful tools to help understanding these processes by real measurements with known error characteristics. The user needs for ground-based remote sensing observations were reviewed at the first COST 720 workshop, incidentally held in L'Aquila in 2002. Of course, all observing systems have strengths and weakness, but none meet the breakthrough levels of user requirements for all aspects. The solution to these requirements could be best met by a composite of different observing systems.

The ISSAOS 2007-invited lecturers were Thomas Ackerman, Pier Paolo Alberoni, Paolo Antonelli, Stefania Argentini, Laura Bianco, Stefano Decesari, Piero Di Carlo, George L. Frederick, Frank S. Marzano, John Nash, Christian Pagé, Vincenzo Rizi, Herman Russchenberg, David D. Turner, and James M. Wilczak.

A total of 70 people from 10 countries and 4 continents participated in ISSAOS 2007. The primary audience was constituted by graduate students in remote sensing and atmospheric sciences, PhD students, and remote sensing researchers willing to broaden their view concerning ground-based instrumentation, their synergy, and applications. Following the tradition of ISSAOS, participants were asked to provide an evaluation of the school at its conclusions. The results indicate that generally the participants liked the school, including the quality of lecturers, the methodology, and the venue. The overall organization and the social program were especially appreciated by the vast majority.

The discussion during and following ISSAOS 2007 has been the starting point for the preparation of the contributions in the present volume. The first part reports a number of papers addressing the basic principles and the recent advances in ground-based remote sensing of the atmosphere. The second part of the book reviews a list of state-of-the-art applications of ground-based remote sensing integrated systems to the study of climate, weather, and natural hazards. Even though this volume is published after almost 3 years after the conclusion of ISSAOS 2007, it represents a valuable sample of the state-of-the-art on ground-based remote sensing technology and applications.

For the organization of ISSAOS 2007 we acknowledge the Center of Excellence CETEMPS of the University of L'Aquila. We also acknowledge the financial contribution from our sponsors (in alphabetic order): ELDES (http://www.eldes.it/), HIMET (http://www.himet.it/), Kipp & Zonen (http://www.kippzonen.com/), Leosphere (http://www.leosphere.com/), METEX (http://www.metek.de/), Radiometrics (http://www.radiometrics.com/), Selex/Gematronik (http://www.gematronik.com/), and Vaisala (http://www.vaisala.com/). We greatly appreciated the sponsors' delegates, the invited lecturers, and all the participants for enthusiastically manifesting their interest in our idea. We are also grateful to Livio Bernardini, Klaide De Sanctis, Sabrina Gentile, Emanuela Pichelli, Daniela Ronconi, Enrico Stagnini, and Paolo Stocchi for helping with the organization and the logistic. Federica Casilli and Luigi Margherita deserve particular gratitude for their kind help throughout the project.

Finally, this book inevitably carries signs of the tragic earthquake event in L'Aquila on April 6, 2009. Our most sincere thoughts go the many that have lost lives and beloved ones during that tragic event.

Potenza, Italy
Roma, Italy
L'Aquila, Italy
January 21, 2010

Domenico Cimini,
Frank S. Marzano,
Guido Visconti

Contents

Contributors

Paolo Antonelli CIMSS/University of Wisconsin, Madison, WI, USA, paoloa@ssec.wisc.edu

Stefania Argentini ISAC/CNR, via del Fosso del Cavaliere, Roma, Italy, s.argentini@isac.cnr.it

Laura Bianco Cooperative Institute for Research in Environmental Sciences (CIRES), University of Colorado, Boulder, CO, USA; NOAA/Earth System Research Laboratory (ESRL)/Physical Sciences Division (PSD), Boulder, CO, USA, laura.bianco@noaa.gov

Domenico Cimini IMAA/CNR, C.da S. Loja, Tito Scalo (PZ), Italy, cimini@imaa.cnr.it

Susanne Crewell Institute for Geophysics and Meteorology, University of Cologne, Cologne, Germany, crewell@meteo.uni-koeln.de

Stefano Decesari Institute of Atmospheric Sciences and Climate (ISAC), CNR, Bologna, Italy, s.decesari@isac.cnr.it

Piero Di Carlo Dipartimento di Fisica and Centro di Eccellenza CETEMPS, Universita' di L'Aquila, via vetoio, Coppito L'Aquila, L'Aquila, Italy, Piero.Dicarlo@aquila.infn.it

George L. Frederick Falcon Consultants LLC, Georgetown, TX, USA, falconsultants@aol.com

Frank S. Marzano Department of Electronic Engineering, Sapienza University of Rome, Rome, Italy; Centre of Excellence CETEMPS, University of L'Aquila, L'Aquila, Italy, marzano@die.uniroma1.it

Mario Montopoli Centre of Excellence CETEMPS and Department of Electrical and Information Engineering, University of L'Aquila, L'Aquila, Italy, mario.montopoli@univaq.it

Christian Pagé CERFACS, Toulouse Cedex, France, christian.page@cerfacs.fr

Ilaria Pietroni ISAC/CNR, Roma, Italy, ilaria.pietroni@artov.isac.cnr.it

Bernhard Pospichal University of Cologne, Cologne, Germany, pospichal@meteo.uni-koeln.de

Vincenzo Rizi CETEMPS/Dipartimento di Fisica, Universitá Degli Studi dell'Aquila, L'Aquila, Italy, Vincenzo.Rizi@aquila.infn.it

Herman Russchenberg IRCTR, Delft University of Technology, Delft, The Netherlands, H.W.J.Russchenberg@tudelft.nl

James M. Wilczak NOAA/Earth Systems Research Laboratory, Boulder, CO, USA, James.M.Wilczak@noaa.gov

Ed R. Westwater CU/CET, CU/CIRES and ESRL/NOAA, Boulder, CO, USA, Ed.R.Westwater@colorado.edu

List of Acronyms

2DVD	Two-Dimensional Video Disdrometer
AAS	Atomic Absorption Spectroscopy
ABL	Atmospheric Boundary Layer
AERI	Atmospheric Emitted Radiance Interferometer
AMMA	African Monsoon Multidisciplinary Analysis
AMS	Aerosol Mass Spectrometer
AMSU	Advanced Microwave Sounding Unit
AOT	Aerosol Optical Thickness
APS	Aerodynamic Particle Sizer
AQ	Air Quality
ARM	Atmospheric Radiation Measurement
AWS	Automatic Weather Station
BSA	Backward Scattering Alignment
CART	Cloud and Radiation Testbed
CAT	Clear Air Turbulence
CCD	Charge-Coupled Device
CESAR	Cabauw Experimental Site for Atmospheric Research
COHO	COHerent Oscillator
CPC	Condensation Particle Counter
CPR	Cloud Profiling Radar
CRADA	Cooperative Research and Development Agreement
DC	Direct Current
DMA	Differential Mobility Analyzer
DMPS	Differential Mobility Particle Sizer
DOAS	Differential Optical Absorption Spectroscopy
DPC	Italian Department of Civil Protection
DSD	Drop Size Distribution
ECMWF	European Center for the Medium Range Weather Forecast
EGA	Evolved Gas Analysis
EM	Electromagnetic
EMEP	European Monitoring and Evaluation Programme
ESA	European Space Agency
ESTEC	European Space TEchnology Centre

EUSAAR	European Superistes for Atmospheric Aerosol Research
FAR	False Alarm Ratio
FDMS	Filter Dynamic Measurement System
FDDA	Four Dimensional Data Assimilation
FFT	Fast Fourier Transform
FIR	Far Infrared
FSA	Forward Scattering Alignment
FTIR	Fourier Transform InfraRed
FWHP	Full Width Half Power
EISAR	Emission Infrared Spectrometer for Atmospheric Research
GCM	Global Climate Model
GPS	Global Position System
HITRAN	High-Resolution Transmission
HKIA	Hong-Kong International Airports
H-TDMA	Hygroscopicity Tandem DMA
IC	Ion Chromatography
INTAβ	Integrated Aerosol Backscatter Coefficient
IOP	Intensive Observations Period
IPT	Integrated Profiling Technique
IR	InfraRed
ITCZ	Inter-Tropical Convergence Zone
ITD	Inter-Tropical Discontinuity
IWV	Integrated water vapor
JWD	Joss & Waldvogel Disdrometer
LBLRTM	Line-by-Line Radiative Transfer Model
LDR	Linear Depolarization Ratio
LIDAR	Light Detection and Ranging
LIF	Laser-Induced Fluorescence
LISISI	LIdar Signal Simulator program
LLJ	Low-Level Jet
LN	Lightening Network
LR	Lidar Ratio
LWC	Liquid Water Content
LWP	Liquid Water Path
MAP	Maximum a posteriori probability
MCP	Mean Convective Preciptation
MDZ	Minimum Detectable Reflectivity factor
METOP	Meteorological Operational Satellite
MMCR	Millimeter-Wave Cloud Radar
MPL	Micropulse Lidar
MSG	Meteosat Second Generation
MTP	Microwave Temperature Profiler
MWR	Microwave Radiometer
MWRP	Microwave Radiometer Profiler
NASA	National Aeronautics and Space Administration
NCAR	National Center for Atmospheric Research

NEAQS	New England Air Quality Study
NIR	Near InfraRed
NIST	National Institute of Standards and Technology
NOAA	National Oceanic and Atmospheric Administration
NRC	National Research Council
OPC	Optical Particle Counter
PC	Precipitating Clouds
PDF	Probability Density Function
PILS	Particle-Into-Liquid Sampler
PIXE	Particle-Induced X-ray Emission
POD	Probability Of Detection
PPI	Plan-Position Indicator
PR	Precipitation Radar
PRF	Pulse Repetition Frequency
PROBE	Pilot Radiation Observation Experiment
PSD	Particles Size Distribution
QME	Quality Measurement Experiment
R&D	Research and Development
RADAR	Radio Detection and Ranging
RASS	Radio Acoustic Sounding System
RR	Rain Rate
rms	Root-Mean-Square
RSD	Raindrop Size Distribution
RTE	Radiative Transfer Equation
RRTM	Rapid Radiative Transfer Model
SAF	Satellite Application Facility
SGP	Southern Great Plains
SHEBA	Surface Heat Budget of the Arctic
SI	Scattering Index
SODAR	Sound Detection and Ranging
SNR	Signal-to-Noise Ratio
SPECTRE	Spectral Radiance Experiment
SRI	Surface Rainfall Intensity
STALO	STAble Local Oscillator
SWIR	ShortWave InfraRed
TexAQS	Texas Air Quality Study
TIR	Thermal InfraRed
TOPAZ	Tunable Optical Profiler for Aerosol and oZone lidar
TRMM	Tropical Rainfall Measuring Mission
TSP	Total Suspended Particulate
TWDR	Terminal Doppler Weather Radar
UV	Ultraviolet
VAOD	Vertical Aerosol Optical Depth
VARR	Volcanic Ash Radar Retrieval
VIS	Visible
WPR	Wind Profiler Radar

Part I
Basic Instrumentation and Integration Techniques

Chapter I.1
Principles of Radiometric Remote Sensing of the Troposphere

Domenico Cimini and Ed R. Westwater

1 Introduction

Surface-based radiometric measurements of natural radiation are useful in a variety of applications, including planetary energy budget, meteorological observations and forecasting, climate benchmarking and model parameterization, satellite validation, and fundamental physics. One reason for the utility of these measurements is that with careful design, radiometers can be operated in a long-term unattended mode in nearly all weather conditions (Hogg et al., 1983; Philippona et al., 1995; Knuteson et al., 2004a, b). An important feature is the nearly continuous observational capability on time scales of seconds to minutes. The measurements with calibrated radiometers can enable the continued development of absorption and radiative transfer models in both clear (Liebe, 1989; Rosenkranz, 1998; Clough et al., 2005), cloudy (Liebe et al., 1991), and precipitating (Marzano et al., 2005; Battaglia et al., 2009) atmospheres. In addition, the continued development of retrieval and data assimilation algorithms (Clothiaux et al., 2000; Rodgers, 2000) provides more accurate and new products, combining radiometric observations with external data sources, such as forecasts or soundings from active sensors. This contribution gives an overview of some applications of ground-based radiometry in the electromagnetic spectrum from the visible (VIS) to microwave (MW) ranges for the remote sensing of troposphere.

2 Physical Principles

Passive ground-based remote sensing instruments rely on measurements of solar radiation transmitted through the atmosphere and of thermal radiation, both infrared and microwave, emitted by the atmosphere. The basic ideas of natural emission of electromagnetic (EM) radiation and radiative transfer are given in Liou (1980),

D. Cimini (✉)
IMAA/CNR, C.da S. Loja, Tito Scalo (PZ), Italy
e-mail: cimini@imaa.cnr.it

D. Cimini et al. (eds.), *Integrated Ground-Based Observing Systems*,
DOI 10.1007/978-3-642-12968-1_1,

Goody and Yung (1995), and Petty (2006) and their application to radiometric remote sensing is outlined in Elachi (1987) and Stephens (1994).

The radiatively significant atmospheric constituents are gas molecules, aerosol particles, and water in the form of cloud droplets, ice crystals, and precipitation. Because the transmission and emission depend on specific properties of the atmosphere, one can use these passive measurements to analyze the state of the atmosphere.

2.1 Radiation Quantities

Several quantities are commonly used to describe and quantify the main properties of EM radiation; these are summarized herewith with the corresponding physical units in the International Standard System. The energy carried by an EM wave is called radiant energy [Joule]; the time rate at which radiant energy passes a certain location is called wave power or radiant flux [Watt]. The wave power or radiant flux intercepted by a unit area of a plane surface is the radiant flux density [W/m^2] but it is usually called irradiance for flux incident upon the surface or emittance for flux leaving the surface. The radiant flux density illuminating (irradiance) or emerging from (emittance) an extended object in a given direction per unit projected area is called radiation intensity [W/m^2 st], which is often called radiance. Thus, the radiance expresses the EM wave power per unit projected area per unit solid angle. All the radiation quantities have equivalent spectral quantities, which are function of the EM wavelength, describing each quantity in a given wavelength interval, called spectral width or bandwidth. For example, the spectral radiance expresses the EM wave power per unit projected area per unit solid angle per unit wavelength interval [W/m^2 st m].

2.2 Extinction, Transmission, and Emission

When a monochromatic EM wave propagates through an homogeneous medium, it interacts with matter. The radiation may be attenuated by the absorption from the medium (conversion of radiation energy into heat or chemical energy) or scattered (redirection of radiation out of the original direction of propagation). The residual radiation at any point of the medium is called the transmitted radiation up to that point. However, the medium may also enhance the radiation intensity by thermal emission (conversion of thermal or chemical energy into radiation energy) or by scattering (redirection of isotropic radiation into the considered direction of propagation).

For energy conservation, the sum of the absorbed, transmitted, and scattered radiation energy must be equal to the incident energy. Thus, calling I_i the incident radiant flux intensity and I_a, I_s, and I_t the radiant flux intensity as absorbed, scattered, and transmitted by the medium, respectively, then

$$I_\mathrm{a} + I_\mathrm{s} + I_\mathrm{t} = I_\mathrm{i}. \tag{1}$$

This equation can be written in terms of the unitless quantities absorptance A, reflectance R (in analogy with a reflecting surface), and transmittance T, just by diving for I_i:

$$A + R + T = 1. \tag{2}$$

2.2.1 Atmospheric Extinction

Consider the passage of radiation of wavelength λ through a infinitesimal layer of air ds, measured along the direction of propagation. If the intensity is initially I, and calling β_e the extinction coefficient, then the reduction in I due to extinction is

$$dI_e = -\beta_e I ds. \tag{3}$$

The relative contributions of scattering and absorption to the total extinction are given by the additive scattering and absorption coefficients:

$$\beta_e = \beta_a + \beta_s, \tag{4}$$

while the relative importance of scattering versus absorption is given by the single scattering albedo, defined as

$$\omega = \beta_s/\beta_e = \beta_s/(\beta_a + \beta_s). \tag{5}$$

In the equations above, it is the extinction coefficient β_e that links absorption and scattering to the composition of the atmosphere.

Gaseous Absorption

When the radiant energy is absorbed/emitted by a gas molecule, there must be a corresponding increase/decrease of its internal energy. In particular, the internal energy may change in the presence of a change in translational kinetic energy, rotational kinetic energy, vibrational energy, and/or distribution of electric charge within the molecules.

The energy carried by photons in the EM spectrum considered here covers the range from 10^{-23} J at microwaves to 10^{-18} J at the ultraviolet (UV) edge. Therefore, different wavelength bands lead to different types of transitions, associated with different modes of energy storage. For example, transitions between rotational states usually involve low-energy photons, i.e., infrared (IR) and MW, because rotational states of most molecules are close in energy. Low-energy transitions often occur simultaneously with higher energy transitions, giving a fine scale structure to the total absorption spectrum.

– *Rotational* transitions may occur in the interaction of an EM wave with molecules possessing either a magnetic or a electric dipole, so that the externally applied magnetic field can exert a torque on the molecule. Thus, atmospheric molecules

that present neither an electric nor a magnetic dipole (such as N_2) have no rotational spectrum. Rotational absorption bands are associated with low-energy transition and thus are located in the far infrared to microwave spectrum. Oxygen has no electric dipole but it does have a permanent magnetic dipole moment, which causes rotational absorption bands at 60 and 118 GHz. All other atmospheric molecules exhibit permanent electric dipole and thus rotational absorption bands.
- *Vibrational* transitions are associated with considerably larger energies than rotational transition, giving rise to absorption/emission lines in the thermal and near IR bands. However, vibrational and rotational transitions may occur simultaneously, resulting in a more complex absorption spectrum, with additional transitions slightly more or less energetic than that of a pure vibrational transition.
- *Electronic* transitions happen when a photon is absorbed/emitted in association with an electron changing its orbit in the molecule. For the EM spectrum considered here, typically the outermost electrons are of interest, since transitions between the ground state and the first excited state are associated with wavelengths in the near IR, visible, and UV bands.

The combination of all three modes of excitation leads to a set of discrete energy levels forming the total absorption line spectrum. In addition, there are three distinct processes, whose relative importance depends on local environmental conditions, that cause the broadening of the line absorption, permitting a given atmospheric constituent to absorb radiation not only at the nominal wavelength but also in an interval around it. These three processes are natural, Doppler, and pressure broadening.

- The natural broadening is a consequence of the Heisenberg uncertainty principle; it is negligible compared to the other two throughout most of the atmosphere.
- The Doppler broadening is caused by the translational motions of individual molecules which slightly shift the transitions wavelengths randomly. This broadening becomes important in the upper atmosphere only.
- The pressure broadening is caused by the collisions between molecules which perturb the natural transitions between energy states. The pressure broadening is the primary mechanism in the troposphere, where collisions occur with very high frequency.

For the purpose of this overview, the pressure broadening is usually described adequately by the Lorentz line shape. Note that the Lorentz line shape is known to underestimate the effect of the far wings contributions. Another limitation is that the Lorentz model is only valid when the line width is very small compared to the center frequency. Thus, in the microwave band, the preferred line model is the van Vlack–Weisskopf function (Petty, 2006). An example of the pressure broadening effect on line absorption is evident on the rotovibrational oxygen complex from 50 to 70 GHz; individual lines are evident for pressure below 100 mb, while they form a nearly continuous absorption band at surface pressures.

Outside the major resonant absorption lines some level of absorption is generally found that does not exhibit line-like structure. This feature is known as continuum

absorption (since it varies slowly with wavelength) and results from three causes: photoionization, photodissociation, and longwave continuum absorption. The first two affect primarily the short wavelength edge (UV) of the considered spectrum and refer to high energetic photons that can extract an electron from an atom (ionization) or break a molecule (dissociation). The third cause affects spectral windows throughout the IR and MW regions and it is due primarily to water vapor. Although its mechanism is not completely understood, it is probably due to a combination of the far wing contributions of shorter wavelength lines and/or to the formation of H_2O molecule clusters that exhibit far more complex vibrational and rotational transitions (which tend to a continuum) than the isolated molecules.

Atmospheric Scattering

Apart from the atmospheric absorption, the extinction of radiation propagating in atmosphere happens through scattering of radiation. In order to formulate quantitatively the effect of scattering, the angular distribution of the scattered radiation must be specified. This is described by the scattering phase function $p(\cos\alpha)$ where α is the angle between the incident and scatted radiation. The simplest case is when the scattering is isotropic, then $p(\cos\alpha) =$ constant. In general, the phase function can be written as a series of Legendre polynomials and is often rather complex. For practical applications it is useful to introduce the asymmetry parameter g, which may be interpreted as the average value of $\cos\alpha$ for a large value of scattered photons, as

$$g = \frac{1}{4\pi}\int_{4\pi} p(\cos\alpha)\cos\alpha d\Omega. \tag{6}$$

Note that $-1 \leq g \leq 1$ and in general $g > 0$ implies preferential scattering in the forward direction, $g < 0$ implies scattering in the backward direction, while $g = 0$ corresponds to isotropic scattering. In terms of g, the phase function may be modeled with the Henyey–Greenstein phase function

$$p_{\mathrm{HG}}(\cos\alpha) = \frac{1-g^2}{(1+g^2-2g\cos\alpha)^{3/2}}\,. \tag{7}$$

Any atmospheric constituent (gas and particles) may be seen as a scatterer of EM radiation, strongly depending on its size, shape, and composition. It is usually useful to introduce the nondimensional size parameter:

$$x = \frac{2\pi r}{\lambda} \tag{8}$$

in which r is the radius of a spherical particle or of a sphere having the same volume of the particle. This assumption is usually appropriate for most of the atmospheric constituents, such as molecules, cloud droplets, and rain, but it is rather crude for ice crystals, snowflakes, and solid-phase aerosols. In general, particles that are far smaller than the wavelength will scatter only weakly (though they may still absorb

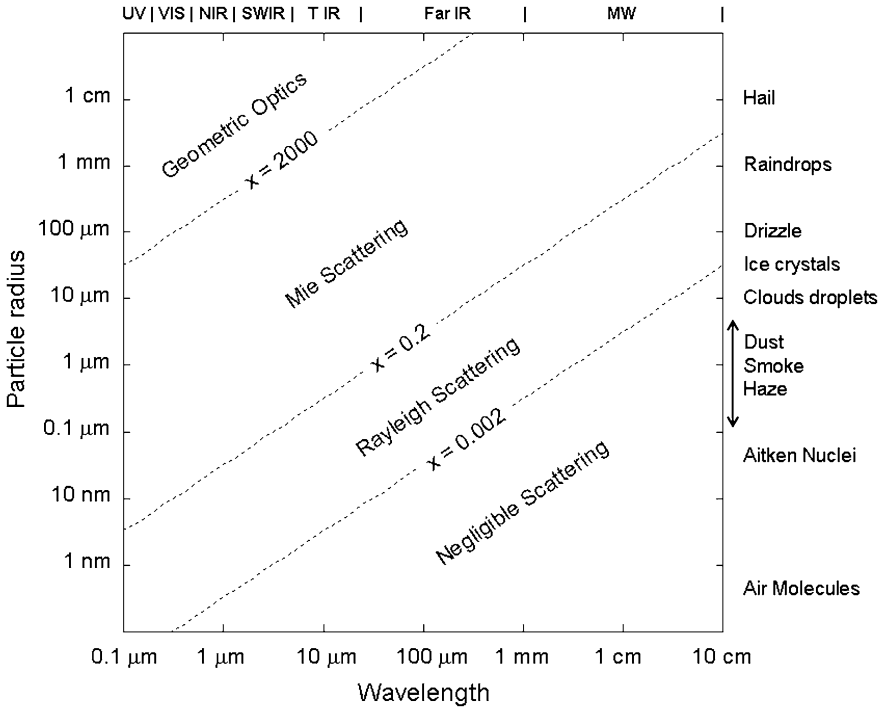

Fig. I.1.1 Relationship between particle size, radiation wavelength, and scattering behavior (adapted from Petty, 2006)

radiation). On the other hand, particles that are very large compared to the wavelength of radiation will interact with radiation following the laws of geometric optics for homogeneous media. For other particles falling in between the two extremes above, more complex methods are needed to compute their scattering properties. Given the size of a particle and the incident wavelength (and thus, the value of x), it can be readily determined whether scattering is likely to be significant and which scattering regime is most applicable (Rayleigh, Mie, or geometric optics), as pictured in Fig. I.1.1. Finally, the particle composition affects the scattering properties through the relative index of refraction with respect to air, which in turn is a function of wavelength.

Scattering by Atmospheric Molecules

In clear air, i.e., in the absence of clouds and aerosols, it is mostly absorption by gas that controls the atmospheric extinction. However, at shorter wavelengths (visible and UV), air molecules can significantly scatter radiation.

When a particle is sufficiently small relative to incident wavelength, i.e., $x \ll 1$, the whole particle experiences simultaneously the same externally imposed

oscillating electric field and becomes partially polarized. This corresponds to the classical model for interpreting the Rayleigh scattering, which leads to the following phase function and scattered intensity:

$$p(\cos\alpha) = \frac{3}{4}(1 + \cos^2\alpha), \tag{9}$$

$$I \propto \frac{1}{\lambda^4}(1 - \sin^2\alpha\cos^2\varphi), \tag{10}$$

where φ is the polar angle of the incident radiation taken from an arbitrary starting direction. Thus, in the Rayleigh scattering regime the intensity of scattered radiation is inversely proportional to the fourth power of the radiation wavelength. Calling m the relative refraction index of the particle with respect to the surrounding medium, the absorption and scattering efficiencies, respectively, are

$$Q_\mathrm{a} = 4x\Im\left(\frac{m^2-1}{m^2+2}\right), \tag{11}$$

$$Q_\mathrm{s} = \frac{8}{3}x^4\left|\frac{m^2-1}{m^2+2}\right|^2, \tag{12}$$

where $\Im$ indicates the imaginary part of a complex number. Noting that Q_a is proportional to x while Q_s to x^4, it follows that for sufficiently small particles, like molecules, assuming a complex relative index of refraction (otherwise $Q_\mathrm{e} = 0$), $Q_\mathrm{s} << Q_\mathrm{a} \sim Q_\mathrm{e}$. Therefore, for sufficiently small particles with complex refractive index, scattering is negligible and absorption is proportional to mass path only. As sketched in Fig. I.1.1, atmospheric molecules exhibit negligible scattering for wavelength longer than visible and exhibit Rayleigh scattering in the visible-to-UV range.

Scattering and Absorption by Atmospheric Particles

In addition to the gas molecules, there is a large variety of particles floating in the atmosphere, including cloud droplets, ice crystals, rain drops, snowflakes, smoke, dust, and pollen. The typical size of these particles ranges from fraction of a micrometer to a few centimeters. Depending on the size and composition these particles can scatter and/or absorb radiation. The rigorous theory of Mie can be used for dielectric spheres of arbitrary size, which leads to the following absorption and scattering efficiencies:

$$Q_\mathrm{e} = \frac{2}{x^2}\sum_{n=1}^{\infty}(2n+1)\Re(a_n + b_n), \tag{13}$$

$$Q_\mathrm{s} = \frac{2}{x^2}\sum_{n=1}^{\infty}(2n+1)\left(|a_n|^2 + |b_n|^2\right), \tag{14}$$

where $\Re$ indicates the real part of a complex number and the coefficients a_n and b_n are referred to as Mie scattering coefficients, which are functions of x and m.

For $x = 0$, the asymmetry parameter g is also zero, as in the Rayleigh regime. As x increases, g increases very rapidly up to a plateau at about 0.8–0.95; this indicates that particles comparable to or larger than the wavelength tend to strongly forward scattering. The Mie solution yields results that converge to the geometric optics for large x values (i.e., >50) and to Rayleigh solution for small x values (<0.6).

For any particle type, usually there will be a combination of sizes given by the particle size distribution function $n(r)$ (number of particles of radius r per unit volume of air). The volume extinction coefficient (and analogously for the scattering and absorption coefficients) for the distribution of particles described by $n(r)$ is

$$\beta_e = \int_0^\infty n(r) Q_e(r) \pi r^2 dr. \tag{15}$$

As sketched in Fig. I.1.1, the Rayleigh regime is valid at microwave wavelengths for particles as large as raindrops. In the Rayleigh regime, a cloud behaves like an homogeneous medium rather than a collection of discrete scatterers. Clouds in the visible band strongly scatter sunlight but absorb very little, practically zero. Smoke on the other hand absorbs strongly visible radiation.

2.2.2 Atmospheric Transmission

The fall off of the radiation intensity at wavelength λ as a function of the geometric distance along an arbitrary propagation direction s can be expressed as

$$I_\lambda(s) = I_\lambda(0) \exp(-\beta_e(\lambda) s). \tag{16}$$

Considering an infinitesimal distance ds over which the extinction coefficient may be assumed constant, the equation above leads to Eq.(3), rewritten here as

$$dI_\lambda(s) = -I_\lambda(s) \beta_e(\lambda, s) ds. \tag{17}$$

By integrating we obtain a general form of the Beer's law:

$$I_\lambda(s_b) = I_\lambda(s_a) \exp\left(- \int_{s_a}^{s_b} \beta_e(\lambda, s) ds \right). \tag{18}$$

The integral quantity is called the optical depth (or thickness) τ_λ from which we obtain the atmospheric transmittance:

$$T_\lambda(s_a, s_b) = e^{-\tau_\lambda(s_a, s_b)}. \tag{19}$$

In a plane parallel approximation of the atmosphere, which assumes that the extinction coefficient depends only on the vertical distance z, the optical thickness becomes

$$\tau_\lambda(z_a, z_b) = \int_{z_a}^{z_b} \beta_e(\lambda, z) dz \tag{20}$$

and the transmission for the radiation propagating with direction $\mu \equiv |\cos \vartheta|$, where ϑ is the angle of propagation relative to the zenith direction, is

$$T_\lambda(z_a, z_b) = \exp\left(-\frac{\tau_\lambda(z_a, z_b)}{\mu}\right). \tag{21}$$

The atmosphere is composed of a mixture of gases and particles (hydrometeors and aerosols) which have the capacity to absorb and/or scatter radiation in different ways at different spectral bands. In general, both absorption and scattering concur in attenuating the radiation traveling through the atmosphere. The total volume extinction coefficient (and analogously for the scattering and absorption coefficients) for the atmosphere is the sum of the corresponding coefficients for the individual components $\beta_e(\lambda) = \sum_i \beta_{e,i}(\lambda)$, where i indicates the ith constituent.

The overall transmittance of the cloud-free and aerosols-free atmosphere is controlled primarily by absorption due to constituent gases. In fact, in the absence of particles in the atmosphere, the extinction is largely dominated by the gaseous absorption; however, at visible and shorter wavelengths, air molecules significantly scatter the EM radiation. The scattering cross section is approximately proportional to λ^4 and thus it is stronger in the UV while becomes almost negligible in the IR.

The characteristics of cloud-free and aerosols-free atmospheric transmission for the EM spectrum from UV to MW are shown in Fig. I.1.2. Note that the transmittance was computed for a standard mid-latitude atmosphere; in a much drier (moister, respectively) environment the water vapor amount would be much less (more) so that the atmosphere would be substantially more (less) transparent in the H_2O absorption bands. Starting in the UV band, we see that the atmosphere is almost completely opaque to radiation with $\lambda < 0.3$ μm, due to oxygen and ozone absorption. Conversely, the atmosphere is quite transparent throughout most of the visible band ($0.4 < \lambda < 0.7$ μm). From 0.7 to 4 μm, in the near IR (NIR) and shortwave IR (SWIR) regions, the atmosphere presents many features due to the absorption of mostly water vapor (WV) and in less extent CO_2, CH_4, N_2O. Through the thermal IR (TIR) band, from 4 to 50 μm, the atmosphere presents broad bands of near-total absorption due to CO_2 (near 4 μm), H_2O (from 5 to 8 μm), ozone (near 9.6 μm), and again CO_2 ($\lambda > 13$ μm) as well as fairly transparent bands, so-called atmospheric windows (8–13 μm). From 50 μm to 1 mm, the far IR range, the atmosphere is almost completely opaque due to the strong absorption of H_2O. At longer wavelengths, in the microwave region from 1 to 100 mm (300 to 3 GHz), the atmospheric

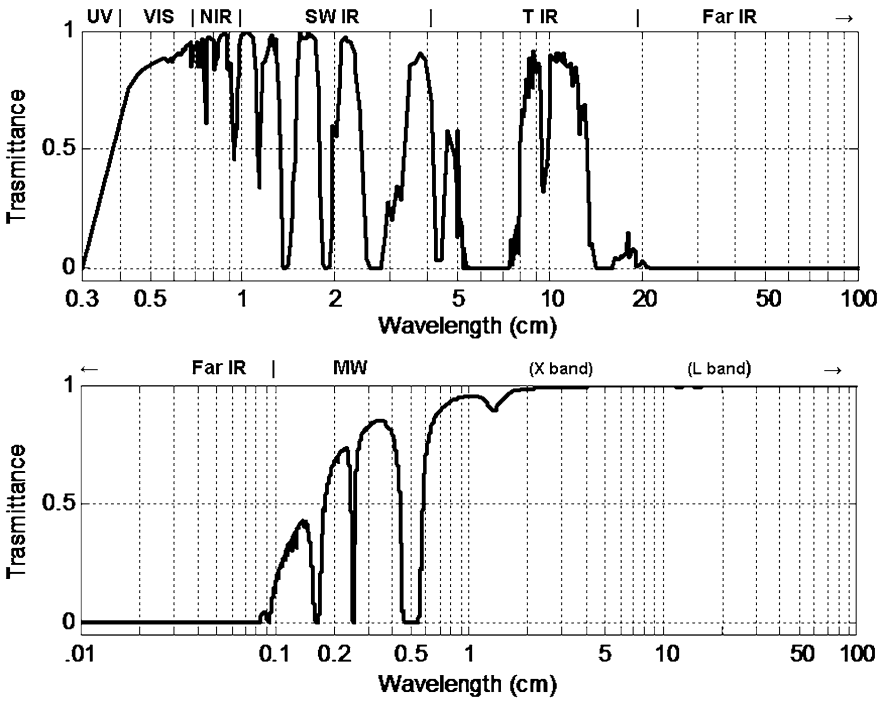

Fig. I.1.2 Transmission of cloud-free and aerosols-free atmosphere from the UV to the MW range. Calculations were made with a line-by-line radiative transfer code for a standard mid-latitude atmosphere (adapted from Elachi, 1987; data courtesy of Tiziano Maestri, University of Bologna)

absorption is dominated by water vapor and oxygen contributions. In particular, the atmosphere is increasingly transparent with longer wavelengths, due to the wing of strong WV absorption in the far IR, except that WV presents selective absorption near 183 and 22 GHz ($\lambda \sim 1$ and 10 mm, respectively), while oxygen near 120 GHz ($\lambda \sim 2.5$ mm) and from 50 to 70 GHz ($\lambda \sim 5$ mm). Then, the atmosphere becomes nearly transparent for $\lambda > 15$ mm (20 GHz).

In the presence of particles (such as aerosols and/or hydrometeors forming clouds), their contribution to the extinction is a combination of both absorption and scattering which strongly depends on the size, composition, and chemical–physical properties of the particle.

Aerosols' optical depths are usually less than a tenth of unit and only reach comparatively large values (unity or greater) in case of smoke, dust storms, and severe pollution events. Conversely, clouds may easily achieve large optical depths. The contribution of clouds to extinction is almost purely scattering at shorter wavelengths, while it becomes strongly absorbing in the IR range. At longer wavelengths, the scattering contribution tends to become negligible, and also the absorption decreases substantially, so that clouds in the microwave region are rather, but not completely, transparent.

2.2.3 Atmospheric Emission

From the concept of an ideal black body and Kirchoff's law, it is known that the emission from a black body depends only on its temperature and that the higher the temperature of the body, the more is its emission. The spectral distribution of a blackbody emission is given by the Planck's law, which expresses the radiance $B_\lambda(T)$ emitted from a blackbody at temperature T and wavelength λ as

$$B_\lambda(T) = \frac{2hc^2}{\lambda^5} \frac{1}{(\exp(hc/\lambda kT) - 1)}, \tag{22}$$

where h and k are the Planck's and Boltzmann's constants, respectively. From simple consideration about Kirchoff's law, it is known that atmosphere both absorbs and emits radiation. Therefore, the same thin layer of ds thickness discussed above will emit radiation as

$$dI_{\text{emit}} = -dI_{\text{a}} = \beta_{\text{a}} B ds, \tag{23}$$

where we drop the wavelength λ index for convenience and thus B indicates the Planck function $B_\lambda(T)$. The net change in radiant intensity at the boundaries of the thin layer is given by the Schwartzschild's equation:

$$\frac{dI}{ds} = \beta_{\text{a}}(B - I). \tag{24}$$

This equation represents a fundamental description of radiative transfer equation (RTE) in a non-scattering medium, which is a reasonable approach for most of the problems involving IR and MW. This equation can be solved for the intensity reaching a sensor looking at a particular direction of propagation:

$$I(0) = I(\tau)e^{-\tau} + \int_o^\tau B e^{-\tau} d\tau. \tag{25}$$

Considering the case of a plane parallel non-scattering atmosphere and a sensor located at the surface, the RTE can be written as

$$I^{\downarrow}(0) = I^{\downarrow}(\infty)e^{-\tau(0,\infty)/\mu} + \int_o^\infty B(z)\frac{\beta_{\text{a}}(z)}{\mu} e^{-\tau(0,z)} dz, \tag{26}$$

where $z = \infty$ represents an arbitrary point beyond the top of the atmosphere. For sensors sensitive to flux rather than intensity, the flux at the surface is obtained simply by integrating the intensity over one hemisphere of solid angle:

$$F^{\downarrow}(0) = 2\pi \int_0^1 I^{\downarrow}(0,\mu)\mu d\mu. \tag{27}$$

Finally, one may take this equation and simply integrate over wavelength to obtain broadband radiative flux at surface.

2.2.4 Radiative Transfer with Scattering

In the case where the atmosphere contains clouds and/or aerosols, the scattering source term in the radiative transfer equation becomes important; all of the above interactions, absorption, emission, scattering, and transmission will simultaneously take place, and their relative importance depends on wavelength, atmospheric composition, and the size, shape, and composition of the particles. In the situation considered here, namely upward-looking radiometers viewing an absorbing and scattering medium, the equation that relates the primary observable, radiance, to the atmospheric state becomes:

$$\mu \frac{dI(\mu,\phi)}{d\tau} = I(\mu,\phi) - J(\mu,\phi). \tag{28}$$

Here, the source function for both emission and scattering is a weighted sum of thermal emission and scattering from other directions, the single scattering albedo controlling the weight assigned to each term:

$$J(\mu,\phi) = (1-\omega)B + \frac{\omega}{4\pi}\int_0^{2\pi}\int_{-1}^{1} p(\mu,\phi;\mu',\phi')I(\mu',\phi')d\mu' d\phi', \tag{29}$$

where $\mu \equiv |\cos\vartheta|$, $\mu' \equiv |\cos\vartheta'|$, and $\vartheta, \phi, \vartheta', \phi'$ are the spherical angular coordinates of the incident and scattered radiation, respectively. Finally, the RTE in the presence of absorption, emission, and scattering for a plane parallel atmosphere is given by

$$\mu \frac{dI(\mu,\phi)}{d\tau} = I(\mu,\phi) - (1-\omega)B - \frac{\omega}{4\pi}\int_0^{2\pi}\int_{-1}^{1} p(\mu,\phi;\mu',\phi')I(\mu',\phi')d\mu' d\phi'. \tag{30}$$

3 Instrumentation

Radiometer is a generic term used to indicate all the passive instruments measuring radiation. There is a large variety of ground-based radiometric instruments that are used for atmospheric research and applications. Some instruments work in the shortwave range (UV to visible), other in the longwave range (IR to MW), some

instruments observe radiation intensities, other fluxes of radiation, some in broad other in narrow to quasi-monochromatic bands. This section introduces just a few of these instruments, selecting those that are treated in the later chapters of this book. Since some of these are commercially available, we, of course, do not endorse any particular instrument.

3.1 Calibration

A key issue of radiometric instrument and observations is accurate calibration. In fact, the naturally emitted signal may be of the same order or even smaller than the noise emitted by the instrument itself. Thus, to derive quantitative information on the atmosphere from radiometric measurements, accurate calibration is required.

Some radiometric receivers have one or two internal noise sources that provide some measure of calibration. However, component losses, lack of complete knowledge of radiometric parameters, and a host of other causes usually dictate that some external calibration method also be employed. Assuming square law detectors, in which the output voltage is proportional to the input power, a seemingly straightforward calibration method is to view two external blackbody targets that are kept at two widely separated temperatures. Preferably, the target radiances bracket the range of radiances emitted from the scene. It is important to construct targets with high emissivity such that reflections from external sources are negligible and to have the targets sufficiently large to fill the instrument field of view. Targets are frequently constructed with a surface having high thermal conductivity covered with a thin layer of very absorbing material. The target is frequently embedded in a thermal insulator that is transparent to incoming radiation. Finally, when a target is placed in a thermal environment in which the environmental temperature differs greatly from desired target temperature, measurements of target temperatures at several locations within the target are essential.

The use of blackbody targets immersed in cryogenic fluids, such as liquid nitrogen (LN_2), is another commonly used method of establishing calibration (McGrath and Hewison, 2001; Cimini et al., 2003c). In this method, a blackbody target is immersed in the cryogen and the radiometer looks directly at the target. Allowance for the reflection of the ambient scene must be made, and the reflection coefficient of the cryogen must also be known.

For radiometers operating at transmission window wavelengths, the so-called tipping curve calibration method (or tipcal) can give a high degree of accuracy. In this method, brightness temperatures are measured as a function of elevation angle θ and are then converted to opacity $\tau(\theta)$ (Westwater, 1993). If the system is in calibration, then the linear fit of $\tau(\theta)$ as a function of optical air mass will pass through the origin; conversely, if the linear fit does not pass through the origin, then a single parameter in the radiometer equation is adjusted until it does. The most serious errors affecting this method are those caused by non-stratified atmospheric conditions and can occur due to clouds and horizontal variations in the water vapor field.

3.2 Pyrometers

The term pyrometer is generally used to indicate a remote sensing device that intercepts and measures broadband thermal radiation; the word pyrometer comes from the Greek words pyro (fire) and meter (to measure). A pyrometer consists of an optical system and a detector. The optical system focuses the thermal radiation onto the detector. The output signal of the detector is related to the irradiance [W/m^2] of the target through the Stefan–Boltzmann law. Depending on the range of wavelengths they are sensitive to, pyrometers may be used to measure direct and/or diffuse visible radiation, atmospheric, or ground IR radiation or to determine the temperature of an object's surface; in all these cases, the instruments acquire more specific names, as discussed below.

3.2.1 Pyrgeometer

A pyrgeometer is a device that measures the irradiance investing a plane surface detector and emitted by the Earth (geo in Greek) in a broad IR band that extends approximately from 4.5 to 100 μm. This is commonly used for measuring the incoming thermal radiation from the sky and clouds or the outgoing thermal radiation from the ground. The pyrgeometer thermopile detector measures the net radiation balance between the incoming and outgoing longwave radiation flux and converts it to a voltage according to $E_{\text{net}} = U/S$ where E_{net} is the net radiation at sensor surface [W/m^2], U is the thermopile output voltage [V], and S is the sensitivity/calibration factor of instrument [V/W/m^2]. The value for S is determined during calibration of the instrument, which is performed at the production factory with a reference instrument traceable to a regional calibration center.

To derive the absolute downward longwave flux, the temperature of the pyrgeometer has to be taken into account. It is measured using a temperature sensor inside the instrument, near the cold junctions of the thermopile, and assuming the pyrgeometer to approximate a black body. Thus, it emits longwave radiation according to $E_{\text{out}}=\sigma \cdot T^4$, where E_{out} is the longwave radiation emitted by the Earth's surface [W/m^2], σ is the Stefan–Boltzmann constant [W/(m^{2}K^4)], and T is the absolute temperature of pyrgeometer detector [K]. From the calculations above the incoming longwave radiation can be derived. This is usually done by rearranging the equations above to yield the so-called pyrgeometer equation:

$$E_{\text{in}} = U/S + \sigma T^4. \tag{31}$$

As a result, the detected voltage and instrument temperature yield the total global longwave downward radiation.

Finally, the net longwave radiation can be calculated using two pyrgeometers, one looking up and one looking down, ideally mounted on the same plate such that the temperature of the pyrgeometers is the same and is irrelevant for the net radiation calculation.

3.2.2 Pyranometer

A pyranometer is a device used to measure broadband visible irradiance coming from the sky (*ano* in Greek) on a planar surface from a field of view of 180°. This irradiance contains of course both direct and diffuse solar radiation in a range extending approximately from 0.3 to 2.8 μm. Similarly to pyrgeometers, with two pyranometers, one pointing at zenith the other at nadir, it is possible to measure the net shortwave radiation: the upper sensor measures incoming global solar radiation and the lower sensor measures solar radiation reflected from the surface below.

Converting the two signal outputs to irradiance [W/m^2], the surface albedo (I_r/I_i) can be simply calculated; therefore such a system is also called albedometer.

3.2.3 Pyrheliometer

A pyrheliometer is an instrument designed specifically to measure the normal incidence direct beam solar irradiance. This is achieved by the shape of the collimation tube, always pointing orthogonally to the radiation beam the sun disk with a field of view limited to 5°, and by the quartz window acting as a filter that passes solar radiation only between 0.2 and 4 μm.

3.2.4 Infrared Thermometers

Instruments capable of measuring thermal radiation from an object and providing an output signal calibrated in temperature units are called radiation thermometers. In accordance with Planck's law, the radiances are clearly related to the temperatures, provided the relative spectral response is known. The output signal of a linear detector is proportional to the measured radiance, and thus it is possible to calibrate the output signal in temperature units (i.e., Kelvin).

A radiation thermometer measuring the radiance in an IR broad band is called IR thermometer (IRT). It provides measurements of the equivalent blackbody brightness temperature of the scene in its field of view. In this contest, IR thermometers are used to measure either the radiating temperature of the ground surface or the sky temperature in a given direction for detecting the presence of clouds. For calibration purposes, the IRT is placed in front of a blackbody calibration source (with known and high emissivity) whose temperature must be measured by means of a calibrated probe.

3.2.5 Examples

Kipp & Zonen CN1

Kipp & Zonen (http://www.kippzonen.com/) is marketing a range of net radiometers for the measurement of incoming and outgoing short- and longwave radiation. Moreover, Kipp & Zonen offers a variety of broadband radiometers measuring thermal radiation. All types are virtually maintenance-free and designed for continuous outdoor use. The main applications are in agrometeorology (evapo-transpiration and

Fig. I.1.3 Picture of the Kipp & Zonen CNR 1 net radiometer (*right*) and the MT5 microwave radiometer (*left*) during the outdoor deployment at ISSAOS 2007 in L'Aquila

crop damage prevention) and in climatology, meteorology, and hydrology for measurement of the radiation balance, and in renewable energy industry (heat exchange in thermal solar systems). The CNR 1 is a net radiometer combining two thermopile pyranometers for shortwave radiation measurements (including incoming solar radiation, reflected radiation, albedo, radiation balance) with two pyrgeometers for far infrared measurements (sky radiation, ground surface radiation, radiation balance) providing four separate signal outputs. The CNR 1 is very accurate and reliable and it is often used as the reference instrument for a network of lower performance net radiometers. A picture of the CNR 1 net radiometer deployed during the outdoor lectures at ISSAOS 2007 is shown in Fig. I.1.3.

3.3 Microwave Radiometers

A device measuring radiant intensity in discrete bands in the wavelength range from 10 cm to 0.5 mm is called a microwave radiometer (MWR). The MWRs commonly deployed for remote sensing of the troposphere use either single or multi-channel with frequency in the range between 10 and 400 GHz. The calibration of MWR relies on opportune combinations of internal noise sources, external targets, cryogenic loads, and tipping curve methods (Cimini et al., 2007a). The major advantage of microwave remote sensing is that even in the presence of thick clouds, fog, or drizzle, thermodynamical properties of the atmosphere can be determined with good accuracy. In the last decade, since it was recognized that the implementation of operational networks of microwave radiometers was hampered

by the cost and complexity of the available instruments, a major objective has been to develop network-suitable low-cost and robust microwave radiometers. A short list of commercially available and commonly used MWR is given hereafter. More information on the hardware design, observations techniques, and applications of MWR is available in Janssen (1993) and Westwater et al. (2005).

3.3.1 Single-Channel Temperature Profiler

A single-channel MWR can be used for the retrieval of atmospheric temperature profiles in the atmospheric boundary layer (ABL) from 0 to 600 m above ground level. The technique consists of measuring atmospheric emission at different angles in a wavelength band that exhibits relatively high atmospheric attenuation. Usually this kind of MWRs operates near the peak of the strong oxygen band at 60 GHz (wavelength 5 mm). From the downwelling radiation at different elevation angles we can retrieve atmospheric air temperature gradients with respect to horizontal air temperature. In fact, the radiation in the horizontal direction can be used as a reference level since the brightness temperature (T_b) is essentially equal to the air temperature at the measurement height. Thus, an accurate air temperature measurement provides a calibration of the radiometer offset. The versatility and the robustness of the technique outline the potential of these instruments as a useful tool for integrated ground-based remote sensing systems.

3.3.2 Multi-Channel Temperature and Humidity Profilers

Atmospheric temperature and humidity profiles can be retrieved by multi-channel MWR observations. The set of channels is selected to observe atmospheric brightness temperatures in few frequency bands from 22 to 30 GHz, sensitive to water vapor and liquid water, and in few other bands from 51 to 59 GHz, sensitive to air temperature (Solheim et al., 1998; Ware et al., 2003; Rose et al., 2005).

MWR operating at higher frequencies (50–400 GHz) has been demonstrated to provide enhanced sensitivity and accuracy in the retrieval of humidity profiles in extremely dry environments (Cimini et al., 2007a). These instruments typically observe brightness temperatures in few channels from 51 to 59 GHz, sensitive to air temperature, few other channels around the 183.31 and/or 380.2 GHz water vapor absorption lines, plus few more channels in atmospheric windows, as at 90, 150, and 340 GHz.

3.3.3 Examples

Kipp & Zonen MTP5

Kipp & Zonen (http://www.kippandzonen.com) is marketing a radiometer that was originally designed and deployed by the Russian firm ATTEX (Kadygrov and Pick, 1998; Westwater et al., 1999). The radiometer is a single-channel (60 GHz) solid-state Dicke-type super-heterodyne receiver that is electronically chopped at 1 KHz between the sky and a reference noise source. The antenna is a scalar

horn with a full-width-half-power (FWHP) beam width of 6º and scans by viewing a flat reflector at each of 11 scanning angles. Because of the 2 GHz bandwidth and a low receiver noise temperature of 600 K, a high sensitivity of 0.04 K is achieved. Calibration of the receiver is achieved by 0.1°C temperature control and a switched internal noise generator. A one-point absolute calibration is achieved either by viewing an external target or by knowing the emission temperature in the horizontal direction. A variation of this radiometer, developed at NOAA, scans continuously in a 360º vertical plane and, in addition to temperature profiles, can also be used to measure air–sea temperature difference (Trokhimovski et al., 1998; Cimini et al., 2003a–c). A picture of the MTP5 microwave radiometer deployed during the outdoor lectures at ISSAOS 2007 is shown in Fig. I.1.3.

Radiometrics MP-3000

Radiometrics Corporation (http://www.radiometrics.com) has developed a multi-frequency microwave radiometer that is based on a highly stable, tunable, and synthesized local oscillator in the receiver. This design overcomes errors caused by receiver frequency drift while allowing observation of a large number of frequencies across wide tuning ranges (currently 35). The total power receiver has a highly stable noise diode that is used as a gain reference. It also measures zenith infrared temperature, surface temperature, humidity, and pressure. The instrument is portable and has automated elevation- and azimuth-scanning capability, and the observation interval can be as short as several seconds (Fig. I.1.4).

Fig. I.1.4 Picture of the Radiometrics MP-3000A, a multi-channel MWR for temperature and humidity profiling

RPG-HATPRO

The Radiometer Physics GmbH (http://www.radiometer-physics.de) is commercializing a 14-channel humidity and temperature profiler (RPG-HATPRO) from 22 to 60 GHz. The RPG-HATPRO comprises total-power radiometers utilizing direct detection receivers at all frequencies. The receivers of each frequency band are designed as filter banks in order to acquire each frequency channel in parallel. This approach avoids problems that might arise from mixers or local oscillators and possible interferences caused by communication systems that frequently operate near the IF frequencies. In addition, the flexibility to adjust each channel bandwidth individually allows for optimizing temperature profiling for both boundary layer and full troposphere.

3.4 Infrared Interferometers

A spectrometer in general is a device that measures radiant intensity as a function of wavelength. Fourier transform infrared (FTIR) spectroscopy is a passive technique for the observations of thermal radiation with high spectral resolution. FTIR radiometers measure the absolute infrared spectral radiance (W/m^2 st cm^{-1}) of the sky with a spectral range of typically 500–3,000 cm^{-1} (wavelength ~20–30 μm), a spectral resolution of the order of 1.0 cm^{-1}, and an instrument field of view of about 1°–2°. The instrument core is a Michelson interferometer, which allows the downwelling atmospheric emission in the entire bandwidth to be viewed simultaneously. Thus, FTIR spectrometers measure the interferogram of the EM spectrum of interest and a fast Fourier transform of the measured interferogram then yields the radiance spectrum. The advantages of the interferometric approach with respect to other spectral-resolving techniques (such as filters, grids) are multifold and can be summarized in the delivery of fast, simultaneous, fine, and accurately resolved radiance spectra.

Spectra observed from two blackbodies at known temperatures are used to calibrate the atmospheric spectrum (Revercomb et al., 2003). Two well-characterized blackbody targets are used, and a rotating gold-plated scene mirror is used to direct radiation from the target (either the sky or one of the blackbodies) into the interferometer. Collection of each spectrum takes few seconds, but averaging is performed to reduce random noise. Calibrated atmospheric spectra are typically available every few minutes (5 to 15), though rapid sampling mode is also available at 1 min temporal resolution (Demirgian and Dedecker, 2005). To estimate the uncertainty in the FTIR observation, uncertainties in the blackbody temperatures and emissivities must be propagated via the linear calibration equation to derive a root sum of square error in the observed spectrum (Knuteson et al., 2004b). The calibration procedure also accounts for detector nonlinearity, spectral calibration, including the removal of interferometer self-apodization effects and spectral scale normalization. Typical residuals of a side-by-side comparison of two instruments show radiance differences smaller than 0.5 mW/ m^2 st cm^{-1}.

In the last 2 decades, significant efforts have been spent for advancing FTIR interferometers toward an unattended instrument for 24/7 deployment. This requirement for 24/7 unattended operation leads to the implementation of hardware (e.g., mechanical coolers) and robust software. The state-of-the-art of operational FTIR has demonstrated radiometric accuracy of better than 1% of ambient radiance, with a reproducibility of better than 0.2%. The spectral calibration is known to be better than 1.5 ppm using known spectral positions of atmospheric lines.

The measured atmospheric IR spectra have a variety of applications, including the evaluation of line-by-line radiative transfer codes (Tobin et al., 1999), cloud and aerosol detection and quantification (Turner et al., 2003a), and the retrieval of vertical profiles of temperature and water vapor in the atmospheric boundary layer (Feltz et al., 2003).

3.4.1 Examples

AERI

The atmospheric emitted radiance interferometer (AERI) is a fully automated, ground-based, passive interferometer that measures high spectral resolution downwelling infrared radiance from 500 to 3,000 cm^{-1} (19–3.3 μm), developed by the University of Wisconsin—Madison (Revercomb et al., 2003). An extended range (ER) unit, reaching 25 μm (400 cm^{-1}), was developed for the study of the extremely dry atmosphere typical of the poles. The maximum optical path delay is approximately ± 1 cm, resulting in a maximum unapodized spectral resolution of 0.5 cm^{-1}.

The calibration goal for the AERI is to observe downwelling atmospheric radiance with an accuracy of better than 1% of the ambient (near surface) radiance (Revercomb et al., 1993). The blackbodies are high-emissivity (greater than 0.995) targets that contain accurate National Institute of Standards and Technology (NIST) traceable temperature sensors. The temperature of one of the blackbodies is fixed at 60°C, while the other is allowed to float at the ambient temperature. One of the advantages to using an ambient calibration target is that much of the emission measured by the AERI is from the atmosphere very close to the instrument. Therefore, the calibration error is very small for temperatures very near the surface temperature.

More details on the AERI instrument, calibration, and the uncertainties in its observations are provided by Knuteson et al. (2004a, b). AERI observations are routinely acquired at ARM sites in tropical, mid-latitude, and Arctic environments.

EISAR

The emission infrared spectrometer for atmospheric research (EISAR) belongs to the German Meteorological Service (DWD) and it is used for routine observations

at the Lindenberg Meteorological Observatory as part of their atmospheric long-term monitoring commitment (Reichardt and Güldner, 2009). Its detector offers an effective spectral range from 600 to 3,000 cm^{-1} with a maximum spectral resolution of 0.3 cm^{-1}. A typical EISAR observation starts with a view to a calibration wide-aperture blackbody set to a temperature 5°C above the dew point, then it performs a series of sky measurements, and finally it concludes with a view to the blackbody set to a temperature of about 50°C. The two blackbody reference spectra are used to correct the detector nonlinearities and thus to achieve the radiometric precision of 0.1 K and accuracy of 1.0 K. Calibrated atmospheric spectra are collected once every 15 min, though a rapid sampling mode is also possible at 1-min resolution.

4 Retrieval Techniques

Techniques to derive meteorological information from radiation measurements are generally based on the radiative transfer equation (RTE) in Eq. (30) or its linearized perturbation form. Because only a finite number of imperfect radiation measurements are available, and a continuum of parameters is needed to describe atmospheric profiles, a rigorous mathematical solution does not exist and the inverse problem is said to be ill-posed (Twomey, 1977). Therefore, it is better to regard the measurements as constraints and to blend them with supplementary sources of information or to drastically reduce the dimensionality of the inverse problem by projecting the profiles onto their linear functionals. Useful supplementary information can be provided by a priori information obtained from past data or by model simulations.

The RTE can be approximated by a Fredholm integral equation of the first kind (Rodgers, 2000) and in its discrete form is written as

$$g_e = Kf + \varepsilon, \tag{32}$$

where g_e is a vector composed of n measurements, f is an m-vector whose components represent the atmospheric parameters that we want to determine, K is an $n \times m$ matrix relating the measurements to the unknowns, and the n-vector ε explicitly denotes that the measurements have an unknown error component that will affect the solution to some degree. For mildly nonlinear problems, the perturbation form expressed is frequently used as the basis of subsequent iterations.

An excellent review article discussing techniques for solving the above Eq. (32) was written by Rodgers (1976) and further insights are given in Rodgers (2000). Many retrieval methods are used to solve Eq. (32), and we mention just a few frequently used in ground-based applications: statistical regression (Westwater, 1993), neural network inversion (Solheim et al., 1998), and Kalman filtering (Han et al., 1997). Finally, another technique developed in the last decade and of great promise is to combine radiometer data with a numerical forecast model (Löhnert et al., 2004; Hewison, 2007; Cimini et al., 2009).

5 Radiometric Sensing of Atmospheric Variables

This section provides a list of some selected applications of radiometric remote sensing to the monitoring of atmospheric variables that are important for meteorology, climatology, and weather hazards.

5.1 Energy Balance

The radiative equilibrium temperature of the Earth is determined by the balance between the energy absorbed from the sun and that emitted by the planet in the infrared. Climate studies and cloud/radiation interaction require breaking the Earth's energy budget down into its components. The radiative balance at the Earth surface is played by broadband shortwave (solar) and longwave (atmospheric/ground) irradiances with both their downwelling and upwelling components. Therefore, an integrated station for monitoring the total radiative flux exchange may be assembled

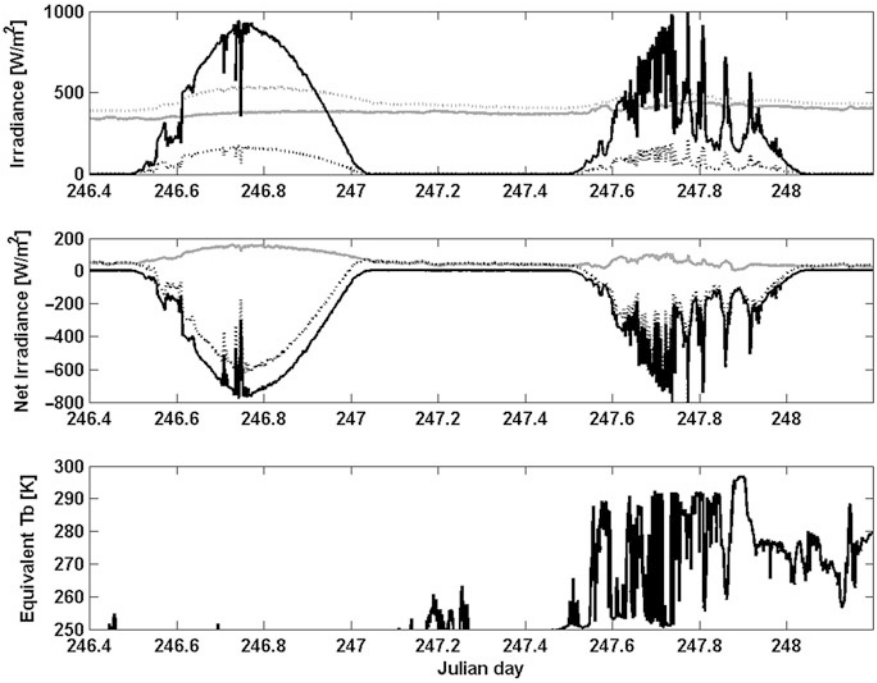

Fig. I.1.5 *Top*: Observations of shortwave (*black*) and longwave (*grey*) downwelling (*solid*) and upwelling (*dotted*) irradiances. *Center*: Total net irradiance (*dotted*) and net shortwave (*black*) and longwave (*grey*) irradiances. *Bottom*: Observations of sky temperature by an IRT indicate that day 246 was mainly cloud-free, while day 247 was prevalently cloudy (data courtesy of the ARM program)

using pyranometers, pyrgeometers, and pyrheliometers, providing continuous measurements of as many components as possible:

- Pyrheliometer: direct normal shortwave (solar beam)
- Pyranometers: global horizontal shortwave (total hemispheric), diffuse horizontal shortwave (no direct component), and upwelling shortwave (reflected)
- Pyrgeometers: downwelling longwave (atmospheric emission) and upwelling longwave (ground emission)

A time series of observed shortwave and longwave downwelling and upwelling irradiances at mid-latitude in fall is shown in Fig. I.1.5. The time series is extending for almost two complete days and thus it shows the diurnal cycle of solar insulation. Note that the first day was mainly cloud-free while the second day was prevalently cloudy as confirmed by the corresponding IRT sky temperature. The net shortwave and longwave irradiances are shown, which contribute to the total net radiation received by the Earth's surface; shortwave energy accumulated throughout the day is released by outgoing longwave radiation during the night. Considering the two pyranometers, one pointing at zenith the other at nadir, measuring the global shortwave irradiance it is possible to measure the net shortwave radiation and the surface albedo (I_r/I_i): the upper sensor measures incoming global solar radiation and the lower sensor measures solar radiation reflected from the surface below.

5.2 Integrated Contents of Water Vapor and Cloud Liquid Water

Both water vapor and cloud liquid are important variables in meteorology and climate. Due to thermodynamic processes of evaporation and condensation, as well as transport by winds, these quantities vary greatly in space and time. Water vapor is characterized by density as a function of spatial coordinates and time. Water vapor density is limited, depending on temperature, such that the relative humidity is in the range of 0–100%.

Dual-frequency measurements of brightness temperature at an optimum frequency near the 22.235 GHz water vapor line and in a transmission window have been used to measure the integrated water vapor (IWV) and liquid water path (LWP) for about 25 years (Hogg et al., 1983). This technique relies on the fact that the two channels respond in substantially different ways to IWV and LWP, so that the opacity contribution of these constituents can be separated with as little ambiguity as possible. Indeed, although both channels are sensitive to both IWV and LWP, the channel near 22.2 GHz has a proportionally larger response to IWV, while the reverse is true for the window channel. In particular, the water vapor channel is usually selected at one of the two so-called hinge points (Cimini et al., 2003a–c), where the pressure (i.e., height) dependence is minimized and thus the radiance is sensitive entirely to the integrated amount. For the retrieval of IWV, the window channel corrects for the changing LWP in the atmosphere. Similarly, the liquid water path

can be estimated from atmospheric emission measurements in the microwave region because in this spectral region, the cloud contribution strongly increases with frequency. For the retrieval of LWP, the channel close to the water vapor absorption line corrects for the changing water vapor concentration of the atmosphere.

The general accuracy of dual-frequency radiometric measurement of IWV has been shown to be better than 1 mm rms (Revercomb, 2003). Because of the lack of in situ measurements of cloud liquid, an adequate experimental evaluation of LWP over a range of cloud conditions is not available. The estimated accuracy for LWP retrievals is of the order of 25 g/m^2, of which about 10 g/m^2 is attributed to the measurement error while the rest can be attributed to the underdetermined retrieval problem. An example of IWV and LWP retrievals taken during the 2004 Arctic Winter Radiometric Experiment (Westwater et al., 2004) at the atmospheric radiation measurement (ARM) site in Alaska is shown in Fig. I.1.6.

The accuracy of IWV and LWP retrievals can be enhanced by using higher frequency channels, typically 90 and 183 GHz, as demonstrated for dry environments in the Arctic (Cimini et al., 2007b).

Improvements on the dual-channel method can be made with multi-frequency observations. For example, the additional use of the 90 GHz channel further constrains the LWP retrieval problem and improves its accuracy to less than 15 g/m^2

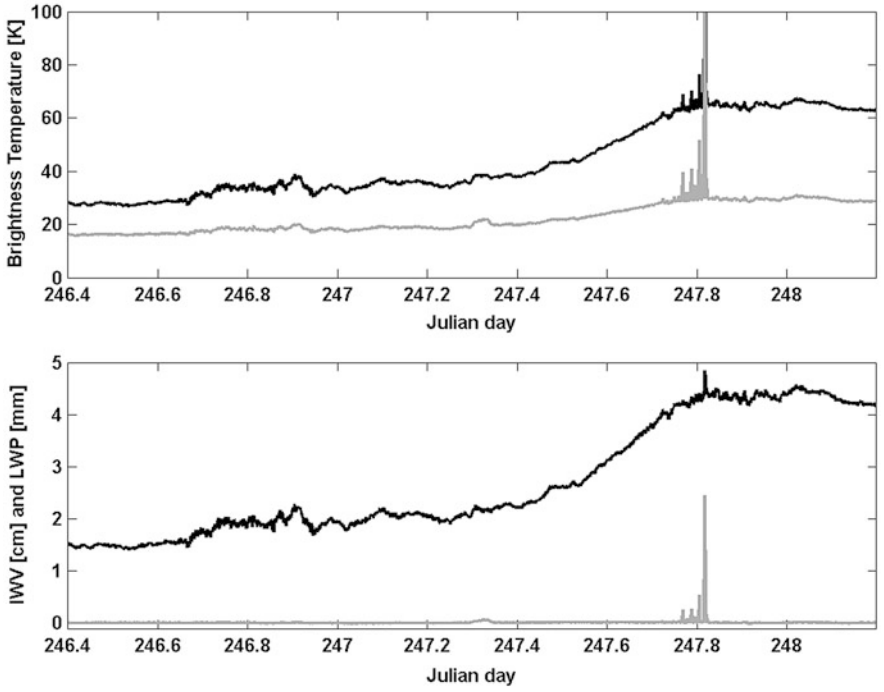

Fig. I.1.6 *Top*: Time series of brightness temperatures from a dual-channel MWR at 23.8 GHz (*black*) and 31.4 GHz (*grey*). *Bottom*: Corresponding IWV (*black*) and LWP (*grey*) (data courtesy of the ARM program)

(Crewell and Löhnert, 2003). Another recently developed method relies on the synergy of MWR and FTIR observations (Turner, 2007).

5.3 *Boundary Layer Temperature Profiling from Scanning Observations*

Angular techniques for measuring emission were developed by NOAA in the early 1970s (Westwater et al., 1975), but due to mechanical simplicity, the zenith-viewing multi-spectral radiometers were commonly deployed. However, in 1992, Russian scientists developed a scanning single-channel radiometer for routine monitoring of the boundary layer (Kadygrov and Pick, 1998). From the downwelling radiation at different elevation angles, atmospheric air temperature profiles can be obtained. As a simple way of explaining the technique, we know that for a constant absorption coefficient, for horizontally stratified atmosphere, and for temperature profile that changes linearly with height, the brightness temperature is equal to the air temperature at the position where the opacity is equal to 1. For more complex profiles, an inversion method must be used. The vertical resolution of the retrieved profiles is a function of altitude and ranges from about 10 m near the surface to about 300 m at the 500 m altitude. The retrieval accuracy (rms error) was shown to be better than 0.5 K below 500 m. Because of the simplicity and portability of the instrument and its extremely flexible characteristics, it has been used from airborne, ship-, and ground-based platforms (Westwater et al., 1999; Cimini et al., 2003a–c; Leuskii et al., 2000). An example of temperature profiles retrieved by such a single-channel radiometer during the NAURU99 field campaign (Cimini et al., 2003a–c) is shown in Fig. I.1.7.

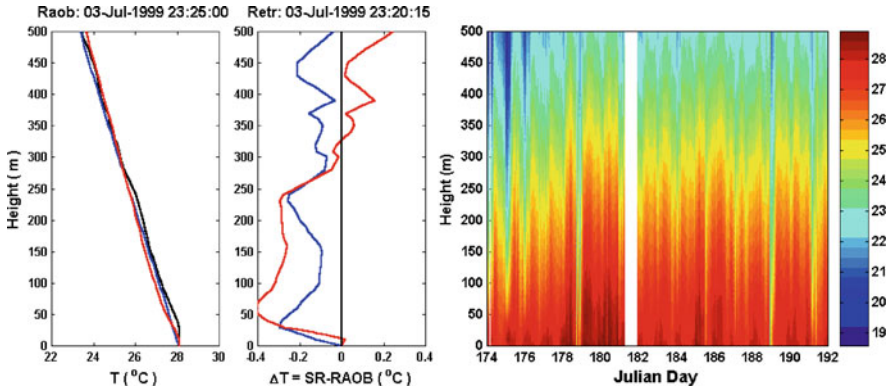

Fig. I.1.7 Boundary layer temperature profiles as measured by a radiosonde and retrieved by two independent single-channel scanning radiometers (*left*). Temperature residual between retrievals and radiosonde (*center*). Two-week time–height time series of temperature profiles (°C) retrieved by a single-channel scanning MWR (*right*) in the tropics

5.4 Temperature and Humidity Profiling by Multi-Frequency Observations

Radiometric temperature and humidity profiling can be accomplished by measuring the spectrum of radiation intensity at points along the side of an absorption line (Westwater et al., 1993). By scanning outward from the band center, where the opacity is larger, onto the wings of the band, where the radiometer "sees" deeper (higher) into the atmosphere, altitude information is obtained. Either shoulder of the band center is suitable for retrieval of temperature and humidity profiles information. Emission at any altitude is proportional to local temperature and abundance of the absorbing gas; channels close to water vapor lines (22.2 GHz, 183.2 GHz) are then used for humidity profile retrievals, while in case the absorbing gas has constant concentration, as for example for oxygen, the temperature profile can be retrieved.

Temperature and humidity profiles are estimated from radiometric observations by means of inversion methods, relying on a priori information on the statistics of

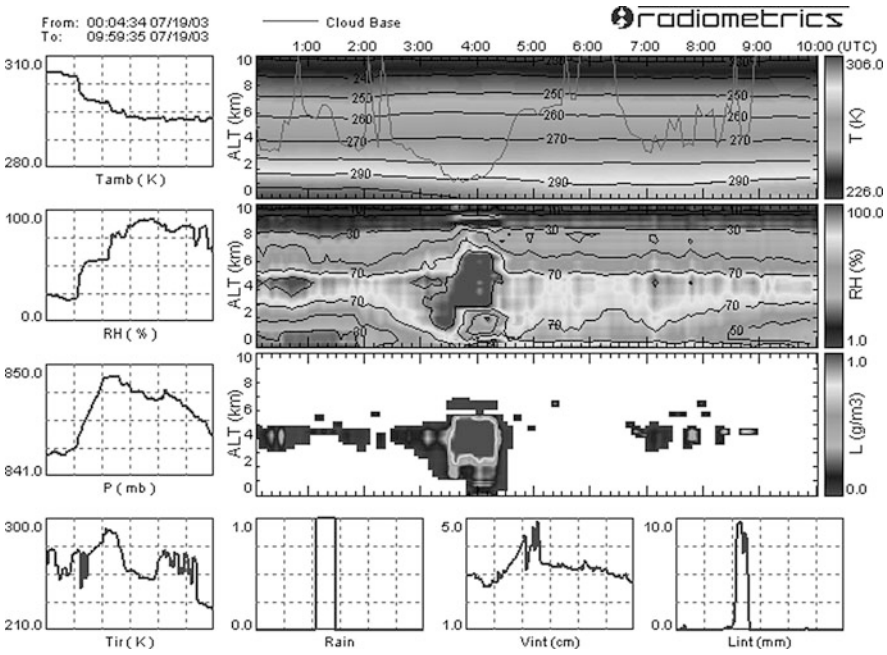

Fig. I.1.8 Screenshot of the real-time output from the Radiometrics MP-3000. Plots refer to data collected during July 19, 2003, in Boulder, CO, USA. A rain shower happened roughly at 0400 UTC. Contour plots show time–height cross sections of atmospheric temperature (*top*), relative humidity (*middle*), and liquid water (*bottom*). Surface temperature, relative humidity, and pressure are shown on the *left*. Infrared cloud temperature, rain detection, integrated content of vapor and liquid are shown on the *bottom*

the field to be retrieved. Historical radiosonde and neural network or regression are usually used for profile retrieval (Ware et al., 2003); more recently, variational methods have been developed to combine radiometer data with numerical forecast model output (Löhnert et al., 2004; Hewison, 2007; Cimini et al., 2009). Comparisons between radiosondes and retrieved profiles in the lower troposphere are shown in Güldner and Spänkuch (2001) and Cimini et al. (2006) and demonstrate that temperature and humidity retrieval accuracy is best near the surface and degrades with height to <1.5 K, < 0.7 g/m3, respectively. A screenshot of the real-time output of a commercial MWR profiler is shown in Fig. I.1.8.

Profile retrievals from MWR have much coarser vertical resolution than radiosonde soundings, especially above the boundary layer, but have temporal resolutions of minutes. Retrieval error is smaller than radiosonde sounding error for boundary layer temperatures and higher above the boundary layer. The dominant radiosonde error is the representativeness error that results from the characterization of a model cell volume by a point measurement. This type of error is especially important when there are strong temporal or horizontal spatial gradients in the meteorological profiles. Radiometric retrievals can be temporally averaged and in these strong gradient (temporal or horizontal) conditions may be less susceptible to representativeness error than radiosonde soundings.

Note that in clear-sky conditions, vertical profiles of temperature and water vapor in the atmospheric boundary layer can be retrieved by FTIR spectral observations. Due to the high spectral resolution of FTIR observed spectra, the optimal vertical resolution is of the order of 100 m in the atmospheric boundary layer (up to ∼3 km) (Feltz et al., 2003).

6 Conclusions

Surface-based radiometry has provided useful data on energy budget, temperature, water vapor, clouds, and other atmospheric constituents. Steady progress has been made in the development of robust, sensitive, and accurate instrumentation. This has been accompanied by continued development of suitable forward and inverse models for the accurate calculation of radiation intensity and the retrieval of atmospheric parameters. The advances in forward modeling positively affect surface-, airborne-, and satellite-based remote sensing, as well as telecommunication.

It now seems likely that assimilation of data with forecast models is a very promising technique for exploiting radiometer data (Nehrkorn and Grassotti, 2004). Of equal promise is the synergism of active and passive sensors as has been achieved in cloud sensing (Löhnert et al., 2001), in moisture profiling (Stankov et al., 1996; Han and Westwater, 1995), and in the use of wind profiler estimates of significant moisture gradients to improve humidity profile retrieval (Bianco et al., 2005). All the above topics will be discussed in the second part of this volume.

References

Battaglia A, Saavedra P, Rose T, Simmer, C (2009) Rain observations by a multifrequency dual polarized radiometer. IEEE Geosci Remote Sens Lett 6(2):354–358

Bianco LD, Cimini FS, Marzano, Ware R (2005) Combining microwave radiometer and wind profiler radar measurements for high-resolution atmospheric humidity profiling. J Atmos Oceanic Tech 22:949–965, July 2005

Cimini D, Hewison TJ, Martin L, Güldner J, Gaffard C, Marzano FS (2006) Temperature and humidity profile retrievals from ground-based microwave radiometers during TUC. Meteorol Zeitschrift 15(1):45–56

Cimini D, Shaw JA, Han Y, Westwater ER, Irisov V, Leuski V, Churnside JH (2003a), Air temperature profile and air-sea temperature difference measurements by infrared and microwave scanning radiometers. Radio Sci 38(3):8045. doi:10.1029/2002RS002632

Cimini D, Westwater ER, Han Y (2003b) Theoretical analysis of the frequency allocation of the hinge points around 22.235 GHz. In: Proceedings of the 13th ARM Science Team Meeting, Broomfield, Colorado, 31 March–4 April 2003

Cimini D, Westwater ER, Han Y, Keihm SJ (2003c) Accuracy of ground-based microwave radiometer and balloon-borne measurements during the WVIOP2000 field experiment. IEEE Trans Geosci Remote Sens 41(11):2605–2615

Cimini D, Westwater ER, Gasiewski AJ, Klein M, Leusky V, Dowlatshahi S (2007a) The ground-based scanning radiometer: a powerful tool for study of the arctic atmosphere. IEEE Trans Geosci Remote Sens 45(9):2759–2777

Cimini D, Westwater ER, Gasiewski AJ, Klein M, Leusky V, Liljegren J (2007b) Ground-based millimeter- and submillimeter-wave observations of low vapor and liquid water contents. IEEE Trans Geosci Remote Sens 45(7):2169–2180

Cimini D, Westwater ER, Gasiewski AJ (2009) Temperature and humidity profiling in the Arctic using millimeter-wave radiometry and 1DVAR. IEEE Trans Geosci Remote Sens. doi:10.1109/TGRS.2009.2030500

Clothiaux EE, Ackerman TP, Mace GG, Moran KP, Marchand RT, Miller MA, Martner BE (2000) Objective determination of cloud heights and radar reflectivities using a combination of active remote sensors at the ARM CART sites. J Appl Meteorol 39(5):645–665

Clough SA, Shephard MW, Mlawer EJ, Delamere JS, Iacono MJ, Cady-Pereira K, Boukabara S, Brown PD (2005) Atmospheric radiative transfer modeling: a summary of the AER codes. J Quant Spectros Radiative Transfer 91:233–244

Crewell S, Löhnert U (2003) Accuracy of cloud liquid water path from ground-based microwave radiometry. Part II. Sensor accuracy and synergy. Radio Sci 38(3):8042. doi:10.1029/2002RS002634

Elachi C (1987) Introduction to the physics and techniques of remote sensing, Wiley, New York, NY, p 444

Demirgian J, Dedecker R (2005) Atmospheric emitted radiance interferometer handbook, ARM TR-054. http://www.arm.gov/publications/tech_reports/handbooks/aeri_handbook.pdf. Accessed on Jan 2005

Feltz WF, Howell HB, Knuteson RO, Woolf HM, Revercomb HE (2003) Near continuous profiling of temperature, moisture, and atmospheric stability using the atmospheric emitted radiance interferometer (AERI). J Appl Meteorol 42:584–597

Goody RM, Yung YL (1995) Atmospheric radiation: theoretical basis, 2nd edn. Oxford University Press, New York, NY, pp 519

Güldner J, Spänkuch D (2001) Remote sensing of the thermodynamic state of the atmospheric boundary layer by ground-based microwave radiometry. J Atmos Ocean Technol 18:925–933

Han Y, Westwater ER (1995) Remote sensing of tropospheric water vapor and cloud liquid water by integrated ground-based sensors. J Atmos Ocean Technol 12(5):1050–1059

Han Y, Westwater ER, Ferrare RA (1997), Applications of Kalman filtering to derive water vapor from raman lidar and microwave radiometers. J Atmos Ocean Technol 14(3):480–487

Hewison T (2007) 1D-VAR retrievals of temperature and humidity profiles from a ground-based microwave radiometer, IEEE TGRS 45(7):2163–2168

Hogg DC, Decker MT, Guiraud FO, Earnshaw KB, Merritt DA, Moran KP, Sweezy WB, Strauch RG, Westwater ER, Little CG (1983) An automatic profiler of the temperature, wind and humidity in the troposphere. J Appl Meteorol 22(5):807–831

Janssen MA (1993) An introduction to the passive remote sensing of atmospheres. In: Michael A. Janssen (ed), Atmospheric remote sensing by microwave radiometry. Wiley, New York, NY, pp 1–36

Kadygrov EN, Pick DR (1998) The potential performance of an angular scanning single channel microwave radiometer and some comparisons with in situ observations. Meteorol Appl 5: 393–404

Knuteson RO et al (2004a) Atmospheric emitted radiance interferometer (AERI). Part I: Instrument design. J Atmos Ocean Technol 21(December):1763–1776

Knuteson RO et al (2004b) Atmospheric emitted radiance interferometer (AERI). Part II: Instrument performance. J Atmos Ocean Technol 21(December):1777–1789

Leuskii V, Irisov V, Westwater E, Fedor L, Patten B (2000) Airborne measurements of the sea-air temperature difference by a scanning 5-mm wavelength radiometer. In: Proceedings of IGARSS2000, Honolulu, 24–28 July 2000, pp 260–262

Liebe HJ (1989) MPM, an atmospheric millimeter wave propagation model. Int J Infrared Millimeter Waves 10(6):631–650

Liebe HJ, Hufford GA, Manabe T (1991) A model for the complex permittivity of water at frequencies below 1 THz. Int J Infrared Millimeter Waves 12(7):659–675

Liou K-N (1980) An introduction to atmospheric radiation. Academic Press, New York, NY, pp 392

Löhnert U, Crewell S, Simmer C (2004) An integrated approach toward retrieving physically consistent profiles of temperature, humidity, and cloud liquid water. J Appl Meteorol 43:1295–1307

Löhnert U, Crewell S, Macke A, Simmer C (2001) Profiling cloud liquid water by combining active and passive microwave measurements with cloud model statistics. J Atmos Ocean Technol 18:1354–1366

Marzano F, Cimini D, Ciotti P, Ware R (2005) Modeling and measurements of rainfall by ground-based multispectral microwave radiometry. IEEE Trans Geosci Remote Sens, 43:1000–1011

McGrath A., Hewison T (2001) Measuring the accuracy of MARSS – an airborne microwave radiometer. J Atmos Ocean Technol, 18:2003–2012

Nehrkorn T, Grassotti C (2004) Mesoscale variational assimilation of profiling radiometer data. In: 16th conference on numerical weather prediction. American Meteorological Society, Seattle, WA

Petty GW (2006) A first course in atmospheric radiation, 2nd edn. Sundog Publishing, Madison. pp 460. ISBN-10: 0-9729033-1-3

Philipona, R, Frohlich C, Betz Ch (1995) Characterisation of pyrgeometers and the accuracy of atmospheric long-wave radiation measurements. Appl Opt 34:1598–1605

Reichardt J, Güldner J (2009) Fourier transform infrared radiometer. In: Engelbart D, Monna W, Nash J, Matzler C (eds) EUR 24172 – COST Action 720 final report. Cost office, Brussels, pp 95–103

Revercomb HE, Turner DD, Tobin DC, Knuteson RO, Feltz WF, Bannard J, Bosenberg J, Clough S, Cook D, Ferrare R, Goldsmith J, Gutman S, Halthorne R, Lesht B, Liljegren J, Linne H, Michalsky J, Morris V, Porch W, Richardson S, Schmid B, Splitt M, Van Hove T, Westwater E, Whiteman D (2003) The ARM programs's water vapor intensive observation periods: overview, initial accomplishments, and future challenges. Bull Am Meteorol Soc 84(1):217–236

Rodgers CD (1976) Retrieval of atmospheric temperature and composition from remote measurements of thermal radiation. Rev Geophys Space Phys 14:609–624

Rodgers CD (2000) Inverse methods for atmospheric sounding: theory and practice. World Scientific, Singapore

Rose T, Crewell S, Löhnert U, Simmer C (2005) A network suitable microwave radiometer for operational monitoring of the cloudy atmosphere. Atmos Res 75(3):183–200, May

Rosenkranz PW (1998) Water vapor microwave continuum absorption: a comparison of measurements and models. Radio Sci 33(4):919–928

Solheim F, Godwin J, Westwater E, Han Y, Keihm S, Marsh K, Ware R (1998) Radiometric profiling of temperature, water vapor, and liquid water using various inversion methods. Radio Sci 33:393–404

Stankov BB, Westwater ER, Gossard EE (1996) Use of wind profiler estimates of significant moisture gradients to improve humidity profile retrieval. J Atmos Ocean Technol 13(6):1285–1290

Stephens GL (1994) Remote sensing of the lower atmosphere – an introduction. Oxford University Press, New York, NY, p 523

Tobin DC et al (1999) Downwelling spectral radiance observations at the SHEBA ice station: water vapor continuum measurements from 17 to 26 microns. J Geophys Res 104(D2):2081–2092

Trokhimovski YG, Westwater ER, Han Y, Leuskiy VY (1998) The results of air and sea surface temperature measurements using a 60 Ghz microwave rotating radiometer. IEEE Trans Geosci Remote Sens 36(1):3–15

Turner DD (2007) Improved ground-based liquid water path retrievals using a combined infrared and microwave approach. J Geophys Res 112 (D15204):15. doi: 10.1029/2007JD008530

Turner DD, Ackerman SA, Baum BA, Revercomb HE, Yang P (2003a) Cloud phase determination using ground-based AERI observations at SHEBA. J Appl Meteorol 42:701–715

Turner D, Lesht B, Clough A, Liljegren J, Revercomb H, Tobin D (2003b) Dry bias and variability in Väisälä RS80-H radiosondes: the ARM experience. J Atmos Ocean Technol 20(1):117–132

Twomey S (1977) Introduction to the mathematics of inversion in remote sensing and indirect measurements. Elsevier, New York, NY

Ware R, Carpenter R, Güldner J, Liljegren J, Nehrkorn T, Solheim F, Vandenberghe F (2003) A multi-channel radiometric profiler of temperature, humidity and cloud liquid. Radio Sci 38(4):8079–8032

Westwater ER (1993) Ground-based microwave remote sensing of meteorological variables. In: Michael A. Janssen (ed) Atmospheric remote sensing by microwave radiometry. Wiley, New York, NY, pp 145–213

Westwater ER, Crewell S, Matzler C (2005) Surface-based microwave and millimeter wave radiometric remote sensing of the troposphere: a tutorial. IEEE Geosci Remote Sens Newslett 16–33(March). ISSN 0161-7869

Westwater ER, Snider JB, Carlson AC (1975) Experimental determination of temperature profiles by ground-based microwave radiometry. J Appl Meteorol 14(4):524–539

Westwater ER, Han Y, Irisov VG, Leuskiy V, Kadygrov EN, Viazankin SA (1999) Remote sensing of boundary-layer temperature profiles by a scanning 5-mm microwave radiometer and RASS: comparison experiment. J Atmos Ocean Technol 16(7):805–818

Westwater ER, Klein M, Leuski V, Gasiewski AJ, Uttal T, Hazen DA, Cimini D, Mattioli V, Weber BL, Dowlatshahi S, Shaw JA, Liljegren JS, Lesht BM, Zak BD (2004) The 2004 north slope of Alaska arctic winter radiometric experiment. In: Proceedings of 14th Atmospheric Radiation Measurement (ARM) Science Team Meeting, April, 2004

Chapter I.2
Meteorological Radar Systems

Mario Montopoli and Frank S. Marzano

1 Introduction

During the beginning of 1941, while someone were trying to eliminate natural meteorological echoes from radar returned signals to better distinguish moving manmade sensible targets, others were attempting to study them. It was the beginning of the radar era within the meteorological context.

The first studies were addressed in identifying the rain formation, whereas quantitative rain estimation were available only around 1960 (see Atlas, 1954).

Nowadays, radar systems are quite diffuse instrument with multiple applications and products which are continuously improved both by hardware innovations and by algorithms developments. Most diffuse radar systems are labeled with the term "weather radars" which are mainly ground-based systems. They are able to detect radar signal from precipitating droplets in different phases which are basically rain, ice, and snow of variable sizes (of the order of 1–10 mm) and shapes. Weather radars operates at wavelengths from about 15 cm to 3 cm (i.e., between 2 and 10 GHz respectively) and, as will be discussed later, they have, in their advanced configuration, Doppler and polarization capability which means that they can measure radial wind speed and classify the shape and type of the sensed hydrometeors (Vivekanandan et al. 1999; Baldini et al. 2004; Gorgucci et al. 2002; Marzano et al. 2006; Vivekanandan et al. 2004; Zrnic et al. 2001).

The perspective from the ground has several advantages but suffers from too limited spatial coverage (i.e., nearly 200 km with 1 km resolution) to observe large rain formations. Radar from satellite tends to compensate the above-mentioned problem but many additional challenging problems rise, including cost, size constraints, reliability issues, and temporal sampling. It is obviously impossible to continuously sample every precipitating cloud from radar orbiting the Earth. An example of space-borne precipitation radar (PR) is aboard of the Tropical Rainfall Measuring Mission (TRMM) satellite launched in 1997 (Toshiaki et al., 2009).

M. Montopoli (✉)
Centre of Excellence CETEMPS and Department of Electrical and Information Engineering, University of L'Aquila, L'Aquila, Italy
e-mail: mario.montopoli@univaq.it

D. Cimini et al. (eds.), *Integrated Ground-Based Observing Systems*,
DOI 10.1007/978-3-642-12968-1_2,

The precipitation radar was the first space-borne instrument designed to provide three-dimensional maps of storm structure. It operates at 2-cm wavelength (i.e., 15 GHz) and it has a swat width of 247 km with a resolution of 5 km. These measurements yield needful information on the intensity and distribution of the rain, on the rain type, on the storm depth, and on the height at which the snow melts into rain. The estimates of the heat released into the atmosphere at different heights based on these measurements can be used to improve models of the global atmospheric circulation.

Radars to study precipitations are not the unique existing radar systems. Another class of radars, called cloud radars, are designed to monitor cloud structure with wavelengths about 10 times shorter than those used in conventional storm surveillance radars, i.e., at 8.6 mm or 3.3 mm or in frequency domain, respectively, at 35 and 90 GHz. When installed on the ground, they monitor clouds which pass over the radar site or in other words they are vertically pointed. When installed on space platform they are nadir looking as in the case of cloud profiling radar (CPR) aboard of CloudSat space platform (Graeme et al., 2002).

These types of radars are aimed to estimate the cloud boundaries (e.g., cloud bottoms and tops) and due to the shorter wavelength used, they are able to detect tiny water and ice droplets that conventional radars are unable to sense. The cloud radar also helps to estimate microphysical properties of clouds, such as particle size and mass content, which help to understand how clouds interact with radiant energy passing though the atmosphere.

Radar are also those operating at wavelengths from 30 cm to 6 m, mainly used to probe the clear air or regions without clouds where the airflow characteristics can be determined up to 10 km above the Earth's surface. For these applications radars are known as profilers. The basic principle is that the gradient variations of index of refraction of air, that is quantity observed by the profiler, are connected to small fluctuations in air temperature and moisture content.

Eventually, belong to the class of radars are also those operating at optical frequencies as LIDARs, used to accomplish studies on aerosol particles and air molecules and allowing air motions to be determined, especially in thin, high tropospheric clouds, and in the Earth's boundary layer (approximately the lowest 1 km of the Earth's atmosphere)

This chapter attempts to give the reader the basic principles of radar systems, first introducing concepts which are common to all radar categories and second focusing the discussion on weather radar polarimetry of precipitation. Throughout the chapter, the ground-based perspective will be followed in order to facilitate the comprehension of the basic concepts without introducing the complication of the geometry of observation.

2 Radar Systems

Precipitation radars are widely used to determinate the location, size, and intensity of rain formation. Ground-based scanning precipitation radars are used in short-term weather and flood forecasting, to estimate the distribution and the amount

of cumulative rainfall over a region (typically of 200×200 km^2) and thanks to polarimetric radars to classify the types of hydrometeors. Weather radars of many countries have networks of operational radars that monitor precipitation near population centers [see a Europe and American example in Holleman et al. (2008), Saffle et al. (2002), and Alberoni et al. (2002)]. The output of these operational radar networks can be combined to provide a picture of the distribution of precipitation over synoptic-scale regions. Precipitation radars, developed by the British and Americans during the World War II, are also used to map the three-dimensional structure of storms.

Radars transmit a pulse of electromagnetic energy, by means of an antenna, and when the transmitted energy encounters a particle, such as, for example, a raindrop for water radars, part of the transmitted energy is scattered back toward the antenna where it is received and amplified. The time delay between the original pulse transmission and the receipt of the backscattered energy is used to deduce the distance to the reflector antenna. The frequency used by weather radars is divided into several bands which are usually S band (2–4 GHz), C band (4–8 GHz), and X band (8–12 GHz) for ground-based station, and Ku (12–18 GHz) and Ka (27–40 GHz) bands for mobile and spaceborne radars (Chandrasekar et al., 2008). On the other hand, for cloud radars, the frequencies of interest are 35 and 90 GHz.

The choice of the frequency for precipitating radar is a trade off between the practical constraints of size, weight, cost, and the relation between the wavelength and the size of the target hydrometeors. Theoretical considerations favor the choice of the longer wavelength at S and C bands for many precipitation applications. However, the use of these longer wavelengths is not always practical. The beam width for aperture antennas is proportional to λ/D_a, where D_a is the antenna diameter. In comparison to shorter wavelengths, longer ones necessitate of a larger antenna to obtain a focused beam of the same angular aperture (typically of the order of 1°). Larger antennas are heavier, require more powerful motors to move them, and are more expensive than smaller ones.

In the next sections a typical block diagram of a weather radar system will be discussed together with the derivation of the fundamental equations and the basic observable definitions and their physical significance.

2.1 Radar Scheme

The precipitation radar principally consists of a transmitter, a receiver, a transmitter/receiver switch (or circulator), and an antenna. Fig. I.2.1 shows a typical block diagram of a weather radar. The transmission section (blocks on the left side of the circulator) consists of a pulse modulator that switches the continuous sinusoidal waveform, generated by the STAble Local Oscillator (STALO) and the COHerent Oscillator (COHO), on and off to form discrete pulses. The radar sends out a pulse of a prescribed time width (T_0) and then switches to the receiver section (blocks below the circulator) to listen for possible radar echoes. The range to the targets is obtained by comparing the instants of transmission of pulses with the instants where the backscattered signal is received. In precipitation radars, the pulses are

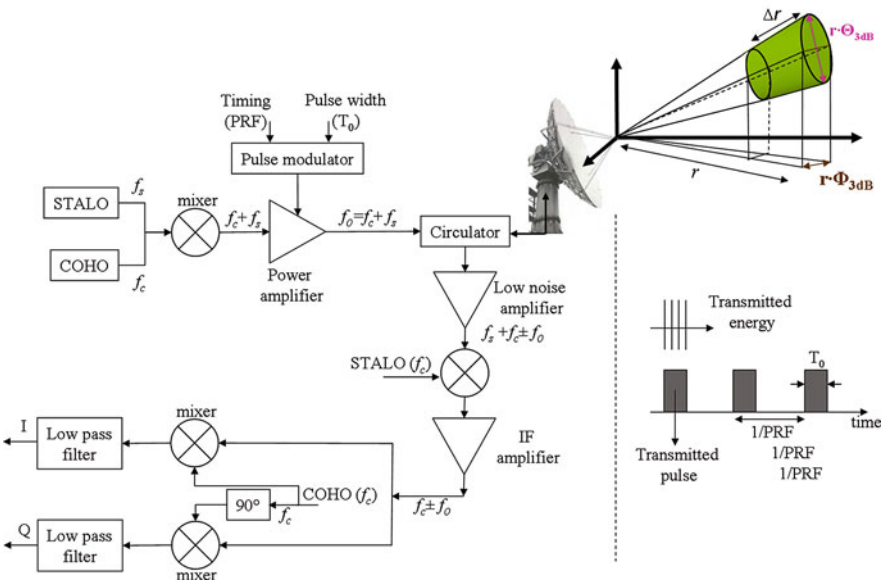

Fig. I.2.1 Block diagram of a weather radar partially taken from Bringi and Chandrasekar (2001)

transmitted at a pulse repetition frequency (PRF) of about 300–2,500 Hz and each pulse time duration is of the order of 10^{-6} s. The time interval between successive transmitted pulses limits the maximum range ($r_{\max}$) that the electromagnetic wave can run before the next pulse is transmitted. In formulas $r_{\max}$ can be expressed as follows:

$$r_{\max} = \frac{c}{2\mathrm{PRF}}, \tag{1.2.1}$$

where c (m/s) indicates the light velocity and the factor 2 is due to the two-way trip (from the antenna to the target and from the target to the antenna) of the transmitted pulses.

While the PRF limits the maximum detectable range $r_{\max}$, the time duration of the pulses T_0 limits the radial horizontal spatial resolution Δr (see Fig. I.2.1), i.e., targets separated in space by at least Δr will be completely resolved in range. Consider two targets located at ranges r_1 and r_2, with $r_1 < r_2$. The signals corresponding to these targets, after sending a pulse, will be received, respectively, at the instants t_1 and t_2. Then, the distance between the targets $\Delta r_t = (r_2 - r_1)$ can be computed as $\Delta r_t = c(t_2 - t_1)$. If the two targets are at least of $cT_0/2$ apart, the trailing edge of the received pulse from the first target is well separated (i.e., it is not overlapped) to the leading edge of the received pulse from the second target. Therefore, the radial horizontal spatial resolution of radar is given by

$$\Delta r = \frac{cT_0}{2}. \tag{1.2.2}$$

In the latter, Δr is expressed in meters when T_0 in seconds and c in meter·per second.

The receiver detects the radar signal, amplifies it, converts from analog to digital, and averages the returned pulses over defined time periods. If the observed target is moving, the received signal shows a Doppler frequency shift f_0 which can be detected by the coherent receiver (see blocks after the IF amplifier on Fig. I.2.1). The in-phase (I) and the in-quadrature (Q) components at the output signal of the coherent receiver are then used to retrieve the Doppler velocity of the observed target. Typical peak transmitted power is 10^5–10^6 W, whereas typical received power is 10^{-10} W. The circulator protects the sensitive receiver from the powerful transmitter.

Eventually, radar antennas focus the transmitted energy and direct it along a narrow angular beam. For scanning radars (i.e., radars that are able to roundly move its antenna for several elevation angles), this direction is often described in terms of an elevation angle relative to the ground and an azimuth angle relative to the north. The radar energy is higher along the center of the beam and decreases outward with increasing angular width. The beam width is defined as the angular width where the power is exactly half the maximum power (or –3 in dB scale). Along the vertical and horizontal directions these angles are, respectively, labeled as $\Theta_{3\text{dB}}$, $\Phi_{3\text{dB}}$. Then the resolution volume ΔV (m^3), illuminated by a transmitted pulse along the beam, is approximated by a cylinder as shown in Fig. I.2.1. Therefore, the volume of this cylinder can be expressed as follows:

$$\Delta V = \Delta r \cdot \Delta S \cong \left(\frac{cT_0}{2}\right)\left(\frac{r\Theta_{3\text{dB}}}{2}\right)\left(\frac{r\Phi_{3\text{db}}}{2}\right)\pi = \frac{cT_0\Theta_{3\text{dB}}\Phi_{3\text{db}}}{8}\pi r^2. \quad (1.2.3)$$

As can be observed from the latter expression, the resolution volume becomes more and more large as the distance from the radar increases.

Last consideration concerns the polarimetric radar schemes where both the transmission and receiver sections are, in some way, replicated to, respectively, transmit and receive the horizontal and vertical polarized waves. Indeed, either alternate dual-polarization schemes (with a suitable switch) or a hybrid slant linear polarization transmitting scheme can be used, the latter being nowadays the most applied.

2.2 Radar Equation for Single Target

The radar equation expresses the relationship between the transmitted power (W_t) and the backscattered received power (W_r) from precipitation targets in terms of the radar's hardware characteristics and the distance between the transmitter and the target.

Let us consider a single target, shown in Fig. I.2.2, at distance r from the radar. The incident power density (P_i) on the target, expressed in W/m^2, is given by the

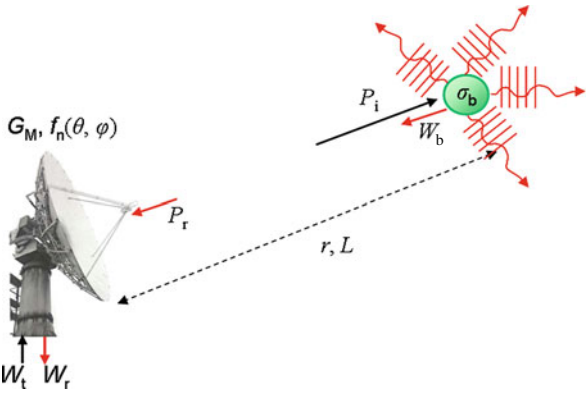

Fig. I.2.2 Transmission and reception of radar pulses from a single target. W_r, received power; W_t, transmitted power; P_r, received power density; P_i, incident power density on the target; W_b, radar backscattered power from the target; G_M, maximum antenna gain; f_n, normalized antenna radiation pattern; σ_b, radar backscattering cross section

power, distributed over a sphere or ray r, weighted by the antenna gain G which reassumes the antenna radiation efficiency and its directive properties:

$$P_i(r, \theta, \varphi) = \frac{W_t}{4\pi r^2} G(\theta, \varphi) L(r). \tag{1.2.4}$$

In Eq. (1.2.4) $L(r)$ is the loss factor of the medium which separates the target from the antenna, θ and φ are, respectively, the antenna elevation and the azimuth angle. $G(\theta, \varphi)$ can be split up, for convenience, into two terms as follows:

$$G(\theta, \varphi) = G_M \cdot |f_n(\theta, \varphi)|^2 , \tag{1.2.5}$$

where G_M represents the maximum antenna gain, whereas f_n accounts only for the directional properties of the antenna. After interacting with the target, the incident wave is partially scattered back to the radar. More in detail, when an electromagnetic wave hits on a dielectric particle, both scattering and absorption contribute to the loss of energy of the incident wave. The absorption causes the loss of power from the incident wave since the power is absorbed by the target and dissipated as heat. On the other hand, the scattering diffuses the incident power in many directions and the loss of energy manifests when these directions are those undesired with respect to the location of the transmitter and the receiver. The combination of the absorption and scattering is called extinction of the electromagnetic wave. The extinction can be described by the radar cross section or also called extinction cross section (σ_e) usually expressed in square meter. It can be defined as the ratio between the resulting power after the extinction of the wave (W_e) and the incident power density (P_i). Obviously σ_e is a function of the direction through the angles θ and φ. If the line of sight between the radar and the target is considered, only the backscattered power (W_b) has to be accounted for the computation of the received power W_r. Therefore the backscattering radar cross section ($\sigma_b = W_b/P_i$), instead of σ_e, will be used in

the next formulas. With the definition of σ_b in mind, the received power density (P_r) at the radar antenna aperture is given by

$$P_r(r,\theta,\varphi) = \frac{P_i(r,\theta,\varphi)\cdot\sigma_b}{4\pi r^2}\cdot L(r). \tag{1.2.6}$$

The received power (W_r) can be obtained exploiting the characteristic of a receiving antenna to transform the intercepted power density at its aperture into a power at its output. This characteristic is the antenna equivalent area (A_e). For whatever antenna (Balanis, 1997) the following holds:

$$A_e(\theta,\varphi) = \frac{\lambda^2}{4\pi}\cdot G(\theta,\varphi). \tag{1.2.7}$$

The received power can be then expressed as follows:

$$W_r = P_r(r,\theta,\varphi)\cdot A_e(\theta,\varphi). \tag{1.2.8}$$

Substituting Eq. (1.2.4) in Eq. (1.2.6) and using both Eqs. (1.2.7) and (1.2.8) for the expressions of A_e and G, the received power can be explicated as indicated below:

$$W_r = \underbrace{\left(\frac{W_t G_M^2\,|f_n(\theta,\varphi)|^4\,\lambda^2}{(4\pi)^3}\right)}_{c_1}\cdot L^2\cdot\frac{\sigma_b}{r^4} = C_1\cdot L^2\cdot\frac{\sigma_b}{r^4}. \tag{1.2.9}$$

In the latter expression the radar constant C_1 has been introduced. This is made possible since the single target is supposed to be perfectly enclosed in the main lobe of the antenna along the direction of maximum radiation where $f_n = 1$.

2.3 Radar Equation for Distributed Target

Precipitation particles, such as raindrops, snowflakes, hail, and graupel, act as distributed scatters in the volume of the atmosphere illuminated by the precipitation radar. The backscattered signal from a volume of randomly distributed targets is the sum of the signals scattered by each of the single target within that volume. It is suitably defined as a quantity called radar reflectivity for unit volume, that is,

$$\eta = \frac{\sum_i \langle\sigma_{bi}\rangle}{\Delta V}, \tag{1.2.10}$$

where the summation is extended to all the radar backscatter cross sections σ_{bi} of the particles within the radar resolution volume ΔV (m^3), which is specified in Eq. (1.2.3), and "<·>" is the time average operator that considers all the received samples in a given time interval. Considering all the terms which depend on the

position within the resolution volume in Eq. (1.2.9) and weighting them with the antenna gain function $G(\theta, \varphi)$, the average received power assumes the following form:

$$\langle W_r \rangle = \frac{W_t \lambda^2}{(4\pi)^3} L^2 \int_{\Delta V} \frac{G^2(\theta, \varphi)}{r^4} \eta dV \tag{1.2.11}$$

Exploiting again Eq. (1.2.9) for expressing the antenna gain function $G(\theta, \varphi)$ and expressing the infinitesimal element of volume dV equals to $r^2 \cdot dr \cdot d\Omega$ and dr as $cT_0/2$ as in Eq. (1.2.2), Eq. (1.2.11) becomes

$$\langle W_r \rangle \cong \frac{W_t \lambda^2 G_M^2}{(4\pi)^3} \left(\frac{c}{2} T_0\right) \frac{\eta}{r^2} L^2 \int_{\Omega} |f_n(\theta, \varphi)|^4 d\Omega \tag{1.2.12}$$

Assuming a Gaussian function for describing the radiation pattern f_n of the radar antenna, the integral in Eq. (1.2.12) can be approximated (Probert-Jones, 1962) as written below:

$$\int_{\Omega} |f_n(\theta, \varphi)|^4 d\Omega \cong \frac{\pi \Theta_{3dB} \Phi_{3dB}}{8 \ln 2} \tag{1.2.13}$$

Substituting Eq. (1.2.13) in Eq. (1.2.12), the average received power, in its final form, assumes the following expression:

$$\langle W_r \rangle \cong \underbrace{\left(\frac{W_t G_M^2 \lambda^2 c T_0 \Theta_{3dB} \Phi_{3dB}}{1024 \cdot \ln 2 \cdot (\pi)^2} \right)}_{C_2} \cdot L^2 \cdot \frac{\eta}{r^2} = C_2 L^2 \frac{\eta}{r^2} \tag{1.2.14}$$

As in the case of the single target, the radar calibration constant (C_2) includes all the dependencies from the hardware specifications. We observe that the dependence of W_r is now on r^{-2} instead of r^{-4} as for single target equation but this is simply the consequence of the integration of all the distributed targets. The knowledge of the constant C_2 and the measure of W_r allows the retrieving of the reflectivity for unit volume η. The constant C_2 is calculated through a calibration process, for example, measuring the power received by a target of known radar reflectivity. Typical lower bounds for C_2 are 0.5–1 dB. In the next section, the average power <Wr> will be expressed as a function of the widely used radar reflectivity factor instead of the radar reflectivity for unit volume as done in Eq. (1.2.14) (Fig. I.2.3).

2.3.1 Microwave Backscattering Models

To be valuable in precipitation studies, the average returned power, measured by weather radars, expressed by Eq. (1.2.14), must be related to the physical characteristics of the precipitation particles within the radar resolution volume. To pursue

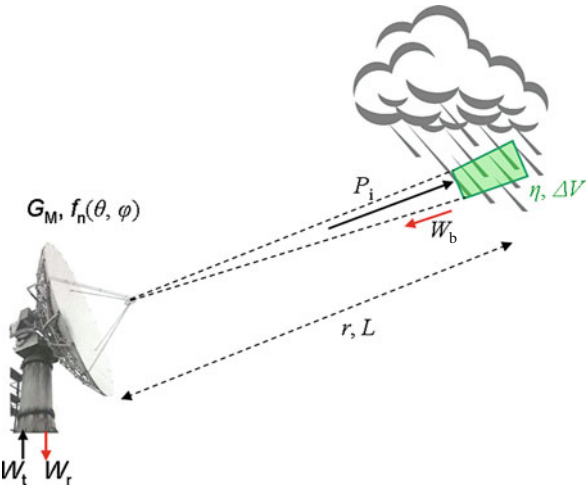

Fig. I.2.3 Transmission and reception of radar pulses from a distributed target. W_r, received power; W_t, transmitted power; P_i, incident power density on the target; η, volumetric reflectivity; ΔV, radar resolution volume; G_M, maximum antenna gain; f_n, normalized antenna radiation pattern

this aim and to maintain the treatment also valid for polarimetric radars, in the next sections, the polarimetric radar principles will be introduced and expressions of the reflectivity will be derived for the spherical particles in the Rayleigh and the Mie approximations, i.e., respectively, the case where the wavelength of the transmitted signal is much larger than the geometrical cross section of the target and the opposite situation. The case of non-spherical particles will be discussed as well.

2.4 Radar Polarimetry

It is well established (Jones, 1959; Pruppacher and Beard, 1970; Pruppacher and Pitter, 1971; Bringi et al., 1998) that small raindrops (i.e., with diameter less than 1 mm) are spherical, whereas larger raindrops are deformed by aerodynamic forces into horizontally oriented oblate spheroids. An oblate spheroid is the body of revolution formed when an ellipse with minor axis dimension (a) and major axis dimension (b) is rotated about its minor axis. Raindrops usually fall with their maximum dimension oriented horizontally. This orientation may be temporarily disturbed by turbulence, drop collision, or aerodynamic instability. The differences in the ratio between the horizontal and vertical dimensions of larger drops result in different electromagnetic properties of the scattered energy when the incident energy is horizontally versus vertically polarized. A special type of precipitation radar, called polarimetric radar, is designed to measure these properties by transmitting and receiving radiation in more than one orientation. Ongoing research (e.g., Gorgucci et al., 2000; Vivekanandan et al., 2004; Marzano et al., 2008) has shown that polarization radar variables involving the differential amplitude and phase of the received power at orthogonal polarizations can be related to the physical characteristics of the precipitation. Among others, two commonly used polarimetric variables in precipitation applications are the differential reflectivity (Z_{dr}), related to the axis

ratio of the precipitation particles and specific differential propagation phase shift (K_{dp}), related to liquid water content. These radar observables and the polarimetric radar principles will be introduced in the next sections.

2.4.1 The Polarization State

The polarization of the radiated wave, which is coincident by definition with the antenna polarization, is defined as "that property of an electromagnetic wave describing the time varying direction and relative magnitude of the electric field vector (**E**); specifically the figure traced as a function of time by the extremity of the vector **E** at a fixed location in space and the sense in which it is traced, as observed by the along the direction of propagation" (Balanis, 1997).

Polarization then is the curve traced by the end point of the arrow representing the instantaneous electric field. The field must be observed along the direction of propagation. A typical trace as a function of time is shown in Fig. I.2.4. The polarization of a field is generally elliptic that is the arrow representing the instantaneous electric field describes an ellipse as indicated in panel (b) of Fig. I.2.4. Special cases of the elliptical polarization are the circular polarization, which occurs when the major (OA) and minor (OB) axes of the ellipse coincide and the linear polarization which is the degeneration of the ellipse in a line.

2.4.2 The Scattering Matrix

Before describing the scattering of a plane electromagnetic wave by a drop and more in general by a non-spherical particle in an arbitrary orientation, it is necessary to

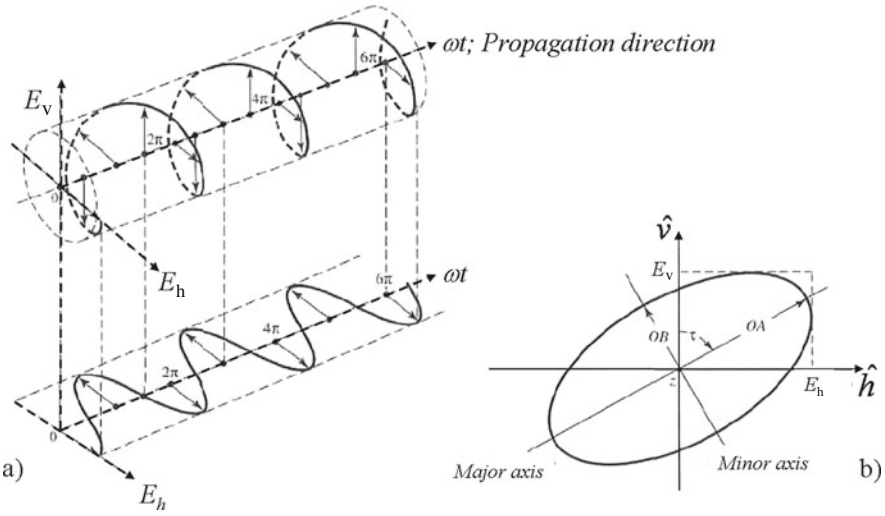

Fig. I.2.4 Rotation of a plane electromagnetic wave (panel **a**) and its polarization ellipse, at ωt=0 (panel **b**), as a function of time (Balanis, 1997)

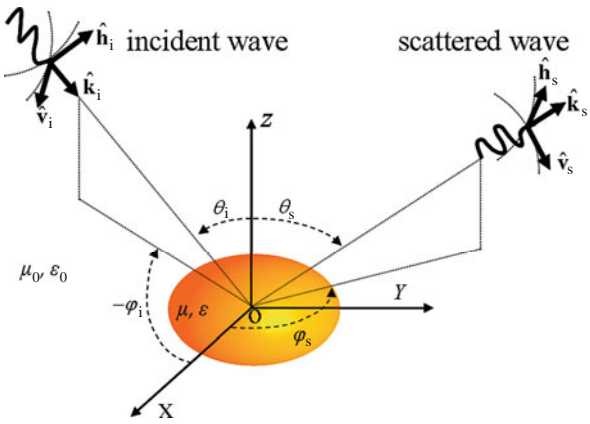

Fig. I.2.5 FSA convection for representing incident and scattered waves

specify the directions of the incident and the scattered waves and the orientation of the particle with respect to a reference frame.

In this section the concepts of polarization and the scattering from a single particle will be introduced. Following the notation used in Zly and Ulaby reported in Bringi and Chandrasekar (2001), consider a particle positioned at the origin of a Cartesian reference system as shown in Fig. I.2.5. The direction of incidence (i) of the plane wave is specified by the angles θ_i and φ_i or alternatively by the triplet $\hat{k}_i$, $\hat{h}_i$, $\hat{v}_i$ shown in the same figure, where h and v define the plane where the incident electric field ($\mathbf{E}_i$) varies. With this notation in mind the electric field vector can be formulated as follows:

$$\mathbf{E}^i(O) = E_i^h \hat{h}_i + E_E^v \hat{v}_i \Rightarrow \mathbf{E}^i(O) = \begin{bmatrix} E_i^h \\ E_i^v \end{bmatrix} \tag{1.2.15}$$

In Eq. (1.2.15) $\mathbf{E}_i$ has been expressed as a function of the two components, respectively, along the horizontal (E_i^h) and vertical (E_i^v) directions. The directions h and v assume a useful descriptive significance when $\theta_i \approx 90°$ and the plane XY becomes the Earth's surface and k_i is parallel on it. In order to express the scattered electric field ($\mathbf{E}_s$), a reference system analogous to that just introduced for the incident wave can be used. Then, the vector $\mathbf{E}_s$ can be described by the triplet $\hat{k}_s, \hat{h}_s, \hat{v}_s$ as shown in Fig. I.2.5.

The geometrical convention just introduced is called forward scattering alignment (FSA) as opposed to the backward scattering alignment (BSA), where the scattered field is seen from an observer positioned at the location of the receiver antenna (and not inside the particle as in the FSA convention). However, BSA is simply formulated from FSA just considering $\mathbf{k}_r = -\mathbf{k}_s$, $\mathbf{v}_r = \mathbf{v}_s$, and $\mathbf{h}_r = -\mathbf{h}_s$, where the subscript "r" indicates the received wave from the radar.

When a plane wave hits a particle, in it, an electrical field ($\mathbf{E}_{int}$) is generated. $\mathbf{E}_{int}$ can be considered as the source of the scattered field ($\mathbf{E}_s$) from the particle. The exact formulation of the scattered field can be obtained solving the Helmholtz

equation which is directly derived from the Maxwell ones. At great distance from the spherical particle of dielectric constant ε_r the following expression holds:

$$\begin{aligned}\mathbf{E}_s(\mathbf{k}_s) &= \frac{k_0^2}{4\pi}(\varepsilon_r - 1)\frac{e^{-jk_0 r}}{r}\int_V \left[\mathbf{E}_{int}^T(\mathbf{k}) - \hat{k}_s\left(\hat{k}_s \cdot \mathbf{E}_{int}^T\right)\right] e^{jk_0 \cdot \mathbf{k}\cdot\mathbf{k}_s} d\tau \\ &= \frac{e^{-jk_0 r}}{r} \cdot \mathbf{f}\left(\hat{k}_i,\ \hat{k}_s\right),\end{aligned} \tag{1.2.16}$$

where r is the distance between the particle and an observation point in the free space, V the volume of the particle, k_0 the propagation constant in the free space, and $\mathbf{f}$, in the third term of Eq. (1.2.16), the complex scattering amplitude function which describes the scattering properties of the considered particle.

The solution of the scattering problem reduces to the computation of the function $\mathbf{f}$ from the knowledge of the induced internal field $\mathbf{E}_{int}$. If $\mathbf{E}_s$ is expressed in the same form of the incident field in Eq. (1.2.15) in terms of their horizontal and vertical components, Eq. (1.2.16) can be expressed by means of the scattering matrix ($\mathbf{S}$). The scattering matrix accounts for the scattering properties of a single particle. Using the FSA convection the scattered field is linked to the incident one, through $\mathbf{S}$, as follows:

$$\mathbf{E}_s = \frac{e^{-jk_0 r}}{r} \cdot \mathbf{S}_{FSA} \cdot \mathbf{E}_i \Rightarrow \begin{bmatrix} E_h^s \\ E_v^s \end{bmatrix} = \frac{e^{-jk_0 r}}{r} \cdot \begin{bmatrix} S_{hh} & S_{hv} \\ S_{vh} & S_{vv} \end{bmatrix}_{FSA} \cdot \begin{bmatrix} E_h^i \\ E_v^i \end{bmatrix} \tag{1.2.17}$$

where h and v represent the horizontal and vertical polarizations for the transmitted (given by the second subscript) and received (given by the first subscript) signals. The FSA convection is oriented to give more importance to the direction of propagation of the scattered wave. For radar applications the BSA convection is used instead of the FSA one. According to BSA, the received electrical field can be expressed as follows:

$$\mathbf{E}_r = \frac{e^{-jk_0 r}}{r} \cdot \mathbf{S}_{BSA} \cdot \mathbf{E}_i \Rightarrow \begin{bmatrix} E_h^r \\ E_v^r \end{bmatrix} = \frac{e^{-jk_0 r}}{r} \cdot \begin{bmatrix} -1 & 0 \\ 0 & 1 \end{bmatrix} \cdot \begin{bmatrix} S_{hh} & S_{hv} \\ S_{vh} & S_{vv} \end{bmatrix}_{FSA} \cdot \begin{bmatrix} E_h^i \\ E_v^i \end{bmatrix} \tag{1.2.18}$$

It is worth mentioning that the scattering matrix elements depend on the directions of incidence and scattering of the electromagnetic wave as well as on the size, morphology, and composition of the particle. In general, it seems reasonable to find a connection between the scattering matrix elements and the radar cross section of the particle seen from the radar from different polarizations. Indeed, this relationship exists and is reported here (see Bringi and Chandrasekar, 2001 for details):

$$\sigma_{ij} = 4\pi \left|S_{ij}\right|^2 \tag{1.2.19}$$

where the indexes "i" and "j" indicate all the possible combinations of the polarizations h and v and S_{ij} are the elements of the scattering matrix $\mathbf{S}$. For monostatic

radars (i.e., radars where one single antenna transmits and receives signals), the reciprocity theorem is valid and the cross-polarization elements of the scattering matrix are identical:

$$(S_{\mathrm{hv}} = S_{\mathrm{vh}})_{\mathrm{BSA}} \tag{1.2.20}$$

For spherical particles the radar sees the same section whatever polarization h of v is used, then the following two relations hold:

$$S_{\mathrm{hh}} = S_{\mathrm{vv}} = S_{\mathrm{sphere}} \tag{1.2.21}$$

and

$$S_{\mathrm{hv}} = S_{\mathrm{vh}} = 0 \tag{1.2.22}$$

The analytical expression for S_{sphere} will be shown in the next section.

For non-spherical drops S_{hh} and S_{vv} will not be equal and, furthermore S_{hv} and S_{vh} will not be 0. However, if we assume that every single raindrop is uniformly oriented with zero canting angle (i.e., with their axes of symmetry vertically aligned with respect to the direction of incidence of the transmitted radar signal), S_{hv} and S_{vh} continue to be 0.

2.5 Scattering from Spherical Particles

In this section the expression of the received average power ,Wr> formalized in Eq. (1.2.14) will be further developed by better specifying the expression of the volume radar reflectivity η. If the radar volume is filled by some particles with a distribution $N(D)$ and equivalent diameter D, Eq. (1.2.10) that represents the sum of the radar backscattering cross section σ_{bi} of individual particles over unit volume can be extended as follows:

$$\eta = \frac{\sum_i \sigma_{\mathrm{b}i}}{\Delta V} = \int_0^\infty \sigma_{\mathrm{b}}(D) N(D) dD, \tag{1.2.23}$$

where $N(D)$ is expressed in $\mathrm{mm}^{-1}\cdot\mathrm{m}^{-3}$, the radar backscattering cross section σ_{b} in square meter, and D in millimeter. The radar reflectivity characterizes the target properties and its definition is independent from the nature of the scattering medium. If $D/2 << \lambda$ (it is often assumed in equivalent manner D less than $\sim\lambda/16$), the expression of the backscattering cross section, for a spherical particle, assumes a simple form as follows:

$$\sigma_{\mathrm{b}} = \frac{k_0^4}{4\pi} \cdot \left| \frac{3 \cdot (\varepsilon_{\mathrm{r}} - 1)}{\varepsilon_{\mathrm{r}} + 2} \right|^2 \cdot V_{\mathrm{Sphere}}^2 = \frac{\pi^5}{\lambda^4} \cdot |K_l|^2 \cdot D^6 \tag{1.2.24}$$

where $V_{\text{sphere}} = (\pi/6) \cdot D^3$ is the volume of the equivalent sphere, $k_0 = 2\pi/\lambda$ is the propagation constant in the free space, and $|K_l|^2 = |(\varepsilon_r - 1)/(\varepsilon_r + 2)|^2$ is a quantity called dielectric factor of the microphysical species "l" (e.g., $l = w$ for water and $l = i$ for ice) which depends on wavelength (λ), temperature, and dielectric constant (ε_r). $|K_l|^2$ can assume different values such as $|K_w|^2 = 0.93$ for water and for temperatures in the range 0–20°C and $|K_i|^2 = 0.208$ for ice with density of about 1 g/m^3.

Equation (1.2.24) is referred to as the Rayleigh approximation of the backscattering cross section. Under the Rayleigh regime, the normalized radar cross section, with respect to the geometrical cross section (also called backscattering efficiency ξ_b), increases as the fourth power of the ratio D/λ (see Fig. I.2.6 in logarithm coordinates). When the equivalent diameter is greater than $\sim\lambda/16$ Mie or optical scattering occurs. In contrast to Rayleigh scattering, under conditions of Mie scattering, the backscattered returned power fluctuates as the size of the scatter increases. This phenomenon is shown in Fig. I.2.6.

Following the Rayleigh theory and substituting Eq. (1.2.24) in Eq. (1.2.23), an expression of the volumetric reflectivity as a function of size distribution of diameters, dielectric properties, particle sizes, and the radar frequency is obtained and is made explicit here in the following equation:

$$\eta = \frac{\pi^5}{\lambda^4}|K_l|^2 \cdot \underbrace{\int_0^\infty D^6 \cdot N(D)dD}_{z} = \frac{\pi^5}{\lambda^4}|K_l|^2 \cdot Z, \tag{1.2.30}$$

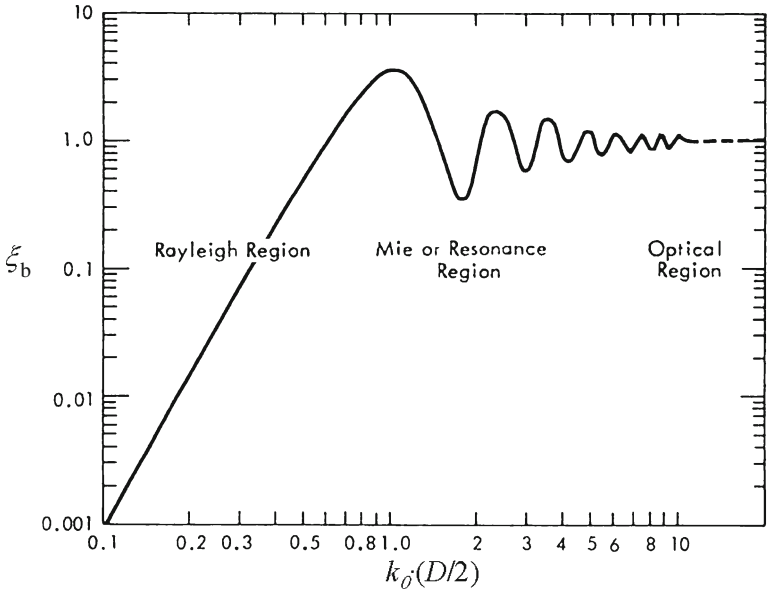

Fig. I.2.6 Backscattering efficiency $\xi_b = \sigma_b \cdot \left[\pi(D/2)^2\right]^{-1}$ as a function of $k_0 \cdot D/2$ for different backscattering regimes

where Z is the radar reflectivity factor (it should not be confused with the radar reflectivity for unit of volume η) expressed in mm^6/m^3 and as can be observed from Eq. (1.2.30), under Rayleigh approximation, it coincides with the statistical moment of order six of the size distribution of rainy drops.

Similarly to η, the reflectivity factor Z can be also interpreted as an average characteristic of the population of scatters distributed in a given radar volume. Z is independent from the wavelength and this property makes easier the comparison of reflectivity factors derived from different radar systems.

If the Rayleigh condition is not satisfied and Mie scattering holds, an equivalent reflectivity factor, Z_e, is conveniently introduced and the third term of Eq. (1.2.30) is still valid when Z_e instead of Z is considered and $l{=}w$, indicating a dielectric factor K referred to water. Z_e can be interpreted as the reflectivity factor of a population of liquid and spherical particles satisfying the Rayleigh approximation and producing a signal of the same power produced by a generic set of targets within the radar volume. Thus, in the Mie scattering Z_e is given by

$$Z_e = \frac{\lambda^4}{\pi^4 \cdot |K_w|^2} \cdot \eta \tag{1.2.31}$$

With Eqs. (1.2.30) and (1.2.31) in mind, the average power received by a radar in Eq. (1.2.14) can be updated and, in general, it depends, among other parameters, on the equivalent radar reflectivity and then on the physical characteristics of the observed particles. It is important to note that Z describes the characteristics of the target in a way independent of the wavelength. In addition, in the case of spherical particles, as discussed before the scattering matrix is completely defined through the expression of the radar cross section.

2.6 Scattering from Spheroidal Particles

The solution of the scattering and absorption problems of the electromagnetic waves from dielectric spheres with arbitrary size has been obtained by Mie in 1908 (Ulaby et al., 1986). The Mie solution is well known and it has been used for studying a lot of physical systems. However, various problems, such as the interaction of the electromagnetic waves with the hydrometeors, are related to the scattering from non-spherical bodies at wavelength comparable with the size of the observed particles. The extended boundary condition method (EBCM) also called T-matrix method (where "T" stands for transition) provides the solution of this class of problems and allows the computation of the scattering matrix through a numerical implementation. This technique was initially introduced by Waterman (1971) as a technique for computing electromagnetic scattering by single, homogeneous, arbitrarily shaped particles based on the Huygens principle. An important feature of the T-matrix approach is that it reduces exactly to the Mie theory when the scattering particle is a homogeneous or layered sphere composed of isotropic materials. Even though the T-matrix is potentially applicable to arbitrarily shaped particles, most of the

implementation refers to the computation of the scattered field for revolution solids such as cones, cylinders, and spheroids (Mishchenko and Travis, 1998).

More in detail, the aim of this method is to compute the scattered field from an arbitrarily shaped particle when it is illuminated by an incident plane wave. The field in every point of the space is given from the sum of the incident wave and the scattered one, where the incident wave is considered without the presence of the particle. The scattered field can be thought to be generated from superficial currents which have been induced on the particle by the incident wave. Then the T-matrix determinates the scattered field as a function of the incident field and the physical characteristics of the particle. This can be obtained by applying the equivalence theorem (of Love) in which the scattered field is assumed generated by some induced superficial currents which are supposed to be localized on the extreme surface of the particle. The core of the procedure consists of the following steps:

1. Relate the field internal to the particle to the external one
2. Determinate the superficial currents as a function of the internal field found at the previous step
3. Compute the scattered field generated by the superficial currents

Without considering all the mathematical passages, in formulas, the T-matrix approach expresses both the incident and the scattered fields as a linear combination of vectorial functions of the spheric waves which are solutions of the vectorial Helmholtz equation. These functions, indicated as $\mathbf{M}_{nm}$ and $\mathbf{N}_{mn}$ are called multipole. Therefore, an incident electric field polarized along the x-direction and propagating along the z-direction is expressed as follows:

$$\underline{\mathbf{E}}^i = \hat{x}E_0 e^{-jk_0 z} = \sum_{n=1}^{\infty} [a_{\mathrm{o}1n} \cdot \mathbf{M}_{\mathrm{o}1n}(k_0 r,\ \theta,\ \varphi) + b_{\mathrm{e}1n} \cdot \mathbf{N}_{\mathrm{e}1n}(k_0 r, \theta, \varphi)], \quad (1.2.32)$$

where a_{01n} and b_{01n} are known coefficients. The same expansion can be done for the scattered field in terms of the unknown coefficients f_{01n} and g_{01n}:

$$\underline{\mathbf{E}}^s = \sum_{n=1}^{\infty} \left[f_{\mathrm{o}1n} \cdot \mathbf{M}_{\mathrm{o}1n}(k_0 r,\ \theta,\ \varphi) + g_{\mathrm{e}1n} \cdot \mathbf{N}_{\mathrm{e}1n}(k_0 r, \theta, \varphi) \right] \quad (1.2.33)$$

Due to the linearity of the Maxwell's equations and boundary conditions, the relation between the scattered field coefficients (f_{01n} and g_{01n}) and the incident field coefficients (a_{01n} and b_{01n}) must be linear and is given by the transition matrix T (or T-matrix) (Waterman, 1971; Mishchenko, 2000):

$$\begin{bmatrix} f_{\mathrm{o}1n} \\ g_{\mathrm{e}1n} \end{bmatrix} = \underbrace{\begin{bmatrix} T^{11} & T^{12} \\ T^{21} & T^{22} \end{bmatrix}}_{T} \times \begin{bmatrix} a_{\mathrm{o}1n} \\ b_{\mathrm{e}1n} \end{bmatrix} \quad (1.2.34)$$

Once the T-matrix for a given particle is known, Eq. (1.2.33) can be used to determine the scattered field and then to derive the scattering matrix introduced before. The T-matrix, which is completely independent of the propagation directions and polarization states of the incident and scattered fields, depends only on the scattering particle characteristics (size relative to the wavelength, shape, relative refractive index, and orientation with respect to the laboratory reference frame). This means that for any particular particle, the T-matrix only needs to be calculated once and can then be used for repeated calculations. This is a significant advantage over many other methods of calculating scattering where the entire calculation needs to be repeated.

2.7 Radar Observables

In this section a review of the main radar observables is exposed. For major details about these observables refer to Bringi and Chandrasekar (2001). References about algorithms that use polarimetric radar observables for rain estimation can be found in Chandrasekar and Bringi (1987), Testud et al. (2000) and Ryzhkov et al. (2005). For the attenuation correction problem see for example Bringi et al. (2001), Vulpiani et al. (2005).

2.7.1 Reflectivity Factor

As mentioned before the reflectivity factor depends, in general, on the size distribution of hydrometeors, the backscattering cross section, and its physical characteristics. Since the radar signals can be received in the vertical or horizontal polarization it is opportune to refer to the co-polar reflectivity factor, expressed in Eq. (1.2.31), as follows:

$$\begin{aligned} Z_{\mathrm{e\,hh,vv}} = Z_{\mathrm{hh,vv}} &= \frac{\lambda^4}{\pi^5 |K|^2} \eta_{\mathrm{hh,vv}} = \frac{\lambda^4}{\pi^5 |K|^2} \int_{D_{\min}}^{D_{\max}} \sigma_{\mathrm{b,hh,vv}}(D) \cdot N(D) \cdot dD \\ &= \frac{4\lambda^4}{\pi^4 |K|^2} \left\langle |S_{\mathrm{hh,vv}}|^2 \right\rangle \end{aligned} \tag{1.2.35}$$

where $D_{\min}$ and $D_{\max}$ are the minimum and maximum particle diameters, $S_{\mathrm{hh,vv}}$ are the backscattering co-polar components of the scattering matrix **S** at horizontal and vertical polarizations, respectively, $|K|^2 = |(\varepsilon_{\mathrm{r}} - 1)/(\varepsilon_{\mathrm{r}} + 2)|^2$ is the complex dielectric constant of scattering particle which is a function of wavelength and temperature, and the operator "<·>" indicates the ensemble average over the drop size distribution. In the fourth term of Eq. (1.2.35), Eq. (1.2.24) has been used. The reflectivity factor has the unit of $\mathrm{mm}^6 \cdot \mathrm{m}^{-3}$ but it is often expressed in decibels of Z (dBZ) defined as $10 \log_{10}(Z_{\mathrm{ehh,vv}})$. Henceforth, for simplifying the notation, the equivalent reflectivity factor Z_{e} will be indicated as Z.

2.7.2 Differential Reflectivity

Among the main important observables of polarimetric radars, the differential reflectivity Z_{dr} plays a relevant role. To obtain radar reflectivity, energy is transmitted and received at the same polarization, usually horizontal. Differential reflectivity is the difference between the horizontally transmitted and horizontally received reflectivity factor (Z_{hh}) and the vertically transmitted and vertically received reflectivity factor (Z_{vv}). This is expressed, in logarithmic scale, in the following equation:

$$Z_{dr} = 10 \cdot \log_{10} \frac{Z_{hh}}{Z_{vv}} = 10 \cdot \log_{10} \frac{\langle |S_{hh}|^2 \rangle}{\langle |S_{vv}|^2 \rangle} \tag{1.2.36}$$

Differential reflectivity is a measure of the reflectivity-weighted mean axis ratio (a/b) of precipitation particles in a resolution volume. Z_{dr} depends on the shape and on the common orientation degree but it is independent from the number of particles in the radar volume. The measurement process of Z_{dr} can be obtained alternatively transmitting and receiving h and v in linear polarization. These measurements should be made very fast with respect to the time variation of the target geometry or in other words within the correlation time of the received time series.

Differential reflectivity has many potential applications, such as rainfall estimation, discrimination between liquid and frozen precipitation, and detection of biological scatterers (Zrnic, and Ryzhkov, 1998). For rain, as raindrops increase in volume, the drop diameter D increases, the shape of the drop becomes more oblate, the axis ratio decreases, and the associated Z_{dr} value increases. For spherical drops or spherical ice particles, the axis ratio a/b approximates the unity and $Z_{dr} \approx 0$. Table I.2.1 summarizes typical ranges of differential reflectivity values for several types of precipitations.

For ideal radar systems, differential reflectivity, being the ratio of reflectivity at horizontal and vertical polarizations, would not be affected by radar calibration errors. Nevertheless, because of unequal paths or gains in the horizontal- and vertical-polarized channels of the radar receiver, Z_{dr} can be biased. When viewed vertically, raindrops of all sizes appear circular and have an associated Z_{dr} value equal to 0. Thus, a Z_{dr} bias, accounting for the relative difference in calibration

Table I.2.1 Typical ranges of observed differential reflectivity values for several types of precipitations between S and X bands

Z_{dr} (dB)	Associated precipitation types
<–0.5	Marginally detectable precipitation
–0.5 to 0.5	Drizzle, very light rain, light snow
>1	Moderate rain and heavier snow
0.5 to 4	Moderate to heavy rain
–2 to 0.5	Hail and graupel
0.5 to 4	Melting snow particles

Values adapted from Straka et. al. (2000).

between the horizontal and vertical polarizations, can be estimated by pointing the radar beam directly upward in rain.

2.7.3 Linear Depolarization Ratio

Radiowave depolarization is characterized by the presence of an anisotropic propagation medium which produces different effects (i.e., different attenuations and phase shifts) on radio waves with different polarizations. The wave will have its polarization state altered such that power is transferred (or coupled) from the desired polarization state to the undesired orthogonal polarization state, resulting in interference or crosstalk between the two orthogonally polarized channels. Hydrometeors whose principal axes are not aligned with the electrical field of the transmitted wave (see Fig. I.2.7 panel b) will cause a small amount of energy to be depolarized and to appear at the orthogonal polarization (see Fig. I.2.7 panel a). The effect is measured by the linear depolarization ratio (the term linear is used to indicate linear polarization) defined as the ratio of the cross-polar to the co-polar signals.

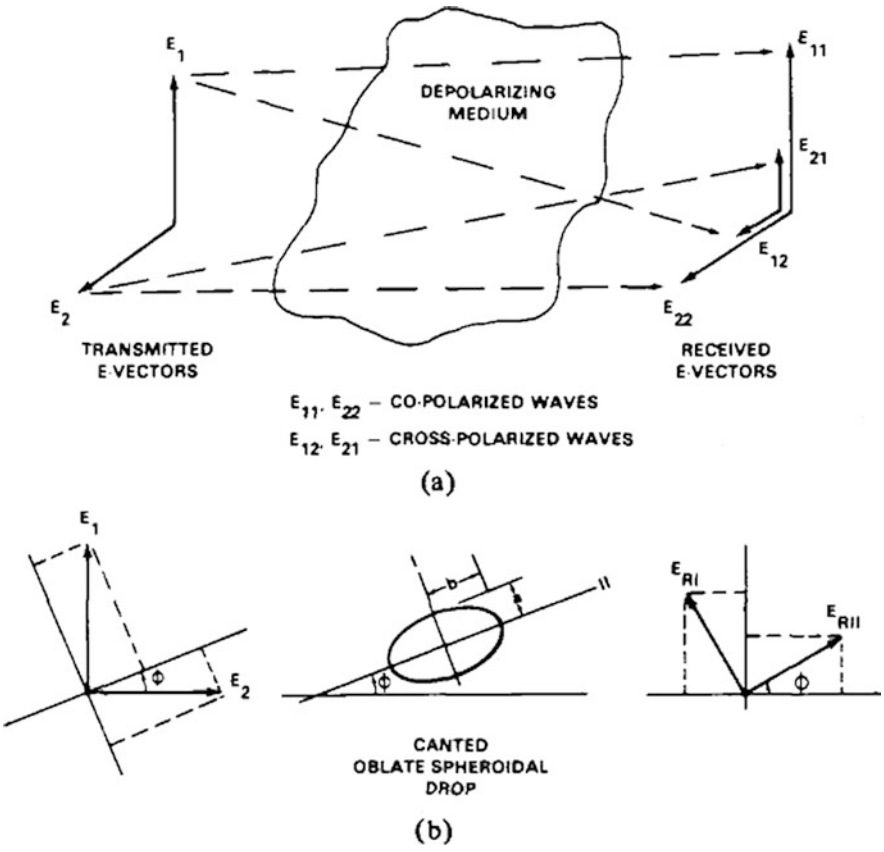

Fig. I.2.7 Vector relationships for a depolarizing medium: (**a**) co- and cross-polarized waves for linear transmission and (**b**) classical model for a canted oblate spherical rain drop

$$LDR_{\mathrm{hv}} = 10 \cdot \log_{10} \frac{Z_{\mathrm{hv}}}{Z_{\mathrm{vv}}} = 10 \cdot \log_{10} \frac{\langle |S_{\mathrm{hv}}|^2 \rangle}{\langle |S_{\mathrm{vv}}^2| \rangle}$$
$$LDR_{\mathrm{vh}} = 10 \cdot \log_{10} \frac{Z_{\mathrm{vh}}}{Z_{\mathrm{hh}}} = 10 \cdot \log_{10} \frac{\langle |S_{\mathrm{vh}}|^2 \rangle}{\langle |S_{\mathrm{hh}}|^2 \rangle}, \tag{1.2.37}$$

where the operator "<·>" indicates the ensemble average over the drop size distribution. $\mathrm{LDR_{hv}}$ and $\mathrm{LDR_{vh}}$ have similar properties because they differ only by the differential reflectivity. The depolarized signal derives from non-spheroidal particles which oscillate while falling, creating a distribution of canting angles, and from irregularly shaped particles. LDR depends on the orientation of the polarization plane of the transmitted wave, on the hydrometeors orientation, on their shape, and on their degree of common orientation.

Since LDR is a ratio between reflectivities, it is insensitive to the absolute radar calibration and to the RSD multiplicative intercept parameter. Because the cross-polar power is usually two to three orders of magnitude smaller than the co-polar signal, the linear depolarization ratio is affected by noise contamination, propagation effects, and antenna misalignments. For radars which change polarization for consecutive transmitted pulses, LDR can be contaminated by second-trip echoes. Thus, it can also be used to detect range-folded echoes. Typical values of LDR for different types of hydrometeors are listed in Table I.2.2.

2.7.4 Correlation Coefficients

The co-polar correlation coefficient is defined as

$$\rho_{\mathrm{hv}} = \frac{\int_{D_{\min}}^{D_{\max}} S_{\mathrm{vv}}(D) \cdot S_{\mathrm{hh}}^{*}(D) \cdot N(D) \cdot dD}{\sqrt{\int_{D_{\min}}^{D_{\max}} |S_{\mathrm{hh}}(D)|^2 \cdot N(D) \cdot dD \cdot} \sqrt{\int_{D_{\min}}^{D_{\max}} |S_{\mathrm{vv}}(D)|^2 \cdot N(D) \cdot dD \cdot}} = |\rho_{\mathrm{hv}}| \cdot e^{j\delta_{\mathrm{hv}}}, \tag{1.2.38}$$

where δ_{hv} (deg) is the raindrop volume backscattering differential phase shift. The magnitude is sensitive to the dispersion in particle eccentricities, canting angles,

Table I.2.2 Typical ranges of observed linear depolarization ratio values for several types of precipitations between S and X bands

LDR (dB)	Associated precipitation types
–30	Drizzle, very light rain, light snow
–25 to –30	Moderate rain and heavier snow
−15	Moderate to heavy rain
−10	Melting snow particles

Values taken from Sauvageot (1992).

irregular shapes, and the presence of mixed phase precipitation. The correlation coefficient is independent from the intercept parameter of the drop size distribution and it is insensitive to hardware calibration. Besides, it is sensitive to signal-to-noise ratio and can be contaminated by side lobes and ground clutter. Thus, it can be used to discriminate precipitation and ground clutter echoes. Radar measurements revealed that ρ_{hv} is weakly related to differential reflectivity (Balakrishnan and Zrnic, 1990; Aydin and Giridhar, 1992). As Z_{dr} increases ρ_{hv} slightly decreases.

2.7.5 Differential and Specific Differential Phase Shift

As an electromagnetic wave passes through a precipitation volume, incident energy is scattered back toward the radar and forward along the beam. The forward scattered (propagated) component of the wave becomes shifted (or in other words delayed) compared to the free space component of the wave transmitted from the radar. Within horizontally oblate raindrops, the propagating horizontal-polarized wave undergoes a larger phase shift per unit of length and travels more slowly than the vertically polarized wave. After passing through a volume filled with horizontally oblate raindrops, the horizontally polarized wave will have a larger propagation phase shift than the vertical-polarized wave. Figure I.2.8 shows a schematic interpretation of the phenomenon just exposed.

The one-way differential propagation phase (Φ_{dp}) is defined as the difference between the propagation phase shift of the horizontally transmitted and horizontally

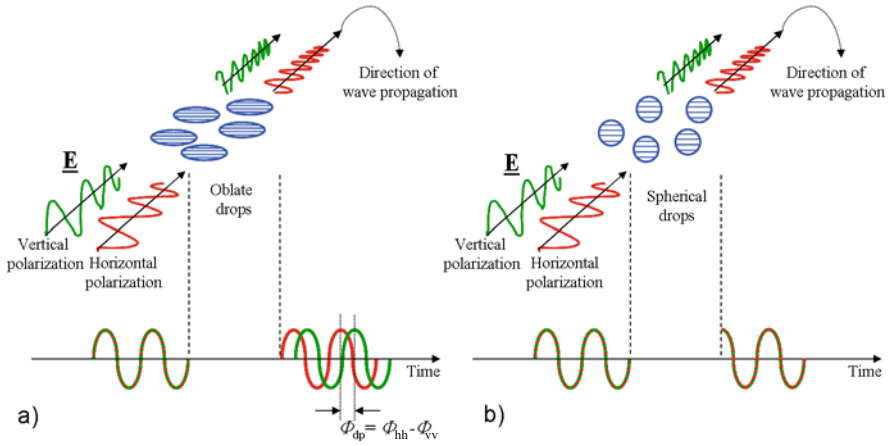

Fig. I.2.8 Schematic view of the propagation phase shift of horizontally and vertically polarized electromagnetic waves passing through a precipitation-filled volume. For simplicity the horizontally and vertically polarized waves are assumed to be in phase prior entering the volume. Panel (**a**): when the waves encounter horizontally oblate raindrops, the phase of the horizontally polarized wave is delayed more than the vertically polarized wave. Panel (**b**): when the waves encounter spherical particles such as small raindrops or hail the horizontally polarized wave and the vertically polarized wave are shifted to the same amount and $\Phi_{dp}=0$

received energy (Φ_{hh}) and the propagation phase of the vertically transmitted and vertically received energy (Φ_{vv}), that is:

$$\Phi_{dp} = \Phi_{hh} - \Phi_{vv}, \tag{1.2.39}$$

where $\Phi_{hh,vv}$ are the two-way phase angles, expressed in degrees, of the radar signal at horizontal and vertical polarizations at a particular range distance. As the radar wave passes through a region of precipitation filled with oblate drops, Φ_{dp} accumulates with increasing range. To remove range effects, Φ_{dp} is differentiated with respect to the distance from the radar "r" in order to yield the specific differential propagation phase shift (K_{dp}) which assumes the following form:

$$K_{dp} = \frac{d\Phi_{dp}}{dr}, \tag{1.2.40}$$

where K_{dp} is usually expressed in degree per kilometer.

Being K_{dp} related to the difference of phases of a plane wave propagating through a non-homogeneous medium composed of a mixture of water and air, it seems natural to relate K_{dp} to the real part of the effective propagation constant $k_{eff} = k_{\underline{eff}}^{Re} - jk_{eff}^{Im}$ (derived from the effective dielectric constant ε_{eff}).

$$K_{dp} = 10^{-3}\frac{180}{\pi} \cdot \left(k_{eff_h}^{Re} - k_{eff_v}^{Re}\right). \tag{1.2.41}$$

To highlight this aspect it is sufficient to remember that the exponential term of a plane wave which propagates, for example, along the r-direction in a medium of dielectric constant ε_{eff} is $-j \cdot k_{eff} \cdot r$ and then k_{eff}^{Re} represents a phase term, whereas k_{eff}^{Im} represents an attenuation term. Omitting all the mathematical passages [refer to Bringi and Chandrasekar (2001) for the rigorous treatment] k_{eff} assumes the following expression in the case of a slab of air with n spherical particles per unit volume:

$$k_{eff} = k_0 + \frac{2\pi n}{k_0}\hat{e}_i \cdot \underline{\boldsymbol{f}}(\hat{k}_i, \hat{k}_i) \tag{1.2.42}$$

where $\mathbf{f}$ is the vectorial scattering function introduced in Eq. (1.2.16) and $\hat{e}_i$ is the unit vector which describes the polarization of the electric field. In this case, $\mathbf{f}(\hat{k}_i, \hat{k}_i))$ describes the scattering behavior along the direction $\hat{k}_i$ in response to an incident plane wave which propagates along the same incident direction $\hat{k}_i$ (forward scattering). Substituting Eq. (1.2.42) in Eq. (1.2.41), the expression of K_{dp} for a portion of air with n particles per unit volume becomes

$$K_{dp} = 10^{-3}\frac{180}{\pi} \cdot \frac{2\pi n}{k_0}\mathrm{Re}\left[\hat{h} \cdot \underline{\boldsymbol{f}}(\hat{k}_i, \hat{k}_i) - \hat{v} \cdot \underline{\boldsymbol{f}}(\hat{k}_i, \hat{k}_i)\right] \tag{1.2.43}$$

Table I.2.3 Typical ranges of observed specific differential phase in several precipitation types

K_{dp} (deg/km)	Associated precipitation types
<–0.5	Marginally detectable precipitation
–0.5 to 0.5	Drizzle, very light rain, light snow
0.5 to 1	Moderate rain and heavier snow
0.5 to 5	Moderate to heavy rain
–0.5 to 1	Hail
–0.5 to 1	Melting snow particles

Values adapted from Straka et. al. (2000) and Bringi and Chandrasekar (2001).

In the general case, where a size distribution of particles $N(D)$ exists, Eq. (1.2.40) can be reformulated as follows:

$$K_{\mathrm{dp}} = 10^3 \frac{180}{\pi} \lambda \mathrm{Re} \left\{ \int_0^\infty N(D) \left[f_{\mathrm{hh}}(r, D) - f_{\mathrm{hh}}(r, D) \right] dD \right\}, \tag{1.2.44}$$

where the components $f_{\mathrm{hh,vv}}$ are the projection of the vectorial scattering function in the forward direction of the wave propagation $\mathbf{f}(\hat{k}_{\mathrm{i}},\ \hat{k}_{\mathrm{i}})$, along the vertical $\left(\mathbf{f}(\hat{k}_{\mathrm{i}},\ \hat{k}_{\mathrm{i}}) \cdot \hat{v}\right)$and horizontal $\left(\mathbf{f}(\hat{k}_{\mathrm{i}},\ \hat{k}_{\mathrm{i}}) \cdot \hat{h}\right)$directions.

The observable K_{dp} is not affected by electromagnetic wave attenuation since it is based on the measurement of the phase shift of the wave rather than the amplitude of the returned power. Being based on the phase shift concept, K_{dp} can be obtained when the radar beam is partially blocked as well. Beam blocking can be caused by mountainous or terrain roughness for example. In addition, K_{dp} is a very important parameter being insensitive to radar calibration, propagation effects, and system noise. Potential uses of K_{dp} include estimation of moderate and heavy rain rates, correction for attenuation losses, and verification of radar hardware calibration. Nevertheless, it is more readily contaminated by side lobe signals than the power measurements (Sachidananda, and Zrnic, 1987). A disadvantage of K_{dp} is its insensitivity to precipitation composed of small spherical raindrops, where D<1 mm and the axis ratio $a/b \approx 1$, associated with low liquid water contents and low rain rates. Typical values for K_{dp} are listed in Table I.2.3.

References

Atlas D (1954) The estimation of cloud parameters by radar. J Meteorol 11:309–317

Alberoni PP, Ferraris L, Marzano FS, Nanni S, Pelosini R, Siccardi F (2002) The Italian radar network: current status and future developments. In: Proceedings of ERAD02. pp 339–344

Aydin K, Giridhar V (1992) C-band dual-polarization radar observables in rain. J Atmos Ocean Technol 9:383–390

Balakrishnan N, Zrnic DS (1990) Use of polarization to characterize precipitation and discriminate large hail. J Atmos Sci 47:1525–1540

Balanis CA (1997) Antenna theory: analysis and design, 2nd edn. Wiley, New York, NY

Baldini L, Gorgucci E, Chandrasekar V (2004) ydrometeor classification methodology for C-band polarimetric radars. In: Proceedings of ERAD04. pp 62–66

Bringi VN, Chandrasekar V (2001) Polarimetric Doppler weather radar. Cambridge University Press, Boston, MA

Bringi VN, Chandrasekar V, Xiao R (1998) Raindrop axis ratio and size distributions in Florida rainshafts: an assessment of multiparameter radar algorithms. IEEE Trans Geosci Remote Sens 36:703–715

Bringi VN, Keenan TD, Chandrasekar V (2001) Correcting C-band radar reflectivity and differential reflectivity data for rain attenuation: a self-consistent method with constraints. IEEE Trans Geosci Remote Sens 39(9):1906–1915

Chandrasekar V, Bringi VN (1987) Simulation of radar reflectivity and surface measurements of rainfall. J Atmos Ocean Technol 4(3):464–478

Chandrasekar V, Hou A, Smith E, Bringi VN, Rutledge SA, Gorgucci E, Petersen WA, Jackson GS (2008) Potential role of dual polarization radar in the validation of satellite precipitation measurements: rationale and opportunities. Bull Am Meteorol Soc 89:1127–1145

Gorgucci E, Chandrasekar V, Bringi VN, Scarchilli G (2002) Estimation of raindrop size distribution parameters from polarimetric radar measurements. J Atmos Sci 59(15):2373–2384

Gorgucci E, Scarchilli G, Chandrasekar V, Bringi VN (2000) Measurement of mean raindrop shape from polarimetric radar observations. J Atmos Sci 57:3406–3413

Graeme LS, Vane DG, Ronald JB, Mace GG, Sassen K, Wang Z, Illingworth AJ, O'Connor EJ, Rossow WB, Durden SL, Miller SD, Austin RT, Benedetti A, Mitrescu C, the CloudSat Science Team (2002) The cloudsat mission and the A-Train, a new dimension of space-based observations of clouds and precipitation. Bull Am Meteorol Soc 83(12):1771–1790

Holleman I, Delobbe L, Anton Zgonc A (2008) The European weather radar network (OPERA): an opportunity for hydrology. In: Proceedings of ERAD, Helsinky

Jones DMA (1959) The shape of raindrops. J Meteorol 16(October):504–510

Marzano FS, Scaranari D, Celano M, Alberoni PP, Vulpiani G, Montopoli M (2006) Hydrometeor classification from dual-polarized weather radar: extending fuzzy logic from S-band to C-band data. Adv Geosci 7:109–114

Marzano FS, Scaranari D, Vulpiani G, Montopoli M (2008) Supervised classification and estimation of hydrometeors using C-band dual-polarized radars: a Bayesian approach. IEEE Trans Geosci Remote Sens 46:85–98

Mishchenko MI (2000) Calculation of the amplitude matrix for a nonspherical particle in a fixed orientation. Appl Opt 39:1026–1031

Mishchenko MI, Hovenier JW, Travis LD (eds) (2000) Light scattering by nonspherical particles: theory, measurements, and applications. Academic Press, San Diego, CA

Mishchenko MI, Travis LD (1998) Capabilities and limitations of a current Fortran implementation of the T-Matrix method for randomly oriented, rotationally symmetric scatterers. J Quant Spectros Radiative Transfer 60(3):309–324

Probert-Jones JR (1962) The radar equation in meteorology. Q J R Meteorol Soc 88:485–495

Pruppacher HR, Beard KV (1970) A wind tunnel investigation of the internal circulation and shape of water drops falling at terminal velocità in air. Q J R Meteorol Soc 96(April):247–256

Pruppacher HR, Pitter RL (1971) A semi-empirical determination of the shape of cloud and rain drops. J Atmos Sci 28(January):86–94

Ryzhkov AV, Schuur TJ, Burgess DW, Heinselman PL, Giangrande SE, Zrnić DS (2005) The joint polarization experiment. Polarimetric rainfall measurements and hydrometeor classification. Bull Am Meteorol Soc 86(6):809–824

Sachidananda M, Zrnic DS (1987) Rain rate estimates from differential polarization measurements. J Atmos Ocean Technol 4:588–598

Saffle R, Istok M, Johnson LD (2002) NEXRAD product improvement – progress and plans. In: Preprints of 18th international conference on IIPS, Orlando, FL, Am Meteorol Soc. Paper 5.1

Sauvageot H (1992) Radar meteorology. Artec House, Boston, MA

Straka JM, Zrnić DS, Ryzhkov AV (2000) Bulk hydrometeor classification and quantification using polarimetric radar data: synthesis of relations. J Appl Meteorol 39(8):1341–1372

Testud J, Le Bouar E, Obligis E, Ali-Mehenni M (2000) The rain profiling algorithm applied to polarimetric weather radar. J Atmos Ocean Technol 17(3):332–356

Toshiaki K, Iguchi T, Shimomai T, Kashiwagi N (2009) Raindrop size distribution modeling from a statistical rain parameter relation and its application to the TRMM precipitation radar rain retrieval algorithm. J Appl Meteorol Climatol 48(4):716–724

Ulaby FT, Moore RK, Fung AK (1986) Microwave remote sensing, active and passive. From theory to applications. vol III. Artech House, Boston, MA

Vivekanandan J, Zhang G, Brandes E (2004) Polarimetric radar estimators based on a constrained gamma drop size distribution model. J Appl Meteorol 43(2):217–230

Vivekanandan J, Zrnić DS, Ellis SM, Oye R, Ryzhkov AV, Straka J (1999) Cloud microphysics retrieval using S-band dual-polarization radar measurements. Bull Am Meteorol Soc 80(3):381–388

Vulpiani G, Marzano FS, Chandrasekar V, Lim S (2005) Constrained iterative technique with embedded neural-network for dual-polarization radar correction of rain path attenuation. IEEE Trans Geosci Remote Sens 43(10):2305–2314

Waterman PC (1971) Symmetry, unitarity, and geometry in electromagnetic scattering. Phys Rev D 3:825–839

Zrnic DS, Ryzhkov A (1998) Observations of insects and birds with polarimetric radar. IEEE Trans Geosci Remote Sens 36:661–668

Zrnić DS, Ryzhkov AV, Straka J, Liu Y, Vivekanandan J (2001) Testing a procedure for automatic classification of hydrometeor types. J Atmos Ocean Technol 18(6):892–913

Chapter I.3
Principles of Aerosol LIDAR Systems

Vincenzo Rizi and Marco Iarlori

1 Introduction

This lecture is dedicated to the description of the fundamentals of the aerosol lidar theory (of course it is not a complete overview!).

I will talk about aerosol LIDAR technique, discussing a kind of classical representation of the LIDAR technique; in other words: monitoring the fate of coherent and undistinguishable photons travelling in and interacting with a non-homogeneous medium: atmosphere (including aerosols).

Hopefully, it will be clear, along this lecture, how LIDAR can measure some fundamental aerosol optical properties; in this context I will try to connect to other lectures.

I will try to keep alive your attention presenting the architecture of LIDAR instruments (i.e., UV/Visible – Rayleigh/Mie and Raman LIDARs), which are mainly devoted to aerosol observations. Using, in real time, our own software, I will also discuss the down- and upsizing of the different lidar components (lasers, telescopes, detectors) for the best observational strategy of the various atmospheric aerosols (including clouds).

Maybe exaggerating and upon my ability, the expected outcomes are the following. You will be able to:

- understand how LIDAR techniques are used to characterize atmospheric aerosols,
- perform tradeoffs among the engineering parameters of a LIDAR system to achieve a given measurement capability, and
- evaluate the performance of LIDAR systems.

V. Rizi (✉)
CETEMPS/Dipartimento di Fisica, Università Degli Studi dell'Aquila, L'Aquila, Italy
e-mail: Vincenzo.Rizi@aquila.infn.it

Presented at International Summer School on Atmospheric and Oceanic Sciences, L'Aquila, Italy, 3–7 September 2007

D. Cimini et al. (eds.), *Integrated Ground-Based Observing Systems*,
DOI 10.1007/978-3-642-12968-1_3,

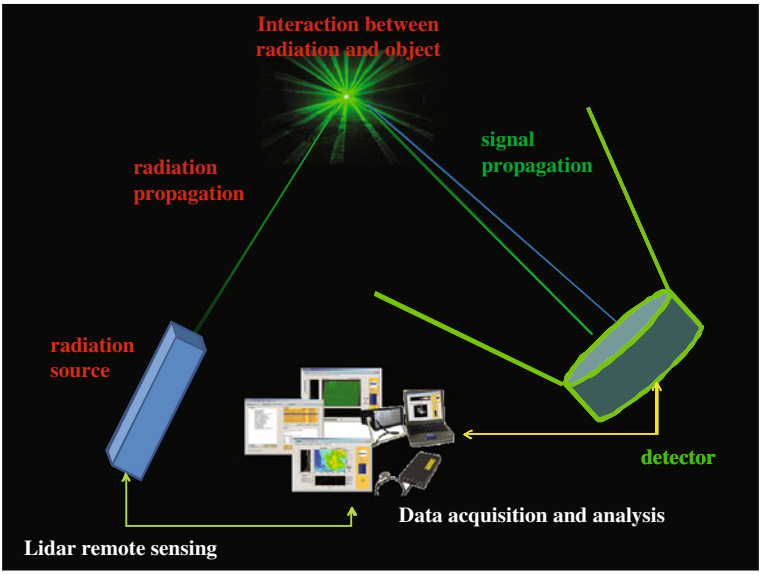

Fig. I.3.1 Layout of a lidar system

The lidar layout in Fig. I.3.1 is typical: the generated radiation (a laser pulse) propagates in the medium (the atmosphere), interacts with the medium, and propagates back to the detector (telescope). All is driven by instrumentations that set the timescale of the radiation travel, or the range from where the signal returns back (carrying information concerning the interaction with the medium and its components).

A short history of the lidar technique: searchlight technique, very similar to the modern lidar technique, has been used for aerosol observations (Hulburt, 1937); Johnson et al. (1939) and Tuve et al. (1935) modulated the searchlight beam with a mechanical shutter, increasing the sensitivity of technique; Elterman (1951) has used searchlight technique to study stratosphere. After the laser technology became widely available, the lidar started to be a fundamental instrument for the atmospheric aerosol observations. The first (ruby) laser was invented in 1960 (Schawlow and Townes, 1958; Maiman, 1960); laser pulse technique (Q-Switch) (McClung and Hellwarth, 1962) constituted another fundamental step. The first laser studies of the atmosphere were undertaken by Fiocco and Smullin (1963) for upper region and by Ligda [1963] for troposphere. The indicated papers are very interesting, and after reading, my personal feeling is that we (lidar people) are playing with well-proofed toys.

2 Lidar Architecture

In the next slides, I will give more details and highlights about the lidar components: transmitter, receiver, system control, and data acquisition (Fig. I.3.2).

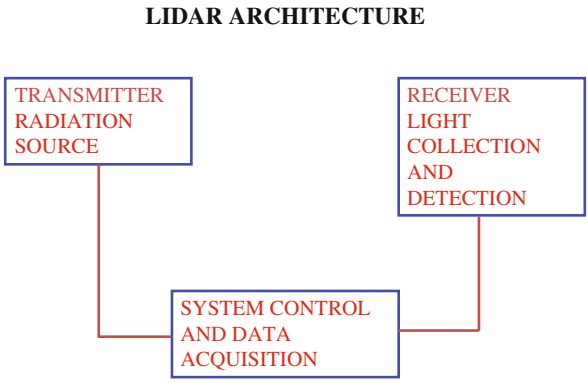

Fig. I.3.2 Lidar architecture

2.1 Transmitter

It provides laser pulses (Fig. I.3.3) that meet certain requirements depending on application needs (e.g., wavelength, pulse duration, pulse energy, repetition rate, divergence angle). Transmitter consists of lasers, collimating and steering optics, and diagnostic equipment (for checking the laser stability, etc.).

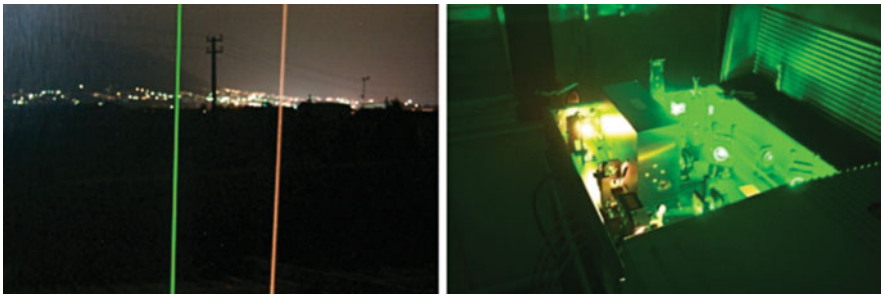

Fig. I.3.3 Laser and laser beams

2.2 Receiver

It collects and detects returned photons, It consists of telescopes, optical filters, collimating optics, photon detectors, and fast electronics, etc. (Fig. I.3.4). The receiver can spectrally distinguish the returned photons.

2.3 System Control and Data Acquisition

It records returned data and corresponding time of flight and provides the coordination to transmitter and receiver. It consists of multi-channel scaler which has very precise clock, discriminator, computer, and software (Fig. I.3.5).

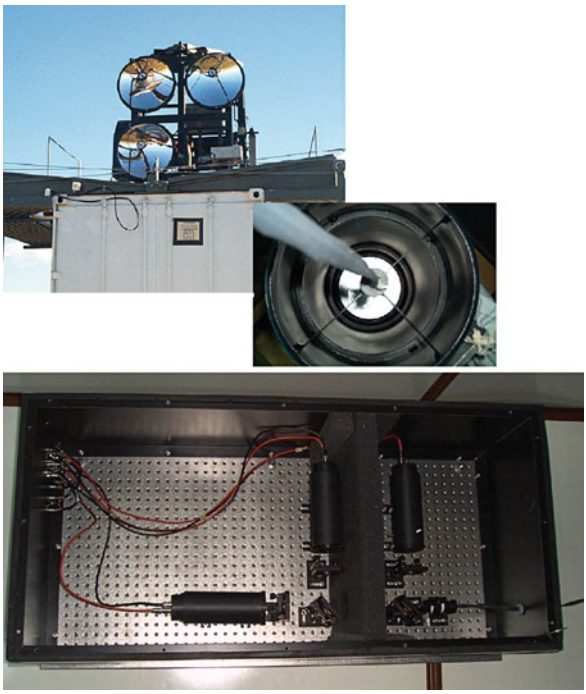

Fig. I.3.4 Telescopes and detectors

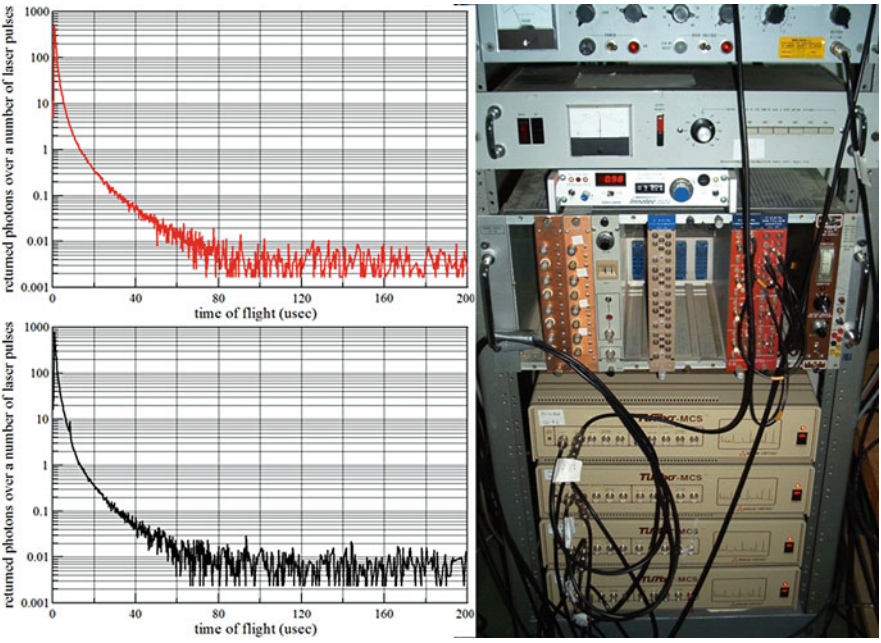

Fig. I.3.5 Lidar electronics and recorded signals

2.4 Lidar Return

Then the typical lidar return appears like in Fig. I.3.6. A number of photons collected as a function of the flight time/range. The question is: which kind of information (focusing on aerosols) is carried back by the detected photons?

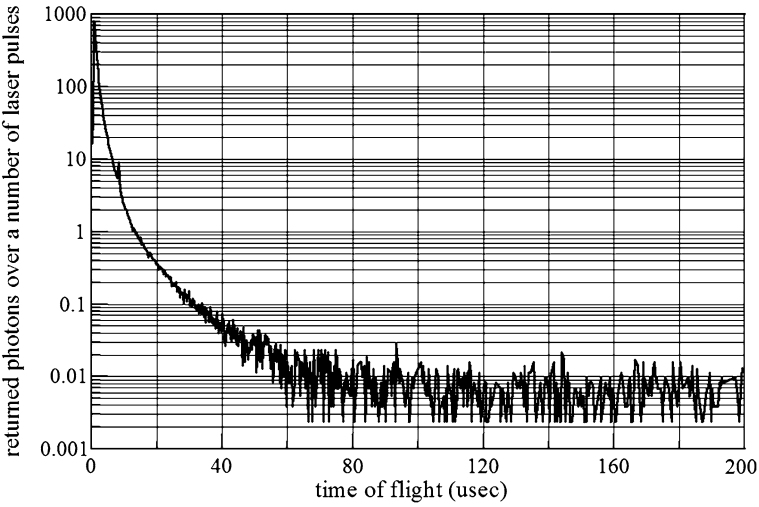

Fig. I.3.6 Lidar return: number of photons vs. flight time

3 Lidar Equation

The description of lidar returns is done setting up the right equation: the lidar equation relates the received photon counts with the transmitted laser photons, the light transmission in atmosphere or medium, the physical interaction between light and objects, the photon receiving probability, and the lidar system efficiency and geometry.

The lidar equation is based on the physical picture of lidar remote sensing and derived under two assumptions: only independent and single scattering processes. Different lidars may use different forms of the lidar equation, but all come from the same picture. I will limit my discussion to the UV-Visible wavelength lidars.

Let us introduce some notation. In general, the interaction between the light photons and the particles is a scattering process.

The expected photon counts are proportional to the product of the

- number of transmitted laser photons,
- probability that a transmitted photon is scattered,
- probability that a scattered photon is collected,

- light transmission through medium, and
- overall system efficiency.

Background photon counts and detector noise also contribute to the expected photon counts. The number of collected photons in a time interval Δt (from range interval between s and $s + \Delta s$, where $\Delta s = c \cdot \Delta t/2$, c is the speed of light) is

$$N_S(\lambda_o, \lambda, R) = N_o(\lambda_o)T(\lambda_o, s)[\beta(\lambda_o, \lambda, s)\Delta s]T(\lambda, s)\frac{d\Omega}{4\pi}\eta(\lambda, \lambda_o)G(s) + N_B, \quad (1)$$

where

$N_o(\lambda_o)$	number of emitted photons
$T(\lambda_o, s)$	laser transmission through the medium
$\beta(\lambda, \lambda_o, s) \cdot \Delta s$	probability of a transmitted photon to be scattered
$T(\lambda, s)$	scattered photon transmission through the medium
$d\Omega/4\pi$	probability of a scattered photon to be collected
$\eta(\lambda, \lambda_o)G(s)$	lidar system efficiency and geometry factor

3.1 Transmitter Laser Photons

From the datasheet of a standard 355-nm pulsed laser (4 mW output power, few micro Joules per pulse), it is possible to evaluate the number of the photons emitted per laser pulse: for the above laser's specifications it is about 6.7×10^{12} photon per pulse.

3.2 Transmission

It accounts for the processes that could extinguish the travelling photons; it can be interpreted as the relative fraction of propagating photons that travel a distance without interacting. About the interacting photons I will say more in the next paragraphs.

$$T(\lambda, s) = T^{\lambda}_{\text{mol}}(s) \cdot T^{\lambda}_{\text{aer}}(s) \cdot T^{\lambda}_{\text{abs}}(s),$$

where $T^{\lambda}_{\text{mol}}(s)$, molecular scattering transmission; $T^{\lambda}_{\text{aer}}(s)$, aerosol scattering transmission; $T^{\lambda}_{\text{abs}}(s)$, gas absorption transmission; and

$$T^{\lambda}_{\text{mol}}(s) = \exp\left(-\int_0^s \sigma^{\lambda}_{\text{mol}} n_{\text{mol}}(s)ds\right)$$

$$T^{\lambda}_{\text{aer}}(s) = \exp\left(-\int_0^s \left[\int_0^{\infty} dr\pi r^2 Q_{\text{ext}}(r, m, \lambda)n_{\text{aer}}(s, r)\right] ds\right)$$

$$T^{\lambda}_{\text{abs}}(s) = \exp\left(-\sum_i \int_0^s \sigma^{i}_{\text{abs}}(\lambda)n^{i}_{\text{abs}}(s)ds\right)$$

where n_{mol}, atmospheric molecular number density; n_{aer}, aerosol size distribution; n^i_{abs}, ith absorbing gas number density; $\sigma^{\lambda}_{\mathrm{mol}}$, molecular scattering total cross section; $Q_{\mathrm{ext}}(r, m, \lambda)$, Mie scattering extinction efficiency of an aerosol particle (r, radius; m, index of refraction); $\sigma^i_{\mathrm{abs}}(\lambda)$, ith gas absorbing cross section.

3.3 Backscattering

The volume backscattering coefficient is the probability per unit distance travel that a photon is backscattered (per unit of solid angle) or scattered in the direction of the receiver:

$$\beta(\lambda_o, \lambda, s) = \sum_i \frac{d\sigma_i(\lambda_o, \lambda)}{d\Omega} n_i(s).$$

If the scattering objects are aerosols,

$$\beta^{\lambda}_{\mathrm{aer}}(s) = \frac{1}{4\pi} \int_0^{\infty} dr \cdot \pi r^2 \cdot Q_{\mathrm{bck}}(r, m, \lambda) \cdot n_{\mathrm{aer}}(s, r),$$

where $n_{\mathrm{aer}}(s, r)$, aerosol size distribution and $Q_{\mathrm{bck}}(r, m, \lambda)$, Mie backscattering efficiency of an aerosol particle (r, radius; m, index of refraction).

3.4 Geometrical Collecting Efficiency

This is the probability that a scattered photon is collected by the receiving telescope.

$$\frac{d\Omega}{4\pi} = \frac{A}{s^2}$$

Note that this is proportional to the collecting area, and it depends on the range from where the light is collected (Fig. I.3.7).

3.5 Optical Collecting Efficiencies

Some of these effects are due to the optical setup and optics performances. In the receiver there are filters to discriminate, according to the wavelength, the collected photons [$\eta(\lambda, \lambda_o)$]. In addition the receiving telescope can introduce a geometrical form factor that modulates the collecting efficiency as a function of range, $G(s)$ (Fig. I.3.8).

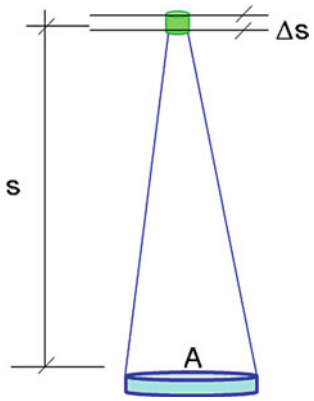

Fig. I.3.7 Receiver field of view

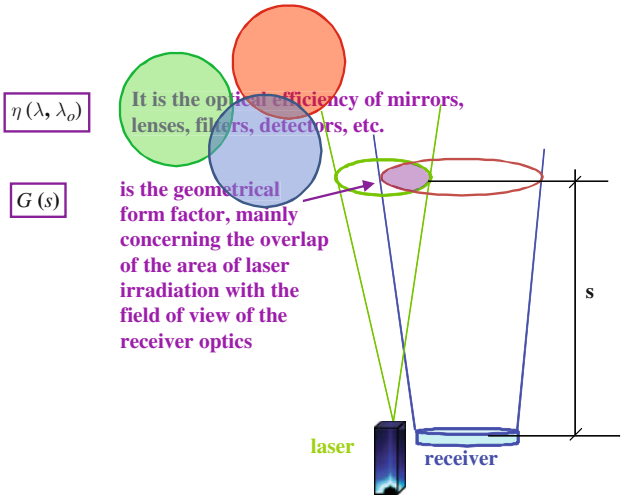

Fig. I.3.8 Schematic of optical collecting efficiency

3.6 Noise

The better one (always mixed up with more subtle noises) is linear, range independent, and white (sky light and detector/electronic noise).

4 Different Forms of Lidar Equation

Lidar equation may change forms to represent each particular physical process (Mie, Rayleigh and Raman scattering, etc.) and lidar application.

Going further into the physical processes (hopefully, I am still discussing what I have promised), let us take a break. I will show a funny representation of the lidar processes.

4.1 A Physics-ological Drama

The cartoon animation presented in Figs. I.3.9–I.3.13 is available upon request to vincenzo.rizi@aquila.infn.it.

SCENE I The laser emission
SCENE II The upward travel

In which photons make different experiences at the beginnings of the travel, several of them will be lost (extinction).

SCENE III Local backscattering

Some lucky guys find the way back, with unchanged identities (aerosol and molecular elastic backscattering) or quite evident differences (depending on the encountered situations, molecular Raman backscattering)

SCENE IV The downward travel

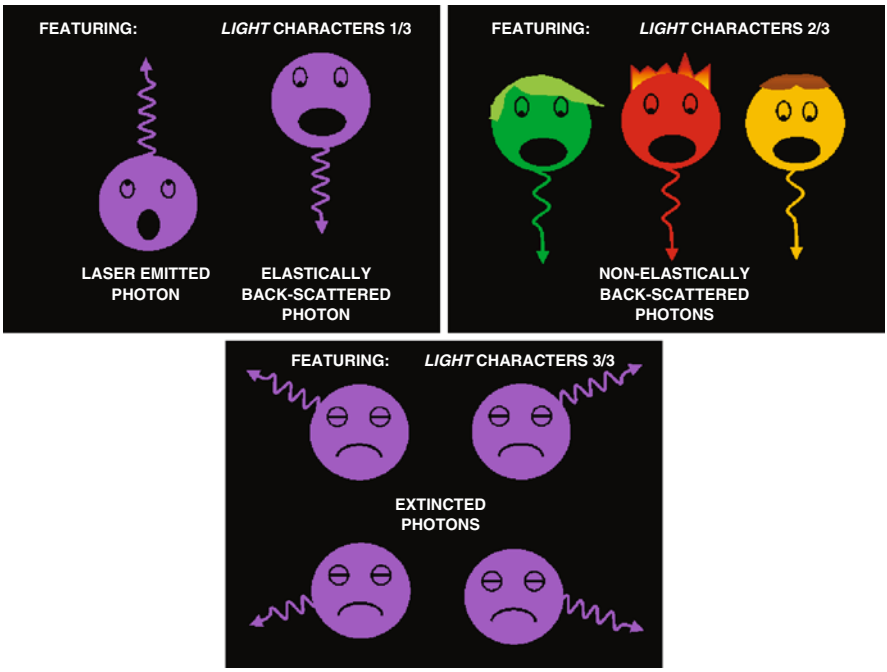

Fig. I.3.9 The cartoon representation of fundamental lidar processes: the main characters

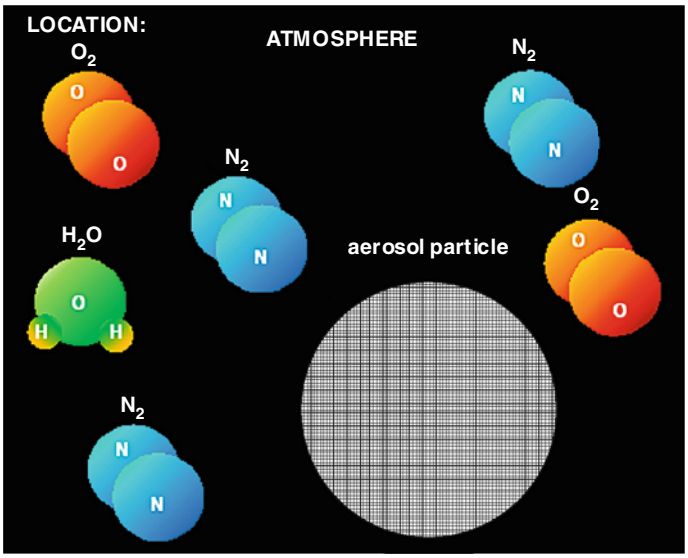

Fig. I.3.10 The cartoon representation of fundamental lidar processes: the location (the atmosphere)

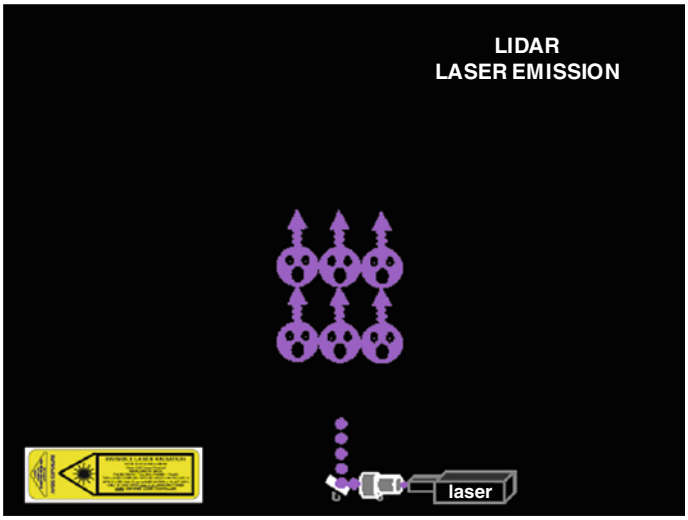

Fig. I.3.11 The cartoon representation of fundamental lidar processes: leaving together . . .

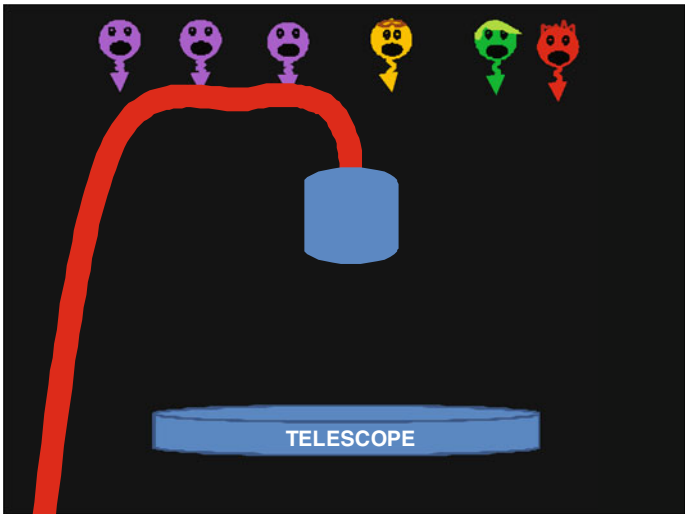

Fig. I.3.12 The cartoon representation of fundamental lidar processes: at home, carrying different information . . .

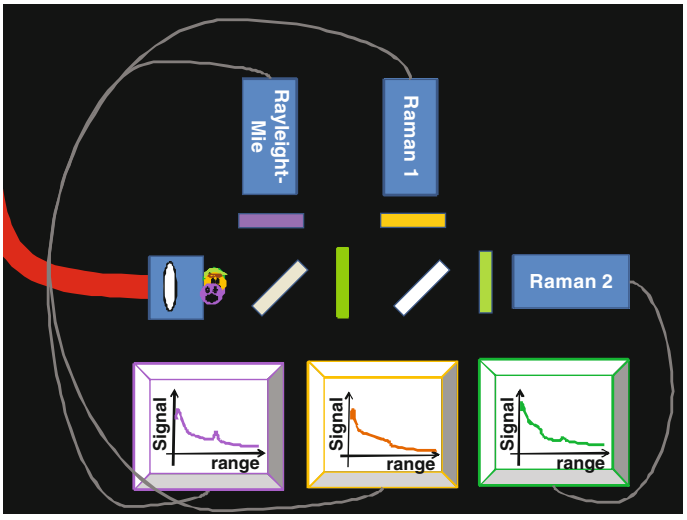

Fig. I.3.13 The cartoon representation of fundamental lidar processes: communicating all the stories (something useful remains): what they have done, where they have travelled

On the way back . . . not fully unexpected losses

SCENE V Detection
SCENE VI

5 Lidar Physical Processes

Then, there are many physical processes involved when the lidar light propagates and interacts in the atmosphere:

- Scattering (elastic and inelastic): Mie, Rayleigh, Raman
- Absorption and differential absorption
- Resonant fluorescence
- Doppler shift and Doppler broadening
- . . .

I will discuss only the scattering processes; before starting let us introduce some additional definitions. Light propagation in atmosphere relies on transmission/extinction, where: Extinction = Scattering + Absorption, and the scattering processes could be elastic and inelastic.

5.1 Rayleigh Scattering

Rayleigh scattering is referred to the *elastic scattering* from atmospheric molecules (particle size is much smaller than the wavelength), i.e., scattering with no apparent change of wavelength, although still undergoing Doppler broadening and Doppler shift. However, depending on the resolution of detection, Rayleigh scattering consists of the Cabannes scattering (really elastic scattering from molecules) and pure rotational Raman scattering.

5.2 Raman Scattering

Raman scattering is the *inelastic scattering* with rotational quantum state or vibration-rotational quantum state change as a result of scattering. The Raman scattered photons are shifted in wavelength, this shift is the signature of the stationary energy levels of the irradiated molecule. The Raman spectroscopy in a gas mixture identifies and measures the different components. Example: the nitrogen and oxygen molecules show Raman shifts (roto-vibrational transitions) of 2,327 cm^{-1} and 1 556 cm^{-1}, respectively.

5.3 Mie Scattering for the Other Object (Aerosol) in the Atmosphere

Mie scattering is the *elastic scattering* from spherical particles (Mie, 1908), which includes the solution of Rayleigh scattering. However, in lidar field, first, Mie scattering is referred to the elastic scattering from spherical particles whose size is comparable to or larger than the wavelength. Furthermore, Mie scattering is generalized to elastic scattering from overall aerosol particles and cloud droplets, i.e., including non-spherical particles.

5.4 Lidar Backscattering and Extinction

A lidar is designed to observe the atmospheric backscattering and the extinction; we will concentrate on the systems which are able to sample the aerosol backscattering and extinction.

Physical process	Back-scattering cross section
Mie (aerosol) scattering	$10^{-8} \div 10^{-10}$ **cm**^{2} **sr**$^{-1}$
Rayleigh scattering	10^{-27}**cm**^{2} **sr**$^{-1}$
Raman scattering	10^{-30}**cm**^{2} **sr**$^{-1}$

The numbers in the table give an idea of the magnitude of the different scattering processes. Note how small is the effect of the Raman scattering with respect to the elastic processes. In spite of this, a lidar with the capabilities of discriminate between inelastic (RAMAN) and elastic (MIE/Rayleigh) backscatter photons is a very powerful instrument for the observation of the aerosol optical properties (more details in the next paragraphs).

Figure I.3.14 shows the complete spectrum of the Raman backscattered photons; when the emitted ones are in the UV range (355-nm wavelength), for each specific molecule (N_2, O_2, and H_2O) the wavelength shift of the vibrational line and of the roto-vibrational wings is the signature of the molecule itself.

6 Aerosol-Devoted Lidar

I will discuss the main features of a simple lidar systems designed to measure the vertical profile of the aerosol extinction coefficient, $\alpha_{\text{aer}}^{\lambda_o}(s)$ and of the aerosol backscatter coefficient, $\beta_{\text{aer}}^{\lambda_o}(s)$. Their dependence from the aerosol optical and physical parameters is described by

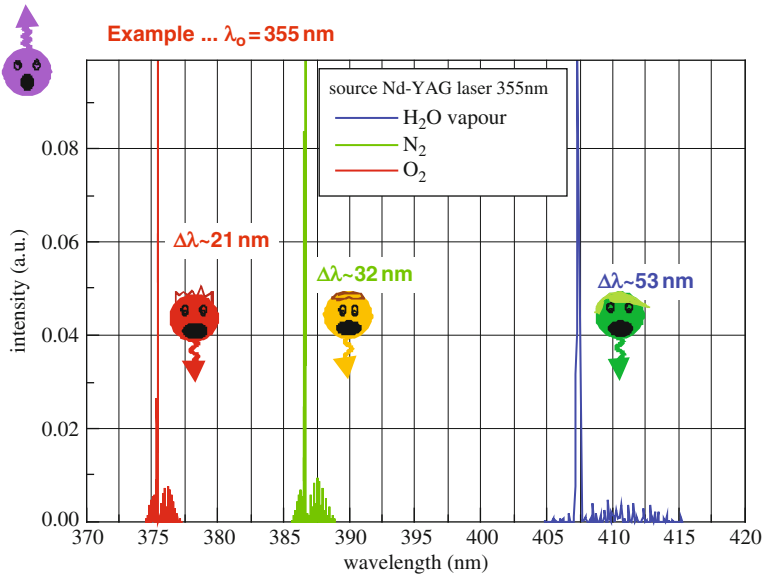

Fig. I.3.14 The Raman backscatter photons when the emitted wavelength is 355 nm (Nd-Yag laser-third harmonics)

$$\alpha_{\text{aer}}^{\lambda_o}(s) = \int_0^\infty dr\pi r^2 Q_{\text{ext}}(r, m, \lambda_o) n_{\text{aer}}(s, r) \tag{2}$$

and

$$\beta_{\text{aer}}^{\lambda_o}(s) = \int_0^\infty dr\pi r^2 Q_{\text{bck}}(r, m, \lambda_o) n_{\text{aer}}(s, r), \tag{3}$$

where $n_{\text{aer}}(s, r)$ is the aerosol size distribution, and $Q_{\text{ext}}(r, m, \lambda)$ and $Q_{\text{bck}}(r, m, \lambda)$ are the Mie extinction and backscattering efficiencies of an aerosol particle of radius r, index of refraction m, at wavelength λ.

6.1 Aerosol Raman Lidar

It should be said that the use of single wavelength (elastic) lidar suffers from the fact that two physical quantities, the aerosol backscatter and extinction coefficients, must be determined from only one measured lidar signal. This is not possible without assumptions about the relation between the two and estimate of a boundary or reference value of the aerosol extinction.

If we are able to detect the Raman backscattered photons, then the Raman return is more or less a direct measurement of the aerosol extinction (Fig. I.3.15).

The Raman lidar technique can provide unbiased measurements of the aerosol optical properties: extinction and backscatter coefficients (Ansmann et al., 1992),

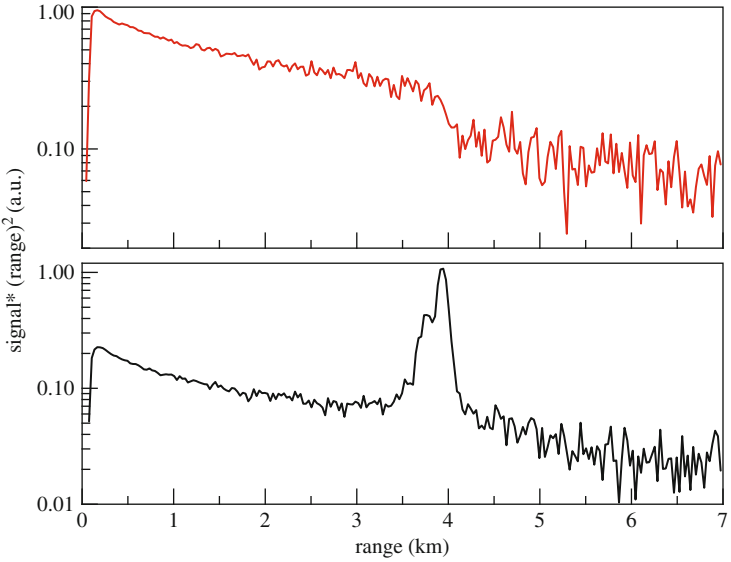

Fig. I.3.15 Raman lidar signal (*above*) and the elastic lidar backscatter (*below*) in the presence of cloud aerosols. Note the quite clear signature of the cloud transmission in the Raman return

both of them, straightforwardly used for the assessment of the atmospheric optical transmission, are indirect measurements of the aerosol concentration. For example, the analysis of the extinction and backscatter vertical structures gives information about the planetary boundary layer (Matthias and Bosenberg, 2002).

Rayleigh/Mie and Raman lidar inversion methods are well known (Ferrare et al., 1998), and it has been demonstrated that the combination of the different methods leads to an improvement of the results. With regard to these measurements, a complete description of algorithms and assessment of the data quality can be found in Bockmann et al. (2004) and Pappalardo et al. (2004).

The aerosol extinction can be determined from N_2 Raman lidar return through the application of the following expression:

$$\alpha_{\text{aer}}^{\lambda_o}(s) = \frac{\frac{d}{dz}\left\{\ln\left[\frac{n_{\text{mol}}(s)}{s^2 N_R(s)}\right]\right\} - \alpha_{\text{mol}}^{\lambda_o}(s) - \alpha_{\text{mol}}^{\lambda_R}(s)}{1 + \left(\frac{\lambda_o}{\lambda_R}\right)^k}, \tag{4}$$

where $N_R(s)$ is the Raman return at wavelength $\lambda_R = (\lambda_o + \Delta\lambda_{N_2})$ [$\Delta\lambda_{N_2}$ is the Raman shift of N_2], $n_{\text{mol}}(s)$ is the atmospheric molecular number density, $\alpha_{\text{mol}}^{\lambda_o}(s)$ and $\alpha_{\text{mol}}^{\lambda_R}(s)$ are the extinction coefficients due to absorption and Rayleigh scattering by atmospheric gases; the Mie aerosol scattering is assumed to be proportional to λ^{-k}. Then, it needs to evaluate a numerical derivative for the estimation of the aerosol extinction coefficient; both $\alpha_{\text{aer}}^{\lambda_o}(s)$ and its uncertainty could be misevaluated if data acquisition and analysis are not correctly accomplished.

The uncertainties affecting $\alpha_{\mathrm{aer}}^{\lambda_o}(s)$ are mainly due to:

- the statistical error due to signal detection;
- the systematic error associated with the estimation of $n_{\mathrm{mol}}(s)$ (i.e., from pressure and temperature profiles);
- the systematic error associated with the evaluation of k, aerosol scattering wavelength dependence;
- the errors introduced by operational procedures such as signal binning (smoothing) and averaging (accumulating lidar returns);

The above expression for $\alpha_{\mathrm{aer}}^{\lambda_o}(s)$ can be applied to the altitude range where the lidar overlap is complete [$G(s) = 1$], otherwise an additional systematic error should be accounted for.

The aerosol backscattering coefficient is evaluated according to:

$$\beta_{\mathrm{aer}}^{\lambda_o}(s) = \beta_{\mathrm{mol}}^{\lambda_o}(s)\left[\frac{N(s)}{N_{\mathrm{R}}(s)} \cdot \frac{A_{\mathrm{R}}}{A_o} \cdot \frac{\sigma_{\mathrm{Raman}}^{\lambda_R}(\pi)\cdot f}{\sigma_{\mathrm{mol}}^{\lambda_o}(\pi)} \cdot \frac{T_{\mathrm{mol}}^{\lambda_R}(s)}{T_{\mathrm{mol}}^{\lambda_o}(s)} \frac{T_{aer}^{\lambda_R}(s)}{T_{\mathrm{aer}}^{\lambda_o}(s)} - 1\right], \quad (5)$$

where $N(s)$ is the Rayleigh/Mie elastic return, $T_{\mathrm{mol}}^{\lambda}(s)$ is the molecular transmission, $T_{\mathrm{aer}}^{\lambda}(s)$ is the aerosol transmission at wavelength λ; A_o and A_{R} account for the optical and electronic efficiencies of the corresponding lidar channel; $\sigma_{\mathrm{mol}}^{\lambda_o}(\pi)$ and $\sigma_{\mathrm{Raman}}^{\lambda_R}(\pi)$ are the differential backscattering cross section for Rayleigh and Raman molecular scattering; f is the volume mixing ration of N_2. The aerosol backscattering calculation needs to evaluate $\frac{A_{\mathrm{R}}}{A_o} \cdot \frac{\sigma_{\mathrm{Raman}}^{\lambda_R}(\pi)\cdot f}{\sigma_{\mathrm{mol}}^{\lambda_o}(\pi)}$, and this is done by imposing $\beta_{\mathrm{aer}}^{\lambda_o}(s) = 0$ in the range of altitude free of aerosols.

The uncertainties affecting $\beta_{\mathrm{aer}}^{\lambda_o}(s)$ are mainly due to:

- the statistical error due to signal detection;
- the systematic error associated with the estimation of $n_{\mathrm{mol}}(s)$ (i.e., from pressure and temperature profiles); and
- the errors introduced by operational (retrieval) procedures.

The design of the Raman lidar receiver (the telescope can be coupled to the detector box through an optical fiber) assigns the same overlap function to the Rayleigh/Mie elastic and N_2 Raman lidar channels; because the evaluation of $\beta_{\mathrm{aer}}^{\lambda_o}(s)$ involves the ratio between the two lidar returns, the retrieval procedure of the aerosol backscattering coefficient results independent of the lidar geometrical overlap.

Other quantities are usually evaluated: the vertical aerosol optical depth (VAOD) and the integrated aerosol backscatter coefficient (INTAβ) up to 4–5 km range, and, also, the *mean* lidar ratio (LR). The VAOD and INTAβ, between the range heights s_1 and s_2, are defined as

$$\mathrm{VAOD}(s_1, s_2) = \int_{s_1}^{s_2} \alpha_{\mathrm{aer}}^{\lambda_o}(s')ds', \tag{6}$$

$$\mathrm{INTA}\beta(s_1, s_2) = \int_{s_1}^{s_2} \beta_{\mathrm{aer}}^{\lambda_o}(s')ds'. \tag{7}$$

And, the *mean* LR is calculated according to

$$\mathrm{LR} \cong \frac{\mathrm{VAOD}(s_1, s_{\mathrm{PBL}})}{\mathrm{INTA}\ \beta(s_1, s_{\mathrm{PBL}})}. \tag{8}$$

Typically, $s_1 \cong 0.5$ km and $s_2 \cong 3 - 5$ km; below s_1 it is assumed that the extinction and backscatter coefficients are constants, $\alpha_{\mathrm{aer}}^{\lambda_o}(s_1)$ and $\beta_{\mathrm{aer}}^{\lambda_o}(s_1)$, respectively.

The evaluation of VAOD can be done directly from the N_2 Raman lidar return:

$$\mathrm{VAOD}(s_1, s_2) = -\frac{\ln\left(\frac{N_{\mathrm{R}}(s)s^2 n_{\mathrm{mol}}(s)}{T_{\mathrm{mol}}^{\lambda} T_{\mathrm{mol}}^{\lambda_o}}\right)}{1 + \left(\lambda_o/\lambda\right)^k} + C. \tag{9}$$

6.2 Lidar Setup

The typical setup of a Raman lidar is shown in Figure I.3.16 (L'Aquila Raman lidar).

The laser, telescope, and a receiver are designed to discriminate among the different Raman backscattered photons (Fig. I.3.17). A possible but not easy task! ... choosing and combining optics and spectrometer-wise components, the efficiencies in collecting photons of the various detectors look like those reported in Fig. I.3.18.

In summary the main characteristics of a Raman lidar are:

- capability of detecting low light levels,
- suppression of cross-talking between the different channels (i.e., suppression of the strong elastically backscattered light in Raman channels), and
- range-independent collecting efficiencies.

7 Raman Lidar Aerosol Observations

The $\alpha_{\mathrm{aer}}^{\lambda_o}(s)$ and $\beta_{\mathrm{aer}}^{\lambda_o}(s)$, reported in Fig. I.3.19, represent the typical products obtained from a single measurement session of the L'Aquila Raman lidar.

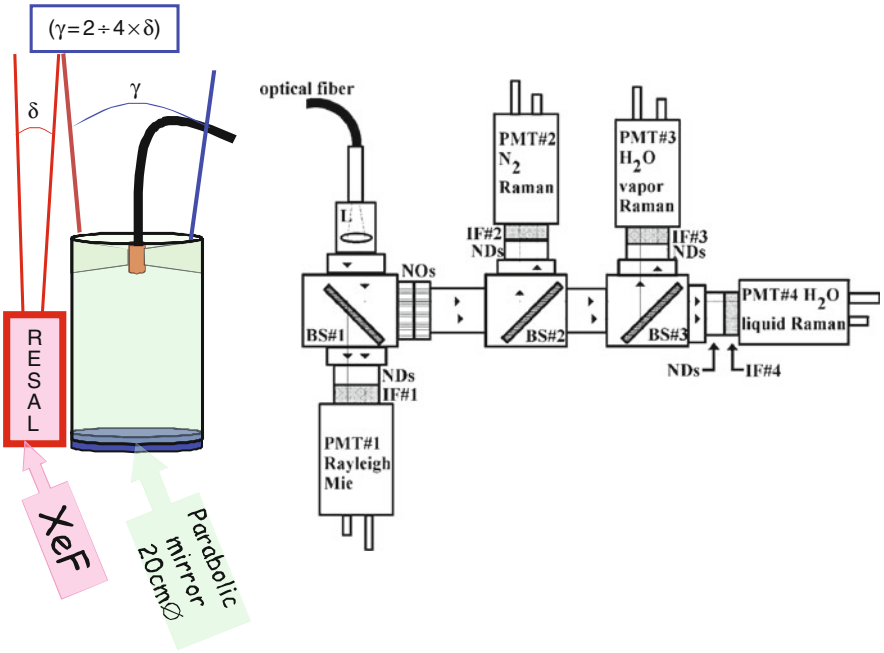

Fig. I.3.16 UV Raman lidar L'Aquila. In the optical layout of the receiver's beam separator, L is a 1-inch plano-convex lens, BS indicates dichroic beam splitters, IF, ND, NO, and PMT labels 2-inch interference filters, the interchangeable neutral density filters, the notch filters, and the photomultipliers, respectively. The spectral features of each channel are indicated by a representative wavelength: 351 nm – Rayleigh/Mie channel, 382 nm – Nitrogen Raman channel, 393 nm – liquid water Raman channel, 403 nm – water vapor Raman channel

As cited, other quantities are usually evaluated: the vertical aerosol optical depth (VAOD) and the integrated aerosol backscatter coefficient (INTAβ) up to 4–5 km range, and, also, the *mean* lidar ratio (LR). In addition, from the analysis of the single aerosol backscatter profile it is possible to estimate the boundary layer height (s_{PBL}).

How to retrieve (practically) this data from the lidar returns will be discussed in the next paragraphs.

7.1 Backscatter and Extinction

The quantities measured by the lidar contain information about the aerosol composition (Q's) and size distribution (n_{aer}).

$$\alpha^{\lambda}_{\mathrm{aer}}(s) = \int_0^{\infty} dr.\pi r^2 \cdot Q_{\mathrm{ext}}(r, m, \lambda) \cdot n_{\mathrm{aer}}(s, r)$$

$$\beta^{\lambda}_{\mathrm{aer}}(s) = \frac{1}{4\pi} \int_0^{\infty} dr \cdot \pi r^2 \cdot Q_{\mathrm{bck}}(r, m, \lambda) \cdot n_{\mathrm{aer}}(s, r)$$

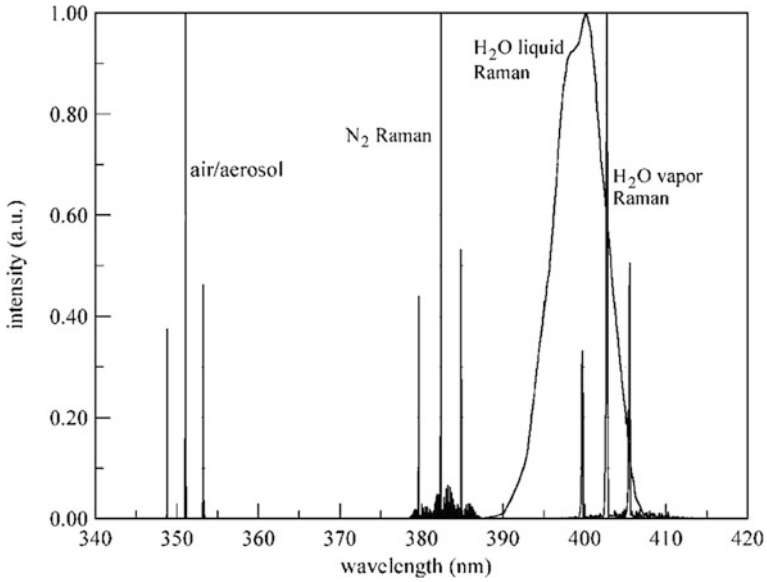

Fig. I.3.17 Schematic drawing of the Rayleigh/Mie and Raman components of the return light spectrum. The Rayleigh/Mie part is a reply of the laser spectrum that has been measured; the different Raman bands have been plotted on wavelength scale, again give a look to the spectrum of the backscattered photons, elastic and inelastic ones. Three spectral lines are for each band, because the emitted photons are distributed over three laser lines (XeF excimer laser)

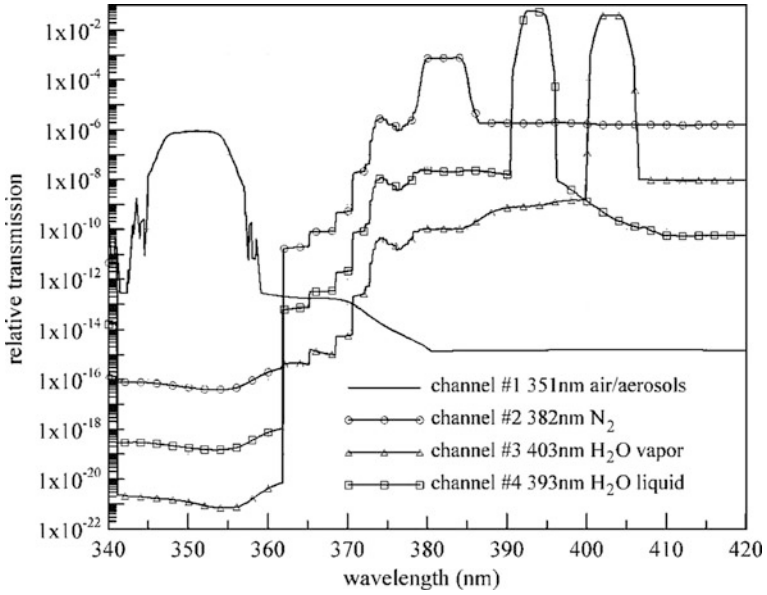

Fig. I.3.18 The wavelength-dependent relative transmissions of the beam separator. These curves have been estimated using the manufacturer's data sheet and the specifications of the various components (filters, mirror, lenses, optical fiber, etc.)

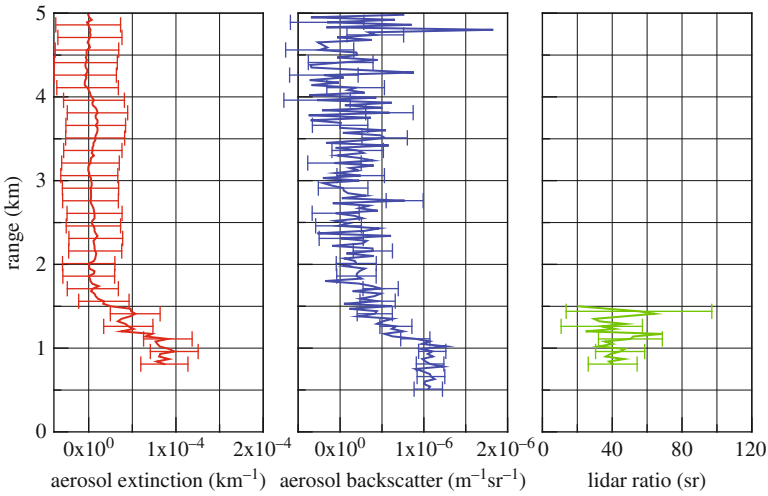

Fig. I.3.19 Typical aerosol extinction, backscatter, and lidar ratio profiles measured by the L'Aquila Raman lidar. The error bars indicate the propagated statistical indetermination

Let us give a look to a couple of (numerical) examples: sulfate aerosols and the cloud droplets (as produced by a cloud model).

7.2 Sulfate Aerosols and Cloud Droplets

Scattering and extinction efficiencies (Q's in Fig. I.3.20) can be estimated using well-known theories (Mie, 1908), but they also have a very complicate dependence on aerosol size and composition. Size distribution is in such a case log-normal (Fig. I.3.21).

In *cloud case*: $\alpha_{\text{aer}}^{\lambda_0}(s) = 0.023\ \text{m}^{-1}$ and $\beta_{\text{aer}}^{\lambda_0}(s) = 0.0015\ \text{m}^{-1}\text{sr}^{-1}$, it is a quite dense cloud; roughly, the visibility is less than 200 m.

A Raman lidar measures the vertical profile of these quantities at quite fast rates. It could be realized how powerful could be the lidar technique, if applied at different wavelengths. It is possible to measure the aerosol backscattering and extinction in a range of wavelengths, and from these information it is possible to estimate (with a certain precision) the aerosol composition and size distribution.

8 Lidar Signal Simulator

As promise some examples down- and upsizing the different lidar components (using a LIdar Signal Simulator program LISISI, available at vincenzo.rizi@aquila.infn.it) for evaluating the better configuration of the lidar system

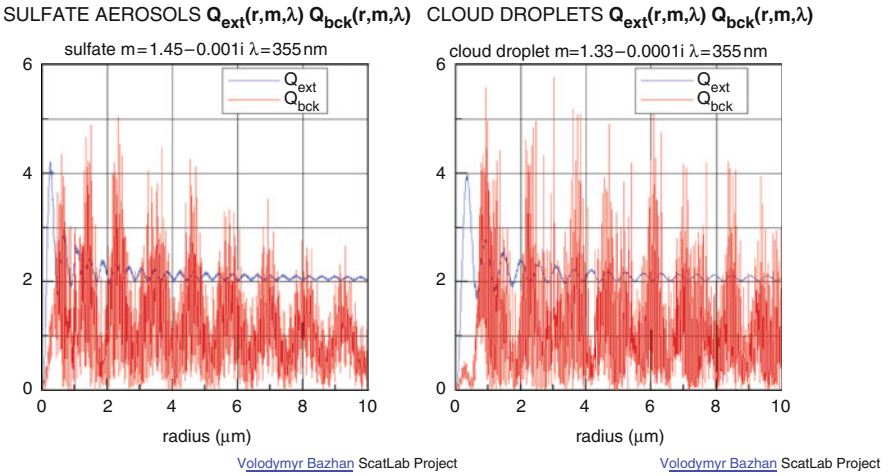

Fig. I.3.20 The scattering and extinction efficiencies vs aerosol dimensions for the case of sulfate aerosol and water cloud droplets (Volodymyr Bazhan, ScatLab Project)

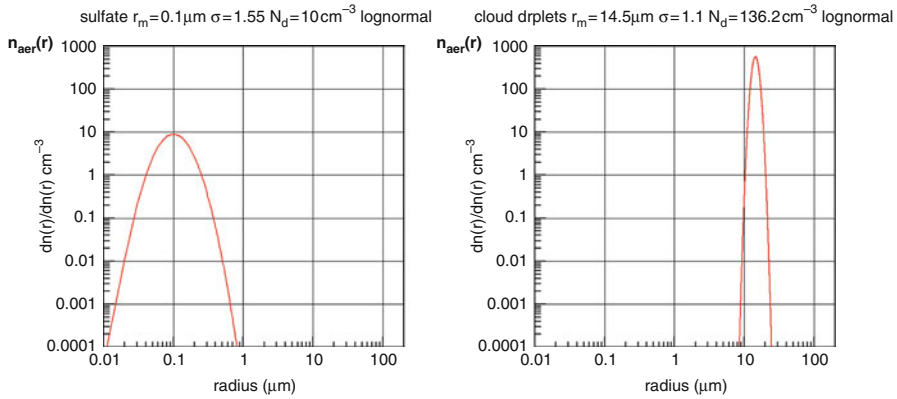

Fig. I.3.21 The typical size distributions of sulfate aerosols and cloud water droplets

in various situation: measuring the aerosol optical properties in the boundary layer or in the case of low-/high-level clouds.

We can also play in figuring out what happens in the case of simple technical variation of the setup (telescope collecting area, laser energy, increasing of the noise, etc.) (Fig. I.3.22).

Example of lidar configuration to be use with LISISI:

ELASTIC LIDAR clean (free of aerosol) atmosphere

	Laser energy (mJ)	Telescope radius (m)	No. laser shots	eff.	Background	Aerosol
Case 1	5 (355 nm)	0.1	18,000	2e-8	1	NO
More background (daytime!)						
Case 2	5(355 nm)	0.1	18,000	2e-8	10	NO
Weaker laser						
Case 3	1(355 nm)	0.1	18,000	2e-8	1	NO
Smaller telescope						
Case 4	5(355 nm)	0.05	18,000	2e-8	1	NO

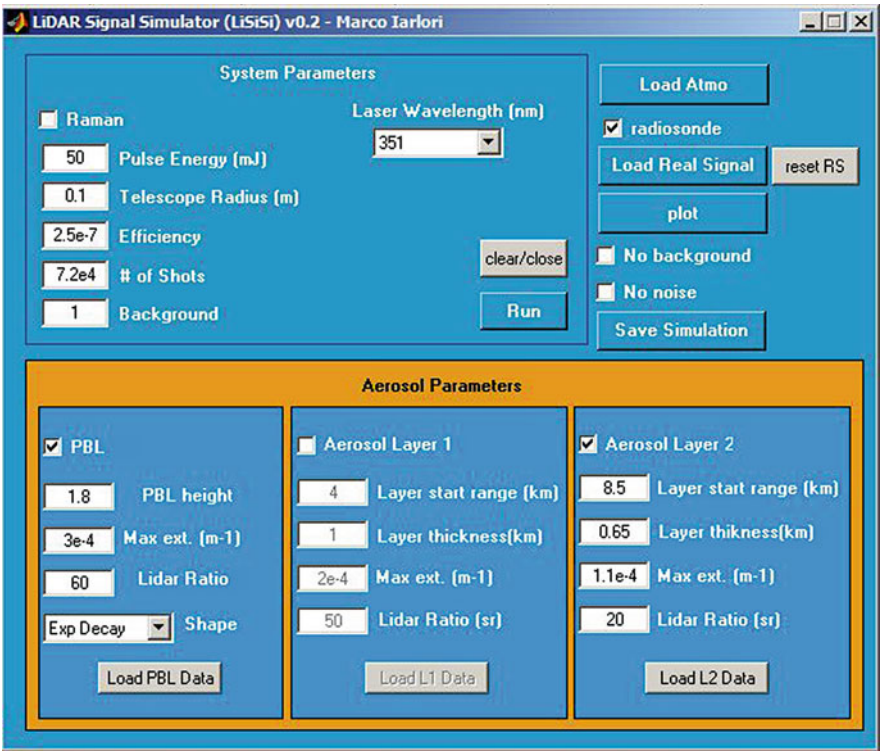

Fig. I.3.22 The user interface of lidar signal simulator. It is possible to set different parameters of the lidar system and of the simulated atmosphere

The evidence is that in cases 2 (higher noise), 3 (lower laser energy) and 4 (smaller telescope), the sampling of the atmosphere is less efficient.

Let us introduce some aerosol (cirrus) a 1-km thick cloud at 10-km range, optical depth of about 0.2, with the parameters of case 1. It happens that the lidar sounding does not show a clear signature of the cloud. What could we do?

Should we buy a more powerful laser, a larger telescope, or better optics? . . . If no money?

Increase the accumulation of laser shots!

ELASTIC/Raman LIDAR atmosphere with aerosols

	Laser energy (mJ)	Telescope radius (m)		No. laser shots	eff.	Background	aerosol
Case 5	5 (355 nm)	0.1	72,000	2e-8	1	cirrus	
Let me set a reference for elastic case (our system!):							
Case 6	50 (355 nm)	0.1	72,000	2e-8	1	cirrus	
And try to change the wavelength . . . from UV to a visible laser							
Case 7	50 (532 nm)	0.1	72,000	2e-8	1	cirrus	
The backscatter sign apparently increases! More information?							
And try to give a look to the Raman return							
Case 8	50	0.1	72,000	2e-4*	1	cirrus	Ram
It evident the effect of the extinction within the cloud							
Finally, we try to see what should be the effect of the aerosol in PBL (constant content in PBL and exp. decay in free troposphere) into the lidar returns.							
Case 9	50	0.1	72,000	2e-8	1	PBL	
Case 10	50	0.1	72,000	2e-4*	1	PBL	Ram

It is evident that the signature of such aerosol load is very weak and, in the next paragraph, I will show how from these signals it is possible to estimate the aerosol optical properties with the appropriate error bars.

Finally, such kind of virtual instrument is very useful for designing the system and planning the observations.

The main task of this part of the lecture is to give an idea of how the aerosol lidar returns can be analyzed to estimate some aerosol optical properties (namely, aerosol backscatter and extinction coefficients). We will play again with some software; hopefully it will be clear how much significant the aerosol lidar products are. This is the expected outcome: have clear the main features concerning the quality and the significance of lidar measurements.

9 Lidar Signal Analysis

Let me refer to a real system (L'Aquila Raman lidar discussed in paragraph 6.2). As first step we can play with the lidar signal simulator for the best fitting to the real signal changing the aerosol content in the simulated atmosphere. It is nice, but we cannot get quantitative information (Fig. I.3.23).

To be more quantitative, from the elastic and N_2 Raman signals it is possible to evaluate the aerosol backscattering coefficient and vertical aerosol optical depth (the cumulative integral of the extinction coefficient). To do this you should have information about the molecular part of the atmosphere (pressure and temperature profiles), and you can use Eqs. (5) and (8), together with some, very common,

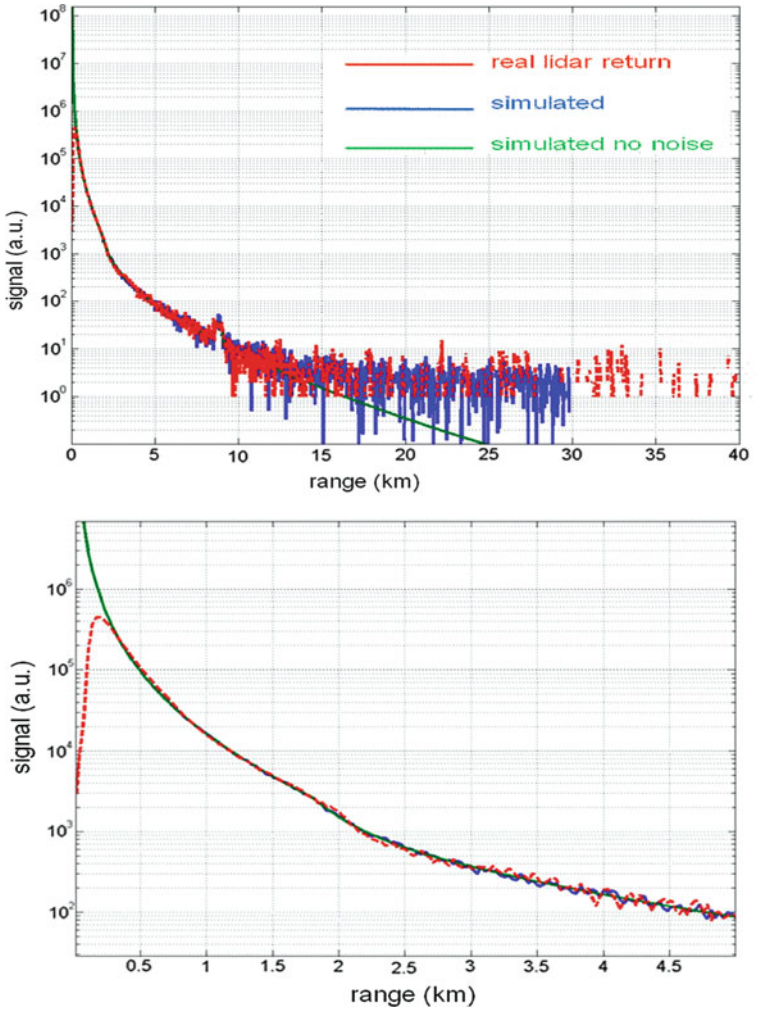

Fig. I.3.23 Real lidar signals (elastic – *upper panel*, Raman – *lower panel*) and simulated returns

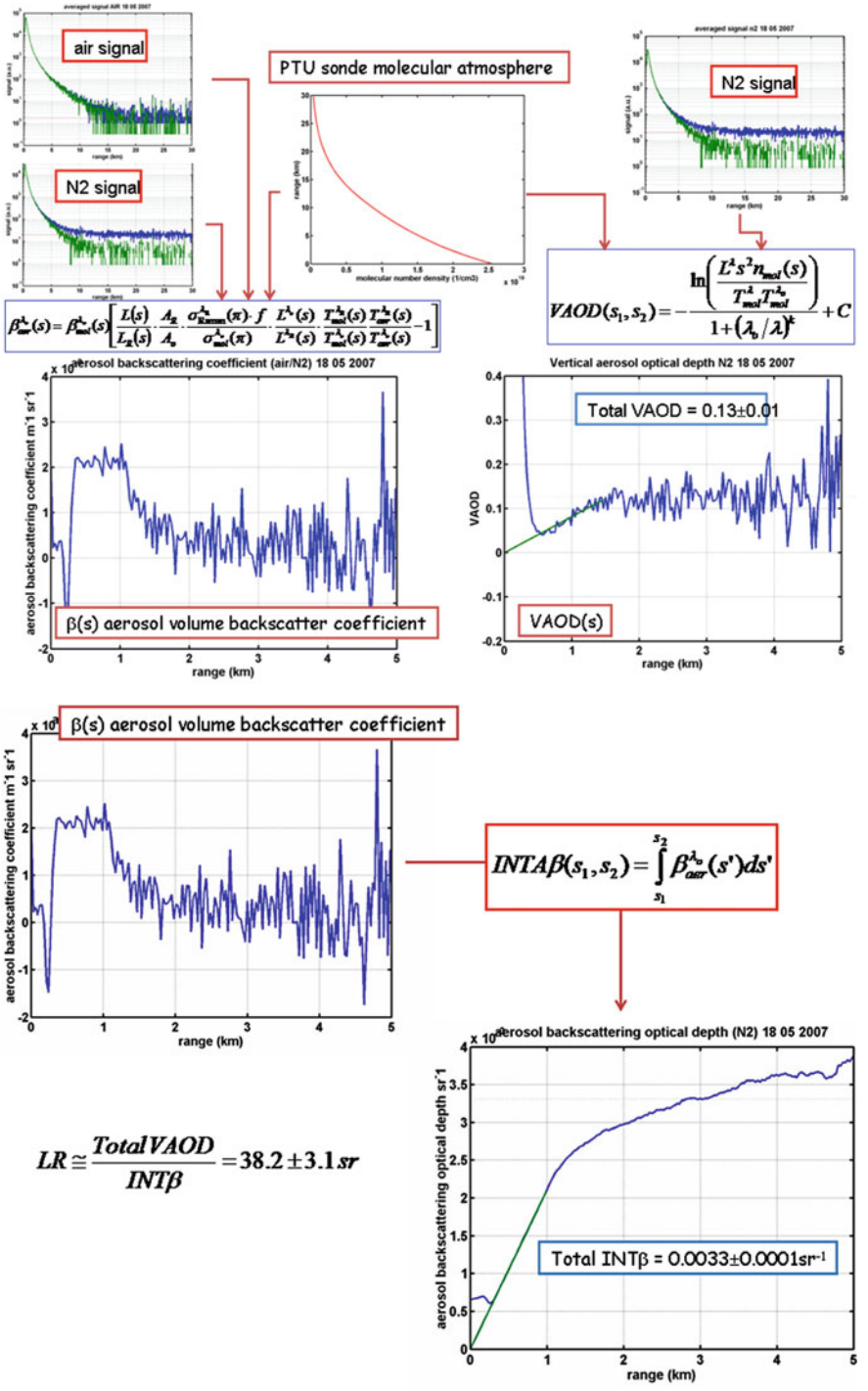

Fig. I.3.24 Procedure for the evaluation of VAOD and aerosol backscatter coefficient profiles, the integrated aerosol backscatter, and the mean lidar ratio

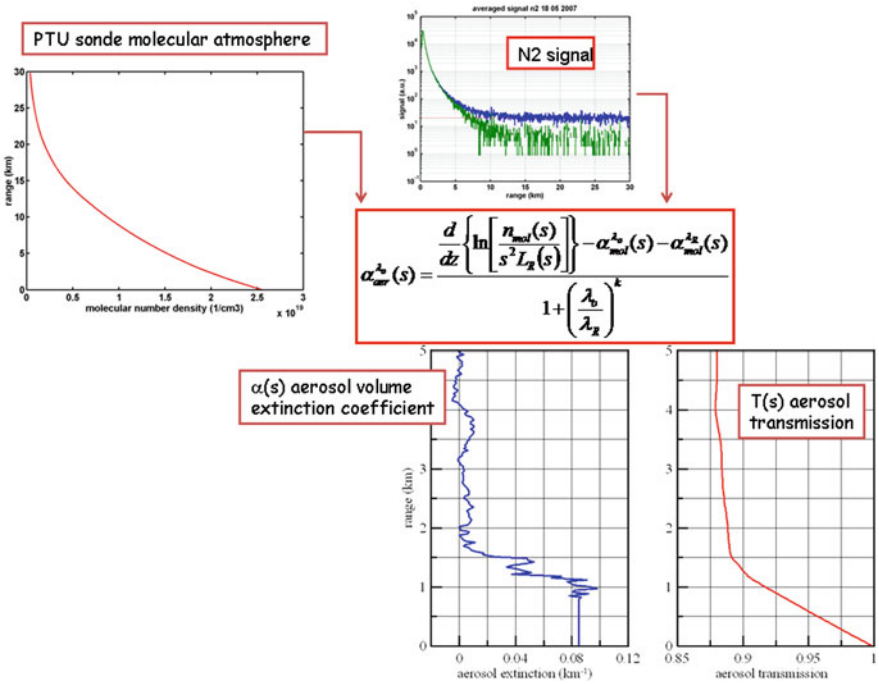

Fig. I.3.25 Procedure for the evaluation of aerosol extinction coefficient profile

numerical filters. After this procedure you can estimate (in this case) the total vertical aerosol optical depth with an indetermination less than 10% (the overall algorithm is reported in Fig. I.3.24).

For another interesting quantity (the vertical profile of the aerosol extinction coefficient) there is a different story, you should apply more sophisticated numerical filters, and their features have a direct effect on the indetermination to be assigned at the observations (Fig. I.3.25).

This Raman aerosol lidar produces such kind of results along 40-min measurement session. Note the typical structure of the aerosol vertical distribution: constant along the PBL (0–1 km range) and decaying faster in the free troposphere (above 1 km range).

10 Aerosol Observation

In this section, I report an example of extensive aerosol observations, and this concludes the lectures.

These aerosol measurements have been taken by a lidar used for the purposes of an ultra high energy cosmic ray experiment (Pierre Auger Observatory, http://www.auger.org/, which is located in Argentina). This experiment studies the

cosmic rays at very high energies and uses the atmosphere as a calorimeter. To evaluate the cosmic ray energy, among the other properties, the optical transmission of the atmosphere should be known. The portion of this transmission due to the presence of the aerosol is the most variable components (this is the point of view of a cosmic ray physicist!). The Raman lidar is the right instrument for monitoring such properties! Using resources from different agencies ... a simple Raman lidar has been funded ... and for about 1 year has taken measurements.

The measurements have been carried on by the AUGER Raman Lidar from August 2006 to July 2007 at Los Leones (35.32 S, 69.30 W, 1,416 m a.s.l., Malargue, Mendoza, Argentina), and they constitute a year-round database of aerosol backscatter and extinction profiles in the UV range. The aerosol observations are presented and discussed, mainly, for assessing their scientific usefulness.

The AUGER Raman lidar is remotely operated. A Nd-YAG laser is the source of the laser pulses (third harmonics of fundamental wavelength: $\lambda_o = 355$ nm) and the backscattered light is collected by an *f*/3 parabolic Ø50 cm mirror that is coupled with an optical fiber to the receiver. The receiver box is set up with dichroic beam splitters, interference filters, and photomultipliers for discriminating (detecting) between the Rayleigh/Mie and Raman backscattered photons. The receiver optics and the data acquisition system have been extensively tested and characterized; a discussion of the technical details and the performances/limitations of the system can be found in Rizi et al. (2006). In summary, the AUGER Raman lidar has the needed spectral performances for an efficient separation between the detection of elastic (Rayleigh/Mie scattering by air molecules and aerosols) and of the weak wavelength-shifted Raman lidar returns (N_2 Raman scattering). The system can measure, with good precision, aerosol extinction and backscatter coefficients accumulating lidar returns for about 40 min (≈48,000 laser shots at 20 Hz laser pulse repetition rate). The aerosol data profiles can be usefully measured along a height range (i.e., altitude above the lidar) spanning from ≈500 m (below the lidar returns are modulated by the range-dependent geometrical overlap function, $G(s)$, that depends on the laser divergence, the receiver field of view, and the distance between telescope and laser axes; and it is a measure of the collecting efficiency of the receiver telescope) up to 5–7 km; the raw altitude resolution is 30 m.

The main results of 1-year measurements are summarized in Figs. I.3.26–I.3.28.

The PBL thickness (s_{PBL}) shows low values in fall/winter and enlarges in spring/summer. The extension of the entrainment region (h) is reduced during late spring/summer, this means that the free troposphere is more stable than in autumn/winter, and the vertical mixing is damped (Note that the lidar is operating in the austral hemisphere, i.e., winter is between the month 6–9).

The annual cycle of the aerosol optical properties is quite evident.

The Raman (monthly mean) VAODs and INTAβ show:

- low values during late fall and early winter,
- high values in summer, and
- relative high content of aerosol in late winter and early spring (is it a diffuse regional meteorological pattern? Do the occurrences of dust storms increase?)

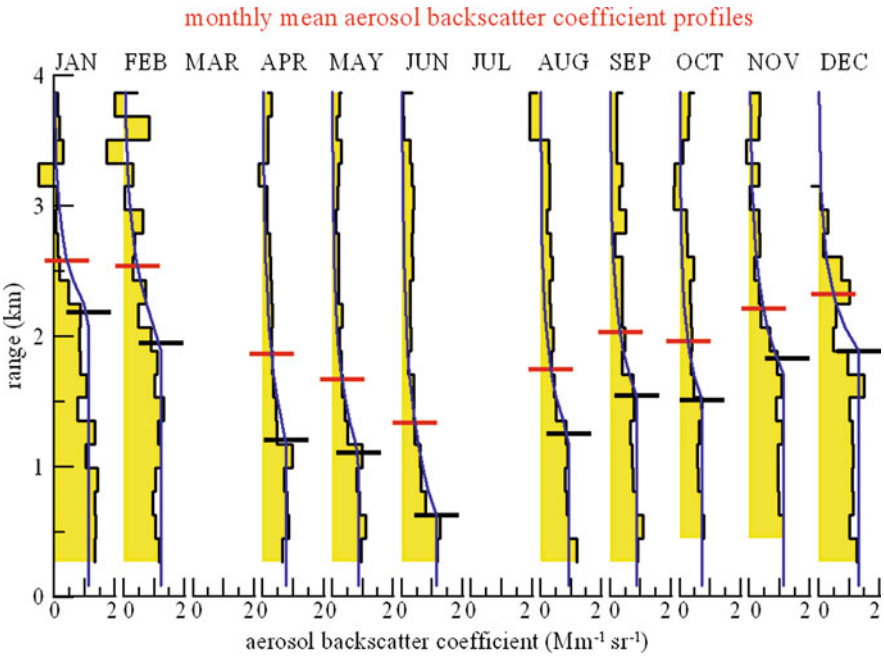

Fig. I.3.26 Monthly mean aerosol backscatter coefficient profiles; the horizontal ticks indicate the positions of the planetary boundary layer (PBL) upper levels and of the extensions of the entrainment zone above PBL over the lidar site

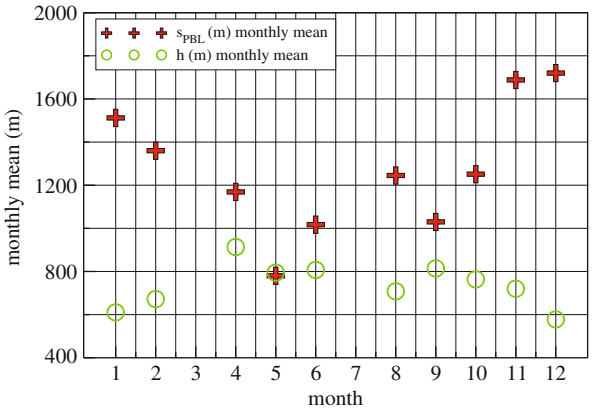

Fig. I.3.27 Monthly mean values of the PBL thickness (s_{PBL}) and the extension of the entrainment region (h)

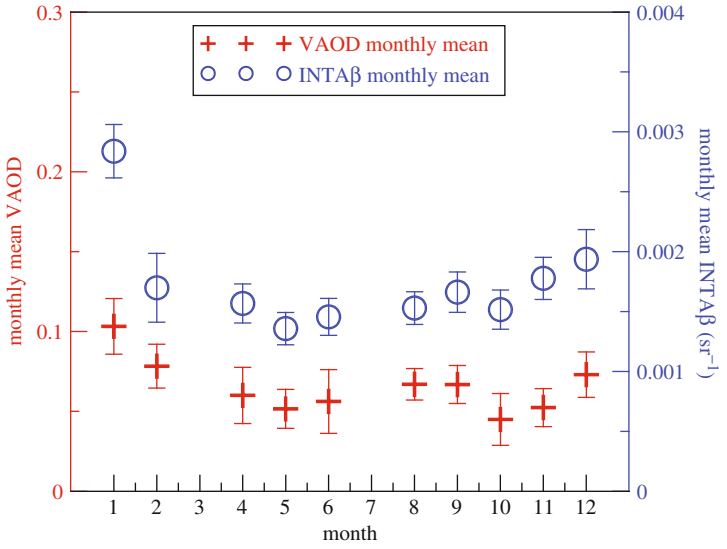

Fig. I.3.28 Monthly mean values of VAOD, INTAβ. The error bars indicate the corresponding standard deviations

References

Ansmann A et al. (1992) Combined Raman elastic-backscatter lidar for vertical profiling of moisture, aerosol extinction, backscatter, and lidar ratio. Appl Phys B 55:18–28.

Bockmann C et al. (2004) Aerosol lidar intercomparison in the framework of the EARLINET project. 2. Aerosol backscatter algorithms. Appl Opt 43:977–989.

Eltermann L (1951) The measurement of stratospheric density distribution with the searchlight technique. J Geophys Res 56:509–520.

Ferrare RA et al. (1998) Raman lidar measurements of aerosol extinction and backscattering, 1, methods and comparisons. J Geophys Res 103:19663–19672.

Fiocco G, Smullin LD (1963) Detection of scattering layers in upper atmosphere. Nature 199:1275–1276.

Hulburt EO (1937) Observations of a searchlight beam to an altitude of 28 kilometers. J Opt Soc Am 27:377–382.

Johnson EA et al (1939) The measurement of light scattered by the upper atmosphere from a search-light beam. J Opt Soc Am 29:512–517.

Ligda MGH (1963) Meteorological observations with a pulsed laser radar. In: Proceedings of the first conference on laser techniques, San Diego, CA, pp 63–72.

Maiman TH (1960) Optical and microwave-optical experiments in ruby. Phys Rev Lett 4:564–566.

Matthias V, Bosenberg J (2002) Aerosol climatology for the planetary boundary layer derived from regular lidar measurements. Atm Res 63:221–245.

McClung FJ, Hellwarth RW (1962) Giant optical pulsations from ruby. J Appl Phys 33:828–829.

Mie G (1908) Beiträge zur Optik trüber Medien speziell kolloidaler Goldlösungen. Ann Phys 25:377–445.

Pappalardo G et al. (2004) Aerosol lidar intercomparison in the framework of the EARLINET project. 3. Raman lidar algorithm for aerosol extinction, backscatter, and lidar ratio. Appl Opt 43:5370–5385.

Rizi V et al. (2006) The Raman lidar receiver at Pierre Auger Observatory: installation and hardware tests, GAP note 2006-015. Available at vincenzo.rizi@aquila.infn.it.
Schawlow AL, Townes CH (1958) Infrared and optical masers. Phys Rev 112:1940–1949.
Tuve MA et al. (1935) A new experimental method for study of the upper atmosphere. Phys Rev 48(11):917–918.

Chapter I.4
Introduction to SODAR and RASS-Wind Profiler Radar Systems

Laura Bianco

1 Introduction

We will start this overview by introducing Doppler radar wind profilers and then expand the discussion to RASS and SODAR systems later in the chapter.

Doppler radars have been used largely in the field of atmospheric research; however, during the first half of the last century, their use was focused mainly on the survey of the echoes obtained from visible structures. To find applications of radars in the study of the clear-air atmosphere, we have to go back to the late 1960s, when attention was focused on the determination of the causes of radar returns from apparently clear-air atmosphere (often referred to as "angels"). The first idea was that those echoes were of biological origin (insects or birds), but subsequent research (Hardy et al., 1966; Kropfli et al., 1968; Lane, 1969) established that, though point sources also provide natural targets, scattering from turbulent irregularities (refractive index inhomogeneities) is the primary cause of clear-air echoes observed at microwave frequencies. Radars designed specifically to sound the clear air were then built (Richter, 1969) and demonstrated unequivocally that clear-air radars could routinely observe profiles of refractive index inhomogeneities. Refractive index fluctuations are carried out by the wind, so they are used as tracers. During subsequent years many results were added to the first applications, making the ability of those radars well established and their use very diffuse. Radars transmit radio frequency energy, which is intercepted and reradiated by land, sea, and atmospheric targets (Fig. I.4.1). Changes in the received signal from that transmitted give clues to important target parameters, such as scattering cross sections as well as their position, as a function of time, in three-dimensional space. Thus, their velocity can be determined.

Doppler radars can operate over a wide range of frequencies, in the VHF (30–300 MHz) and UHF (300–30,000 MHz). According to the Bragg condition the scale of the backscattering target toward the point of origin occurs primary from

L. Bianco (✉)
Cooperative Institute for Research in Environmental Sciences (CIRES),
University of Colorado, Boulder, CO, USA; NOAA/Earth System Research Laboratory
(ESRL)/Physical Sciences Division (PSD), Boulder, CO, USA
e-mail: laura.bianco@noaa.gov

D. Cimini et al. (eds.), *Integrated Ground-Based Observing Systems*,
DOI 10.1007/978-3-642-12968-1_4,

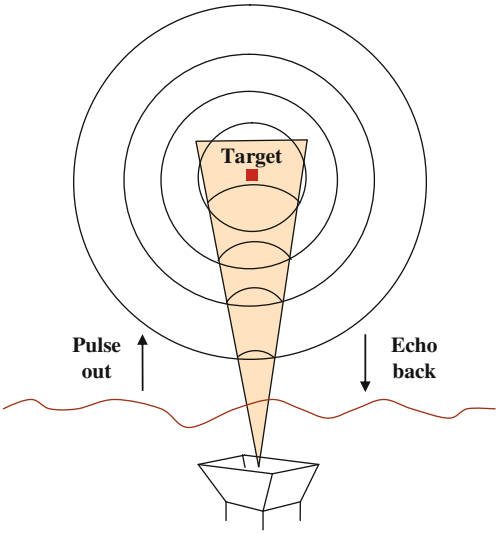

Fig. I.4.1 Scattering from target (adapted from the wind profiler manual)

irregularities of size and on the order of one-half the wavelength of the incident wave. Being capable of retaining information on the phase of the signal returns, Doppler radars are used to measure the frequency spectrum of the incoming signal. Using the principles of the Doppler effect, they are capable of measuring the mean radial component of motion of the scattering elements. The mean Doppler shift (first moment) is a measure of the mean radial component of motion of the scattering element. Furthermore, the magnitude of the echo spectrum (zeroth moment) and the width of the Doppler spectrum (second moment) contain additional information on wind shear, turbulence parameters (White, 1997), and boundary layer structure (Bianco et al., 2008).

The class of radars using fixed-beam-pointing directions is then able to determine the characteristics of the wind vector (speed and direction), and, for this reason, they became to be known as *wind profilers*. Among them UHF radar wind profilers are specifically designed for boundary layer and lower-tropospheric studies (Ecklund et al., 1988).

2 Basic Theory of Doppler Radars

The echoing mechanisms that give rise to backscattering from the clear-air atmosphere have been rather extensively investigated. The main cause of radar returns from the clear air now has been well established to be the inhomogeneities in refractive index that result from turbulence. The radio refractive index n, at commonly used radar wavelengths, is non-dispersive and depends on the atmospheric temperature, humidity, and pressure.

It can be expressed in terms of the *refractivity* $N = (n-1) \times 10^6$ as

$$N = (n-1) \times 10^6 = 77.6\frac{p}{T} + 3.73 \times 10^5 \frac{e}{T^2}, \tag{1}$$

where p is the atmospheric pressure (mb), e is the vapor pressure (mb), and T is the absolute temperature (K).

2.1 Radar Principles

Let a pulsed electromagnetic wave be transmitted at time T_1, the pulse duration of this radar being τ. For simplification the pulse shape is supposed to be rectangular, but in real applications it may be a smoothed trapezoid or triangle or Gaussian shaped. In a non-dispersive propagation medium the pulse travels with the speed of the light c and reaches the range r_a after time $t_1 = r_a/c$. A target at r_a can scatter or reflect the radar signal in some directions. A small fraction returns to the location of the transmitter, where the radar echo will be received after time $t_2 = 2t_1 = 2r_a/c$. This yields the basic relation $r = c \cdot t/2$, which allows the determination of the range r of any radar target by measuring the round-trip time t. This relation holds for monostatic radars (transmitter and receiver are at the same location). For bistatic radars (receiver separated from transmitter by a distance comparable to or larger than the ranges to the target), a modified expression has to be applied.

Since the transmitted pulse has a finite duration τ, its trailing edge will reach the range r_a at a time $t_1 + \tau$ and reach the receiver at $t_2 + \tau$. The pulse of duration τ, thus, at one time illuminates a volume at r_a extended along a range $\Delta r = c \cdot \tau/2$. This is the *range gate* from which the radar echoes are received. Therefore, the transmitter pulse length τ determines the *range resolution* Δr. In contrast, the horizontal size of the scattering volume is obviously defined by the antenna beam width.

In radar applications short pulses are normally transmitted periodically, so that the nth pulse follows the $(n-1)$th pulse after a specific time. This time $(T_n - T_{n-1})$ is called the *interpulse period*, T_{IPP}. Its inverse is called the *pulse repetition frequency*, $f_{\mathrm{PRF}} = 1/T_{\mathrm{IPP}}$. The off–on ratio of the transmitter $T_{\mathrm{IPP}}/\tau - 1$ determines approximately the range from which radar echoes can be unambiguously received (in unit of range resolution). It is more customary, however, to use the ratio $d = \tau/T_{\mathrm{IPP}}$, which is called *duty cycle*.

Because in normal radar operations the pulse repetition frequency is kept constant (the transmitted pulse train is periodic), range aliasing may occur. At time t_a an echo is received from the range r_a, and an echo is received from range r_b. Of course higher-order range aliasing can occur from ranges $r_n = c \cdot (t + (n-1)\,T_{\mathrm{IPP}})/2$. Because these echoes return from separate scatter volumes, the echo signals are uncorrelated, but still their power accumulates in the same receiver range gate. If special arrangements are not being made (i.e., pulse-coding), the maximum unambiguous range is $r_{\max} = c \cdot T_{\mathrm{IPP}}/2$. The minimum range $r_{\min}$ is obviously given by

the pulse duration τ, $r_{\min} = c \cdot \tau / 2$, plus some instrumentally determined transition time between transmission and reception.

A point target within the scattering volume defined by the antenna beam width and pulse duration τ returns a signal whose instantaneous voltage is

$$E(t) = A(t) \cos[\omega_c t + \varphi(t)], \tag{2}$$

where A is the amplitude, $\omega_c = 2\pi f_c$ is the constant carrier frequency, and φ is the phase relative to the carrier phase. If the target is fixed, the phase is constant and a function of the distance r from the radar. A moving target having a radial velocity V_R returns a signal whose phase varies with time and is given by

$$\varphi(t) = \frac{4\pi}{\lambda}(r_0 + V_R t), \tag{3}$$

where λ is the incident radiation wavelength and r_0 is the initial distance.

When the scattering volume contains N point targets, the return signal is the superimposition of individual returns. The instantaneous return voltage is then

$$E(t) = \sum_{n=1}^{N} A_n(t) \cos[\omega_c t + \varphi_n(t)], \tag{4}$$

where A_n is the amplitude and φ_n is the phase of the return signal from the nth scatterer. The above expression assumes that secondary scattering effects are negligible compared to the first-order scattering. With the possible exception of heavy rain, snow, or hail, the above expression is valid for atmospheric scattering.

The time rate of phase exchange, time derivative of Eq. (3), is an angular frequency $\omega_D = 4\pi V_R / \lambda$. It is therefore equivalent to a Doppler frequency shift

$$f_D = \frac{2V_R}{\lambda}. \tag{5}$$

Approaching targets have increasing phase with time, which corresponds to a positive Doppler frequency shift.

In a pulsed Doppler radar system, the time functions for point [Eq. (2)], or for distributed targets [Eq. (4)], are available only at discrete time intervals corresponding to the radar pulse repetition period. Therefore, if the radial velocity of the scatterers is such that the phase changes by more than π (Doppler frequency shift greater than one-half the pulse repetition rate), an ambiguity in velocity exists. This is equivalent to aliasing at the folding or Nyquist frequency given by

$$f_N = \frac{1}{2T_{IPP}}, \tag{6}$$

where T_{IPP} is the pulse repetition period or interpulse period. If positive and negative frequencies can be resolved, the unambiguous frequency range is doubled.

The unambiguous Doppler frequency range is then

$$-\frac{1}{2T_{\mathrm{IPP}}} \leq f_{\mathrm{D}} \leq \frac{1}{2T_{\mathrm{IPP}}}. \tag{7}$$

From the previous equation, the maximum unambiguous velocity is then

$$V_{\max} = \pm\frac{\lambda}{4T_{\mathrm{IPP}}}. \tag{8}$$

2.2 The Radar Equation

A target having a cross-sectional area A_{c} located at a distance r from the radar will intercept an amount of power,

$$P_{\mathrm{i}} = \frac{P_{\mathrm{t}} G A_{\mathrm{c}}}{4\pi r^2}, \tag{9}$$

where P_{t} is the transmitted power and G is the transmitting antenna gain factor (Barrick, 1972). If the target reradiates isotropically, the power intercepted by the receiving antenna is (Battan, 1959)

$$P_{\mathrm{r}} = \frac{P_{\mathrm{t}} G A_{\mathrm{c}}}{4\pi r^2}\frac{A_{\mathrm{e}}}{4\pi r^2} \tag{10}$$

for a receiving antenna having an effective area A_{e}. The relationship between effective area and its gain is (Kraus 1950)

$$A_{\mathrm{e}} = \frac{G\lambda^2}{4\pi}. \tag{11}$$

Since most targets do not scatter isotropically, it is convenient to introduce the backscattering cross section σ, defined as (Battan 1959) "the area intercepting the amount of power, which, if scattered isotropically, would return an amount of power equal to that actually received"; that is

$$\sigma = \frac{(\text{Power reflected toward the receiving aperture per unit solid angle})}{(\text{Incident power density per } 4\pi \text{ steradians})}.$$

Substituting the backscattered cross section for the geometric cross section and replacing the effective area with Eq. (11), the return power [Eq. (10)] becomes

$$P_{\mathrm{r}} = K_{\mathrm{r}}\frac{\sigma}{r^4}, \tag{12}$$

where the constant $K_r = P_t G^2 \lambda^2 / 64\pi^3$ depends only on the particular radar system used and not on the scatterers.

For N targets, where σ_n is the cross section for the nth scatterer, on average, the return power is

$$\overline{P_r} = \frac{K_r}{r^4} \sum_{n=1}^{N} \sigma_n, \tag{13}$$

where r is the range to the center of the scattering volume. A slightly more useful meteorological form is obtained by using the average radar cross section per unit volume and multiplying by the volume, V, effectively illuminated. This leads to

$$\overline{P_r} = \frac{K_r V \eta}{r^4}. \tag{14}$$

The quantity

$$\eta = \frac{1}{V} \sum_{n=1}^{N} \sigma_n \tag{15}$$

is the so-called *radar reflectivity*.

Approximating the antenna pattern by a Gaussian beam (Lhermitte, 1963; Nathanson and Reilly, 1968), the gain is

$$G(\vartheta, \alpha) = G_0 \exp\left[-\left(\frac{\vartheta^2}{2\sigma_\vartheta^2} + \frac{\alpha^2}{2\sigma_\alpha^2} \right) \right], \tag{16}$$

where $\sigma_\vartheta, \sigma_\alpha$ are the standard deviations of the two-way pattern (assumed to be at most a few degrees), ϑ and α are, respectively, the off-axis horizontal and vertical beam angles (assumed to be at most a few degrees), and G_0 is the on-axis gain factor. Accounting for gain variations across the beam, the exact form of the radar equation [Eq. (13)] becomes

$$\overline{P_r} = \frac{P_t \lambda^2}{64\pi^3} \sum_{\text{vol}} \frac{G^2(\vartheta, \alpha)\, \sigma_n}{r_n^4}. \tag{17}$$

Introducing the radar reflectivity $\eta = \eta(r, \vartheta, \alpha)$, the summation can be expressed as a volume integral over the pulse of the contribution region so that

$$\overline{P_r} = \frac{P_t \lambda^2}{64\pi^3} \int_{\text{vol}} \frac{G^2(\vartheta, \alpha)\, \eta(r, \vartheta, \alpha)}{r^4} dV. \tag{18}$$

Using the Gaussian beam approximation over a volume having uniform reflectivity, integration leads to (Probert-Jones, 1960)

$$\overline{P_{\mathrm{r}}} = \frac{c}{1024\pi^2 \ln 2} \left(P_{\mathrm{t}} \tau \lambda^2 G_0^2 \vartheta \alpha\right) \left(\frac{\eta}{r^2}\right), \tag{19}$$

where τ is the pulse width and c is the propagation speed ($\cong 3 \times 10^8$ ms^{-1}).

The previous equation has been grouped according to the constant $\left(c/\left(1024\pi^2 \ln 2\right)\right)$, the measurable radar parameters $\left(P_{\mathrm{t}} \tau \lambda^2 G_0^2 \vartheta \alpha\right)$, and target parameters $\left(\eta/r^2\right)$.

2.3 Method of Wind Measurement

Here we describe the standard technique.

Wind-profiling radars have five possible beam directions (Fig. I.4.2), any one of which having a beam width equal to 3–10° and tilted 14–24° with respect to the vertically pointing beam. Four beams are orthogonal. The beam-pointing sequence is repeated every 1–5 min while local horizontal uniformity of the wind field is assumed.

Wind-profiling radars use fixed-pointing antennas with three or five pointing directions. At least three antenna beam-pointing directions are needed to measure the vector wind. Let us consider a Doppler radar using three antenna beam-pointing directions (Fig. I.4.3).

For simplicity two pointing directions are chosen to observe orthogonal horizontal wind components u and v, and one is chosen to observe the vertical component w. Thus, one antenna beam is pointed vertically and the other two are oblique. Horizontal winds are measured with an antenna elevation-pointing angle

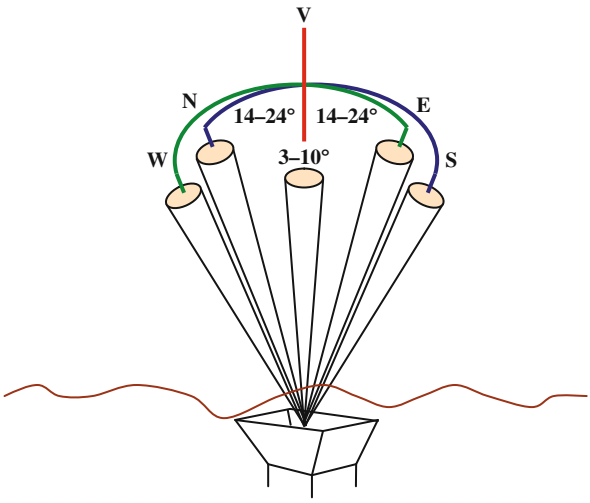

Fig. I.4.2 Possible wind directions for a wind-profiling radar (adapted from the wind profiler manual)

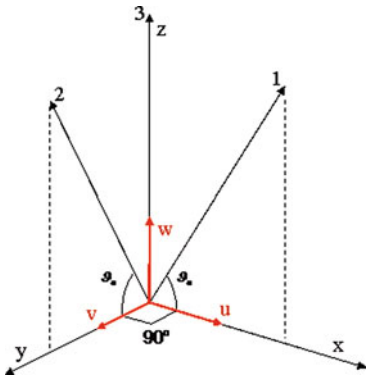

Fig. I.4.3 Wind measurement method

ϑ_e that allows observation at all altitudes of interest. If we consider for simplicity that the azimuth angles for the oblique beams are equal to 0° and 90°, respectively, we obtain that the radar Doppler velocity V_i measured along axes 1, 2, and 3 by the radar is related to the wind as follows:

$$\begin{cases} V_1 = u\cos\vartheta_e + w\sin\vartheta_e \\ V_2 = v\cos\vartheta_e + w\sin\vartheta_e \\ V_3 = w \end{cases} . \tag{20}$$

At each altitude h the three measurements are made at volumes separated in space. Again, horizontal uniformity is assumed when the measurements are combined.

2.4 Data Processing and Averaging

Wind-profiling radars use the data processing scheme illustrated in Fig. I.4.4 (Strauch et al., 1984).

Steps (1) and (2). The input signal is the backscattered signal for each radar resolution volume. Signal-plus-noise values are collected by the receiver and sampled.

Step (3). The next step in signal processing is coherent integration, also referred to as time-domain average. The signal-to-noise ratio (SNR) can be improved for radar wind profiling by summing a number J of consecutively received pulses. Since the noise bandwidth is determined by the radar pulse width, noise samples taken at the pulse repetition period will be uncorrelated. Therefore, the noise power increases linearly with the number of samples added. The signal, however, remains well correlated for approximately $0.2\lambda/\sigma$ s (Nathanson, 1969), where λ is the radar wavelength. Typically $\sigma \cong 1$ ms^{-1}, so the correlation time is milliseconds with microwave radars. If, in addition to being correlated, the phase of the signal samples changes very little between samples, then signal samples can be added so that

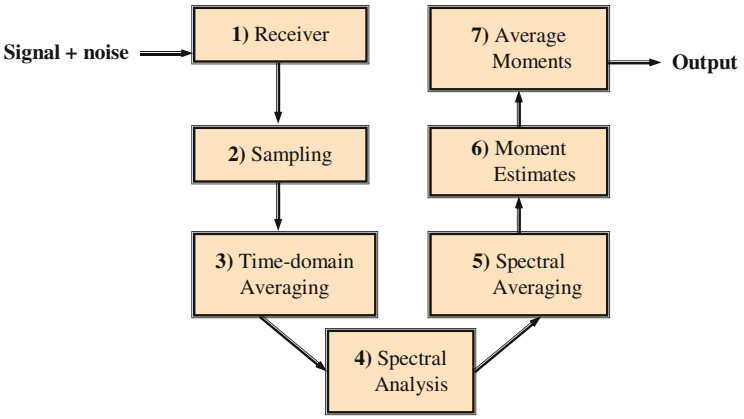

Fig. I.4.4 "Data processing" steps for a Doppler wind-profiling radar

signal power increases with the square of the number of samples added. This occurs for radars whose unambiguous velocity, Eq. (8), is much greater than the radial velocity of the scatterers. The SNR improves by the number J of samples averaged, and the unambiguous velocity [Eq. (8)] decreases to

$$V_{\max} = \pm \frac{\lambda}{4JT_{\mathrm{IPP}}}. \tag{21}$$

Step (4). Next is the computation of the power spectrum over a set of N_{FFT} coherent integrations. The program applies a standard fast Fourier transform (FFT) to the complex sample points from the decoded input array for each range gate. The number of FFT points can be any power of 2 from 8 to 4,096. The direct current (DC) component is zeroed out and the transform is then interpolated across DC. In a more recent version of the radar control program, the long-term mean value at DC is subtracted from the transform. Next, a frequency-domain Hanning window is applied to reduce the effects of spectral leakage caused by using time series of finite length. The program forms the power spectrum by computing the magnitude squared of the FFT array. The process is repeated until the specific number L of spectra is accumulated for each range gate.

Step (5). Next is the averaging of L spectra, each obtained from $J \times N_{\mathrm{FFT}}$ radar pulses. We expect averaging to improve the spectral domain SNR; however, this improvement will occur only if the mean wind is the same for each *dwell time*. The dwell time is the time required to collect and process $J \times N_{\mathrm{FFT}} \times L$ pulses. Thus, it is defined in terms of the number of spectra averaged L, the number of FFT points, N_{FFT}, the interpulse period T_{IPP}, and the number of pulses averaged J as

$$t_{\mathrm{D}} = L \times (N_{\mathrm{FFT}} \times T_{\mathrm{IPP}} \times J + t_0)\,, \tag{22}$$

where t_0 represent a constant for processing time ($\cong 0.5$ s).

In the standard method, before calculating the moments of the spectral signal, the program attempts to identify the spectral components caused by ground clutter which is a form of radar contamination (Riddle and Angevine, 1992). Ground clutter occurs when fixed objects on and near the earth's surface obstruct the radar beam and produce non-meteorological echoes with large intensities centered over zero shifts Doppler.

If there is a symmetrical signal peak centered on the DC point, it is assumed to be ground clutter and that region is excluded from the search for an atmospheric signal. This ground clutter algorithm starts at the operator-specified height and works downward. In order to avoid confusion with low velocity and signals, the ground clutter algorithm is not applied at a range gate if the signal at the height above is near zero velocity. At this stage of the process other methods can be applied to remove further non-atmospheric contamination to the spectral signal.

Step (6). The next step is the estimation of the spectral moments from the average Doppler velocity spectrum corrected by ground clutter influences and additional contamination. Before the moments can be found, the signal spectrum must be isolated from the measured signal-plus-noise spectrum. To achieve this aim, first the mean noise level is found. The algorithm for this calculation is based on the statistical property of Gaussian white noise that the variance of the spectral points should be equal to their squared mean value divided by the number of spectral averages. The program finds the largest number of the lowest-valued spectral points that exhibit the above statistics (Hildebrand and Sekhon, 1974). The noise level of the spectrum is the average of these points.

The signal is then identified within the spectrum by finding the spectral point outside the clutter region that has the maximum power. The signal region is identified to include all contiguous points around this peak that are both above the noise level and outside the clutter bounds. Next, the noise level is subtracted from all points within the signal bounds. The zeroth (power), first (mean Doppler velocity), and second moments are then calculated for the resulting power distribution as schematically illustrated in Fig. I.4.5. The spectral width is twice the square root of the second moment.

This method appears to work well for a wide variety of conditions.

Step (7). The program saves the mean Doppler values for later use in computing an average wind vector at each range gate. The winds are derived from a consensus average of the radial velocities over the chosen averaging interval (typically 30–60 min). The consensus-averaging algorithm examines the velocity values at each range gate and finds the largest subset of values that are within a specified velocity interval of each other (Strauch et al. 1984). If that subset contains less than a preselected percentage of the total values, then the data are rejected for that height. Both the velocity interval (consensus window) and the required percentage (consensus threshold) can be selected by the operator. An average signal-to-noise ratio is associated with each consensus average by averaging the SNR for all the records that were accepted for the radial velocity consensus average. After the consensus-averaged radial velocities are computed for each radar beam position, an average

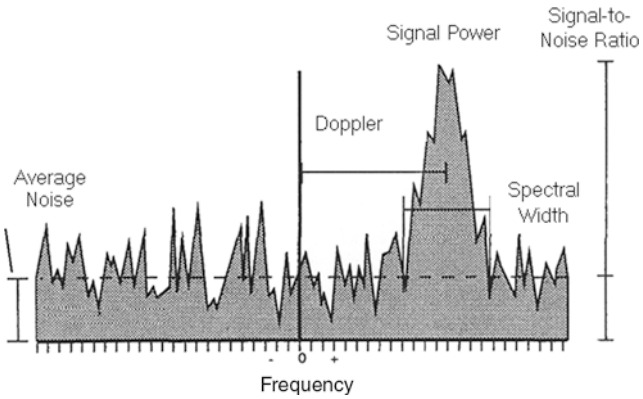

Fig. I.4.5 Example of Doppler spectrum. The x-axis is the radial velocity in ms-1. The y-axis is the signal power normalized to the maximum value of the spectrum. The 0th moment is the mean amplitude of the peak above the noise. The Doppler shift is the 1st moment. The spectral width is twice the square root of the 2nd moment (adapted from the wind profiler manual)

Table I.4.1 Typical specifications for commercially available radar wind profilers

Typical specifications	Lower-tropospheric radar	Mid-tropospheric radar	Tropospheric radar (1)	Tropospheric radar (2)
Operating frequency (MHz)	915 or 1290	449	46–68	449 or 482
Minimum height (m)	120	200–300	500–1,000	400
Maximum height (km)	up to 3	up to 8	up to 16	up to 16
Vertical range resolution (m)	60, 100, 200, 400	100–1,000	150–1,000	250–1,000
Wind-speed accuracy (m/s)	<1	<1	<1	<1
Wind-direction accuracy (°)	<10	<10	<10	<10
Wind-averaging time (min)	3–60	5–60	5–60	3–60
Antenna	Type electrically steerable micropatch-phased array panels	Type electrically steerable coaxial collinear array	Type electrically steerable array of 144 3-element Yagi-Uda antennas	Type electrically steerable coaxial colinear array

horizontal wind vector is calculated. The operator has the option of using the vertical beam consensus value to correct for a vertical wind component in the off-vertical beam radial velocities. From these corrected and combined radial velocity values, the wind components u, v, and w (or speed and direction) are then computed.

Typical specifications for commercially available lower-tropospheric, mid-tropospheric, and tropospheric radar wind profilers are presented in Table I.4.1 (http://www.vaisala.com/weather/products/windprofilers).

A Doppler radar wind profiler can be configured to sample in more than one mode. Those are referred to as "low mode" (smaller vertical range resolution) and "high mode" (larger vertical range resolution). The greater vertical resolution increases the maximum altitude to which the radar wind profiler can sample, but at the expense of coarser vertical resolution and an increase in the altitude at which the first winds are measured. When radar wind profilers are operated in multiple modes, the data are often combined into a single overlapping data set to obtain a better picture of the atmosphere.

3 RASS

The remote measurement of temperature in the lower atmosphere has been achieved with the development of a Radio Acoustic Sounding System (RASS) co-located with the radar wind profilers, through whom a longitudinal acoustic wave propagates upward in the air as a local compression and rarefaction of the ambient air. These density variations cause a corresponding variation in the local refractive index of the atmosphere, tracked by the Doppler radar through the reflection of a small amount of the electromagnetic energy as it propagates through the acoustic pulse. RASS is hence used to measure the speed of sound at various heights above the ground. Though only a small fraction of the electromagnetic energy is reflected, advantage is taken of two phenomena to increase the reflected signal (North and Peterson, 1973).

(1) The acoustic source and radar are located close together so that the spherical wavefronts from each are close to being in coincidence, and energy reflected from the entire acoustic wave is focused at the receiver.
(2) An acoustic pulse consisting of many cycles can be transmitted, resulting in scattering of the electromagnetic energy from successive wavefronts. Furthermore, when the acoustic wavelength, λ_a, is made one-half of the electromagnetic wavelength λ, the energy reflected from each acoustic wavefront adds coherently at the receiver, greatly increasing the return signal strength. The condition $\lambda_a = \lambda/2$ is basically the Bragg scattering condition.

From the measure of the speed of sound, the temperature in the boundary layer can be measured. Under the ideal gas assumption in fact, the speed of sound through dry still air of average atmospheric composition is given by

$$v_S = \sqrt{\frac{\gamma RT}{M}} = H\sqrt{T}, \tag{23}$$

where γ is the ratio of specific heats, R the gas constant, and M the apparent molecular weight, all for an ideal gas having the composition of the average dry atmosphere, and T is the temperature in Kelvin. H is a parameter that varies with humidity. For this reason RASS basically provides profiles of a virtual temperature that is a temperature uncompensated for humidity or pressure. The formal definition of virtual temperature is "the temperature that dry air would have if its pressure and specific volume were equal to those of a given sample of moist air." This parameter allows meteorologists to use the equation of state for dry air even though moisture is present. The equation for the virtual temperature as a function of temperature and mixing ratio is

$$T_{\mathrm{v}} = T\,(1 + 0.61r) \tag{24}$$

where T_{v} is the virtual temperature in Kelvin and r is the mixing ratio.

The data processing and analysis for RASS acquisitions are developed in a similar manner to that of the radar. For that which concerns the estimation of the moments, there is the added feature that two sets of moments are computed. Two separate signals are identified for each RASS spectrum: one for the acoustic return signal at a Doppler shift corresponding to the speed of sound and the other for the wind signal in the lower-velocity region of the spectrum. Since a RASS spectrum has two sets of moments associated with it, three consensus averages are computed. The first is the consensus average of the acoustic signal radial velocity, the second is the consensus average of the wind radial velocity, and the third is the consensus average of the difference between the acoustic and the wind velocities. The average corrected and uncorrected acoustic speeds are then converted to virtual temperature values. The standard RASS retrieval formula is (Angevine et al., 1998)

$$T_{\mathrm{v}} = \frac{c_{\mathrm{a}}^2}{401.92} - 273.16, \tag{25}$$

where T_{v} is the virtual temperature (°C) and c_{a} is the acoustic velocity corrected for vertical wind w.

The maximum height of the RASS signal is determined principally by the radar wavelength and the temperature and moisture structure of the atmosphere. For typical midlatitude conditions, a UHF 915-MHz profiler/RASS system will usually provide temperature measurements to 0.5–1.0 km. In a moist boundary layer the maximum height is generally above 1 km (Wilczak et al., 1996).

Figure I.4.6 shows the 1,290-MHz Doppler radar wind profiler, equipped with a RASS located in Assergi (L'Aquila), Italy.

Typical specifications for commercially available RASS associated with lower-tropospheric, mid-tropospheric, and tropospheric radar wind profilers (http://www.vaisala.com/weather/products/windprofilers) are presented in Table I.4.2.

Fig. I.4.6 Picture of the wind profiler – RASS system located on the top of one building of the National Laboratory of Gran Sasso (LNGS), at an altitude of 981 m ASL. It works at 1,290 MHz, relative to a wavelength of about 23 cm

Table I.4.2 Typical specifications for commercially available RASS associated with radar wind profilers

Typical specifications	RASS/lower-tropospheric radar	RASS/mid-tropospheric radar	RASS/ tropospheric radar (1)	RASS/ tropospheric radar (2)
Minimum height (m)	120	200–300	500–1,000	400
Maximum height (km)	Up to 1.5	Up to 2.5	Up to 5	Up to 5
Vertical range resolution (m)	60, 100, 200, 400	100–1,000	150–1,000	250–1,000
Temperature accuracy (°C)	1	1	1	1
Temperature averaging time (min)	3–60	3–60	5–60	3–60
Audio frequency	2–4 kHz, Bragg matched to transmitter frequency	∼1 kHz, Bragg matched to transmitter frequency	80–150 Hz, Bragg matched to transmitter frequency	∼1 kHz, Bragg matched to transmitter frequency

4 SODAR

SOund Detection And Ranging (SODAR) is a weather observing device that uses sound waves to detect the wind speed and direction at various elevations above the ground (Konrad et al., 1974; Spizzich, 1974; Spizzichino, 1974). The difference between SODARs and wind-profiling radars is that acoustic signals are used rather than electromagnetic signals to remotely sense winds aloft. In a typical implementation, the SODAR can sample along each of the three beams: one is aimed vertically to measure vertical velocity, and two are tilted off vertical and oriented orthogonal to one another to measure the horizontal components of the air's motion (Fig. I.4.7).

Pulses are transmitted consecutively along each of the three beam axes at slightly different frequencies to avoid overlapping of the signal. Again, using appropriate trigonometry, the three-dimensional meteorological velocity components (u, v, and w) and wind speed and wind direction are calculated from the radial velocities with corrections for vertical motions. A profile of the atmosphere as a function of height can be obtained by analyzing the return signal at a series of times following the transmission of each pulse. The return signal recorded at any particular delay time provides atmospheric data for a height that can be calculated based on the speed of sound. In this case the pulse frequency is chosen as a good compromise between the attenuation of the signal (which increases with the frequency) and the environmental noise. The attenuation of propagating acoustic energy increases as a function of increasing frequency, decreasing temperature, and decreasing humidity.

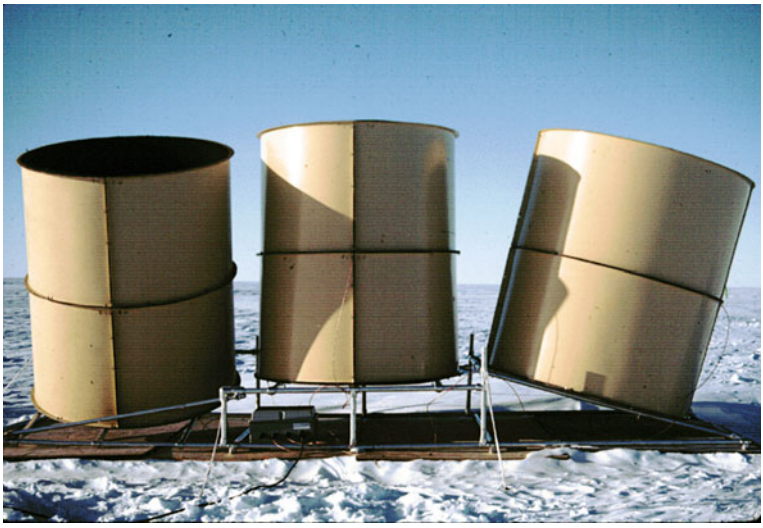

Fig. I.4.7 Picture of a SODAR system with three beam directions

For any transmitted pulse, the received Doppler frequency is computed and converted in wind velocity through the relation:

$$v = \frac{c_a}{2}\left(\frac{f_d}{f_0}\right), \tag{26}$$

where c_a is the sound velocity, f_d the Doppler shift, and f_0 the frequency of the pulse. For example, if $f_0 = 2,000\,\text{Hz}$ we will have a shift equal to 12 Hz in frequency for every ms^{-1} of wind velocity.

4.1 Data Processing and Averaging

Signal processing is another area where SODAR systems are rather similar to radar wind profilers. Again, SODAR systems use a fast Fourier transform (FFT) to derive the signal Doppler shift, but a variety of techniques may be used both before and after FFT processing to improve signal detection. One technique is to average the signal. Signal averaging may be used either in the time domain (before FFT) or in the frequency domain (after FFT) in an attempt to reduce noise level and improve the SNR, which is usually the primary criterion for data acceptance. Data storage and presentation capabilities can be different from system to system. Most systems will provide both text and plotted data showing the profiles of the horizontal and vertical winds and a facsimile display showing intensity data. The individual wind component data may also be provided, which can be very useful for quality control purposes. Data pertaining to signal quality are also usually displayed and recorded. The SNR is normally provided, but there is no common definition of this among SODAR manufacturers. Due to the large volume of data generated by a SODAR system, usually only the data averages are recorded and not the raw input signal.

As for radar wind profilers, one of the most important problems with SODAR systems is ground clutter. Its interference occurs when side-lobe energy radiating from a SODAR antenna on transmit is reflected back to the antenna by nearby fixed objects such as buildings, trees, mountains, or towers. This reflected side-lobe energy can overcome the atmospheric return signal. For this reason, SODAR systems must either be located in areas with no reflecting objects in the area, or they must be designed to substantially eliminate side-lobe energy.

Typical SODAR specifications are introduced in Table I.4.3.

Table I.4.3 Typical specifications for commercially available SODAR systems

	Performances
Height coverage	25–1,500 m
Vertical resolution	13–50 m
Accuracy	$\pm$ 0.2 ms^{-1}
Used frequencies	1,750–2,000–2,250 Hz
Acoustic power	50 W
Geometry	Monostatic

References

Angevine WM, Bakwin PS, Davis KJ (1998) Wind profiler and RASS measurements compared with measurements from a 450-m tall tower. J Atmos Ocean Technol 15:818–825

Barrick DE (1972) Remote sensing of sea state by radar. In: Derr VE (ed) Remote sensing of the troposphere. US Government Printing Office, Washington, DC

Battan LJ (1959) Radar meteorology. University of Chicago Press, Chicago, IL, 161 pp

Bianco L, Wilczak JM, White AB (2008) Convective boundary layer depth estimation from wind profilers: statistical comparison between an automated algorithm and expert estimations. J Atmos Ocean Technol 25:1397–1413

Ecklund WL, Carter DA, Balsley BB (1988) A UHF wind profiler for the boundary layer: brief description and initial results. J Atmos Ocean Technol 5:432–441

Hardy KR, Atlas D, Glover KM (1966) Multiwavelength backscatter from the clear atmosphere. J Geophys Res 71:1537–1552

Hildebrand PH, Sekhon, RS (1974) Objective determination of the noise level in Doppler spectra. J Appl Meteorol 13:808–818

Konrad TG, Arnold A, Dobson EB et al (1974) Unique boundary-layer experiment using radar, SODAR, and instrumented aircraft. EOS Trans-Am Geophys Union 55:271

Kraus JD (1950) Antennas. McGraw-Hill, New York, NY, 553 pp

Kropfli RA, Katz I, Konrad TG, Dobson EB (1968) Simultaneous radar reflectivity measurements and refractivity index spectra in the clear atmosphere. Radio Sci 3:991–994

Lane JA (1969) Radar echoes from clear air in relation to refractive-index variations in the troposphere. Proc. IRE Lond 116:1656–1660

Lhermitte RM (1963) Motion of scatterers and the variance of the mean intensity of weather radar signals. Sperry Rand Res. Rept. No. SRRC-RR-63-57. Sperry Rand Res. Center, Sudbury. 43 pp

Nathanson FE (1969) Radar design principles. McGraw Hill, New York, NY, 626 pp

Nathanson FE, Reilly JP (1968) Radar precipitation echo experiments on temporal, spatial, and frequency correlation, IEEE Trans AES-4(4):505–514

North EM, Peterson AM (1973) RASS, a remote sensing system for measuring low-level temperature profiles. Bull Am Meteoreol Soc 54:912–920

Probert-Jones JR (1960) The analysis of Doppler radar echoes from precipitations. In: Proceedings of 8th weather radar conference. American Meteorological Society, Boston, MA, pp 377–385

Richter JH (1969) High resolution tropospheric radar sounding. Radio Sci 4:1261–1268

Riddle AC, Angevine WM (1992) Ground clutter removal from profiler spectra, STEP, In: Edwards B (ed) Fifth workshop on technical and scientific aspects of MST radar, Aberystwyth, Wales, UK, 6–9 Aug. 1991, SCOSTEP, pp 418–420

Spizzich A (1974) Refraction of acoustic-waves in atmosphere and its influence on measurement of wind by SODAR Ann Telecommun 29:301–310

Spizzichino A (1974) Discussion of operating-conditions of a Doppler SODAR. J Geophys Res 79:5585–5591

Strauch RG, Merritt DA, Moran KP, Earnshaw KB, van de Kamp D (1984) The Colorado wind profiling network. J Atmos Ocean Technol 1:37–49

White AB (1997) Radar remote sensing of scalar and velocity microturbulence in the convective boundary layer. NOAA Tech. Memo. ERL ETL-276. Environmental Technology Laboratory, Boulder, CO. 127 pp. [Available from NOAA/ERL/ETL Broadway, Boulder, CO, 80305]

Wilczak JM, Gossard EE, Neff WD, Eberhard WL (1996): Ground-based remote sensing of the atmospheric boundary layer: 25 years of progress. Boundary-Layer Meteorol 78:321–349

Chapter I.5
An Introduction to Rain Gauges and Disdrometers

Mario Montopoli and Frank S. Marzano

1 Introduction

Rainfall plays a key role within the hydrological cycle. Its accurate and spatially revolved quantitative measurement is one of the main current challenges within the hydro-meteorological community (Marzano et al., 2002). Several techniques may be enumerated for this purpose: local direct instrumentation (such as rain gauges and disdrometers), ground-based remote instrumentation (such as microwave radars and radiometers), and satellite-based remote instrumentation (such as microwave radars, microwave radiometers, infrared sensors). The synergy between all these instruments, with their advantages and drawbacks, is fundamental for a better comprehensive analysis of the rainfall field space-time features. For example, the measurement of hydrometeor size distributions from disdrometers can provide a powerful opportunity to directly investigate the microphysical properties of thunderstorms and allow a comparison from retrievals performed, for example, by polarimetric radars (Vulpiani and Marzano, 2008).

In this chapter an introduction to the main ground-based instruments to measure raindrop size distribution and rain will be given. Rain gauges and disdrometers will be described to provide a useful overview of the local in situ measurements, often used to calibrate and validate rainfall estimates derived from radar observations.

1.1 Rain Gauge

Any instrument which is able to collect and measure the rainfall intensity can be regarded as a pluviometer (or rain gauge) (Ahrens, 2004). The standard pluviometer, which was invented by the English scientist Robert Hooke around the second half of 1600, consists of a funnel connected to a measuring tube for registering the level

M. Montopoli (✉)
Centre of Excellence CETEMPS and Department of Electrical and Information Engineering, University of L'Aquila, L'Aquila, Italy
e-mail: mario.montopoli@univaq.it

D. Cimini et al. (eds.), *Integrated Ground-Based Observing Systems*,
DOI 10.1007/978-3-642-12968-1_5,

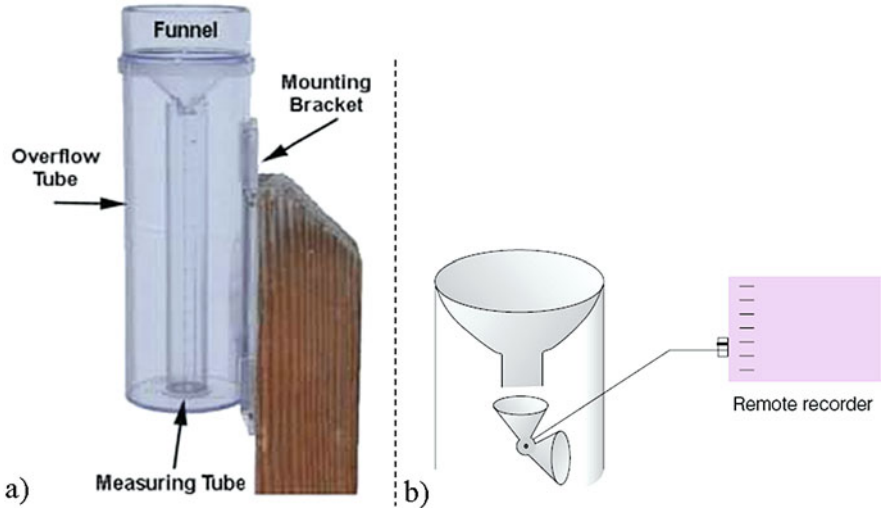

Fig. I.5.1 Two types of pluviometers. **Panel a** standard rain gauge; **panel b** balance rain gauge

of rain (see left panel of Fig. I.5.1). The area of the funnel is larger than that of the measuring tube and, as a consequence, a good degree of precision of the order of 0.1 mm can be achieved. In order to obtain the accumulated rain R_{acc} expressed in mm/m^2 (i.e., the conventional unit) the measure of the volume of water W (l) has to be normalized as follows:

$$R_{\mathrm{acc}} = \frac{W}{A}\,, \tag{1}$$

where A is the area of the funnel tube expressed in m^2 and its inverse is often referred as pluviometric factor. Therefore, if the pluviometer measure 1 l of water (i.e., 1 dm^3 = 0.001 m^3) with $A = 1$ m^2, through Eq. (1), a height of 1 mm will be observed on the measuring tube. The measured (m) rain rate R_{m} expressed in mm/h indicates the level of rain observed after an hour.

Another type of pluviometer, shown on the right panel of Fig. I.5.1, uses a balance to gather the rain. The balance is composed of a couple of little bins which are fixed to each other and they are free to oscillate around an horizontal axis. When one bin accumulates a given quantity of water its increased weight produces the discharge of the accumulated water and the second bin takes the place of the first and the cycle goes on. Every time that the two bins rotate, the quantity of water discharged is registered on a roll of paper. The sum of each registration, provides, according to some proportions, the quantity of rain fallen. This type of pluviometer is often used in the automatic meteorological stations even though the tendency to underestimate the rain quantity has been noticed for intense rainy events. This is due to the loss of water during the bin rotations.

In addition, it should be mentioned that other types of pluviometers use weighing systems where the weight of the gathered water is associated to the rain fallen expressed in millimeter.

1.2 Disdrometer

The microphysics of hydrometeors, their composition, their shape, their size, and their statistical distribution are the key parameters to characterize the precipitation phenomena and their knowledge is very important in order increase the accuracy of estimations obtained by weather radars.

Since around 1977 the measurements of the distribution of the size of raindrops are possible thanks to an instrument called impact disdrometer which was invented by J. Joss and A. Waldvogel and for this reason it is often labeled as Joss & Waldvogel Disdrometer (JWD) (Joss and Waldvogel, 1977). More recent progresses in this field have been yielding a more sophisticated instrument than the JWD. In 1990, the Joanneum Research Center of Graz (Australia), in collaboration with the European Space Agency/European Space TEchnology Centre (ESA/ESTEC) invented the 2D video disdrometer (2DVD).

In the following, instrumental details about the two types of disdrometer mentioned above are given together with a mathematical formulation of the measured quantities. Eventually, section ends with an example on how distrometer observations are converted into quantity of interest for microphysical meteorological studies such as water content, drop concentrations, and mean drop diameter.

1.2.1 Instrument Details

The fundamentals that describe these two instruments are quite different. The JWD is based on the transduction of the mechanical momentum, which is indicted by the impact of a hydrometer on the area of the sensor (A) and to an electrical energy, whereas the 2DVD takes a picture of the shadow that an hydrometeor causes when it goes through two perpendicular beams of light. A schematic view of both the JWD and the 2DVD is shown in Fig. I.5.2.

In detail, the 2DVD is composed of two cameras which are perpendicular to each other and two illumination devices which are positioned in front of each camera. For reasons that will be clear later, both the cameras and the illuminators do not lie on the same horizontal plane but they are spaced of about 6.18 mm. The two beams of light, generated from the illumination devices, overlap defining a sensed area or also called virtual measuring area A. Every particle which goes through A is registered as a shadow from the two cameras. Therefore, the optical signal, collected from the cameras, is transduced into an electrical signal whose intensity is related to the particle sizes. Unlike the JWD, the 2DVD allows the measure of the shape of the hydrometeors exploiting the fact that two pictures, of the same particle, are taken from a different angle of view (i.e., shifted by 90°). In addition, since the vertical

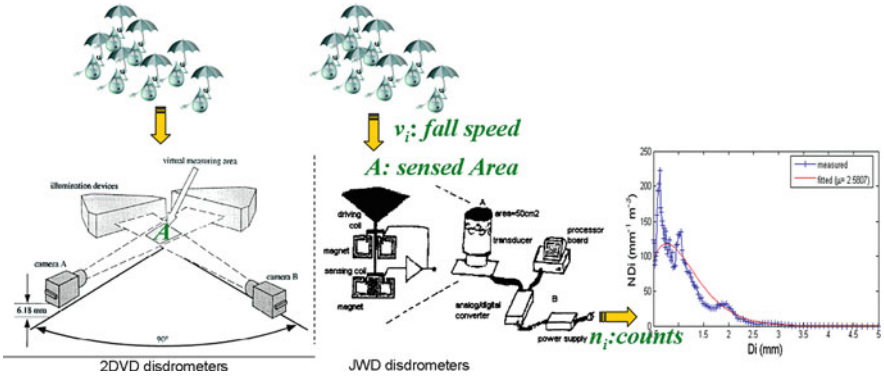

Fig. I.5.2 *Left panel*: components of the 2D video disdrometer. *Middle panel*: components of Joss-Walvogel disdrometer. *Right panel*: an example of the output of a disdrometer expressed in $\mathrm{mm}^{-1}\cdot\mathrm{m}^{-3}$ (instead of counts)

distance between the cameras is known, the vertical fall velocity of drops can also be obtained. More details about this instrument can be found in Hanesch (1999).

On the other hand, the JWD (see middle panel of Fig. I.5.2) is composed of a conical section in which the drops impact producing the downward movement of the conical section between two coils. The first coil registers the amplitude of the displacement of the conical section, whereas the second one contrasts this downward displacement restoring the initial position of the conical section. From this brief exposition it is clear that, unlike the JWD, the 2DVD disdrometer allows to retrieve some important quantities for meteorological applications, such as the vertical fall velocity and the shape of a drop (i.e., its axis ratio).

Both the JWD and the 2DVD, when used for obtaining the RSD, produce, at their output and at the discrete instant t (s), the counts (n) of drops for each interval of diameters as shown in the right panel of Fig. I.5.2. From the JWD and the 2DVD counts, the measured raindrop size distribution (RSD) can be calculated using the following equation:

$$N_{\mathrm{m}}(D_i, t) = \frac{n_i(t)}{A \cdot \Delta t \cdot v_i \cdot \Delta D_i}\,, \tag{2}$$

where the subscript "m" indicates a measured quantity, D_i (mm) is the central rain drop diameter of the "channel" c_i which has been computed as mean value between the drop diameters D_{ci} and D_{ci+1}, $N_{\mathrm{m}}(D_i,t)$ ($\mathrm{mm}^{-1}.\mathrm{m}^{-3}$) the number of rain drops per unit of volume in the channel c_i at the discrete instant t, $n_i(t)$ the number of drops rekoned in the ith channel at the instant t, A (m^2) the sensor area, Δt (s) the sample period, v_i ($\mathrm{m}\cdot\mathrm{s}^{-1}$) is the rain drop fall speed of a rain drop whose diameter is D_i, and ΔD_i (mm) is the ith channel width. A typical parameter setup to calculate $N_{\mathrm{m}}(D_i, t)$ from Eq. (2) for a JWD disdrometer are: $A = 0.005\ \mathrm{m}^2$, $\Delta t = 10$ s, $\Delta D_i = D_{ci+1} - D_{ci}$ for i ranging from 1 to $n_c = 104$ with minimum and maximum diameters equal to 0.5 and 5 mm, respectively, uniformly spaced in a logarithmic scale. On the

contrary, for a 2DVD disdrometer the maximum and minimum detectable range of diameters is, respectively, 0.1 and 10 mm, whereas the sensed area is equal to 0.010 m^2.

The speed v_i, in Eq. (2), can be described by models of terminal velocity of rain drops as, for example, that proposed by Atlas and Ulbrich (1977), which approximated form is reported here:

$$v_i = 3.78 \cdot D_i^{0.67} \,. \tag{3}$$

In the past, starting from measurement experiments of Gunn and Kinzer (1949), exact but relatively complex analytical expressions have been semi-empirically established for various rain regimes (Foote and Toit, 1969; Beard and Pruppacher, 1969; Wobus et. al., 1971; Beard, 1976).

From Eqs. (2) and (3), the computation of the measured rain rate R_{m} (mm/h) is straightforward through the moments of $N_{\mathrm{m}}(D_i,t)$ of order 3.67, as specified by

$$R_{\mathrm{m}}(t) = 3.78 \cdot \frac{\pi}{6} \cdot \mathrm{m}_{3.67}(t) \,, \tag{4}$$

where $m_n(t)$ is the general expression of $N_{\mathrm{m}}(D_i,t)$ moment of order n and can be calculated from disdrometer measurements as

$$m_n(t) = \int_0^{\infty} D^n \cdot N(D,t) \cdot dD = \sum_{i=1}^{n_c} D_i^n \cdot N_{\mathrm{m}}(D_i,t) \,.\, \Delta D_i. \tag{5}$$

In Eq. (5), the third term underlines the discrete nature of the measured RSD, whereas the extremes of the integral point out the untruncated range of diameters (Montopoli et al., 2008a, 2008b).

1.2.2 Particle Size Distribution

Modeling the size distribution of particles is a hard task but, at the same time, very important in order to retrieve some key quantities for characterizing precipitations such as water content and rain rate. In the following, we will refer to the drop size distribution (DSD), instead of the more general definition of particles size distribution (PSD) when the particles are supposed to be precipitating whereas the acronyms RSD will indicate the raindrop size distribution. The major difficulty in modeling the DSD is due to its high variability and to the fact that a given size of hydrometeors can be associated to different drop concentrations for the same rain rate intensity. Disdrometer, before introduced, surely is needful to model DSDs.

Recently, many studies (e.g., Tokay et al., 2002 and Testud et al., 2001) have demonstrated that a gamma distribution can be a valid alternative to the more

consolidated Marshall e Palmer distribution, based on an exponential function, to describe DSD. Gamma distribution assumes the following form:

$$N(D,\mathbf{p}) = N_w \cdot f(\mu) \cdot \left(\frac{D}{D_\mathrm{m}}\right)^{\mu} \cdot \exp\left[-(4+\mu)\cdot\frac{D}{D_\mathrm{m}}\right], \tag{6}$$

where $N(D,\mathbf{p})$ ($\mathrm{m}^{-3}\cdot\mathrm{mm}^{-1}$) is the number of drops per unit volume per unit size interval, D (mm) is the sphere-equivalent drop diameter, N_w ($\mathrm{m}^{-3}\cdot\mathrm{mm}^{-1}$), μ, and D_m (mm) are the intercept, the shape, and the mass-weighted mean diameter parameters, respectively, and $f(\mu)$ takes the following form:

$$f(\mu) = \frac{6}{4^4}\cdot\left[\frac{(4+\mu)^{(4+\mu)}}{\Gamma(4+\mu)}\right], \tag{7}$$

where Γ is the complete gamma function. In general, the parameters N_w, μ, and D_m can be retrieved using the moments of the RSD (e.g., Ulbrich and Atlas, 1998),

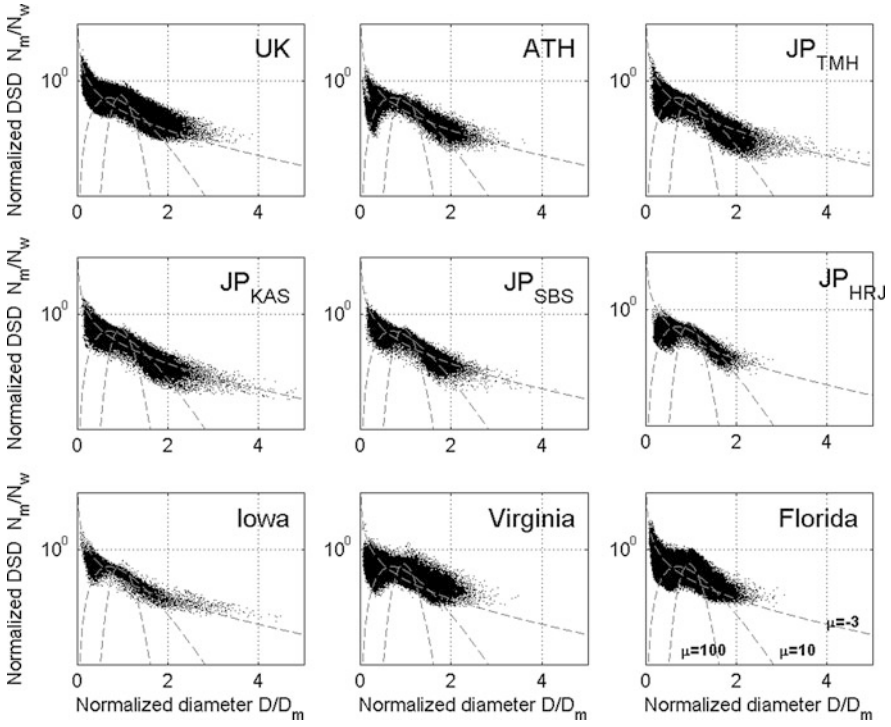

Fig. I.5.3 *Black dots* indicate the scaled RSD ($N_\mathrm{m}(D)/N_\mathrm{w}$) vs normalized diameter (D/D_m) for all the RSD data sets. *Gray-dashed lines* indicate the normalized gamma distributions for values of μ equal to –3 and 10 and 100 as shown in the *lower right corner*

formalized in Eq. (5), such as, for example, the second, the third, the fourth, and the sixth. The mass-weighted mean diameter D_{m} is calculated as the ratio between the fourth and the third empirical moments of the RSD:

$$D_{\mathrm{m}} = \frac{m_4}{m_3} \,. \tag{8}$$

The generalized intercept parameter N_{w} is also computed from the fourth to third moment of the RSD and can be derived from

$$N_{\mathrm{w}} = \frac{256}{6} \cdot \frac{m_3^5}{m_4^4} \,, \tag{9}$$

where the moment m_n of order n is expressed by Eq. (5).

Typical shapes of DSD are shown in Fig. I.5.3 for different regions where distrometer were located (USA: Virginia, Iowa, and Florida; Japan: Kitaashigara Hiratsuka and Shibusawa; Greece: Athens; UK: Chilbolton).

References

Ahrens CD (2004) Essentials of meteorology. Thomson Brooks Cole, Belmont CA 94002–3098

Atlas D, Ulbrich CW (1977) Path and area integrated rainfall measurement by microwave attenuation in the 1–3 cm band. J Appl Meteorol 16(12):1322–1331

Beard KV (1976) Terminal velocity and shape of cloud and precipitation drops aloft. J Atmos Sci 33:851–864

Beard KV, Pruppacher HR (1969) A determination of terminal velocity and drag of small water drops by means of a wind tunnel. J Atmos Sci 6:57–60

Foote GB, du Toit PS (1969) Terminal velocity of raindrops aloft. J Appl Meteorol 8:249–253

Gunn R, Kinzer GD (1949) The terminal velocity of fall for water droplets in stagnant air. J Meteorol 6:243–248

Hanesch M (1999) Fall velocity and shape of snowflakes, PhD thesis. http://www.distrometer.at

Joss J, Waldvogel A (1977) Comments on some observations on the Joss-Waldvogel rainfall disdrometer. J Appl Meteorol 16:112–113

Marzano FS, Mugnai A, Turk J (2002) Precipitation retrieval from spaceborne microwave radiometers and combined sensors. In: Marzano FS, Visconti G (eds) Remote sensing of atmosphere and ocean from space: models, instruments and techniques. Kluwer Acad. Publ., Dordrecht (NL). ISBN 1-4020-0943-7, pp 107–126

Montopoli M, Marzano FS, Vulpiani G (2008a) Analysis and synthesis of rainfall time series using disdrometer data. IEEE Trans Geosci Remote Sens 46(2):466–478

Montopoli M, Marzano FS, Vulpiani G, Anagnostou MN, Anagnostou EN (2008b) Statistical characterization and modeling of raindrop spectra time series for different climatological regions. IEEE Trans Geosci Remote Sens 46:2778–2787

Testud J, Oury S, Black RA, Amayenc P, Dou X (2001) The concept of ‘‘normalized’’ distributions to describe raindrop spectra: a tool for cloud physics and cloud remote sensing. J Appl Meteorol 40:1118–1140

Tokay A. Kruger A, Krajewski WF, Kucera PA, Jose A, Filho P (2002) Measurements of drop size distribution in the southwestern Amazon basin. J Geophys Res 107(D20):8052. doi:10.1029/2001JD000355

Ulbrich CW, Atlas D (1998) Rainfall microphysics and radar properties: analysis methods for drop size spectra. J Appl Meteorol 37(September):912–923

Vulpiani G, Marzano FS (2008) Advanced radar polarimetric techniques for rainfall observation. In: Sorooshian S, Hsu K-L, Coppola E, Tomassetti B, Verdecchia M, Visconti G (eds) Hydrological modelling and the water cycle. Springer, Berlin. ISBN: 978-3-540-77842-4

Wobus HB, Murray FW, Koeing LR (1971) Calculation of terminal velocity of water drops. J Appl Meteorol 10:751–754

Chapter I.6
An Introduction to Measurements of Atmospheric Composition

Piero Di Carlo

1 Introduction

Measurements of the atmospheric composition could help to improve our understanding of the chemistry, climate changes, deterioration of the urban air quality, dynamics of the atmosphere and to verify theoretical ideas. Atmospheric chemistry involves thousands of species; in Fig. I.6.1, for example, the chemistry of the hydroxyl radical (OH) which is the main oxidant of the troposphere is reported. OH and nitrogen oxides (NO_x) control the formation of the ozone (O_3) which is the main pollutant of the troposphere, through the oxidation of the volatile organic compounds (VOC), carbon monoxide (CO), and methane (CH_4). Direct observations of these species help to understand the fundamentals of tropospheric chemistry and the mechanisms of the formation and evolution of air pollution. Continuous measurements of carbon dioxide (CO_2), collected over the last decades, give the experimental evidence that anthropogenic emissions are forcing changes on the climate, since CO_2 is one of the greenhouse gases. Iodine atoms, at the beginning of the 1990s, have been recognized to play a role in the formation of the ozone hole in stratosphere but no role in the tropospheric chemistry was evident. Very selective observations of iodine oxide in the marine surface boundary layer suggested that it can also have importance in the removal of ozone in troposphere and therefore on air quality (Alicke et al., 1999). An indirect use of the observations of atmospheric composition has been shown by Bertram et al. (2007) studying the dynamics of the upper troposphere, with measurements of NO_x and nitric acid (HNO_3) onboard the NASA DC8 aircraft. They showed that the ratio of NO_x/HNO_3 is a unique indicator of the time that a sampled air mass spent in the upper troposphere after a convention, because HNO_3 is preferentially wet scavenged and its solubility is about 10^8 times higher than NO_x. In the middle of the 1980s English researchers at Halley Bay station in Antarctica observed a reduction of the total column amount of ozone

P. Di Carlo (✉)
Dipartimento di Fisica and Centro di Eccellenza CETEMPS, Universita' di L'Aquila, via vetoio, Coppito L'Aquila, L'Aquila, Italy
e-mail: Piero.Dicarlo@aquila.infn.it

D. Cimini et al. (eds.), *Integrated Ground-Based Observing Systems*,
DOI 10.1007/978-3-642-12968-1_6,

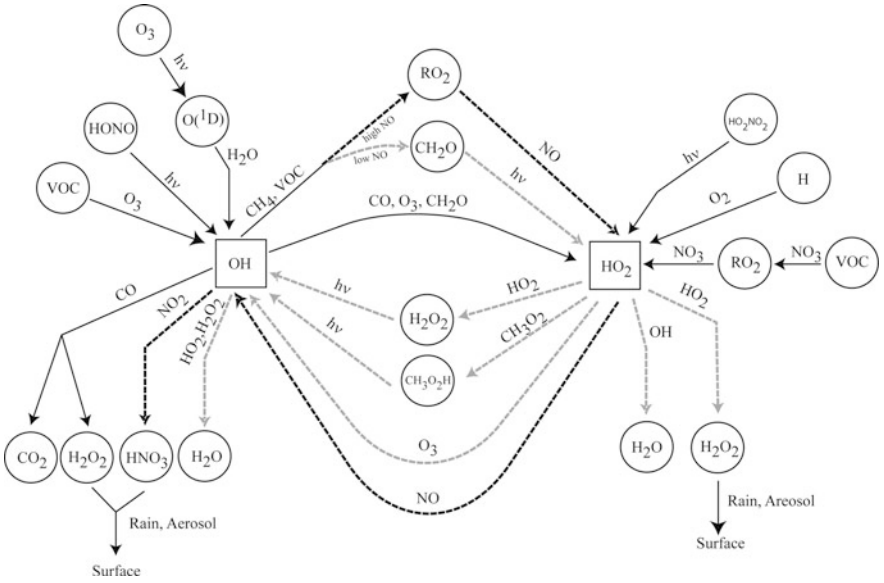

Fig. I.6.1 Schematic view of the main HO_x reactions. Dominant reactions for high NO are marked with *dotted black line*; reactions for low NO are marked with *dotted grey line*. *Black lines* are reactions not influenced by NO concentration

using a ground-base spectrophotometer (Farman, et al., 1985). The spectrophotometer (Brewer) measured the amount of the ultraviolet (UV) light from the sun at five different wavelengths between 306 and 320 nm: they discovered the ozone hole. After confirmations of Farman observations, several theories were proposed to understand the mechanisms of the stratospheric ozone destruction. One of the experiments that unequivocally showed the role of chlorine radicals in the removal of stratospheric O3 was the simultaneous observation of ClO and O_3 onboard the ER-2 aircraft flying inside the polar vortex made by Anderson et al. (1991). O_3 was observed using UV absorption technique, whereas ClO with fluorescence detection of Cl after conversion of ClO through reaction with NO and they showed that as the aircraft flew into the vortex the concentration of O_3 decreased, whereas ClO level increased in comparison with observations outside the vortex: that was the brilliant proof that the chlorine radical is one of the species that destroys ozone during the Antarctic spring months.

Measurement of atmospheric composition is challenging for many reasons. First because we must detect one species in a medium (the atmosphere) where there are thousands of others that can give and interference resulting in incorrect or imprecise observations. Another issue is that the species to be measured are trace gases, in particular those of interest in atmosphere, which have concentrations usually less than a ppm (one part per million). In fact in the atmosphere 99% of the molecules are composed of nitrogen (N_2), oxygen (O_2), and argon (Ar); but the molecules included in that 1% left like O_3, CO_2, nitrogen dioxide (NO_2), ClO are interesting since their concentrations can be modified by human activities and they are involved

in the pollution formation, ozone hole, and climate changes. Two more difficulties in the detection of atmospheric composition arise because temporal and spatial scales are very different from species to species. In Fig. I.6.2 (adapted from Seinfeld and Pandis, 2006) the temporal and spatial scales of the compounds important in atmospheric chemistry are reported. They are grouped into short-lived species (lifetime less than 1 h and spatial scale of 100 m, for example, OH), moderately long-lived species (lifetime from 1 h to 1 year and spatial scale from 0.1 to 1,000 km, for example, NO_x and CO), and finally, long-lived species (lifetime from 1 year to 100 years and spatial scale from hundreds of kilometers to more than 10,000 km, for example, CH_4 and CFCs). Since the temporal and spatial scales are orders of magnitude that differ from species to species, very different instrument techniques are needed to detect species with short lifetime that request fast response instrument compared with long-lived species. The variability of spatial scale implies that some species need to be detected from site to site and eventually using mobile platforms like aircrafts, whereas long-lived species, since well mixed, can be detected only in few sites so that it is not necessary aircraft observation.

Section criteria of instruments for atmospheric composition detection are the selectivity, the detection limit, the accuracy, the precision, and, finally, the mechanical and electrical characteristics like weight, size, power requirement, and autonomy. Selectivity is the instrument specificity of the detection of a given species without interference from other species. Usually systems using optical methods have the advantage that the optical spectra can be used as fingerprint of each species.

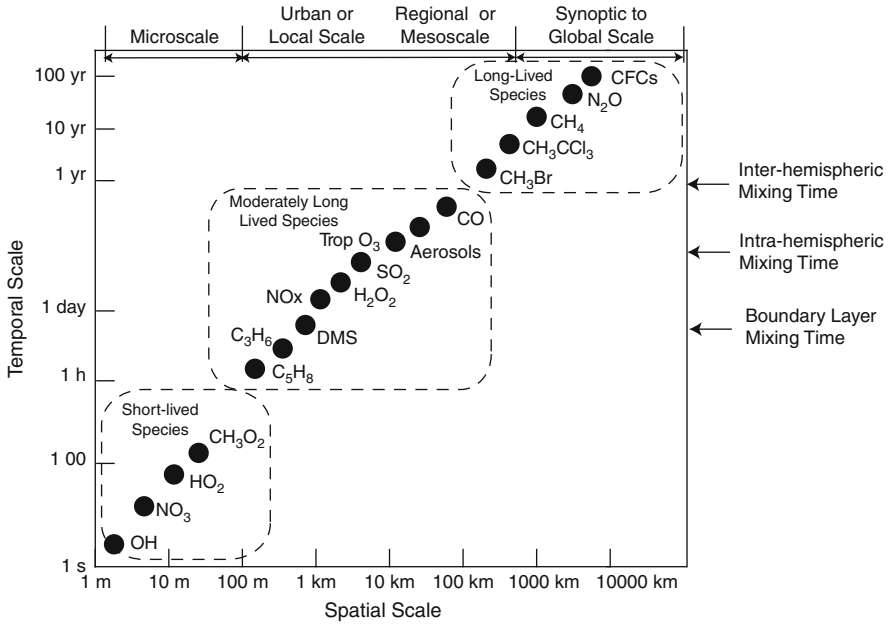

Fig. I.6.2 Spatial and temporal scales of variability for atmospheric constituents (adapted from Seinfeld and Pandis, 2006)

The detection limit is the lowest concentration an instrument can detect. For each compound the detection limit must be significantly lower than the atmosphere concentration, for example, OH concentrations vary in the atmosphere from 0.1 to 1 pptv (parts per trillion) and the detection limit of laser-induced fluorescence systems is 0.001 pptv, whereas detection limit of differential optical absorption spectroscopy instruments is 0.06 pptv, both well below the typical atmospheric level of OH. The accuracy of an instrument is the ability to measure a concentration as close as possible to the real value; this is very important to merge data from global network or from different monitoring stations. The precision is the degree of reproducibility of a measurement under unchanged conditions; this property is required for flux measurements or measurements of concentrations that have to be used to flux retrieval as well as to monitor the long-term trends of a compound. The mechanical and electrical characteristics are very important in the deployment of instruments in remote areas or on platforms like aircrafts where a restrict amount of electrical power and of space is available and there is a limit on the weight of the instrument. In these situations, the design and realization of an instrument with low power consumption, as light and compact as possible, are very important.

A unique technique as well as a unique instrument which are able to detect all the atmospheric species are not available for the motivations above, because each species has its own properties in terms of absorption spectrum, fluorescence wavelength, and so on. Although an "universal" instrument does not exist, a technique to measure as much species as possible is attractive. In this chapter laser-induced fluorescence (LIF) and differential optical absorption spectroscopy (DOAS) techniques will be described, since they can be used to detect several species at the same time or changing some parts of them.

2 Laser-Induced Fluorescence (LIF)

Fluorescence is the emission of light from the relaxation of atoms or molecules from an excited state to a lower electronic state. In the LIF technique the molecules are excited using a laser as light source which emits at wavelengths coincident with the molecular transition from the ground state to an excited electronic state. Molecules after the excitation can lose energy by quenching that converts it into thermal motion of the molecules or by internal excitation of non-fluorescent species. The fluorescence signal is (Wood and Cohen, 2006)

$$S = RQC, \tag{1}$$

where S are counts/s, R the excitation rate, Q the fluorescence quantum yield, and C the collection efficiency of the instrument. The excitation rate is

$$R = E\left\{1 - \exp\left(-cl\int \phi(\nu)\,\sigma(\nu, T, P)\right)d\nu\right\} \tag{2}$$

and approximating $e^{-x} \sim (1 - x)$:

$$R = Ecl \int \phi(\nu)\, \sigma(\nu, T, P) d\nu, \tag{3}$$

where E is the excitation power (photons/s), c the number density of the absorbing species over the path length l, $\Phi(\nu)$ the spectral profile of the excitation source, and σ (ν, T, P) the absorption cross section of the species under detection. The fluorescence quantum yield Q is the fraction of excited molecules that fluoresce:

$$Q = \frac{k_{\text{fluo}}}{k_{\text{fluo}} + \sum_i k_{Qi}\,[M_i]}, \tag{4}$$

where k_{fluo} is the radiative rate constant of the excited species (the inverse of the lifetime τ), k_{Qi} the quenching rate constant due to collision deactivation by bath molecules M_i (mainly nitrogen, oxygen and water vapor) and $[M_i]$ the concentration of the bath molecules. Usually at ambient pressure the quenching rate is much greater than the fluorescence k_{fluo}, so the low pressure in the detection chamber reduces the first (lower bath molecule) that helps to have a bigger fluorescence signal. The collection efficiency, C, is

$$C = \Omega \int T(\nu)\, \eta(\nu)\, \varepsilon(\nu)\, d\nu \int_{t_1}^{t_2} \exp\left(\frac{-t}{\tau}\right) dt, \tag{5}$$

where Ω is the fraction of the fluorescence solid angle intercepted by the collecting lens and focused onto the detector, $T(\nu)$ the transmission through the collection optics, $\eta(\nu)$ the quantum efficiency of the detector, $\Phi(\nu)$ the emission spectrum of the molecule, and the last integral the fraction of fluorescence in the detection time gate t_2–t_1. To calculate all the parameters of the equations above is not easy; it is for this reason that the following equation instead of the relation (1) is used in the LIF technique:

$$S = \alpha \chi, \tag{6}$$

where S is the fluorescence signal in counts/s, α the calibration constant, and χ the mixing ratio of the species to be detected. The calibration constant (counts/s/ppbv) is determinate injecting known amounts of the species in the detection cell of the instrument and measuring the fluorescence as function of the species concentrations. Figure I.6.3 shows the calibration of L'Aquila University LIF system for NO_2 observations. In the calibration the fluorescence signal in terms of counts per seconds is plotted as a function of seven different amounts of NO_2 sent in the detection cell (Fig. I.6.4), the slope of the straight line that fits the observation points is the calibration constant (a) that when substituted in Eq. (6) allows to derive the concentrations from the fluorescence signal.

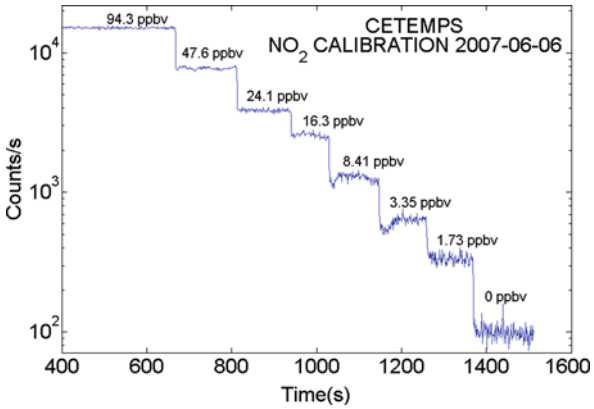

Fig. I.6.3 Example of the increase of the counts/s increases the amount of NO_2 injected in the LIF system of L'Aquila during calibration

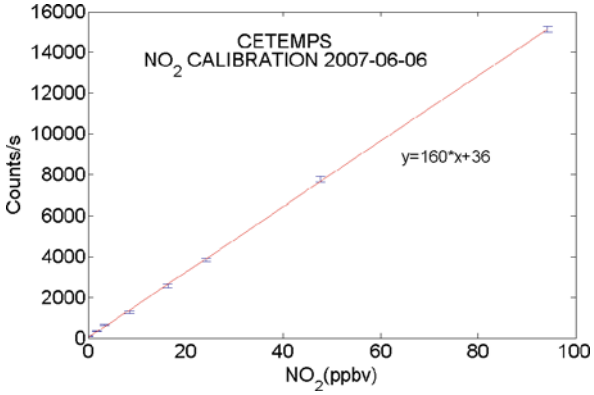

Fig. I.6.4 Fit of the calibration points and equation of the straight line. The slope of this line is the calibration constant used for the LIF concentration measurements

Usually in all kinds of measurements unwanted signals are superimposed at the signal of the species to be detected; they do not give any information and mask the "real" signal. This is the background (B) in the LIF technique, which is due to optical scatter from the surface chamber, Raman, Rayleigh, and Mie scattering, dark current of the PMT, and eventual interference due to fluorescence of other species. The detection limit ($\chi_{\min}$) is the minimum detectable mixing ratio of a species:

$$\chi_{\min} = \frac{\mathrm{SNR}}{\alpha}\sqrt{\frac{2B}{t}}, \tag{7}$$

where $\mathrm{SNR} = St/\sigma_s$ is the signal-to-noise ratio, α the calibration constant, S the fluorescence signal, B the background, t the time interval of the measurements, and σ_s the uncertainty in the fluorescence measurements. In every LIF instrument, fluorescence signal and background are measured and both are very important in determining the detection limit. In Table I.6.1 the detection limits of LIF systems used to detect some important tropospheric species are reported.

Table I.6.1 Detection limit for some tropospheric species measured with LIF systems

Species	Detection limit (pptv)
OH	0.005
HO_2	0.005
NO_2	5
NO	0.07
NO_3	76
N_2O_5	22
ClO	3
$ClONO_2$	10

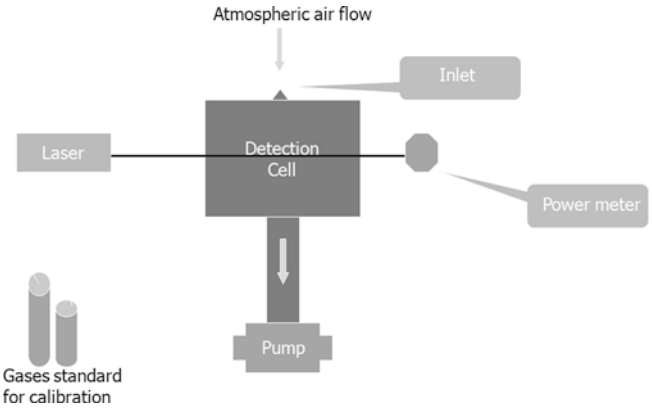

Fig. I.6.5 Sketch with the main parts of LIF system

A schematic view of L'Aquila LIF system is reported in Fig. I.6.5: the main part is the detection cell where the atmospheric air is pulled through a small orifice that is the inlet to be sampled. The air flow is perpendicularly crossed by the laser beam that excites the molecules. Perpendicularly to both air flow and laser beam there is the detection system that includes lens to increase the field of view, interferential filters to cut non-fluorescence light, and the photomultiplier that detects the fluorescence photons. Other important parts of the LIF system are (1) the pump system that takes atmospheric air into the detection cell and keeps it at low pressure to reduce the quenching, (2) the calibration system that for NO_2 instruments includes a cylinder with NO_2 and zero air that will be mixed using a gas-flow controllers to change the NO_2 concentration. For the calibration of the LIF system that measures species like OH a more complicated system is used for real-time OH production since OH which is not stable cannot be stored in cylinders (Faloona et al., 2004), and (3) since the fluorescence is a function of the laser power, the last part of the LIF system is the photodiode that monitors the laser power [see relation (3)]. In Fig. I.6.6 a picture of L'Aquila LIF system is shown and more info about this system is reported in Dari-Salisburgo et al. (2009). The laser is the main part of a LIF system and its emission wavelength has to be selected matching the absorption spectrum of the molecules that must to be detected. In Table I.6.2, the wavelength of the laser used

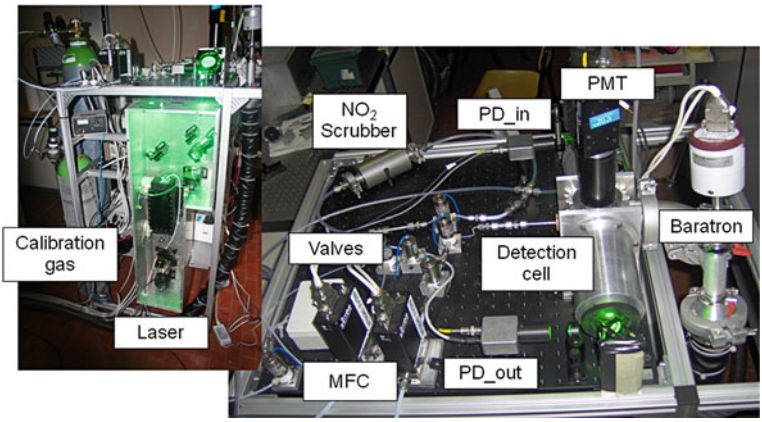

Fig. I.6.6 Pictures of L'Aquila University LIF system for NO_2 measurements

Table I.6.2 Wavelength of lasers used to detect tropospheric species with LIF systems

Species	Laser wavelength (nm)
OH	308
HO_2	308
NO_2	408, 440, 532, 585, 565, 640
NO	226
NO_3	662
N_2O_5	662

for the detection for each species is reported. For NO_2 there are different possible wavelengths, so a variety of lasers can be utilized. It is also worth nothing that HO_2 is not directly detected at 308 nm, but it is indirectly detected measuring the OH produced after the conversion of HO_2 into OH by reaction with NO.

Looking at the expression of the detection limit [Eq. (7)], it is evident that reducing the background signal implies the detection limit is lower so that the instrument is able to detect smaller concentrations. This can be achieved using a time gating, a technique in which the detector (usually a photomultiplier in the LIF) is activated to collect photons only for a period of time. To apply this method a pulsed laser and a low pressure inside the detection cell are required. Pulsed laser is demanded because to reduce the background, the gate will be opened just after the laser pulse since the non-fluorescence signals like Rayleigh and Mie scattering have a time duration similar to the laser pulse. For each pulse (laser pulse in this case is also used as trigger for the gate) the detector is activated until the end of the fluorescence; for example, using a laser at 10 kHz (that gives 10,000 pulses/s) the gate will be opened and closed 10,000 times per second. Opening the gate after the laser pulse excludes most of the non-fluorescence signals and since the fluorescence has a longer time duration it can be detected. The pressure inside the detection cell is kept low (around few

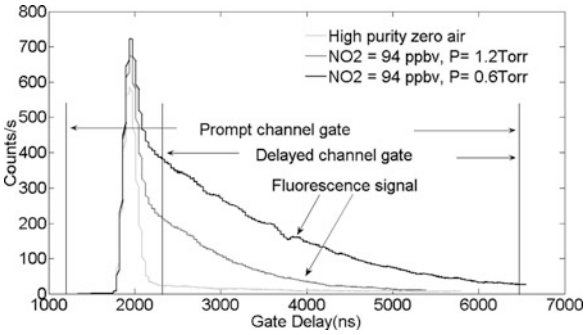

Fig. I.6.7 LIF signals with zero air and with 94 ppbv of NO_2. The fluorescence signal when NO_2 is injected in the detection cell is reported for two different cell pressures. The period in which the gate is open and the photomultiplier detects the fluorescence is signed

Torr) to increase the time duration of the fluorescence; a temporal sketch of the time gating is showed in Fig. I.6.7. The disadvantages of the time gating are the potential surface loss on the pressure-reducing orifice of the inlet (0.3–3 mm of diameter) and the pumps used to reduce pressure that usually are heavy and consume power. Another technique used to reduce the background is to tune the laser emission line on the peak of the absorption cross section of the species to be detected and after the measurements to tune it on one side of the absorption peak to measure the background (Fig. I.6.8). These methods require complicated and expensive lasers with tunable emission wavelengths and a system that controls the tuning.

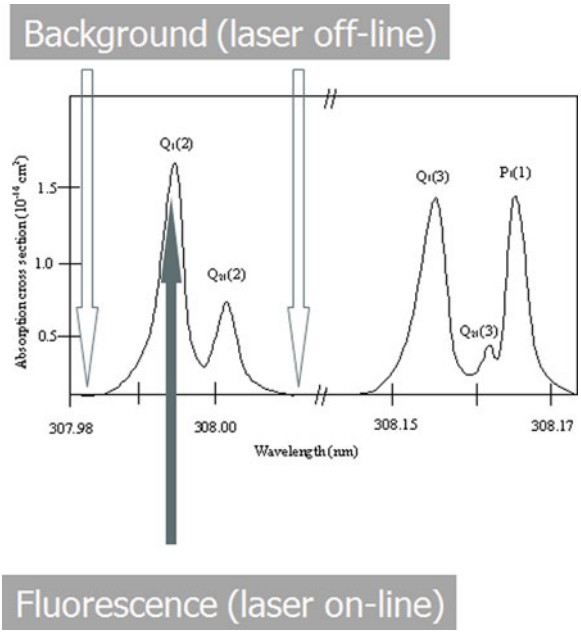

Fig. I.6.8 OH cross section. The *arrows* indicate the parts of the OH spectrum used for the fluorescence detection (laser online) and for the background measurements (laser off-line)

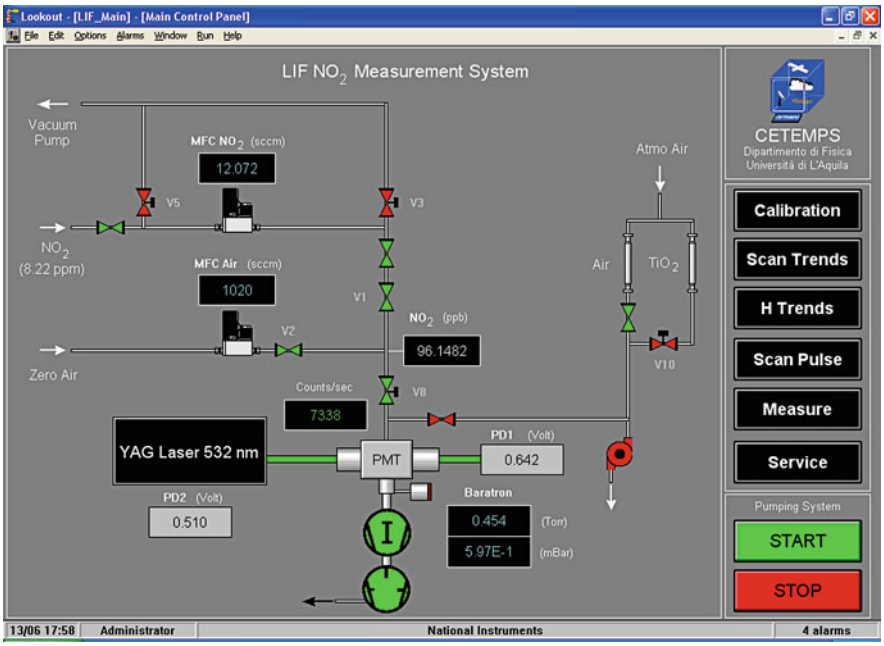

Fig. I.6.9 Picture of the Lookout program developed at the University of L'Aquila to control the NO_2 LIF system

Instruments for atmospheric composition measurements must be able to make continuous observations (24 h a day), sometimes in remote sites or on aircrafts, in some cases, it is not allowed due to the presence of the operator. A completely autonomous instrument must be projected to be used in all the circumstances. In Fig. I.6.9 there is the picture of the control software developed at the University of L'Aquila using LabVIEW and Lookout of National Instrument. This software controls the LIF instrument in all its parts, makes automatic diagnostics, makes automatic calibrations, and allows continuous measurements for several days without the presence of an operator.

In the last decades LIF systems have been used in several ground-base and aircraft campaigns around the world; a detailed list of the campaigns carried out until 2006 can be found in Heard (2006).

3 Differential Optical Absorption Spectroscopy (DOAS)

The absorption of radiation by molecules crossed by lights is described by the Beer–Lambert law:

$$I(\lambda) = I_0(\lambda)\, e^{-L\sigma(\lambda)n}, \tag{8}$$

where $I(\lambda)$ is the intensity of the radiation measured after the absorption, $I_0(\lambda)$ the initial intensity before the absorption, L the pathlength (in cm) where the molecules are crossed by the radiation, $\sigma(\lambda)$ the absorption cross section (in cm^2 $molecules^{-1}$), and n the number density (in molecules cm^{-3}). DOAS technique is mainly used to detect the concentrations of atmospheric molecules and from the expression (8) we have:

$$n = \frac{\log\left(\frac{I_0(\lambda)}{I(\lambda)}\right)}{L \cdot \sigma\ (\lambda)}. \tag{9}$$

The Beer–Lambert law can be used with the simple expression (8) only when one molecule is present and the only interaction between radiation and molecules is absorption. This is not the case of the atmosphere because there are several molecules simultaneously present and also the Rayleigh and Mie scattering that we have to take into account. For the atmosphere, Eq. (8) becomes

$$I(\lambda) = I_0(\lambda) e^{-L\left(\sum_i \sigma_i(\lambda) n_i + \varepsilon^R(\lambda) + \varepsilon^R(\lambda)\right)}, \tag{10}$$

where $\varepsilon^R(\lambda)$ is the Rayleigh extinction coefficient and is equal to $\sigma^R(\lambda) \cdot n_{\text{air}}$ (the first is the cross section of the Rayleigh scattering and the second the concentration of the air) and $\varepsilon^M(\lambda)$ is the Mie extinction coefficient and is equal to $\sigma^M(\lambda) \cdot n_{\text{air}}$ (where the first is the cross section of the Mie scattering). In this case there is the summation over $\sigma_i(\lambda)$ to account for the absorption of all the molecules. The Beer–Lambert law in the form of Eq. (10) is useless to find out the concentration of the molecules, but when Rayleigh and Mie extinctions change slowly as functions of the wavelength the absorption cross section can be written as

$$\sigma_i(\lambda) = \sigma_i'(\lambda) + \sigma_i^S(\lambda), \tag{11}$$

where $\sigma_i'(\lambda)$ is the part of the absorption cross section that changes quickly with wavelength, whereas $\sigma_i^S(\lambda)$ is the part of the absorption cross section that changes slowly with wavelength. Under these hypotheses the relation (10) can be rewritten as

$$I(\lambda) = I_0(\lambda) e^{-L\left(\sum_i \sigma_i'(\lambda) n_i\right)} e^{-L\left(\sum_i \sigma_i^S(\lambda) n_i + \varepsilon^R(\lambda) + \varepsilon^R(\lambda)\right)}, \tag{12}$$

where the first exponential rapidly changes, whereas the second is the slow part of the Beer–Lambert law. Now Eq. (12) can be rewritten in the simple Beer–Lambert form as follows:

$$I(\lambda) = I_0'(\lambda) e^{-L\left(\sum_i \sigma_i'(\lambda) n_i\right)}, \tag{13}$$

where

$$I_0'(\lambda) = I_0(\lambda) e^{-L\left(\sum_i \sigma_i^S(\lambda) n_i + \varepsilon^R(\lambda) + \varepsilon^R(\lambda)\right)}. \quad (14)$$

Equation (14), since it is the part of the cross section that changes slowly multiplied by the emission radiation, is usually calculated with polynomial fit, filter techniques, or FFT (fast Fourier transform) for DOAS using the sunlight or moonlight as source (passive DOAS). It can also be measured in case of active DOAS using laser, lamps, or LED as source.

In Fig. I.6.10 a sketch of a DOAS system is shown; the main parts are: (1) the source that can be a laser when the spectrum of the absorption species is very narrow (for example, OH that absorbs around 308 nm and the spectrum is about 2 pm wide) or a lamp or LED when the absorption spectrum is few nanometers, (2) the spectrometer that has to analyze the absorption spectrum as function of the wavelength to find the fingerprint of the molecule spectrum, (3) the detector that is usually a CCD (charge coupled device), (4) a telescope to collect the absorbed radiation and to collimate light when lamps or LEDs are used as source, and (5) the retroreflector that is usually an array of reflecting prisms fixed some kilometers away from the source and the spectrometer to send back the light after the absorption during the travel in the open atmosphere. In Fig. I.6.11 few picture of the parts of the DOAS system developed at the University of L'Aquila are reported; more details of it can be found in the Di Carlo et al. (2009). The spectral resolution of the spectrometer depends on the source: When a laser is used a very high-resolution spectrometer is needed (less than 0.1 pm) and, in this case, could be helpful for a premonochromator (premono, in Fig. I.6.10) to select the order of the spectrometer and to reduce the unwanted light at wavelengths away from the absorption spectrum of the species under observations. When a broadband source (lamp or LED) is used a small spectrometer, with resolution between 1 and 0.1 nm, is enough. The retroreflector uses

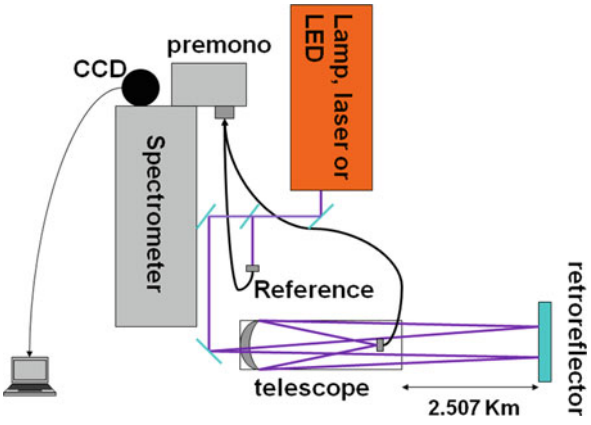

Fig. I.6.10 Schematic view of a DOAS instrument

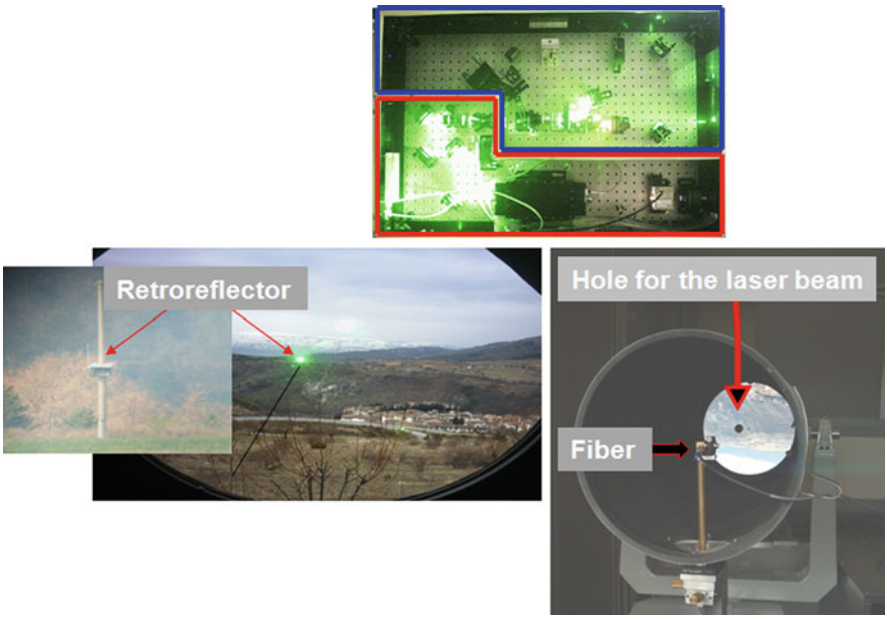

Fig. I.6.11 Pictures of the main parts of L'Aquila University DOAS

an array of prisms instead of a big mirror because it does not need alignment and the configuration with source and spectrometer in one laboratory and the retroreflector at a certain distance allows to double the light path.

Most of the species like ozone, ClO, SO_2, benzene, and toluene absorb in the UV (between 250 and 350 nm), nitrous acid (HONO) and bromine monoxide (BrO) absorb between 300 and 380 nm, NO_2 absorbs between 300 and 500 nm, whereas nitrate radical (NO_3) from 600 to 700 nm. The detection limit of DOAS systems is usually higher than LIF systems: For example, for NO_2 and NO it is 50 pptv, for OH it is 0.06 pptv, for NO_3 it is 0.4 pptv, and for ClO it is 5 pptv. A review of DOAS system can be found in Plane and Sainz-Lopez (2006) or in Platt (1994).

4 Conclusions

LIF and DOAS are optical techniques widely used to observe the atmospheric composition. Usually LIF instruments are smaller and lighter than DOAS and can be used on aircraft platforms. LIF systems allow fast observations so it can also be used for flux measurements and usually data analysis is easier compared to analysis of DOAS data. Looking at the detection limit and selectivity LIF and DOAS are comparable. The big advantage of DOAS systems is that this technique does not need calibration while LIF instruments do. Even if DOAS instruments are usually bigger than LIF, some of them have also been installed on aircraft platforms.

The introduction of LEDs helps to reduce the DOAS instruments size and makes its operation easier compared with those using lamps; the diode laser represents a good opportunity to make cheaper and more compact LIF systems.

Acknowledgments I like to thank G. Visconti, A. D'Altorio, C. Dari-Salisburgo, E. Aruffo, F. Giammaria, F. Del Grande and all the people who helped to develop the LIF and DOAS systems of L'Aquila University.

References

Alicke B, Hebestreit K, Stutz J, Platt U (1999) Iodine oxide in the marine boundary layer. Nature 397:572–573.

Anderson JG, Toohey DW, Brune WH (1991) free-radicals within the Antarctic vortex – the role of CFCS in Antarctic ozone loss. Science 251:39–46.

Bertram TH, Perring AE, Wooldridge PJ, Crounse JD, Kwan AJ, Wennberg PO, Scheuer E, Dibb J, Sachse G, Vay SA, Crawford JH, McNaughton CS, Clarke A, Pickering KE, Fuelberg H, Huey G, Blake DR, Singh HB, Hall SR, Shetter RE, Fried A, Heikes BG, Cohen RC (2007) Direct measurements of the convective recycling of the upper troposphere. Science 315:816–820.

Dari-Salisburgo C, Di Carlo P, Giammaria F, Kajii Y, D'Altorio A (2009) Laser induced fluorescence instrument for NO_2 measurements: observations at a central Italy background site. Atmos Environ 43:970–977.

Di Carlo P, Barone M, D'Altorio A, Dari-Salisburgo C, Pietropaolo E (2009) High-resolution spectrometer for atmospheric studies. J Atmos Solar-Terrestrial Phys 71:1383–1388.

Faloona IC, Tan D, Lesher RL, Hazen NL, Frame CL, Simpas JB, Harder H, Martinez M, Di Carlo P, Ren X, Brune WH (2004) A laser induced fluorescence instrument for detecting tropospheric OH and HO_2: characteristics and calibration. J Atmos Chem 47(2):139–167.

Farman JC, Gardiner BG, Shanklin JD (1985) Large losses of total ozone in Antarctica reveal seasonal Cl0x/NOx interaction. Nature 315:207–210.

Heard DE (2006) Analytical techniques for atmospheric measurements. Blackwell. Oxford, (ISBN 1405123575).

Plane JMC, Saiz-Lopez A (2006) UV-Visible differential optical absorption spectroscopy (DOAS). In: Heard D (ed) Analytical techniques for atmospheric measurements. Blackwell. pp 147–188.

Platt U. (1994) Differential optical absorption spectroscopy (DOAS). In: Sigrist MW (ed) Air monitoring by spectroscopy techniques. Wiley, London, pp 27–83.

Seinfeld JH, Pandis SN (2006) Atmospheric chemistry and physics: from air pollution to climate change. Wiley. New York, NY.

Wood EC, Cohen RC (2006) Fluorescence methods. In: Heard D (ed) Analytical techniques for atmospheric measurements. Blackwell. Oxford. pp 189–228.

Chapter I.7
Concepts for Integration of Measurements and Methods

Domenico Cimini

1 Introduction

Ground-based remote sensing observations of atmospheric variables are collected in many sites worldwide for several applications, ranging from weather monitoring, meteorology, climatology, aviation support, etc.

Since radiation interacts with the atmosphere depending upon its wavelength, spectrally diverse measurements contain different information about the atmospheric state and composition. Each instrument is sensitive to a limited number of atmospheric variables and thus provides information about one or a few aspects of the atmosphere, with the associated uncertainty and limitations. When observations from different instruments are available at the same site and time, a broader view of the atmospheric process can be achieved. Thus, typically an atmospheric observatory operates several different instruments in a single location, simultaneously and continuously. Some instruments use technology that is mature and well understood, while other instruments have been recently developed as research units. A major focus of current remote sensing research is to evaluate the capability of the existing instruments to remotely derive meteorological quantities using sensor synergy. A synergetic approach, relying on the complementary characteristics of different instrumentations, is sometimes able to either improve retrieval accuracy, overcome limitations, or provide additional products with respect to what is possible with single instruments. This contribution reviews the motivations, presents few examples, and discusses present challenges of ground-based remote sensing instrument integration.

D. Cimini (✉)
IMAA/CNR, C.da S. Loja, Tito Scalo (PZ), Italy
e-mail: cimini@imaa.cnr.it

D. Cimini et al. (eds.), *Integrated Ground-Based Observing Systems*,
DOI 10.1007/978-3-642-12968-1_7,

2 Motivations and Challenges

In the last four decades, large efforts have been undertaken to develop ground-based instruments for continuously monitoring the atmosphere. Ground-based remote sensing instruments based on different physical principles and working at different wavelengths of the electromagnetic (EM) spectrum are diversely sensitive to the different atmospheric properties. Thus, instrumentations are able to observe diverse aspects of the atmosphere, such as composition, motion, and thermodynamical properties (temperature, humidity, etc.).

For example, as described in the previous chapters and summarized in Table I.7.1, microwave and infrared radiometers are sensitive to atmospheric temperature, humidity, cloud content, and microphysics; elastic, Raman, and Doppler lidars are sensitive to atmospheric aerosols, temperature, and wind; weather and cloud radars are sensitive to precipitating and non-precipitating hydrometeors; wind profiler radars and sodars are sensitive to wind direction and speed. Each of these atmospheric parameters can be retrieved from ground-based observations with some

Table I.7.1 A list of atmospheric variables and the associated instrumentation which is able to provide useful information (extended from Ackerman and Stokes, 2003)

Atmospheric variables	Instrument type
Surface radiation budget	Broad band solar and IR radiometers
	Shadow-band radiometer (narrow spectral bands)
	Spectrometer (400–3,000 nm)
	Infrared interferometer (3–20 μm)
Atmospheric temperature profile	Microwave radiometer
	Infrared interferometer (3–20 μm)
	Raman lidar
Water vapor profile	Microwave radiometer (24–31 GHz)
	Infrared interferometer (3–20 μm)
	Raman lidar
Aerosol profile	Elastic lidar
Particle optical depth	Narrow-band sun photometer
	Shadow-band radiometer
Cloud presence and location	Ceilometer
	Lidar
	Millimeter-wave radar
Cloud properties	Lidar
	Millimeter-wave radar
	Radiometers (solar, IR, microwave)
Wind profile	Wind profiler radar
	Sodar
	Elastic lidar
Composition (trace gases)	Multichannel narrow-band radiometer
	Infrared interferometer
Precipitation	Weather radar
	Microwave radiometer
	Disdrometer

degree of accuracy and certain advantages and limitations. However, instead of a single instrument, quite commonly a variety of ground-based instrumentation is deployed at the same site in order to cover more than one aspect of the atmosphere at the same time. While these instruments are typically used in standalone mode, their combination offers new possibilities to overcome intrinsic limitations. For example, a single instrument/technique may present limitations related to short range of application, poor spatial resolution, poor accuracy, ambiguous solution, simultaneous sensitivity to more than one parameter, or a combination of the above. In other words, each single instrument provides information about one or more parameters with the accuracy and the limitations associated with the used technology and technique, but sometimes part of these limitations may be overrun by the synergetic use of the other independent instrumentation operating at the same site. In addition, a new set of products may be generated combining complementary information from independent instruments. In a problem-solving framework, a synergetic approach would put further constraints to the solution of the atmospheric state's estimate.

Thus, since theoretical and technology research is dedicated to reducing the limitations and to increasing the performances of remote sensing, it is of uttermost importance to investigate the actual information content that can be gained from the optimal combination of existing instrumentation. For this purpose, a significant effort is dedicated to the establishment of atmospheric observatories equipped with state-of-the-art technology, the so-called anchor stations, where new methods are developed and tested for retrieving the most complete picture of the atmospheric profiles and their errors (Engelbart et al., 2009). One of the most important European atmospheric anchor observatories, the Cabauw Experimental Site for Atmospheric Research (CESAR) in the Netherlands, is pictured in Fig. I.7.1.

Fig. I.7.1 A picture of the CESAR observatory in Cabauw, the Netherlands. CESAR is one of the European anchor station for atmospheric in situ and atmospheric remote sensing (picture courtesy of Herman Russchenberg, Delft University of Technology)

The concept of an integrated approach relies on finding observations that can be used in synergy for either estimating a parameter with better accuracy or getting information about new parameters that can be derived from the ones obtained by the single instruments. Therefore, the characteristics of the instrumentation taking part in an integrated approach should be

– providing independent observations (different instruments)
– providing complementary observations (different spectral regions, viewing angles, active/passive methods)
– measuring different aspects of the atmosphere
– sensing a somewhat common observation volume

However, integrating measurements and methods involves more than one challenge. First of all, an integrated approach requires the development of a multi-input algorithm producing results that are physically consistent with all the observations. This in turn requires a well-understood theory or alternatively the a priori knowledge of a statistically significant data set. Moreover, with regard to the operational implementation there is always a concern for implementing and maintaining algorithms taking input data from independent instrumentation, since it is well known that more data streams bring inevitably more troubles. Finally, it must be demonstrated that the benefits coming from the integrated approach are significant to justify the extra effort and costs involved in the development and maintenance of instruments and methods.

3 Examples from the Field

Several examples of integrated approaches using different ground-based instruments and observations can be found in the open literature from the last decade (Han et al., 1997; Stankov et al., 1996; Mace et al., 2001; Löhnert et al., 2004). In those and other papers both physical and statistical methods are used to retrieve atmospheric parameters from ground-based observations. In case the physical process of the radiation–atmosphere interaction is properly understood, retrieval algorithms can be made physically consistent. This approach is used when the theory is well understood and the relationships between the variables and the observations are analytically solvable and easy to invert and implement. Conversely, if the relationships between the variables and the observations are not analytically solvable and/or difficult to invert and implement, statistical methods are typically used. Thus, this approach is often used when the retrieved parameter is linked to the observations by complex relationships with a large number of degrees of freedom.

In the following, few examples of successful sensor synergy are briefly described; the interested reader may refer to the original papers for further details. Of course, this list does not mean to be complete and many other techniques are available in the open literature.

3.1 Synergy of Active and Passive Observations for Increasing Water Vapor Vertical Resolution

Monitoring of humidity profiles in the lower troposphere has been one of the main goals of recent meteorological research due to its importance for atmospheric dynamics and microphysics. An appealing application to the retrieval of whole-weather high-resolution atmospheric humidity profiles is the synergetic use of ground-based instruments only, such as either a combination of radar wind profilers and global position system (GPS) receivers or either a combination of radar wind profilers and microwave radiometers (Stankov et al., 1996; Gossard et al., 1999; Furumoto et al. 2003; Bianco et al., 2005). In particular, the last approach has significant potential due to the profiling capability of both sensors and the possibility to estimate the atmospheric state in terms of wind, humidity, and temperature. Thus, algorithms to compute atmospheric humidity high-resolution profiles by synergetic use of microwave radiometer profiler (MWRP) and wind profiler radar (WPR) were developed in the last decade. The technique described in Bianco et al. (2005) is based on the processing of WPR data for estimating the potential refractivity gradient profiles and on the combination with MWRP estimates of potential temperature profiles in order to fully retrieve humidity gradient profiles. To retrieve high-resolution humidity profiles in this combined approach, the zeroth, first, and second moments, computed by a fuzzy logic algorithm, are employed to compute the structure parameter of potential refractivity (C_ϕ^2), the horizontal wind (V_h), and the structure parameter of vertical velocity (C_w^2). The quantities C_ϕ^2, V_h, and C_w^2 can then be properly used together to retrieve the potential refractivity gradient profiles ($d\phi/dz$). On the other hand, microwave radiometer data can be used to estimate the potential temperature gradient profiles ($d\theta/dz$). As a final step of the combined retrieval technique, profiles of $d\phi/dz$, derived from WPR, and of $d\theta/dz$, derived from MWRP, are sufficient to fully estimate humidity gradient profiles. The advantage of such a synergetic humidity retrieval technique is to increase the vertical resolution of MWRP, without losing the high accuracy it can provide for integrated values, and to be completely independent from simultaneous radiosonde observations.

The basic principles of the theory used for the retrieval of vertical humidity profiles with the combined use of $d\phi/dz$ from WPR and $d\theta/dz$ from MWRP are summarized below. Radar-obtained values of $d\phi/dz$ are derived combining V_h, C_ϕ^2, and C_w^2, which are respectively related to the first, zeroth, and second moments calculation of the radar-derived spectra acquisitions (Stankov et al., 2003). Gossard et al. (1982, 1998) found that for homogeneous isotropic turbulence in a horizontally homogeneous medium with vertical gradients of mean properties, the vertical gradient of potential refractivity is

$$\left(\frac{d\phi}{dz}\right)^2 \approx \left(\frac{L_w}{L_\phi}\right)^{4/3} \left(\frac{dV_\mathrm{h}}{dz}\right)^2 \left(\frac{C_\phi}{C_w}\right)^2, \tag{1}$$

where L_w and L_ϕ are the outer length scales for potential refractive index and shear defined in Gossard et al. (1982).

Considering the given definition of the potential temperature θ, we can estimate this quantity and its vertical gradient by using the temperature profile as retrieved by the MWRP together with the measurements of surface pressure and a prediction of the atmospheric scale height:

$$\frac{dQ}{dz} = (b_0)^{-1}\left[\frac{d\phi}{dz} + a_0\frac{d\theta}{dz}\right], \tag{2}$$

which gives the vertical profile of humidity gradient as a function of vertical profiles of potential refractivity and potential temperature gradients. By integrating the vertical profile of *dQ/dz* we can, therefore, compute the vertical profile of *Q*.

Figure I.7.2 presents results relative to a case study (Bianco et al. 2005). Note that the humidity profile is scaled in order to match the MWRP water vapor content, integrated up to the maximum height reached by the WPR measurement. This is an

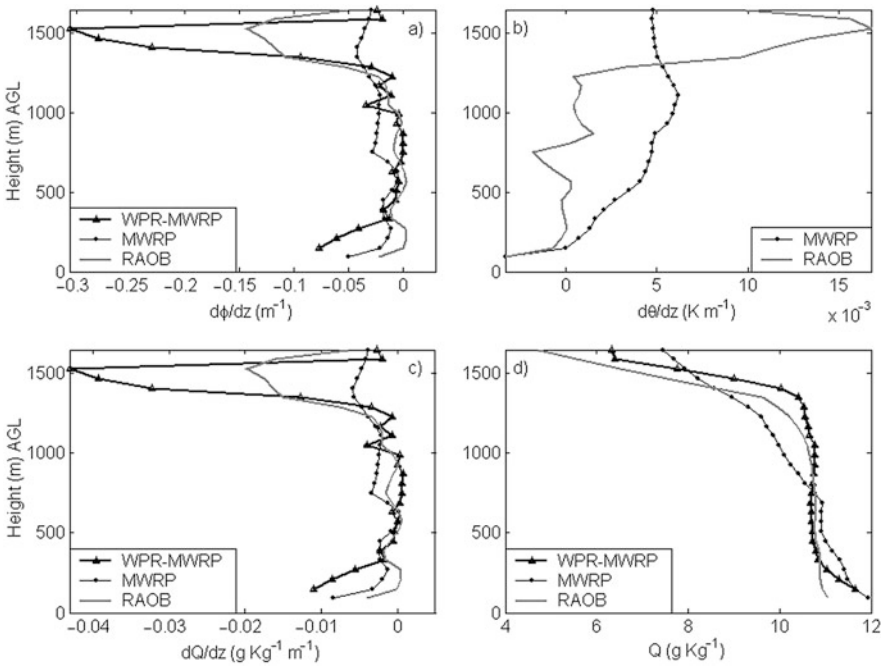

Fig. I.7.2 **a**) Hourly vertical profiles for *dϕ/dz* as measured by radiosonde (*solid grey line*), estimated by MWRP (*dotted line*), and computed with the combined technique (*solid black line with triangles*); **b**) *dθ/dz* as measured by radiosonde (*solid grey line*) and estimated by MWRP (*dotted line*); **c**) hourly vertical profiles for *dQ/dz* as measured by radiosonde (*solid grey line*), estimated by MWRP (*dotted line*), and computed with the combined technique (*solid black line with triangles* at measurement heights); **d**) retrieved humidity vertical profiles (*Q*) obtained from the integration of *dQ/dz* (after Bianco et al., 2005)

important step because it guarantees that the original MWRP accuracy for integrated water vapor content is preserved in the product of the combined technique.

3.2 Integrated Approach for the Retrieval of Physically Consistent Profiles

Continuous and accurate profiles of temperature, humidity, and hydrometeor content at high temporal and spatial resolution are extremely important for evaluating and improving model forecasts, parameterization schemes, and satellite retrieval algorithms.

Integrated methods for deriving physically consistent profiles of temperature, humidity, and cloud liquid water content were developed in the last years (Han et al., 1997; Stankov et al., 1996; Löhnert et al., 2004). The method described in Löhnert et al. (2004) combines a ground-based multichannel microwave radiometer (MWR), a cloud radar, a lidar ceilometer, the nearest operational radiosonde measurement, and ground-level measurements of standard meteorological properties with statistics derived from the results of a microphysical cloud model. The described method, called the integrated profiling technique (IPT), is general and can be extended to include other instruments and observations. All measurements are integrated within the framework of optimal estimation to guarantee a retrieved profile with maximum information content. The IPT uses the so-called optimal estimation equations directly derived from Bayes's theorem considering a linear forward model and Gaussian-distributed variables. Given the set of measurements, the optimal estimation inversion procedure finds a solution that satisfies the measurements after the forward model has been applied to the retrieved parameters. In the context of IPT, the microwave radiative transfer equation and a relationship between the radar reflectivity Z and the liquid water content (LWC) profiles are regarded as the valid forward model.

A prerequisite of the IPT is an accurate knowledge of the error characteristics of each measurement and of the forward model by means of covariance matrices. Measurements with small errors will have a higher weight in the solution than measurements with large errors; the same applies for the accuracy level of the description of the relationship between the observations and the atmospheric parameters.

The forward model F performs the radiative transfer calculation [Eq. (30) in Chap. I.1] where $\mathbf{K}$ is the Jacobi matrix, and $\mathbf{K}=dF/d\mathbf{x}$. The parameter vector $\mathbf{x}$ consists of the profiles of T, q, and LWC. The measurement vector $\mathbf{y}$ consists of the MWR brightness temperatures (Tb), the radar reflectivity profile at detected cloud levels, and the ground-level measurements of temperature and humidity. Following Rodgers (2000), the optimal estimation equation for this problem is written as

$$\mathbf{x}_{i+1} = \mathbf{x}_i + \left(\mathbf{B}^{-1} + \mathbf{K}_i^T \mathbf{R}^{-1} \mathbf{K}_i\right)^{-1} \left[\mathbf{K}_i^T \mathbf{R}^{-1} (\mathrm{y} - F(\mathbf{x}_i)) - \mathbf{B}^{-1} (\mathbf{x}_i - \mathbf{x}_\mathrm{b})\right], \quad (3)$$

where i represents the iteration step, $\mathbf{R}$ the combined measurement and forward model error covariance matrix, and $\mathbf{B}$ the a priori covariance matrix.

Atmospheric temperature and humidity are assumed as Gaussian-distributed parameters, while for LWC the value of 10 $\log_{10}$(LWC) is retrieved, which more closely resembles a Gaussian-distributed parameter than LWC itself. Other assumptions are that the random errors prevail in the Tb and the errors of Z in the units of dBZ are also Gaussian distributed.

Equation (3) is iterated i_{op} times in i ($\mathbf{K}_i$ is recalculated after each iteration step) until a minimum of a cost function is found, yielding the solution $\mathbf{x}_{\mathrm{op}}$. Following Rodgers (2000), the iteration stops upon reaching convergence by considering a quadratic cost function between $F(\mathbf{x}_i)$ and $F(\mathbf{x}_{i11})$:

$$\left[F(\mathbf{x}_{i+1}) - F(\mathbf{x}_i)\right]^{\mathrm{T}} \mathbf{S}^{-1} \left[F(\mathbf{x}_{i+1}) - F(\mathbf{x}_i)\right] \ll n(\mathrm{obs}), \tag{4}$$

where $\mathbf{S}$ is the covariance matrix between the measurement and $F(\mathbf{x}_{\mathrm{op}})$ and n(obs) indicate the number of observations (i.e., the dimension of $\mathbf{y}$). The solution $\mathbf{x}_{\mathrm{op}}$ must be interpreted as the most probable solution of a Gaussian-distributed probability density function, whose covariance can be written as

$$\mathbf{S}_{\mathrm{op}} = \left(\mathbf{K}_{i_{\mathrm{op}}}^{\mathrm{T}} \mathbf{R}^{-1} \mathbf{K}_{i_{\mathrm{op}}} + \mathbf{B}^{-1}\right)^{-1}. \tag{5}$$

The diagonal elements of this matrix give an estimate of the mean quadratic error of $\mathbf{x}_{\mathrm{op}}$. The physical consistency of the retrieval products is ensured by the fact that the retrieved profile will reproduce the measured radiation within the measurement accuracy.

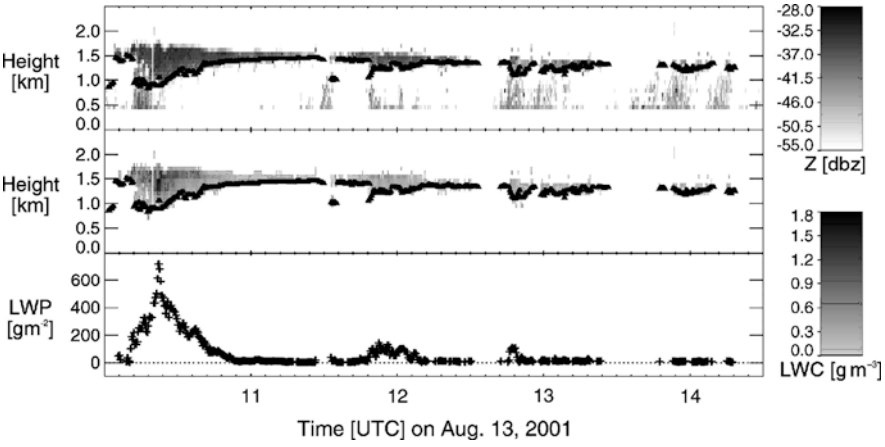

Fig. I.7.3 Time series of (*top*) radar reflectivity, (*center*) IPT-LWC on radar resolution, and (*bottom*) vertically integrated LWC (LWP) at Cabauw, the Netherlands. The *black triangles* in the *upper two panels* indicate the lidar ceilometer cloud base (after Löhnert et al., 2004)

The developed IPT was applied to both synthetic and experimental data. It was shown that the profiles obtained with the IPT are significantly more accurate than those obtained with other more common methods. Error analysis indicates root-mean-square (rms) uncertainties of less than 1 K in temperature and less than 1 g/m^3 in humidity, where the relative error in liquid water content ranges from 15 to 25% (considering liquid phase non-precipitating clouds only). Figure I.7.3 presents time series of radar reflectivity and LWC retrievals over CESAR.

The formulation of IPT allows the incorporation of multiple measurements into the retrieval. Thus, the IPT represents a major step toward the synergy of arbitrary measurements and their integration to form a product that increasingly resembles reality. The natural evolution is the development of an "all encompassing" algorithm that can take into account all instruments operating momentarily at a specific station and deliver the best estimates of profiles of temperature, humidity, and cloud hydrometeors during all weather conditions.

3.3 Combination of Active and Passive Measurements for the Investigation of Cirrus Clouds

Cirrus clouds play an important role in increasing the greenhouse capacity of Earth's climate system. In fact, these high cloud layers are composed of ice crystals and typically reflect less solar radiation than do water clouds, but absorb significant amounts of thermal infrared radiation emitted by the ground and the lower atmosphere. In spite their importance, cirrus clouds are notoriously difficult to model, because the processes that create them are complex and not completely understood. Direct observation from aircraft is problematic because their altitude and laboratory experiments cannot adequately capture the complexity of cirrus cloud formation in the free atmosphere. Conversely, ground-based remotely sensing techniques offer the opportunity to greatly increase the understanding of cirrus clouds microphysics (Ackerman and Stokes, 2003).

As an example, techniques combining millimeter-wave cloud radar (MMCR) observations with thermal infrared interferometry have been developed by the US Department of Energy's Atmospheric Radiation Measurement (ARM) program for the study of cirrus clouds; results are used to compile cirrus cloud statistical distribution and empirical relationships for the parameterization to be used in climate models (Mace et al., 2001).

The method takes advantage of the different instrumental sensitivities to determine the integrated column ice mass and the mean ice particle size. The radar directly measures the height and extent of cirrus clouds, and the magnitude of the backscattered radar signal depends on the total ice mass and the distribution of particle sizes. The downward radiance measured by the infrared interferometer is a combination of thermal emission by atmospheric water vapor and by the cloud ice mass. From the radar and the infrared data, together with balloon measurements of atmospheric temperature and moisture, the developed method deduces the emission from the clouds alone (Mace et al., 1998).

The radar measures the backscatter cross section per unit volume and this cross section can be expressed in terms of the radar reflectivity factor

$$Z = \int_0^\infty N(D) \cdot D^6 \cdot dD. \tag{6}$$

Assuming that the layer-mean particle distribution can be adequately described by a modified gamma function in terms of the modal diameter D_x, the number of particles per unit volume per unit length N_x, and the order of the distribution α:

$$N(D) = N_x \exp(\alpha) \left(\frac{D}{D_x}\right) \exp\left[-\frac{D\alpha}{D_x}\right], \tag{7}$$

then the variables of interest, namely the integrated column ice mass and the mean ice particle size, can be derived as

$$\mathrm{IWP} = \rho_i \frac{\pi}{6} \bar{Z} \frac{\alpha^3 (3+\alpha)!}{D_x^3 (6+\alpha)!} \Delta h \tag{8}$$

$$r_\mathrm{e} = \frac{D_x (3+\alpha)!}{2(2+\alpha)!} \alpha^\alpha. \tag{9}$$

The two unknown parameters of the modified gamma distribution can be determined from the observed downwelling radiance and the radar reflectivity using an expression of the cloud layer emittance. Using the observed radar reflectivity and the layer emittance determined from the downwelling radiance the problem is solved numerically. The ice water path and particle size are finally calculated using Eqs. (8) and (9).

3.4 Observations Synergy for Improving the Understanding of Radiative Transfer

Longwave and solar radiative transfer are the prime physical mechanisms that drive the circulation and temperature structure of the atmosphere, and radiative processes play a central role in most climate change mechanisms.

Parameterization is required to account for the radiant energy transport in global climate models (GCM), as the full treatment of the radiative transfer is prohibitively computationally expensive. Detailed radiative transfer models that incorporate all of the known physics, such as line-by-line models, are typically used to construct significantly faster radiation models to calculate radiative fluxes in GCMs. The line-by-line model used to build these faster models must be accurate, as even 1% changes in radiation are significant for climate. In addition, improvements in the understanding of the spectral radiative transfer are important for computing

the atmospheric cooling rate profiles and for the enhancement of remote sensing applications.

In this perspective, a suite of independent ground-based observations is valuable for investigating the radiative properties of the atmosphere using radiation closure experiments. This kind of approach typically leads to reducing the uncertainties on a radiative-relevant parameter or to solve the ambiguity that may arise from observation taken with a reduced set of instruments.

Research funded by the ARM program has led to significant improvements in high spectral resolution radiative transfer modeling over the last decade. The ARM program supported a variety of projects, including laboratory spectroscopic studies and field experiments, such as the pilot radiation observation experiment (PROBE; Westwater et al. 1999).

At the ARM Cloud and Radiation Testbed sites, quality measurement experiments (QME) that compare observations and state-of-the-art calculations for the improvement of radiative transfer calculations have been ongoing since more than a decade. The QMEs have been used to

(1) validate and improve the absorption models and spectral line parameters used in line-by-line radiative transfer models
(2) assess the ability to define the atmospheric state used in the model calculation
(3) assess the quality of the radiance observations that serve as ground truth for the model

QME can be used to investigate the absorption due to a variety of trace gases; in particular, Turner et al. (2004) focused on water vapor absorption because of the large impact this absorption has on the radiative flux calculations. Turner et al. (2004) used data from the ARM Southern Great Plains site in Oklahoma, hosting a wide variety of ground-based instrumentation designed to meet the goal of collecting a long-term data set that can be used to improve climate models. Of particular importance of this application are the atmospheric emitted radiance interferometer (AERI), radiosondes, microwave radiometer (MWR), Raman lidar, and micropulse lidar (MPL).

In Turner et al. (2004), the measures taken into the QME for reducing and accounting the uncertainties related to the instruments (calibration, accuracy) and the atmospheric state (water vapor content, cirrus cloud presence) are discussed. Improvements made to the various instruments and the data streams resulting from the original analysis allowed to generate a new QME that addressed most of the issues that limited the original data set. For example, new operational calibration routines were developed for the MWR, radiosonde humidity were scaled based on MWR IWV, and Raman lidar depolarization ratio was used to screen cases corrupted by thin cirrus.

A trustworthy data set of observations from all the above instruments has been carefully constructed and used to quantitatively evaluate a state-of-the-art line-by-line radiative transfer model (LBLRTM) in order to reduce its modeling uncertainties.

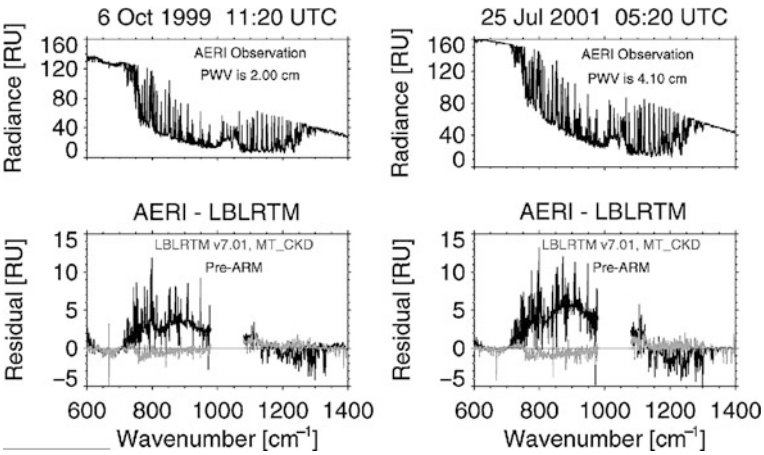

Fig. I.7.4 (*upper left*) Observed AERI spectra for a midlevel (2.0 cm) and (*upper right*) high (4.1 cm) IWV cases, along with (*lower left, lower right*) the observed minus calculated residuals for two different models. The residuals in *black* demonstrate the state of the art in the early 1990s. The residuals in *grey* indicate the improvements obtained by ARM scientists up to 2004 (after Turner et al., 2004)

Figure I.7.4 demonstrates the large improvement in the modeling of high spectral resolution downwelling radiation over the past decade. These improvements, which have generally come in small incremental changes, were made primarily in the water vapor self- and foreign-broadened continuum and the water vapor absorption line parameters. Note that the pre-ARM results had much larger errors in both the line parameters as well as the underlying continuum as compared to the current state of the art. These changes, when taken as a whole, result in up to a 6 W/m^2 improvement in the modeled clear-sky downwelling longwave radiative flux at the surface and significantly better agreement with spectral observations and downwelling longwave fluxes to be calculated with an accuracy of better than 2 W/m^2.

3.5 Radar–Lidar synergy for the Detection of Cloud Boundaries and Target Classification

Frequent and detailed information about the extension of hydrometeor and aerosol layers in the atmosphere is crucial for weather forecast, climate model parameterization, and atmospheric science in general. Therefore, precise detection of fog and cloud boundaries is a major application for ground-based remote sensing sensors, and the combination of a cloud radar and a lidar ceilometer offers a powerful tool for the detection of these parameters. In fact, cloud radars can be used to gain insight into the vertical position and structure of the cloud. However, the radar reflectivity

Z is proportional to the sixth moment of the cloud drop size distribution. Conversely, for lidar ceilometers the backscattered radiation is proportional to the droplet diameter squared because of the wavelength being much shorter than the particle diameter (i.e., optical regime limit). Accordingly, lidar ceilometers are more sensitive to small cloud particles than cloud radars, which in turn are highly sensitive to larger drops. Thus, lidar ceilometer measurements are more accurate in deriving the actual cloud-base height while cloud radars often detect light drizzle below the actual cloud base. Conversely, lidar ceilometers are usually not able to detect the vertical cloud structure because most liquid water clouds are optically thick in the visible range such that the lidar ceilometer signal will almost always be extinguished in the lower part of the cloud. In the detection of cloud boundaries, cloud radar and lidar ceilometer have clearly complementary features.

A radar–lidar combined technique starts searching for one or more cloud layers into the lidar ceilometer backscattered signal, using the fact that to lidar the base of liquid clouds appears as a strong echo that is confined over only a few hundred meters. Liquid cloud base is defined as the lowest pixel for which the difference in the backscattered signal between it and the pixel above exceeds a certain threshold. Lidar cloud top is defined as the last non-zero pixel just below the level where the lidar signal falls to 0. Then the radar profile is analyzed to determine cloud top in the case that the lidar has been extinguished while the radar still has a signal. Thus the bases and tops of each of the liquid clouds in the profile are determined.

In addition, a proper combination of cloud radar and lidar ceilometer observations is able to provide information on the LWC within the cloud and a classification of the liquid cloud into three regimes: non-drizzling cloud, cloud-in-transition, and drizzling clouds (Krasnov and Russchenberg, 2002). Note that such an LWC retrieval works for liquid water clouds only and thus it requires a pre-screening of the atmospheric situation.

For these purposes, target categorization methods have been developed based on ground-based observations. For example, an integrated technique based on instrument synergy for target categorization has been developed within the Cloudnet project (www.cloud-net.org). In this technique, each pixel is categorized in terms of the presence of liquid droplets, ice, insects, aerosol, etc., thereby allowing algorithms specific to one type of target to be applied (Hogan and O'Connor, 2004).

4 Conclusions

In summary, the rationale behind the efforts to combine measurements and methods can be generalized as twofold:

– to derive additional parameters that are not otherwise derived and
– to maximize performances of retrieved parameters.

Therefore, the characteristics of the instrumentation taking part of an integrated suite should be

– independent observations
– complementary observations
– measuring different aspects of the atmosphere, and
– sensing a common observation volume

Note that the successful application of ground-based integrated systems depends upon their cost for deployment and maintenance; as a consequence, the preference should go to sensors and methods that are:

– cost-effective
– robust and easy to apply and maintain, and
– suitable for network deployment

Currently there are several research proposals and ongoing projects that focus on the establishment of a number of integrated observation sites with a selection of different remote and in situ observation instruments.

In summary, the ideal integrated remote sensing station for climate, meteorology, and civil protection applications would be comprised of a number of cost-effective, unattended, easy to maintain, robust, and stable instruments for providing the essential atmospheric variables. The observations would have good quality, with high spatial and temporal resolution and it would be possible to integrate the different measurements into ready-to-use products that meet the user requirements. It must be acknowledged that this goal is still far from being achieved and that advances with existing ground-based remote sensing systems will likely be incremental.

References

Ackerman TP, Stokes GM (2003) The atmospheric radiation measurement program. Phys Today 56(1):38–44.

Bianco L, Cimini D, Marzano FS, Ware R (2005) Combining Microwave radiometer and wind profiler radar measurements for high-resolution atmospheric humidity profiling. J Atmos Ocean Technol 22(July):949–965.

Engelbart D, Monna W, Nash J, Matzler C (eds) (2009). Integrated ground-based remote-sensing stations for atmospheric profiling. EUR 24172 – COST Action 720 final report. COST Office, Brussels.

Furumoto J, Kurimoto M, Tsuda T (2003). Continuous observations of humidity profiles with the MU radar-RASS combined with GPS and radiosonde measurements. J Atmos Ocean Technol 1:23–41.

Gossard EE, Chadwick RR, Neff WD, Moran KP (1982) The use of ground based Doppler radars to measure gradients, fluxes and structure parameters in elevated layers. J Appl Meteorol 21: 211–226.

Gossard EE, Wolfe DE, Moran KE, Paulus RA, Anderson DK, Rogers LT (1998) Measurements of clear-air gradients and turbulence properties with radar wind profilers. J Atmos Ocean Technol 15:321–342.

Han Y, Westwater ER, Ferrare RA (1997) Applications of Kalman filtering to derive water vapor profiles from Raman lidar and microwave radiometers. J Atmos Ocean Technol 14(3):480–487.

Hogan RJ, O'Connor EJ (2004) Facilitating cloud radar and lidar algorithms: the Cloudnet instrument synergy/target categorization product. Cloudnet Project Documentation.

Krasnov OA, Russchenberg HWJ (2002) Retrieval of water cloud microphysical parameters from simultaneous RADAR and LIDAR measurements. International Unin of Radio Science, XXVII General Assembly, Maastricht, The Netherlands.

Löhnert U, Crewell S, Simmer C (2004) An integrated approach toward retrieving physically consistent profiles of temperature, humidity, and cloud liquid water. J Appl Meteorol 43:1295–1307.

Mace G, Ackerman TP, Minnis P, Young DF (1998) Cirrus layer microphysical properties derived from surface-based millimeter radar and infrared interferometer data. J Geophys Res 103:23207–23216.

Mace G, Clothiaux EE, Ackerman TP (2001) The composite characteristics of cirrus clouds: bulk properties revealed by one year of continuous cloud radar data. J Climate 14:2185–2203.

Rodgers CD (2000) Inverse methods for atmospheric sounding: theory and practice. World Scientific, Singapore.

Stankov BB, Westwater ER, Gossard EE (1996) Use of wind profiler estimates of significant moisture gradients to improve humidity profile retrieval. J Atmos Ocean Technol 13:1285–1290.

Stankov BB, Gossard EE, Weber BL, Lataitis RJ, White AB, Wolfe DE, Welsh DC (2003) Humidity gradient profiles from wind profiling radars using the NOAA/ETL advanced signal processing system (SPS). J Atmos Ocean Technol 20:3–22.

Turner DD et al (2004) The QME AERI LBLRTM: a closure experiment for downwelling high spectral resolution infrared radiance 61(22):2657–2675.

Westwater ER et al (1999) Ground-based remote sensor observations during PROBE in the tropical western Pacific. Bull Am Meteorol Soc 80:257–270.

Part II
Applications

Chapter II.1
Observing Microphysical Properties of Cloud and Rain

Herman Russchenberg

1 Introduction

While we know that the climate is changing, it is still difficult to say with certainty how much it will change in the future. One of the reasons for this is the lack of knowledge we have concerning the atmospheric radiation balance. The sun's radiation heats the earth, but on its way to the surface it is scattered and absorbed by atmospheric constituents like clouds, aerosols, and gasses. The same is true for the heat radiation coming from the earth. Part of it will escape into space, while the remainder will warm up the atmosphere (Fig. II.1.1).

Clouds form an important element of the radiation balance. To understand their impact we have to know the relationship with aerosols. The conceptual picture is as a follows (Fig. II.1.2):

(1) In extremely clean air water vapor will not condense into liquid easily. The surface tension is very high, so that other water molecules cannot join an embryonic droplet. The droplet will not grow.
(2) Aerosols lower the surface tension, and consequently droplets can grow more easily around the aerosol.
(3) With an increasing amount of aerosols more droplets are formed, albeit that they will be smaller: the amount of water vapor is limited.

Clouds reflect sunlight. The degree to which they do this depends on the microstructure: the particle number concentration and the particle sizes. The number of particles depends on the aerosol concentration, and consequently the solar reflection also. An increase of aerosols leads to more cloud droplets leading to more reflection (Fig. II.1.3).

A second effect lies in rainfall formation. Large droplets turn into raindrops more easily than small ones. This implies that an increase of aerosols suppresses rainfall formation. It does not have to lead to less rainfall. It merely delays the formation and sustains the impact of clouds on the radiation balance (Fig. II.1.4).

H. Russchenberg (✉)
IRCTR, Delft University of Technology, Delft, The Netherlands
e-mail: H.W.J.Russchenberg@tudelft.nl

D. Cimini et al. (eds.), *Integrated Ground-Based Observing Systems*,
DOI 10.1007/978-3-642-12968-1_8, © Springer-Verlag Berlin Heidelberg 2010

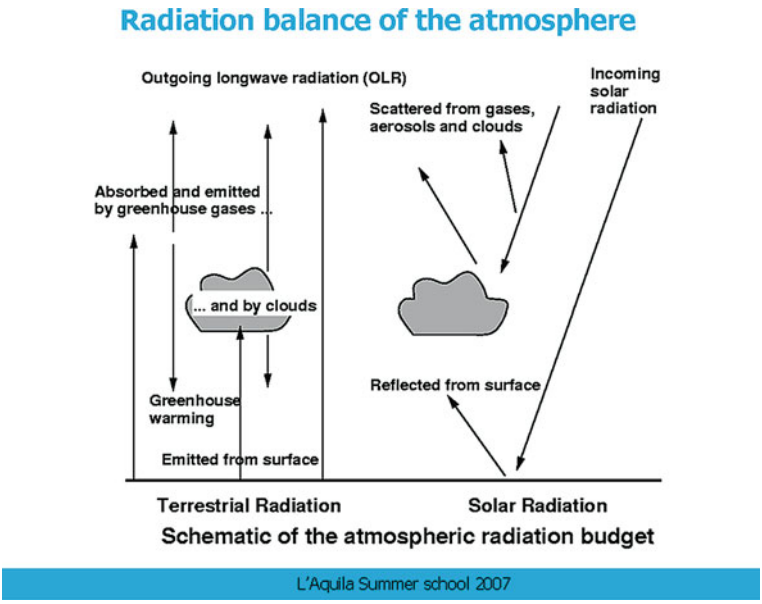

Fig. II.1.1 Schematic of the radiation budget of the atmosphere

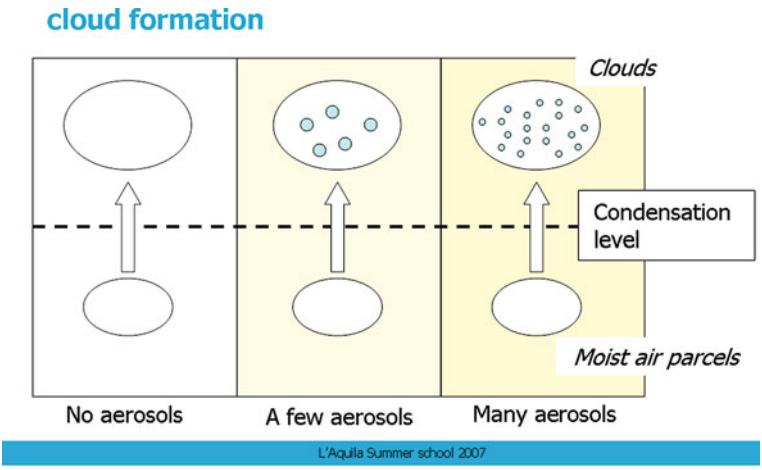

Fig. II.1.2 Conceptual picture of cloud formation as related to aerosol content

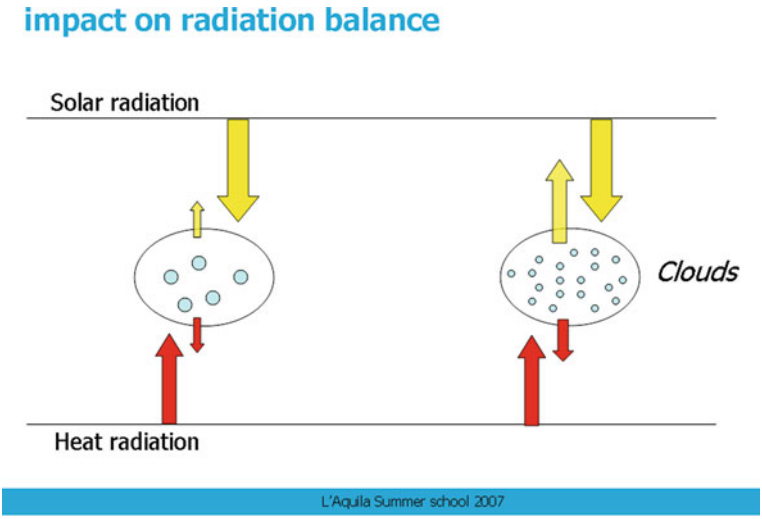

Fig. II.1.3 Clouds impact on radiation balance

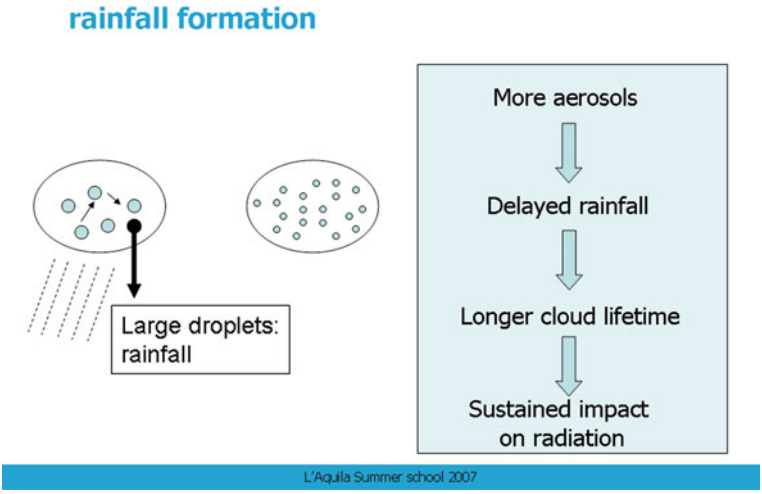

Fig. II.1.4 Aerosol impact on rainfall formation

2 The Role of Clouds and Aerosols

In the International Panel on Climate Change (IPCC) 2007 report, an overview is given of the level of uncertainty in our knowledge of the different radiatively important elements of the climate system. Greenhouse gases are well understood. They warm the earth, and the degree to which they do this is well quantified. This is not the case for the cooling effects of clouds and aerosols. They are by far the least understood, as represented by the error bars in Fig. II.1.5.

Therefore, the following question needs to be answered:

– How do changes in the aerosol background affect the radiation balance through cloud formation?
– What is the anthropogenic component?
– What is the regional variability?

How can these uncertainties be reduced? We have to answer the questions mentioned above. This cannot be done without proper observations, and that is where the difficulty comes in. How to do such observations? Cloud properties can be measured with instrumented aircraft, but that is not the optimum way for long-term monitoring. Aircraft observations have a limited time span and cannot be performed continuously. For this we need remote sensing techniques.

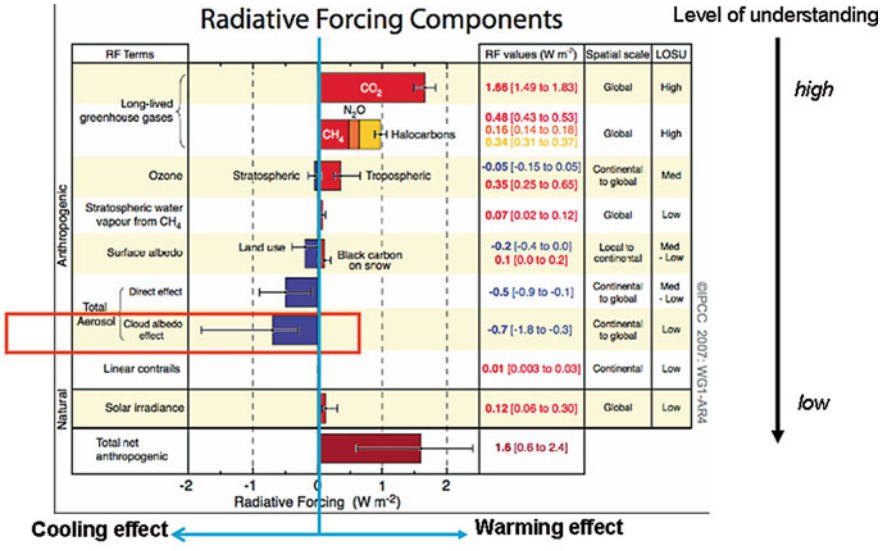

Fig. II.1.5 Level of understanding of radiative forcing components as reported by the IPCC in 2007

What causes the complexity of the problem?

– Many concurrent atmospheric processes (entrainment, mixing, turbulence, advection, etc.).
– A large range of temporal and spatial scales.
– A multitude of different physical parameters.
– Needed observation techniques are not available yet.

Cloud–aerosol interaction is difficult to separate from other physical processes in and around clouds. We want to know the relation between variations in aerosol loading and variations in the number of droplets. A simple observation of these two parameters is not sufficient, because other processes may also change the cloud droplet number concentration.

3 The Need for Multi-Sensor Strategies

Clouds and aerosols are not easy to measure. Single sensors are never enough to depict the whole picture. There are no instruments which can do it all. Different sensors have to be combined in a clever, synergistic way. The combination of instruments should give more than the sum of results of the individual sensors.

The following table lists the geophysical parameters needed to investigate the cloud–aerosol interaction and the typical technique that is used to observe them.

Aerosols	Lidar, passive
Clouds	Radar, lidar, passive
Radiation from ground and space	Passive
Boundary layer dynamics	Radar
Water vapor	Lidar, passive, gps

In Fig. II.1.6, the left panel shows a lidar observation of light rain. The right panel shows a radar measurement of the same event. Both instruments were pointed vertically. Clearly, these two instruments reveal different aspects of the clouds. The layers observed in the lidar image are due to water clouds that the radar does not see. The radar signal is mainly caused by ice, melting ice (the white area), and rain fall. Note the decrease of the lidar signal at the melting layer.

If we want to study the role of clouds in the climate system we have to measure the temporal and spatial distribution of the microphysical properties. Once we have these, we can calculate the impact of the clouds on the radiation balance using the appropriate theories of light scattering.

What do we have to know?

1. Cloud thickness
2. Liquid/ice water content

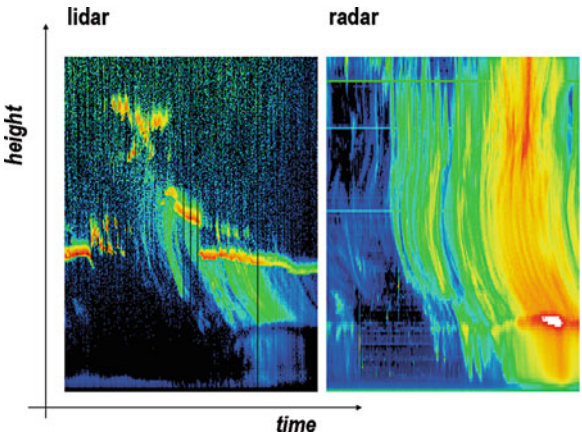

Fig. II.1.6 Observation of light rain with different instruments

3. Effective radius
4. Number concentration
5. Vertical profile

Every remote sensing technique assumes a certain model of the object that is being sensed. In our case we use the model of a quasi-adiabatic water cloud. One of the features of such clouds is that the liquid water content increases with altitude. With this we can predict the qualitative shape of a radar profile and its relationship with cloud property. In this approach we integrate the radar profile with height (iZ) and calculate the link between the liquid water path, the number concentration, and iZ. The liquid water path (the height integral of lwc) is measured by a microwave radiometer. So, by combining radar and radiometry we can derive the number concentration (Fig. II.1.7).

Figures II.1.8 and II.1.9 are the examples of the approach. The measurements were done at the atmospheric radiation measurement (ARM) site in Oklahoma. Figure II.1.8 shows a radar measurement of a water cloud in the ellipse (between 20 and 22 UTC). Figure II.1.9 gives the corresponding liquid water path from a

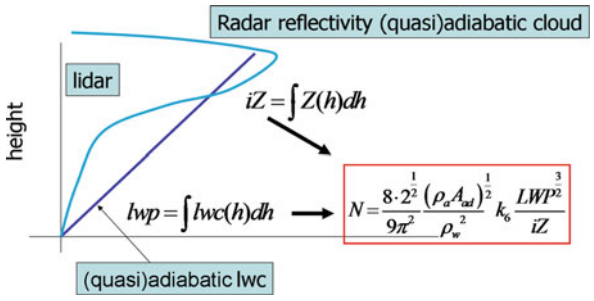

Fig. II.1.7 Schematics of the radar-radiometer technique for the cloud number concentration

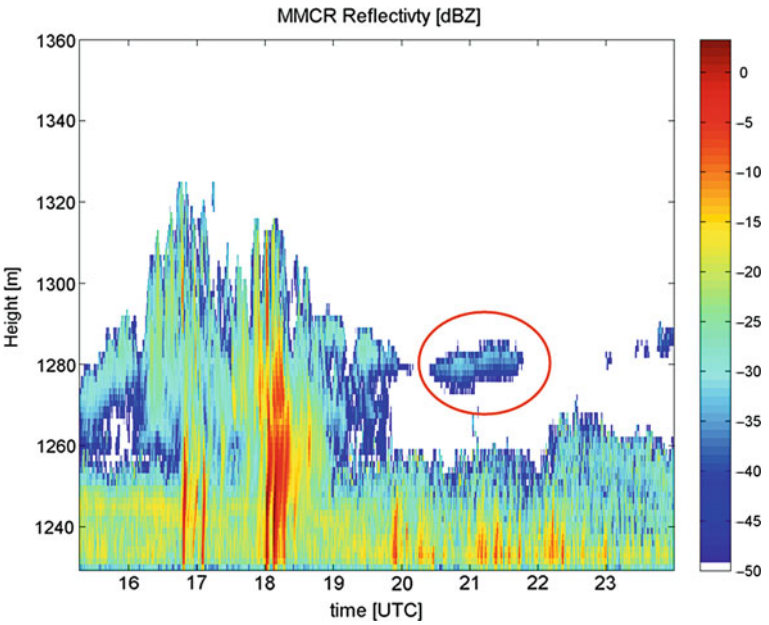

Fig. II.1.8 Time–height cross section of radar reflectivity [dBZ] from a millimeter-wave cloud radar

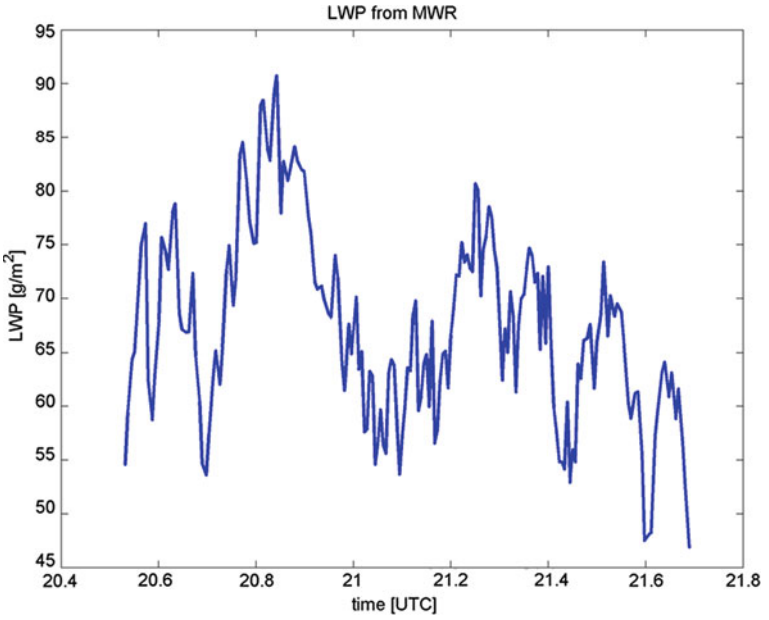

Fig. II.1.9 Liquid water path estimated by a microwave radiometer

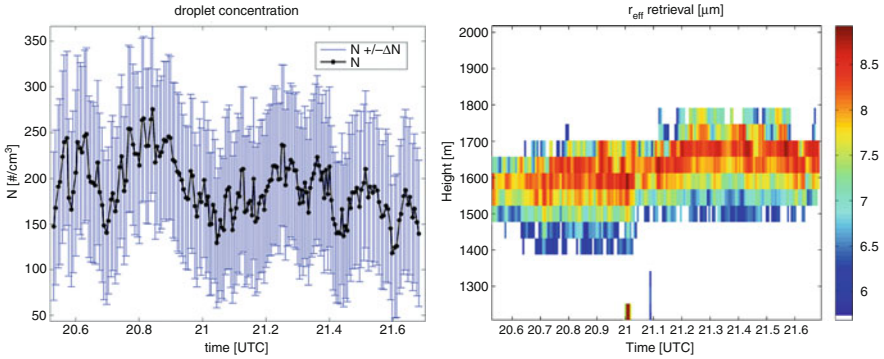

Fig. II.1.10 Droplet concentration (*left*) and effective radius (*right*) as retrieved by the combined approach

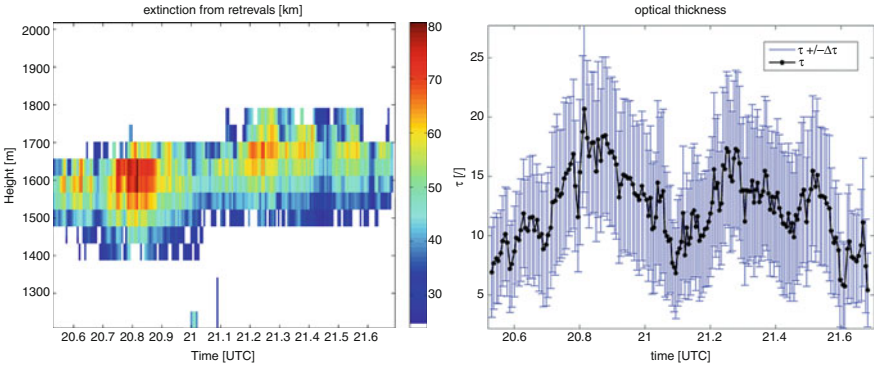

Fig. II.1.11 Extinction profile (*left*) and optical thickness (*right*) as retrieved by the combined approach

microwave radiometer. And out of these two we get the number concentration. Using the number concentration and the assumed cloud model, we can calculate the effective radius and other microphysical properties (Figs. II.1.10 and II.1.11).

When we integrate the extinction profile in Fig. II.1.11, we get the cloud optical thickness. This is the parameter relevant for climate studies. It tells how the cloud is affecting the radiation balance.

4 Zooming in on the Microstructure of Precipitation: The Shape and Size of Raindrops and Ice Crystals

Most rain originates from ice crystals aloft. The physical process is understood in qualitative terms, but quantification is very difficult. Ice crystals occur in a large variety of shapes and sizes, and each category is differently effective in the process

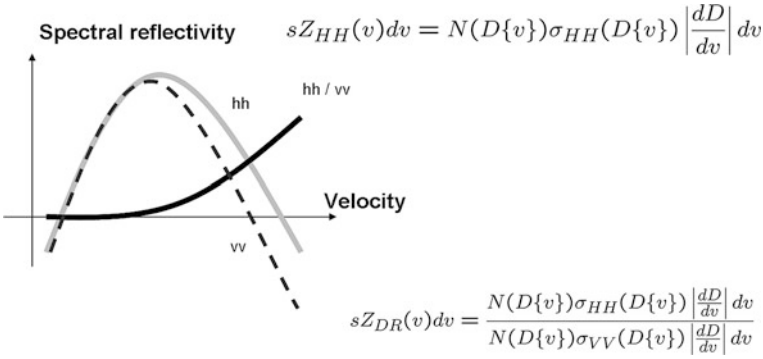

Fig. II.1.12 Introducing the spectral differential reflectivity Zdr

of aggregation, coalescence, or breakup. The need for high quality observations is high. We herewith describe a new technique that combines Doppler and polarization radar measurements to derive the microphysical properties of ice crystals, before they melt into raindrops (Fig. II.1.12).

Spherical particles do not change the polarization of radar waves, whereas oblate particles scatter horizontally polarized waves better than vertically ones. The fall speed of differently shaped particles may also differ. A clear case is rain: small drops are spherical and have a low fall speed, and large particles are oblate with a large fall speed. This leads to the concept of the spectral differential reflectivity: the polarization dependence of radar waves per class of occurring velocities. A Doppler–polarimetric radar can measure this quantity.

Figure II.1.13 is an example of a Doppler–polarimetric radar observation of rainfall. The left panel shows the velocity distribution of the reflectivity as function of height. The right panel shows the corresponding spectral differential reflectivity. Between 1,600 and 2,000 m we can see an enhanced reflectivity. This is the bright band due to melting ice. Above it there is ice and below rainfall. The velocity spectrum is narrow in the ice region, which indicates that the particles have similar fall

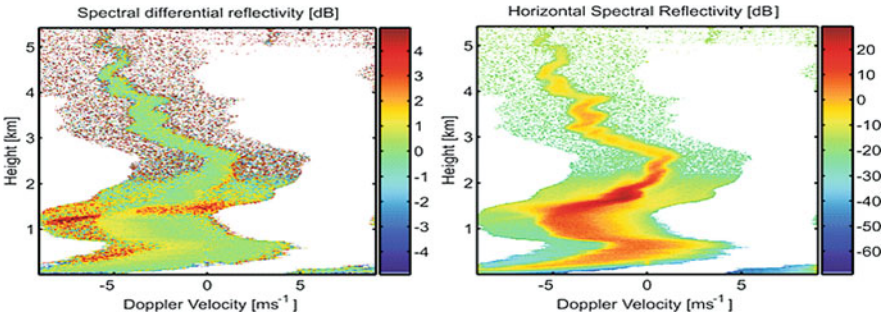

Fig. II.1.13 Examples of polarimetric spectrogram

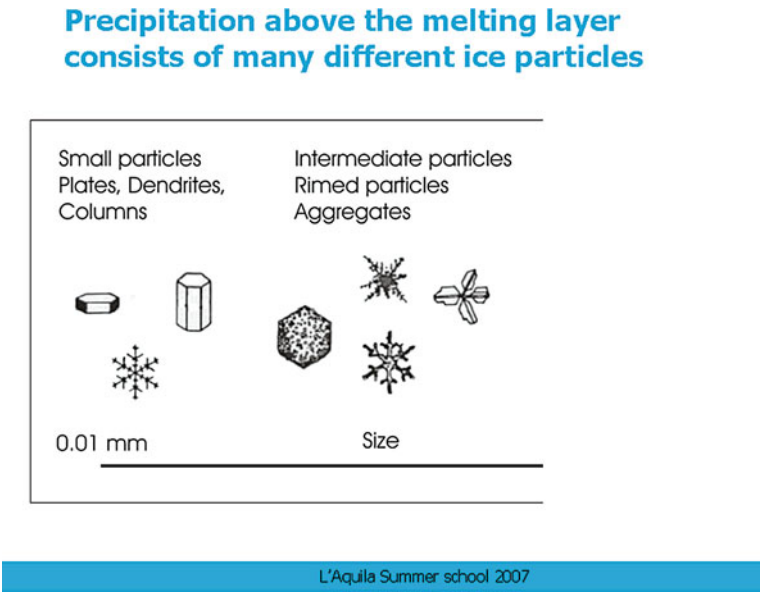

Fig. II.1.14 Size and shape of precipitating ice particles existing in clouds above the melting layer

speeds. Right panel shows that the shape of the particles can change quite a bit in the process of melting.

The retrieval of ice crystal information from such data is not easy. We have to construct a microphysical model that includes the variety of sizes and shapes (Fig. II.1.14) and relate this to the expected radar observables. In the inverse approach we can then derive the microphysical properties from the measurements.

Figure II.1.15 shows some of the results. The radar reflection is given as function of velocity for different types of ice particles. It is clear that plates and aggregates dominate for low velocities. This implies that we can only infer these types from the observations.

What we get then is information like the ones in Fig. II.1.16: the equivolumetric diameter and number concentration as function of time for aggregates and plates. Note the large difference between the two different habits.

With the data in Fig. II.1.16 we can do a consistency check: if we use the numbers to calculate the reflectivity, does it correspond to the observations?

$$Z = \frac{|K|^2}{|K_r|^2} \int_{D=0}^{\infty} N(D) D^6 dD$$

The computed reflectivity is shown in Fig. II.1.17; time dependence of obtained reflectivity shows good correlation with the measured reflectivity.

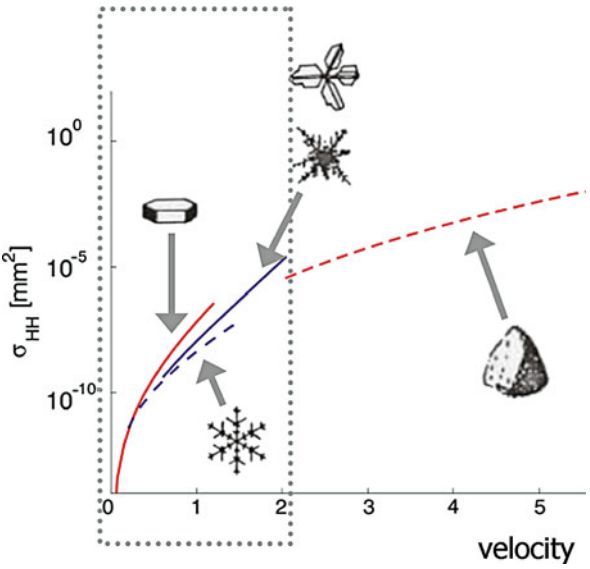

Fig. II.1.15 Radar reflection as function of velocity for different types of ice particles

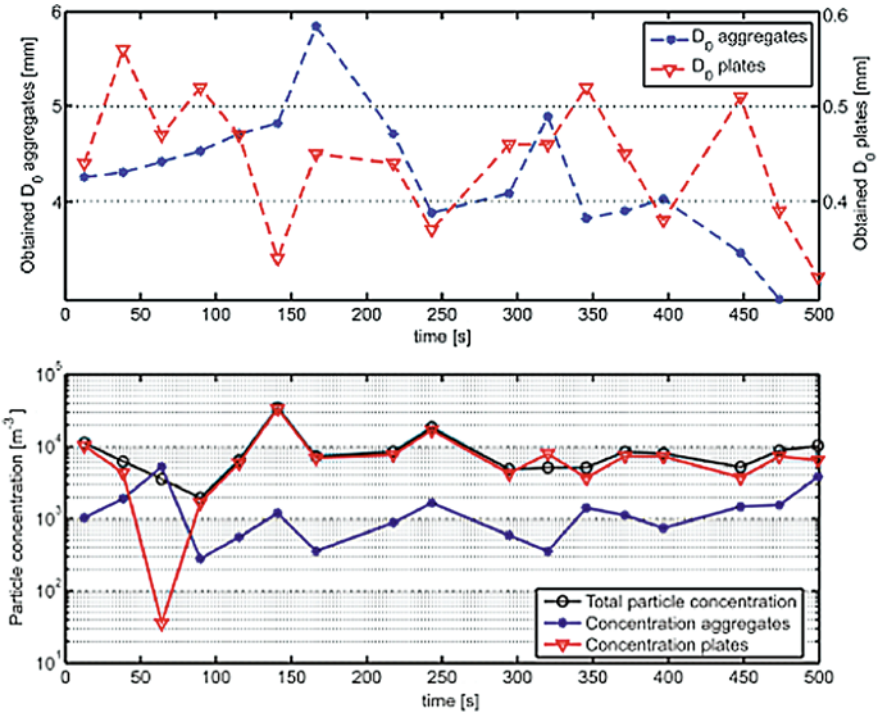

Fig. II.1.16 Retrieved time series: Equivolumetric diameter (*top*) and particle concentration (*bottom*)

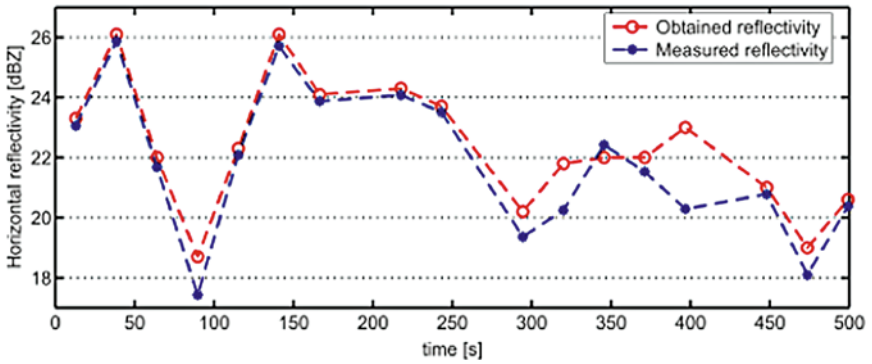

Fig. II.1.17 Time series of equivalent obtained and measured reflectivity

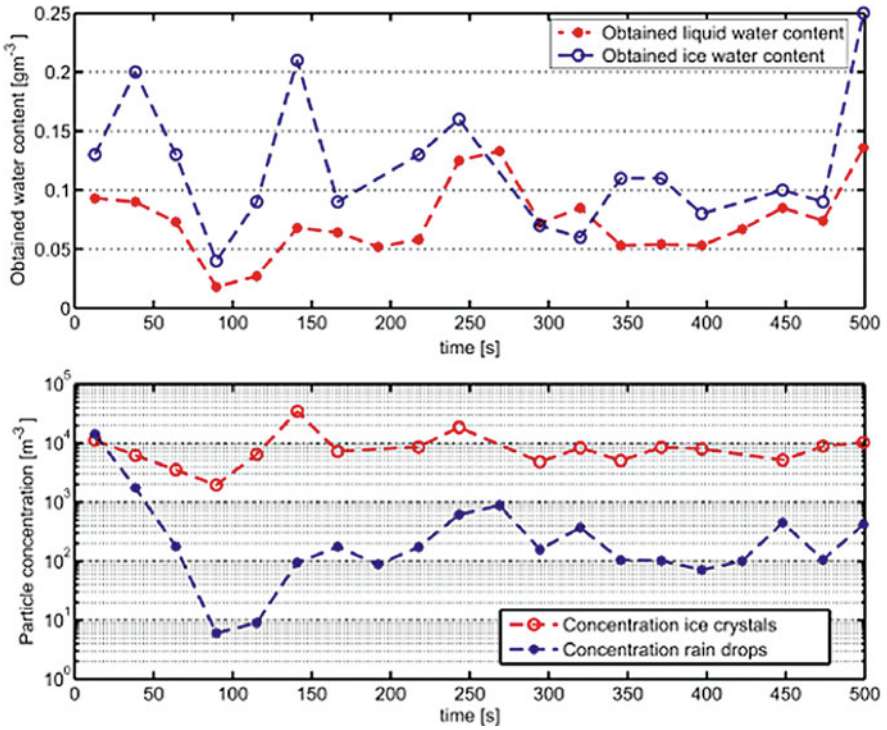

Fig. II.1.18 Ice water content and liquid water content (*top*) and particle concentrations of ice crystals and rain (*bottom*). Trends in radar observables comparable above and below the melting layer

Finally, we can calculate the ice water content and number concentration of rainfall droplet and ice crystals, as illustrated in Fig. II.1.18:

$$\mathrm{IWC} = \int_{D=0}^{\infty} N(D)m(D)dD$$

With these observations we can now study the rainfall process. For instance look into questions like: how stationary is the mass flow through the melting layer? How does the number concentration change during melting? Does it correspond to common assumptions in models?

Chapter II.2
Understanding Aviation Meteorology and Weather Hazards with Ground-Based Observations

Improving Aircraft Safety in Terminal Area

Christian Pagé

1 Introduction

Weather hazards have a significant negative impact on aircraft safety. Based on recent surveys, 20–30% of worldwide air accidents are due to adverse weather conditions. In Europe, as much as 22% of air traffic delays are due to bad weather. The problem is that the latest trends estimate that air traffic will increase by a factor of three within the next 20 years. If the accident rates stay the same, the number of accidents will be increasing significantly and this is considered unacceptable by airline and aircraft companies and government agencies. To mitigate these risks, several actions have been taken in the world.

In Europe, the FLYSAFE consortium is developing a mock-up of a system to uplink, in real-time, weather information in the cockpit and to the air traffic controllers (Pradier-Vabre et al., 2008). In FLYSAFE and in other projects, weather systems are being developed to identify weather hazards using weather data fusion. These systems are trying to combine weather data from different sources and instruments, such as ground-based and space-based observation platforms in combination with meteorological numerical models.

2 Main Weather Hazards for Aviation

There are several weather hazards that are dangerous for aviation. Because of the different scales involved in weather phenomena, the hazards have not the same impact if the aircrafts encounter them En-Route (regional and global scales) or in the airport terminal area (local scale). Furthermore, some phenomena are only present

C. Pagé (✉)
CERFACS, 42 avenue G. Coriolis, 31057 Toulouse Cedex, France
e-mail: christian.page@cerfacs.fr

D. Cimini et al. (eds.), *Integrated Ground-Based Observing Systems*,
DOI 10.1007/978-3-642-12968-1_9,

either at local scale or at high altitude when the aircraft is En-Route. Consequently, the main weather hazards can be tentatively classified as follows:

1. Airports terminal area: local airport weather
   - Wake vortex
   - Thunderstorms: microbursts, hail, wind shear
   - Icing (waiting aircraft stacks)
   - Low ceilings and visibility
2. En-Route: regional and global scales weather
   - Thunderstorms (hail, turbulence)
   - Clear air turbulence (CAT)
   - Icing (regional flights at lower altitudes)

To assess, identify, and predict these weather hazards, observations are needed from different instruments and sources.

3 The Needs of Ground-Based Remote Sensing Observations to Support Aviation Activities

Now, let us focus on the local airport terminal area weather hazards. In this section, we will review weather data that are available for this scale.

The main sources of weather observations at the airport are from the standard meteorological observation system. These provide data appropriate for synoptic scale weather systems, e.g., at the scale of standard high and low pressure weather systems:

1. METAR which gives surface data (temperature, altimeter setting, humidity, winds), cloud types and bases, as well as significant weather such as precipitation, thunderstorms
   - Data taken at 30-min-to-1-h interval.
2. Radiosoundings, which gives a vertical profile of temperature, humidity, and winds
   - Data taken at 12-h interval.

The limitation of these instruments is mainly that the data frequency is quite low and that they are point data. Other types of observation systems have greater data frequencies, such as space-based satellites, which are remote sensing observation systems.

These space-based satellites can be categorized into two main families, respectively, geostationary and polar-orbiting. The geostationary satellites have the following main characteristics and limitations:

- Orbit at 35,000 km altitude
- Limited spatial resolution: 1–6 km
- Typical temporal resolution is 15 min
- Information is limited in the vertical

The polar-orbiting satellites have the following ones:

- Orbit at 700–800 km altitude
- Very high spatial resolution: 250 to 5,000 m
- Limited temporal resolution: 2 passes per day
- Information is also limited in the vertical

One of the main advantages of most of these remote sensing instruments is that their measurements are quasi-continuous. The space-based instruments have the advantage of covering a large part of the Earth, at the expense of either low spatial resolution or temporal resolution.

For local scale weather needs at the airport terminal scale, specific ground-based instruments can be more appropriate. Some are sensor based, such as meteorological towers, which have instruments at different heights and taking measurements at very high temporal resolution, e.g., at each second. However, these instruments also have the following problem: they give only point data and their vertical resolution is quite limited. Other instruments, which are rather based on remote sensing technology, are:

- 1D and 3D weather radars (several band frequencies)
- Vertical wind profilers (several band frequencies)
- Radio acoustic sounding system (RASS)
- Lidar
- Sodar
- Radiometer
- Ceilometer

4 Applications of Ground-Based Remote Sensing Instruments to Aviation

In the previous section, several weather observing instruments that can be used to mitigate weather hazards were briefly introduced. One conclusion that can be set is that the standard meteorological observation system is not always suitable because of limited time and spatial scales, as well as limited 3D coverage. On the other hand, ground-based remote sensing systems are helpful to provide additional weather

information. However, remote sensing data are often difficult to use directly: data post-processing and/or data fusion is needed. In the next sections, practical applications on how remote sensing-based instruments can be used to mitigate aircraft delays and accidents are described.

4.1 San Francisco Marine Stratus Initiative: Burn-off Forecasts

In the United States, low ceilings and visibility are responsible for 35% of all weather-related accidents in the US civil aviation sector. They are also a major cause of flight delays. To mitigate these problems, a project to develop an integrated automated system was initiated by the MIT/LL. The first US airport test site that has been chosen was San Francisco: this became the San Francisco Marine Stratus Initiative (Wilson, 2004). The objective of the project was to develop accurate forecasts of the time that Marine Stratus will clear in the approach to San Francisco Airport (SFO). The integrated system that has been developed was for direct use by forecasters. The display integrated all the weather data available in the airport area along with a consensus forecast of the burn-off time using several numerical meteorological models:

- Statistical model
- 1D column model
- Boundary layer model

The instruments available were high temporal resolution surface data, sodar and ceilometer, infrared satellite data, and radiometers. An array of ground-based instruments were deployed in the San Francisco Bay Area, especially at SFO and San Carlos (Fig. II.2.1).

The sodar provides the boundary layer inversion height using acoustic backscatter. It uses the fact that at the top of stratus clouds, there is a sharp temperature inversion that gives high backscatter energy picked up by the sodar (Fig. II.2.2).

The ceilometer provides the cloud bases of stratus clouds using the reflectivity of very small water droplets.

The data of these two instruments can thus be used in combination with surface and radiosounding data along with a 1D column numerical model to provide burn-off stratus forecasts. The observation data are used to build a vertical profile of temperature and humidity to initialize properly the column model (Fig. II.2.3).

In summary, a fully integrated system approach has been used in this project: it shows the potential of direct and indirect uses of ground-based remote sensing data. The system combined the use of sodar and ceilometer data along with numerical modeling and an array of ground-based observations. The important aspect was also that an integrated display was designed for use directly by forecasters and air traffic controllers.

The technology of this system has been transferred in 2004 to the US National Weather Service (NWS) and it is now running operationally: a great success!

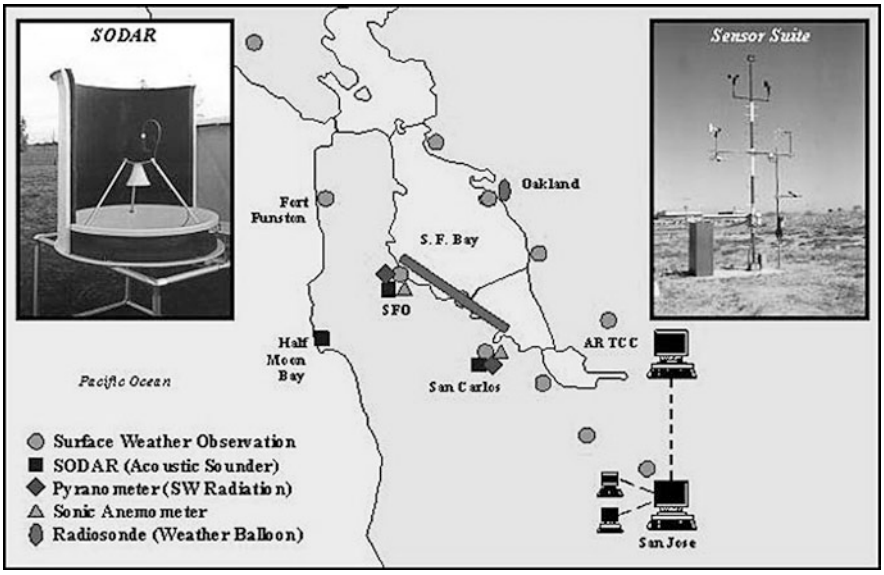

Fig. II.2.1 Array of ground-based instruments in the San Francisco Bay Area for the San Francisco marine stratus initiative

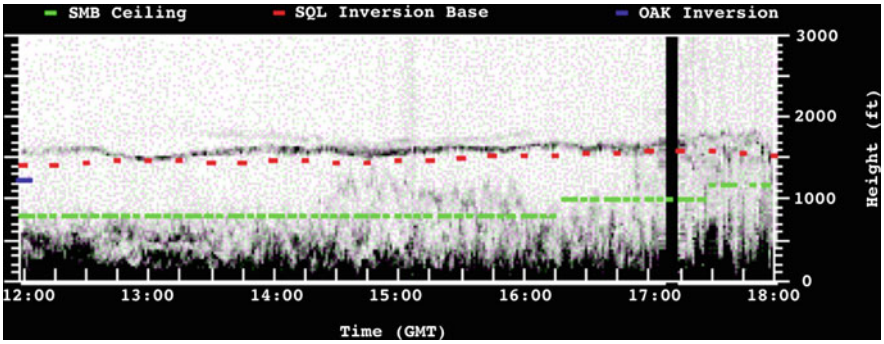

Fig. II.2.2 Sodar estimation of the boundary layer inversion height using acoustic backscatter

4.2 Terminal Ceiling and Visibility in the Northeastern United States

The success of the SFO Marine Stratus Initiative has led to a project follow-up: the Terminal Ceiling and Visibility Product Development Team in the NorthEastern (NE) United States (Clark, 2006). The main problem of this project is that Instruments-Flight-Rules conditions are quite frequent in the NE US during winter (November through April). These conditions are generally the consequence of transient synoptic scale situations, combined with high traffic. The physical phenomena responsible for these conditions are quite various.

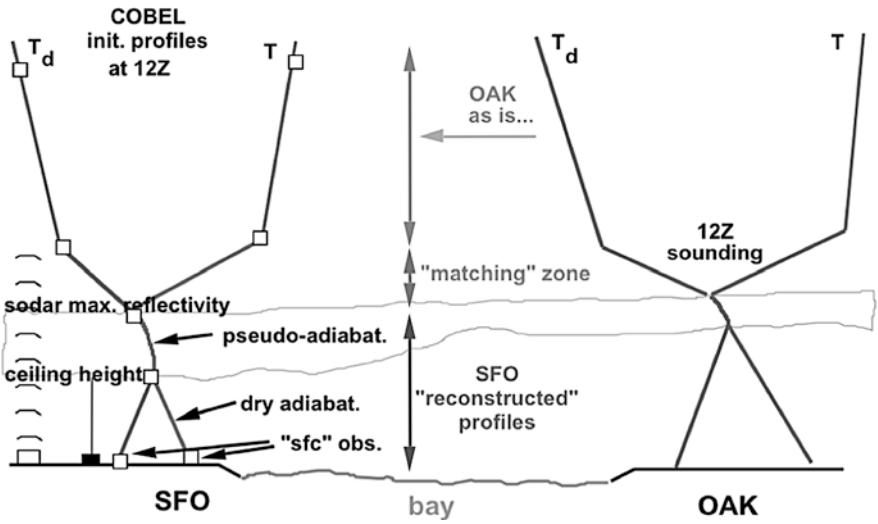

Fig. II.2.3 Reconstruction of a vertical profile of temperature and humidity using information from a numerical column model and observations (figure courtesy of Robert Tardif)

The project objective was to identify independent forecast technologies that are able to give some skill to forecast these IFR conditions, in a terminal-centric approach in high impacted terminals. The project focused on tactical scale forecasts (0–3 h), which involve tracking and trending techniques, using high-resolution observations.

Some techniques were developed to use 3D ground-based radar to detect low visibilities. This technique involved correlating reflectivity and surface-based observations, along with cell tracking (Fig. II.2.4). The calibration of such a technique

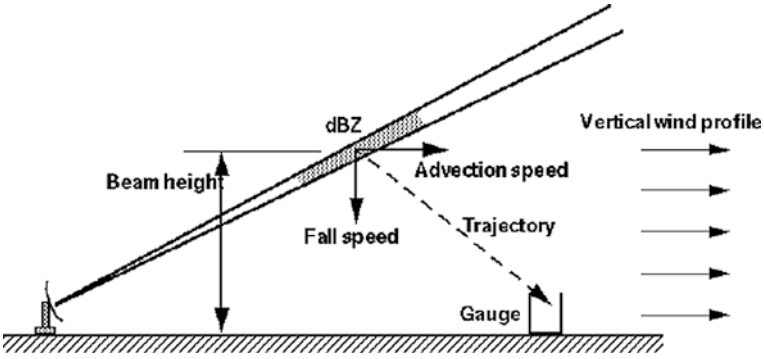

Fig. II.2.4 Particle trajectory for wind profile with no wind shear (Dixon et al., 2005). Technique used to detect low visibilities

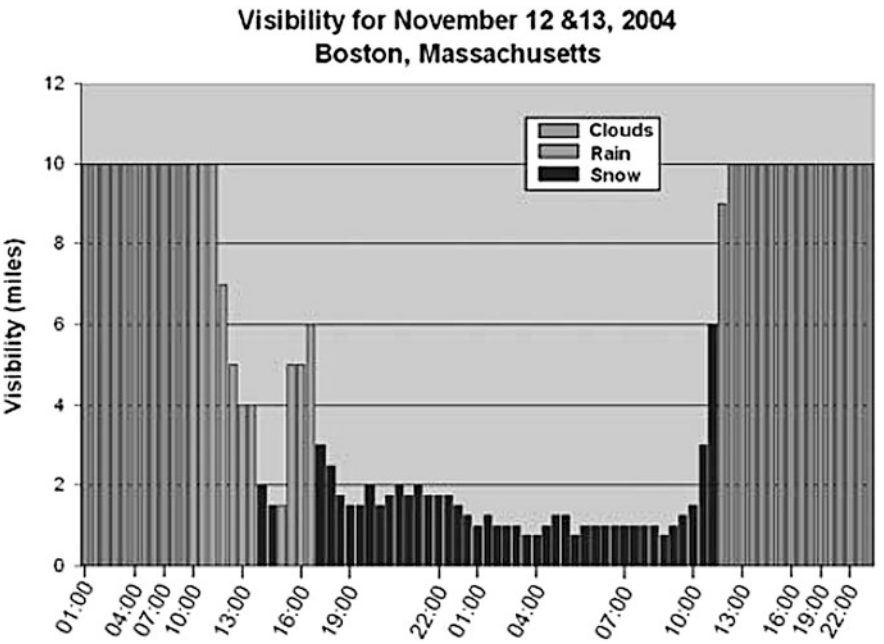

Fig. II.2.5 Variation in observed surface visibilities during transition from rain to snow during winter event at Boston Logan International Airport (Clark, 2006)

(radar-visibility relationship) showed to be quite tricky, because visibilities are quite dependent on precipitation type (snow/rain) (Fig. II.2.5). The results showed that forecasting low visibilities is a non-trivial task, and data fusion techniques must be used to improve the accuracy of the methodologies, such as using wind profiler, sodar, and lidar information combined with 3D ground-based radar data.

4.3 Aircraft In-Flight Icing

Another meteorological condition that can be quite hazardous for aircraft is in-flight icing, especially for regional flights. It causes reduced lift, raise stall speed, imbalance, and increased fuel consumption. In the United States, there were almost 600 accidents in the last 20 years related to in-flight icing. This phenomenon is caused by supercooled water droplets. The main problems are that it cannot be measured by remote sensing and that it is very difficult to predict (fast transient phenomena).

One of the techniques that can be used to infer in-flight icing regions is to identify the melting layer (0°C altitude) along with temperature and humidity. However, in some conditions, there is no melting layer while there is some icing, such as in deep convection and supercooled rain.

Another information that can be used to identify icing regions (and determine its intensity) is precipitation occurrence, which causes aerosol scavenging and an increase in supercooled water potential. In fact, when there are fewer aerosols, especially the ones that act as ice nuclei, the water vapor is forced to condense as water and cannot freeze because there are not enough ice nuclei. It has been shown that precipitation scavenging dominates the aerosol removal process: it is as high as 80%.

Other promising methodologies to diagnose in-flight icing involve a data fusion process. The idea is to combine the information from different data sources according to their potential to detect icing-related features. Such a system was developed at Météo-France, called SIGMA (Le Bot, 2004). Its first version used data from numerical models (temperature, humidity), satellite infrared temperature, along with ground-based weather radar reflectivity (precipitation occurrence). This type of diagnostic system can be run in near-real time, providing diagnostics of aircraft icing potential (Fig. II.2.6).

This type of system can also be extended to provide forecasts using one of the following techniques:

- Extrapolating radar and satellite data (experimental) and perform data fusion with temperature and humidity fields from numerical model forecasts.
- Use a numerical model approach only, without using any remote sensing data, such as in the CIP algorithm from NCAR (Bernstein et al., 2005).

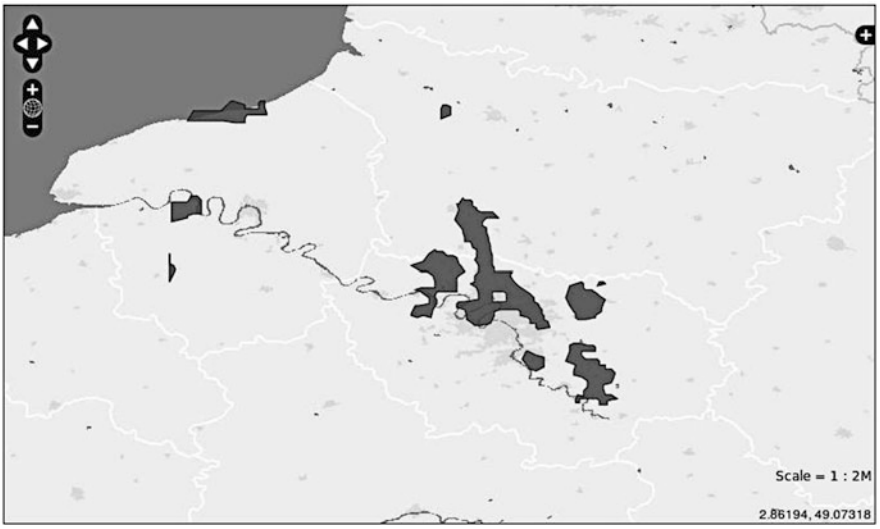

Fig. II.2.6 Severe icing risk diagnosed using data fusion techniques. Figure is showing severe icing risk objects around Charles-de-Gaulle Paris Terminal approach (figure courtesy of Sébastien Geindre, Météo-France)

4.4 3D Wind Field Nowcasting

The 3D wind structure is very important to aviation safety and performance. This is why a good knowledge of the current and future wind field is crucial for aircraft activities. In the terminal airport area, the wind can threaten aircrafts when there is low-level wind shear and turbulence, wave vortex, or convective cells.

In the terminal airport area, there are several ground-based remote sensing instruments that can be used to measure the wind structure. One of these instruments is the ground-based weather radar. This can be achieved using either a network of Doppler radars (at least three) or a bistatic network. A bistatic network was built in Montreal, Canada, using the McGill Weather Doppler Radar (Protat and Zawadzki, 1999). There were two bistatic receivers installed at proper locations to provide good coverage over the Dorval Airport (Fig. II.2.7).

The three radial wind measurements can then be combined using a variational data assimilation approach to compute a 3D wind field. This methodology has also been extended to perform thermodynamic retrievals of pressure and temperature perturbations.

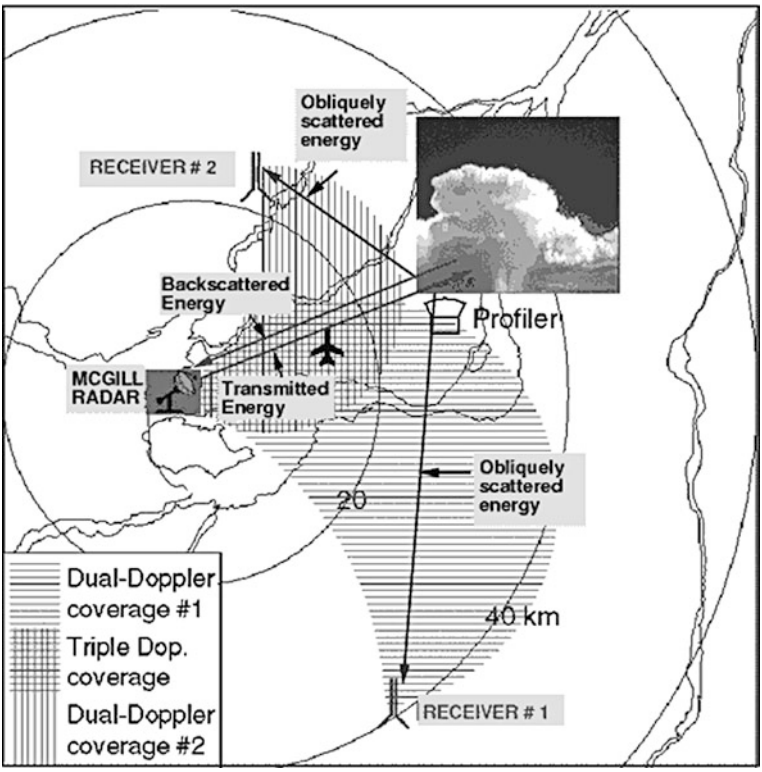

Fig. II.2.7 Schematic of the bistatic radar network at McGill Radar in Montreal, Canada (figure from McGill Radar Observatory website http://www.radar.mcgill.ca/science/ex-instrument/ex-bistatic.html)

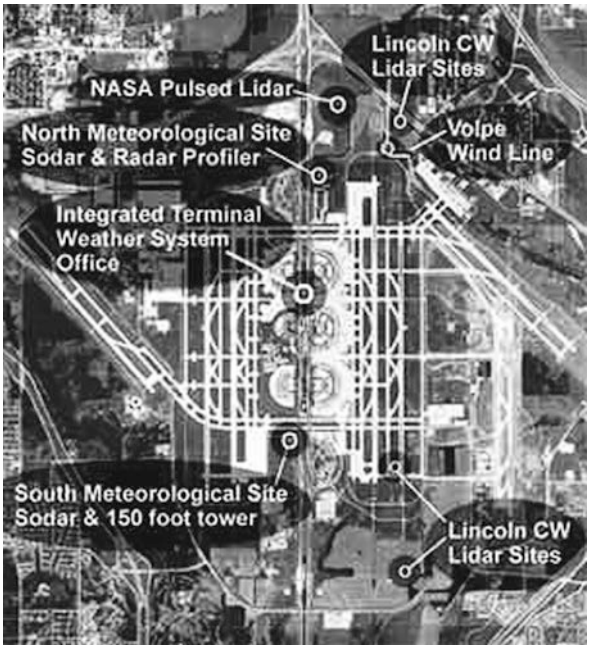

Fig. II.2.8 Instruments deployed during the wake vortex project in Memphis, 1994 (Dasey et al., 1997)

Smaller scale weather phenomena, like wake vortex, can be very dangerous for aircraft and can cause accidents. They limit airport capacity because these vortexes take time to dissipate or be advected away from the runway, thus imposing a minimum aircraft separation. However, these vortexes are sensible to atmospheric conditions such as crosswinds and atmosphere stability, which can cause them to take a longer or a shorter time to dissipate. So, in theory, it would be possible for aircrafts to have a shorter separation between them to increase airport capacity if we can measure or calculate the time it takes for the wake vortex to dissipate or be advected away.

One of the methodologies used is to install a ground-based remote sensing LIDAR network around the airport, such as in the WAKENET Europe project (Paris CDG, Frankfurt, London Heathrow) (Gerz et al., 2005) or Memphis in 1994 (Dasey et al., 1997) (see Fig. II.2.8) or Dallas in 2000 (Dasey et al., 1998). Lidar, along with other instruments, can be used to measure horizontal winds that can be used to determine a wake avoidance strategy to reduce aircraft spacing.

4.5 Low-Level Wind Shear and Turbulence

Important problems can arise from another type of 3D wind level structures, such as turbulence and low-level wind shear. Turbulence can cause many problems to crew and passengers, while low-level wind shear can cause crashes as it

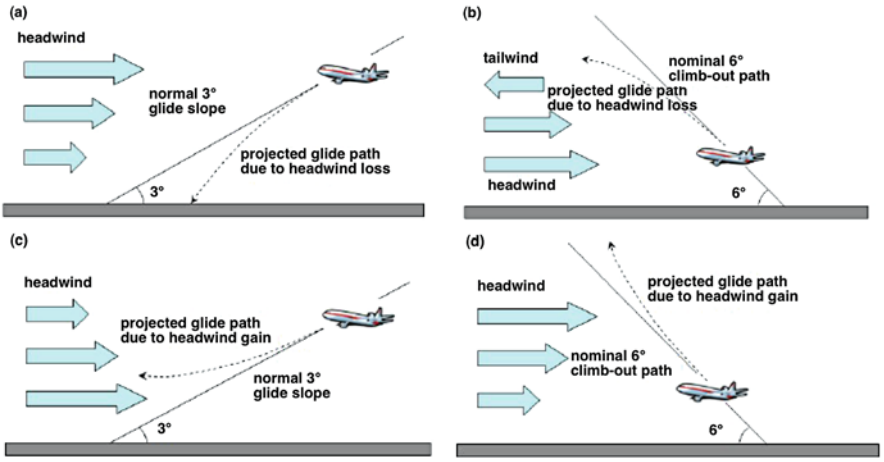

Fig. II.2.9 Vertical wind shear: problems for aircrafts (figure courtesy of Hong-Kong Weather Service)

produces trajectory differences compared to calculated trajectory. Low-level wind shear can be caused, among others, by lee-side mountain peaks, updrafts near coasts (sea breeze), thunderstorm gust fronts and microbursts, and low-level jet streams (Fig. II.2.9).

To mitigate the risks caused by these phenomena, a system based on ground-based weather radar has been designed: the terminal Doppler weather radar (TWDR). It can detect wind shear and also microbursts. This system is designed specially for terminal area in a high-clutter environment and it includes sophisticated clean-up algorithms to eliminate clutter and small moving targets such as insects, birds, and other aircrafts. The wavelength used is 5 cm. For the vertical wind profile, sodar, lidar, and vertical wind profiler can also be used. The TDWR has a major problem though it cannot be used when there is no precipitation. Thus, to complement the TDWR, a system using one or several lidars has been successfully operated using a wavelength of 2 μm. The lidar operates better in rain-free (or fine rain) conditions. An integrated system was developed by the Hong-Kong Weather Service for windshear and turbulence alerts over various runway corridors at Hong-Kong International Airports (HKIA) (Tsui et al., 2000).

4.6 Thunderstorm Avoidance

One of the main weather hazards are thunderstorms. These storms are often accompanied by almost all of the aircraft weather hazards, such as severe icing and turbulence, hail, low ceiling and visibility, microburst and downburst, wind shear, strong surface winds, heavy rain, and lightning. Identification and spotting of

these storms almost always involve the use of ground weather radars. Many algorithms have been developed to detect hail, heavy rain (reflectivity), and outflow (Doppler radial winds and reflectivity). Nowcasting thunderstorm movements are also very important: several cell-tracking algorithms have been developed using ground weather radar data, which are usually based on reflectivity thresholds and time cross-correlation. More sophisticated cell-tracking techniques have also been developed, such as the MAPLE McGill Radar system (Turner et. al., 2004).

5 Conclusion

Weather hazards have a significant negative impact on aircraft safety. The use of ground-based remote sensing instruments can help to mitigate these hazards by observing the weather phenomena associated with these hazards. By using data fusion from several instruments or algorithms, it is possible to better identify and nowcast them to improve airport terminal area security. Several important application projects have been pursued in the last decade to tackle with these problems, and the use of ground-based remote sensing instruments was almost always included. Among many projects, the San Francisco Marine Stratus Initiative, the Terminal Ceiling and Visibility project, and the FLYSAFE project were briefly discussed. These extensive projects showed that it is possible to develop algorithm that post-process and merge data from different sources, especially from quasi-continuous data sources such as remote sensing instruments. By combining data from different instruments, one can capitalize on strengths of each of these instruments to overcome their individual defaults. Results have shown that ground-based remote sensing instruments are useful to improve security in airports terminal area.

References

Bernstein BC, McDonough F, Politovich MK, Brown BG, Ratvasky TP, Miller DR, Wolff CA, Cunning G (2005). Current icing potential (CIP): algorithm description and comparison with aircraft observations. J Appl Meteorol 44:969–986

Clark DA (2006) Terminal ceiling and visibility product development for northeast U.S. airports. In: 12th conference on aviation, range, and aerospace meteorology, Atlanta, GA. Amer. Meteor. Soc., Geneseo (Preprints)

Dasey T, Campbell S, Heinrichs R, Matthews M, Freehart R, Perras G, Salamitou P (1997) A comprehensive system for measuring wake vortex behavior and related atmospheric conditions at Memphis, Tennessee. Air Traff Control Q 5(1):49–68

Dasey TJ, Cole RE, Heinrichs RM, Matthews MP, Perras GH (1998) Aircraft vortex spacing system (AVOSS) initial 1997 system deployment at Dallas/Ft. Worth (DFW) Airport. Project Report NASA/L-3. MIT Lincoln Laboratory, Lexington, MA

Dixon M, Rasmussen R, Landolt S, Simard J (2005) The implementation of short-term forecasting of airport surface visibility using ASOS and radar. Progress report submitted by NCAR to FAA, 31 June 2005

Gerz T, Holzäpfel F, Bryant W, Köpp F, Frech M, Tafferner A, Winckelmans G (2005) Research towards a wake-vortex advisory system for optimal aircraft spacing. Comptes Rendus Phys 6(4/5):501–523. Special issue on Aircraft trailing vortices

Le Bot C (2004) SIGMA: system of icing geographic identification in meteorology for aviation. In: Book of abstracts of 11th conference on ARAM. AMS, Hyannis, MA

Pradier-Vabre S, Forster C, Heesbeen WWM, Pagé C, Sénési S, Tafferner A, Bernard-Bouissières I, Caumont O, Drouin A, Ducrocq V, Guillou Y, Josse P (2008) Description of convective-scale numerical weather simulation use in a flight simulator within the Flysafe project. Meteorol Atmos Phys (Online First). doi:10.1007/s00703-008-0317-4

Protat A, Zawadzki I (1999) A semi-adjoint method for real time retrieval of three-dimensional wind field from multiple-Doppler bistatic radar network data. J Atmos Ocean Technol 16: 432–449

Tsui KC, Cheng CM, Lee BY (2000) emote-sensing the weather to support the Hong Kong Airport. In: The third international symposium on electronics in the air transport industry, Hong Kong, China, 28–29 November 2000

Turner B, Zawadzki I, Germann U (2004) Scale dependence of the predictability of precipitation from continental radar images. Part III: Operational nowcasting implementation (MAPLE). J Appl Meteorol 43:231–248

Wilson FW (2004) An operational Marine Stratus forecast system for San Francisco International Airport. In: 11th conference on aviation, range, and aerospace meteorology, Hyannis, MA. Amer. Meteor. Soc., Geneseo

Chapter II.3
Ground-Based Observing Systems for Atmospheric Aerosol Chemistry and Composition

Stefano Decesari

1 Introduction

The most familiar ground-based measurements of atmospheric aerosols are those performed every day in the monitoring stations for air quality in the cities. Adverse health effects of even low levels of atmospheric aerosol concentrations were demonstrated by long-term epidemiological studies, since that of Dockery et al. (1993), which showed a correlation between increased mortality and the concentrations of PM_{10} and, more tightly, of $PM_{2.5}$. "PM_{10}" and "$PM_{2.5}$" refer to the total dry masses of aerosol particles with diameters lower than 10 and 2.5 μm, respectively. These familiar notations contain important concepts of aerosol observations: ambient aerosol particles have a weighable mass; this mass is affected by humidity; the size of aerosol particles is typically in the micron or sub-micron range, and as a natural consequence, aerosol particles can interact with visible light; finally and most importantly, the mass and, in general, *all properties* of the aerosol particles are a function of their size.

Contrary to gases, the aerosol can be filtered out from a sampled air flow, and the filter weighed in a microbalance. Aerosol concentrations are then usually expressed in microgram per cubic metre and can vary from around 1 $\mu g\ m^{-3}$ in very pristine environments and free troposphere air to 5–10 $\mu g\ m^{-3}$ in the clean continental boundary layer, up to 50–100 $\mu g\ m^{-3}$ of dry PM_{10} mass in polluted areas (Van Dingenen et al. 2004). After collection on filters or other sampling substrates, the aerosol samples can also be subjected to a suite of chemical analyses in the same manner of other environmental matrices like soil or water samples, and the resulting concentrations of aerosol chemical components are also expressed in microgram per cubic metre.

S. Decesari (✉)
Institute of Atmospheric Sciences and Climate (ISAC), CNR, Bologna, Italy
e-mail: s.decesari@isac.cnr.it

D. Cimini et al. (eds.), *Integrated Ground-Based Observing Systems*,
DOI 10.1007/978-3-642-12968-1_10,

Ambient aerosol particles contain also a significant but variable amount of condensed water, which depends on relative humidity and on the occurrence of hygroscopic materials in the aerosol particles. Condensed water is not included in the PM_{10} or $PM_{2.5}$ mass per definition, and it is believed to be irrelevant for the toxicological properties of aerosol, but it is important to remember that condensed water can make up several tenths of microgram per cubic metre in a humid atmosphere. Condensation of water makes the particles grow to larger sizes, allowing them to scatter more radiation, thus affecting visibility and the transparency of the atmosphere with respect to sunlight. Moreover, humid particles form more efficiently hazes and fogs and modify cloudiness, which has also very important climatic effects (Ramanathan et al., 2001; Kaufman and Koren, 2006).

The interaction of aerosol particles with visible light not only has a great importance for visibility and the atmospheric radiative budget, but also provides tools for determining the aerosol concentration using in situ or remote sensing techniques (e.g. lidars, photometers). A comprehensive and elegant theory of light scattering and absorption by aerosols has been developed by Mie, and it is the subject of several treatises (e.g. Bohren and Huffman, 1983). The aerosol scattering coefficient is measured in situ by common instrumentation, called *nephelometers*, and expressed in mm^{-1}, or km^{-1}. The aerosol scattering coefficient is primarily a function of aerosol size and also of relative humidity, which affects the size of aerosol particles by regulating the amount of condensed water. The scattering coefficient of a heated, dried aerosol is a proxy of total aerosol surface and a broad function of aerosol volume, and measuring it is a simple, cheap and useful way to monitor the total concentration of aerosols with diameter larger than 0.2–0.3 μm. The scattering coefficient has only a weak dependence on the chemical composition. By contrast, the absorption coefficient, which is determined by *aethalometers* and other instruments capable to measure the colour or the darkness of an aerosol sample, is completely dependent on the occurrence of chemical compounds, such as mineral oxides or the so-called black carbon (BC). Other major aerosol compounds, like ammonium sulphates and nitrates and many organic compounds, do not absorb visible light; therefore, the aerosol absorption coefficient is usually weakly correlated with the aerosol mass concentration.

The light scattering properties of aerosol particles allow to *count* them too. *Optical particle counters* (OPCs) are widespread instruments where an air stream is sampled at a reduced flow (≤ 1 L min^{-1}) and individual particles are counted by making them scatter a focused light beam. These systems are unsuitable for particles with diameters smaller than 0.1–0.3 μm. More sophisticated instruments, called *condensation particle counters* (CPCs), are able to count also the small particles with diameters down to a few nanometres, using a pre-treatment of the particles in a chamber filled with a supersaturated vapour (usually butanol), where they undergo a condensational growth to larger sizes until they can be counted using optical methods. Aerosol number concentrations span from few tenths per cubic centimetre in very remote environments to some hundreds in relatively pristine environments,

to 10^3 cm^{-3} in polluted areas, up to 10^4 cm^{-3} at kerbside sites (Van Dingenen et al., 2004). Despite this general trend towards higher number concentrations with increasing pollution levels, very high number concentrations have been observed sporadically also in the clean atmosphere and related to bursts of freshly formed ultrafine particles (Kulmala et al., 2004). Since the total number of aerosol particles is often dominated by ultrafine particles which, on the other hand, contribute to a very small extent to total particle mass, it is important to keep in mind that aerosol *number* concentrations are not necessarily correlated with *mass* (PM_{10} or $PM_{2.5}$) concentrations. Bursts of ultrafine particles recorded by a CPC will leave only nanogram levels of material on a filter for daily PM_{10} determination. Therefore, the phenomenology of aerosol, with respect to spatial and time variability, can be very different by looking at number concentrations rather than to mass concentrations. The same applies to the phenomenology of aerosol chemical compounds. For instance, mineral dust can make up a substantial fraction of PM_{10}, but it usually accounts for only a minor fraction of the number of particles which, on the contrary, is mainly apportioned into particle types having a smaller modal diameter (like carbonaceous and ammonium sulphate particles). In summary, number-related and mass-related aerosol properties may follow very different dynamics, and this is a consequence of the large breadth and multimodality of the size spectrum of atmospheric aerosol particles. Atmospheric aerosol is an intrinsically heterogeneous system characterized by a continuum size spectrum from 10^{-9} to 10^{-5} m and by varying particle chemical compositions, *mixing state* (i.e. the degree of mixing of the chemical species in the same particles rather than belonging to distinct particle populations), physical properties (density, shape, optical properties) and *internal* structures of the individual particles for an infinite number of degrees of freedom which are simply irreducible by the existing instrumentation. Therefore, the observations of atmospheric aerosols can be much more complex than those of atmospheric gaseous compounds such as CO_2, CO or O_3: the aerosol measurements provide an inherently partial information, and the most appropriate instrumentation must be chosen according to the goals of the specific experiment.

Ground-based observing systems for atmospheric aerosols can be classified into systems measuring the properties and concentration of the aerosol in situ and those looking at columnar properties and vertical profiles using *remote sensing* techniques. Instruments for in situ measurements exploit all principles of aerosol detection, while remote sensing techniques rely on the optical methods alone; therefore, the characterization that can be achieved in situ is much more sophisticated than that retrieved by remote sensing. In particular, remote sensing methods suffer from two major limitations, which are inherent to all optical measurements of the aerosols: (a) they are not sensitive to ultrafine particles and (b) they provide only an indirect information about chemical composition.

A treatment of lidar systems for aerosol observations is given elsewhere in this issue (Chap. I.3). Here, we deal with measurements in situ, with a focus on the techniques of determination of the aerosol chemical composition.

2 Measurements of Aerosol Concentration and Chemical Composition

The determination of the aerosol concentration, size distribution, composition and optical properties can be performed in situ by a large set of instruments that we summarize schematically and in a very simplified form in Figs. II.3.1, II.3.2, and II.3.3. For a more detailed treatment, the reader is referred to the books by Finlayson-Pitts and Pitts (2000) and Heard (2006).

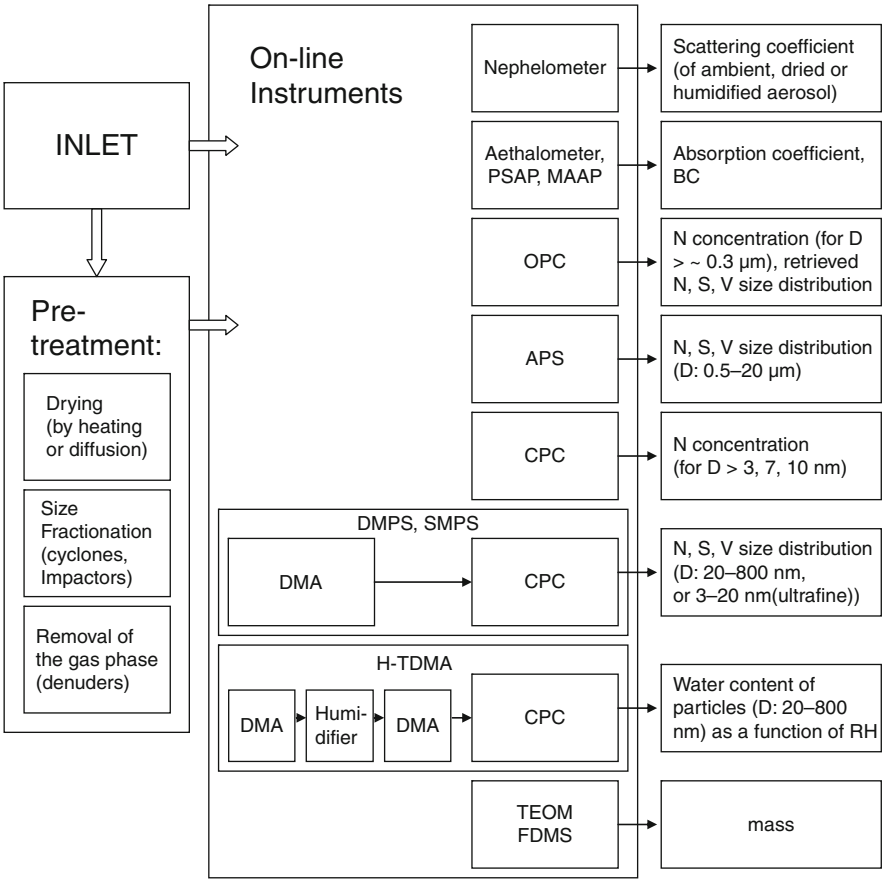

Fig. II.3.1 Online measurements of aerosol concentration and *N* (number), *S* (surface) and *V* (volume) size distributions. APS, aerodynamic particle sizer; CPC, condensation particle counter; DMA, differential mobility analyzer; DMPS, differential mobility particle sizer; FDMS, filter dynamic measurement system; H-TMDA, hygroscopicity tandem differential mobility particle sizer; MAAP, multi-angle absorption photometer; OPC, optical particle counter; PSAP, particle soot absorption photometer; SMPS, scanning mobility particle sizer; TEOM: tapered element oscillating microbalance

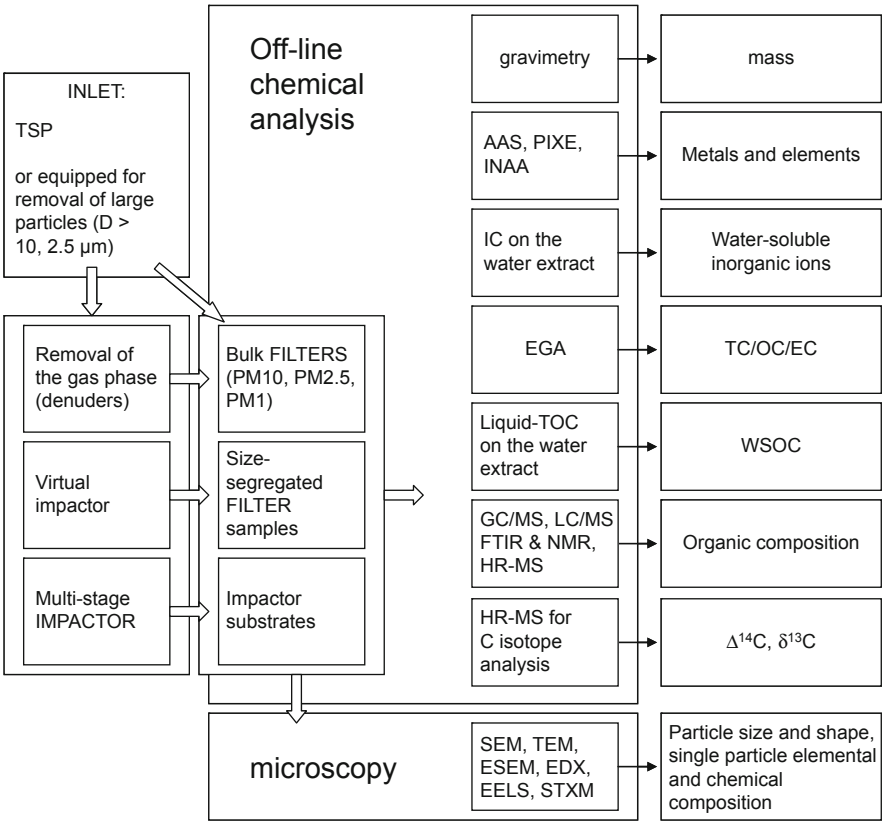

Fig. II.3.2 Off-line chemical, gravimetric determination and microscopic characterization of total suspended particulate (TSP) matter samples and size-segregated aerosol samples. TC, OC, EC and WSOC stand for total, organic, elemental and water-soluble organic carbon. AAS, atomic absorption spectroscopy; EDX, energy-dispersive X-ray spectrometry, EGA, evolved gas analysis; EELS, electron energy loss spectroscopy; ESEM, environmental scanning electron microscopy; FTIR, Fourier transform infrared spectroscopy; GC/MS, gas chromatography/mass spectrometry; HR-MS, high-resolution mass spectrometry; IC: ion chromatography; INAA, instrumental neutron activation analysis; LC/MS: liquid chromatography/mass spectrometry; NMR, nuclear magnetic resonance spectroscopy; PIXE, particle-induced X-ray emission; SEM, scanning electron microscopy, STXM, scanning transmission X-ray microscopy; TEM, transmission electron microscopy; TOC: total organic carbon

All instruments have *inlets* and sampling lines to bring the air sample to the detector/collector. Since aerosol particles have an inertia and tend to deviate from the streamlines, the sampling efficiency can be reduced for particles with a large aerodynamic diameter. Therefore, the inlets can be suitable for sampling the total suspended particulate (TSP) matter or, alternatively, only the aerosol particles smaller than a given size depending on the flow rate and on the geometry of the inlet and of the sampling line. Commercially available inlets with a calibrated geometry

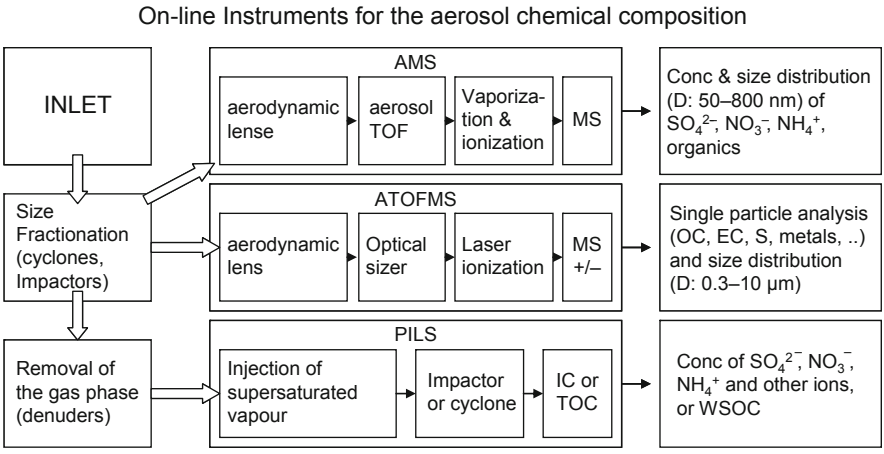

Fig. II.3.3 Online instruments for the aerosol chemical composition. AMS, aerosol mass spectrometer; ATOFMS, aerosol time-of-flight mass spectrometer; IC, ion chromatography; PILS, particle-into-liquid sampler; TOC, total organic carbon analysis; TOF, time-of-flight; WSOC, water-soluble organic carbon

(sampling heads) allow selective preseparation of PM_{10} and $PM_{2.5}$ for standard flow conditions. Inertial fractionation of the particles can be achieved also using cyclones and impactors, which allow the isolation of particles with aerodynamic diameter smaller than 1 μm, down to 0.1 μm in the case of impactors. Once drawn into the instrument, the air sample may undergo further treatments to eliminate possible interference with aerosol detection/collection. For instance, humidity can be removed by heating the sample or by employing diffusion driers, and gas-phase compounds can be eliminated using absorbing plates or cylinders (denuders).

The detection, observation and characterization of aerosol particles exploit several measurement principles already mentioned in Sect. 1 and that can be summarized as follows:

(1) aerosol have a weighable mass
(2) they scatter and absorb visible light
(3) they absorb water vapour (and organic vapours)
(4) after sampling they can be subjected to chemical, biological and mineralogical analysis

Moreover:

(5) they can be ionized in a mass spectrometer
(6) they can be observed using an optical or electronic microscope

There are other principles of detection, like attenuation of β rays, but these will not be treated in this review.

Detection can be carried out *online* with the sampling or *off-line* after the end of the sampling.

Online instruments employ more sensitive techniques allowing continuous or quasi-continuous measurements of the aerosol particles, which, in most of the cases, are analysed directly in their gaseous medium. Conversely, in the off-line methods, time-integrated samplings are performed using filters and other substrates to separate the aerosol particles from the air stream, and the sampled substrates are then transferred to a laboratory for subsequent analysis.

Online systems have been first developed for measuring the aerosol scattering and absorption coefficients, the aerosol number concentrations and the aerosol number size distribution (Fig. II.3.1). All these instruments exploit the sensitivity of the optical detection. OPC can count particles and estimate the size distributions of accumulation mode and coarse particles. More accurate sizing can be achieved exploiting aerodynamic forces (using APSs, aerodynamic particle sizers) or, for smaller particles, their electrical mobility in a magnetic field (with DMAs, differential mobility analyzers, Flagan 1998). The differential mobility particle sizer (DMPS) is DMA coupled to a CPC, and it is by far the most common and accurate instrument for the determination of the number size distributions of ultrafine, Aitken and accumulation mode aerosol particles. DMA and CPC were revolutionary instruments in the aerosol science and they have been used in smart arrangements to characterize several properties of aerosol particles. For instance, a tandem DMA assemble called H-TDMA (hygroscopicity tandem DMA) is used to measure the particle growth from a dry to a humidified atmosphere, hence allowing determination of the aerosol water content as a function of relative humidity.

Measuring particle mass online is a challenging task, because of the very small mass that can be accumulated with a high-frequency sampling. The microbalances equipped with an oscillating tapered element on which the aerosol is continuously deposited are the only available technical solutions for measuring the aerosol mass with a resolution higher than 1 min^{-1} (Patashnick and Rupprecht, 1991). The original products called TEOMs are not widespread because they need to dry the sample heating it at 50°C causing substantial mass losses by evaporation. However, the new version equipped with a FDMS (filter dynamic measurement system) can account for the semivolatile material and it is a promising solution.

In the off-line methods, aerosol particles are collected on a filter for subsequent gravimetry, chemical analysis or for observation using an electron microscope (Fig. II.3.2). For instance, for air quality monitoring purposes, filters are collected typically on a daily basis for gravimetric determination of PM_{10} or $PM_{2.5}$. Routine measurements employ fully automated sampling equipments, called sequential samplers, which can be left unattended for days. The chemical methods that have been used to characterize atmospheric aerosol samples involve a large diversity of techniques that cannot be reviewed comprehensively in this chapter. However, the techniques that allowed the higher recovery, in terms of aerosol mass speciated, are, for $PM_{2.5}$, ion chromatography (IC) and evolved gas analysis (EGA), which determine the water-soluble ionic composition and the carbon concentration, respectively. Atomic absorption spectroscopy (AAS), particle-induced X-ray

emission (PIXE) and other techniques for the quantification of aluminium, silica and metals can account for a non-negligible fraction of $PM_{2.5}$ and a major fraction of PM_{10}. In principle, the mass apportioned into chemical species should approach the aerosol mass obtained by gravimetric determination. However, the closure of the aerosol mass budget is a challenging exercise, because of the uncertainty associated with the amount of oxygen and water contained in the organic matter and in the mineral fraction (Putaud et al., 2000). This problem is more severe for the organic matter which can exhibit a very variable stoichiometry and a very complex molecular composition. Scholars speculate that an aerosol sample can contain 10,000 to more than 100,000 individual organic compounds, each occurring in very low concentrations. On the other hand, state-of-the-art high-resolution mass spectrometric techniques are able to determine the molecular formulas of up to 3,000 compounds (Wozniak et al. 2008). Such techniques are not designed for routine analyses and for samples collected in remote areas where the sampled mass is low and sensitivity of the analytical techniques is critical. Overall, our understanding of the chemical composition of the aerosol organic carbon is still unsatisfactory for most environments, although a lot of new information has been gained in the last 10 years (Fuzzi et al., 2006).

The determination of the aerosol mass size distribution and the size-resolved chemical composition has been attempted using *cascade impactors* (Hering et al., 1978), which allow the collection of aerosol particles in different size intervals on different collection plates, which are then weighed and analysed at the same manner of PM_{10} and $PM_{2.5}$ filters. The number of the stages of cascade impactors varies between 5 and 15 for the size range 0.05–20 μm, hence the size resolution is coarse if compared to that of volume size distributions obtained by DMPS. The number of impactor stages is limited not only by the efficiency of the inertial separation (which is lower compared to that based on the electrical mobility) but also by the need of ensuring enough aerosol mass to be deposited on each impactor plate for subsequent weighing and analysis. Another limiting factor is the chemical analysis, which can be very labour intensive and time expensive. As a result, multistage impactors are not used for monitoring purposes and a very few climatologies of the aerosol composition based on impactor measurements are available in the literature (Cabada et al., 2004). On the contrary, cascade impactors have been widely used in field campaigns (e.g. Cavalli et al., 2006; Herner et al., 2006). An example of a time series of impactor measurements of the aerosol mass distribution taken in parallel with online measurements of PM_{10} and $PM_{2.5}$ from TEOM is given in Fig. II.3.4.

The off-line (i.e. filter-based and impactor-based) techniques allow a more sophisticated chemical characterization than online techniques, but sensitivity, and consequently time resolution, is much lower and it is further reduced by the interference of the substrate matrix with the analysis (the “blank”). Another problem of the off-line techniques is that the time-integrated sampling over a filter or another collection substrates can cause modifications of the aerosol mass and composition, which are usually referred to as *sampling artefacts*. Examples of sampling artefacts are the collection of vapours by the matrice of the filter or the evaporation of semivolatile constituents of the aerosol. There are several technical solutions for

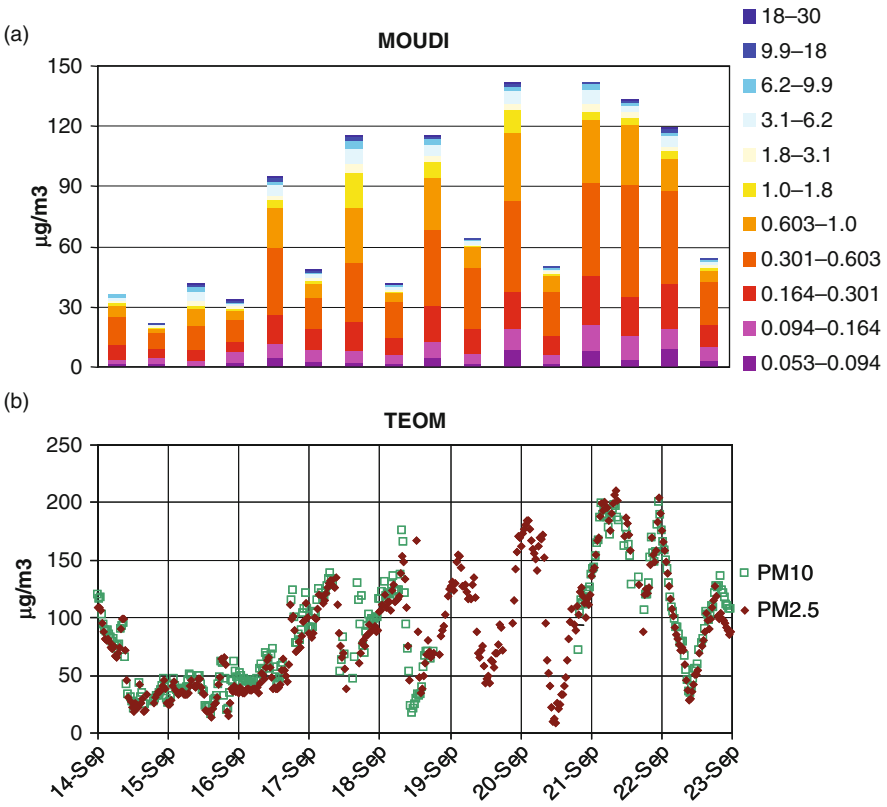

Fig. II.3.4 Measurement of aerosol mass **a** off-line with a cascade impactor (MOUDI: micro-orifice uniform deposition impactor) and **b** online with a tapered element oscillating microbalance (TEOM). MOUDI provides the size-segregated mass in 11 size ranges with 12-h time resolution. The upper and lower size limits (diameters in micrometers) are given in the legend on the right. Two TEOM systems were used equipped with PM_{10} and $PM_{2.5}$ inlets. Time resolution of TEOM measurements is here 30 min

limiting the sampling artefacts but they are not universal and must be evaluated specifically for each experiment.

In order to overcome these major limitations of the off-line chemical analyses, new instruments have been designed without any filter or other sampling substrates and the chemical characterization is performed online (Fig. II.3.3). The particle-into-liquid sampler (PILS) allows the measurement of water-soluble ions and carbon with a time resolution of 5–10 min (Orsini et al., 2003). The time resolution is even higher for the techniques employing mass spectrometry for detection (Heard 2006). The aerosol mass spectrometer (AMS) from Aerodyne is able to measure the concentration of major non-refractory aerosol chemical compounds and provide information on the organic chemical composition and it is also able to measure the size distribution of selected compounds (Canagaratna et al., 2007).

The aerosol–TOF–mass spectrometer (ATOFMS) from TSI provides a more qualitative information on the chemical composition but it is sensitive also to refractory compounds, and it provides the composition of individual particles (Murphy 2007). These instruments represented a real breakthrough for the aerosol chemical measurements. Still, the information that can be gained by their use is less sophisticated than that provided by the off-line methods, especially in respect to the organic molecular composition. At present, PILS and AMS are widely used in the aerosol characterization experiments and are able to provide unsurpassed information about the aerosol processes at short timescales, but they have not been designed for monitoring purposes. By contrast, the traditional samplers employing filters are robust, weather resistant and relatively cheap and are still the best solution for monitoring networks and for routine sampling in remote places.

3 Strategies for Ground-Based Aerosol Observations

We can conclude from the above discussion that an ideal instrument or a simple set of instruments for measuring all relevant properties of the atmospheric aerosol do not exist and appropriate solutions must be identified for the specific applications.

So far, two general strategies have been pursued for implementing ground-based observation systems for atmospheric aerosols (Heard et al., 2006): (1) continuous measurements of the aerosol concentrations from networks of stations covering different spatial scales and (2) multiplatform-intensive observation periods at the regional scale (field campaigns).

In the case of monitoring networks, only the more cost-effective, automated and robust aerosol instruments are employed. For instance, for air quality monitoring in the urban environment, normally only the determination of the daily mass concentrations of PM_{10} and, less commonly, $PM_{2.5}$ is performed. In Europe, routine analysis of the aerosol chemical composition is performed by the EMEP (European Monitoring and Evaluation Programme) network, which, however, has a rather patchy spatial coverage. Another network of stations, equipped with instruments for measuring both the aerosol optical properties, the number size distribution and the chemical composition has just become operative in the frame of the project EUSAAR (European Supersites for Atmospheric Aerosol Research, http://www.eusaar.net/). The monitoring networks for the chemical composition are more diffused in the USA, with the IMPROVE (Interagency Monitoring of Protected Visual Environments, http://vista.cira.colostate.edu/improve/) and the STN (EPA Speciation Trends Network).

In remote locations, also the maintenance needs and power consumption can be limiting factors. Fully automated, standalone, weather-resistant instruments, powered by solar cells and transmitting the data via satellite connection, like the photometers of the AERONET network, are definitely ideal instruments to be used for monitoring purposes. Analogous instruments for the in situ measurement of the aerosol concentration and composition have not been developed yet.

Consequently, such measurements rely on the existence of permanent stations, which can guarantee power and maintenance to the aerosol instruments even in remote locations (Bonasoni et al., 2008; Jourdain et al., 2008).

During multiplatform regional experiments, aerosol measurements are taken simultaneously in situ, using mobile platforms (ships, aircrafts), and by satellite remote sensing, over a spatial scale of 500–1,000 km for ca. 1 month. During these experiments, the state-of-the-art instrumentation is deployed, trying to achieve a comprehensive characterization of the aerosol concentration, composition and distribution, attempting to expand our knowledge about aerosol processes and impacts. The regional experiments have been conducted in several areas of the world but always for limited periods of time and collecting more data in clear-sky conditions. Comparison of the results obtained in the different regions (often after many years between one experiment and the other) is affected by the technological development of the instruments and by the changes in the emissions. Observations were more concentrated in polluted marine coastal areas, where the satellite measurements are more accurate (Quinn and Bates, 2005). The regional experiments have taught us a lot about how aerosols form and are transported and processed in the atmosphere and about their impacts on light extinction and on cloud properties (Quinn et al., 2005; Guo et al., 2007). However, such load of data are biased geographically and temporally, therefore, care must be taken when extrapolating these results to unexplored environments and weather regimes.

The regional studies have shown that the intrinsic limitations of the various aerosol instruments can be overcome by collocating measurements from different observing systems, including ground-based in situ and remote sensing systems, research aircrafts and the satellite sensors. Still, some important issues remain unsolved, e.g. assessing the spatial distribution and chemical composition of ultrafine particles, quantifying the biogenic and anthropogenic sources of aerosol organic matter and understanding the effects of aerosol on precipitating clouds at the global scale.

References

Bohren CF, Huffman DR (1983) Absorption and scattering by small particles. Wiley, New York, NY

Bonasoni P, Laj P, Angelini F, Arduini J, Bonafè U, Calzolari F, Cristofanelli P, Decesari S, Facchini MC, Fuzzi S, Gobbi GP, Maione M, Marinoni A, Petzold A, Roccato F, Roger JC, Sellegri K, Sprenger M, Venzac H, Verza GP, Villani P, Vuillermoz, E (2008) The ABC-Pyramid Atmospheric Research Observatory in Himalaya for aerosol, ozone and halocarbon measurements. Sci Total Environ 391:252–261

Cabada JC, Rees S, Takahama S, Khlystov A, Pandis SN, Davidson CI, Robinson AL (2004) Mass size distributions and size resolved chemical composition offine particulate matter at the Pittsburgh supersite. Atmos Environ 38:3127–3141

Canagaratna MR, Jayne JT, Jimenez JL, Allan JD, Alfarra MR, Zhang Q, Onasch TB, Drewnick F, Coe H, Middlebrook A, Delia A, Williams LR, Trimborn AM, Northway MJ, DeCarlo PF, Kolb CE, Davidovits P, Worsnop DR (2007) Chemical and microphysical characterization of ambient aerosols with the aerodyne aerosol mass spectrometer. Mass Spectromet Rev 26:185–222

Cavalli F, Facchini MC, Decesari S, Emblico L, Mircea M, Jensen NR, Fuzzi S (2006) Size-segregated aerosol chemical composition at a boreal site in southern Finland, during the QUEST project. Atmos Chem Phys 6:993–1002

Dockery DW, Pope CA, Xu XP, Spengler JD, Ware JH, Fay ME, Ferris BG, Speizer FE (1993) An association between pollution and mortality in six US cities. N Engl J Med 329:1753–1759

Finlayson-Pitts BJ, Pitts JN, Jr (2000) Chemistry of the upper and lower atmosphere. Elsevier. Amsterdam, The Nederlands (ISBN: 978-0-12-257060-5)

Flagan RC (1998) History of electrical aerosol measurements. Aerosol Sci Technol 28:301–380

Fuzzi S, Andreae MO, Huebert BJ, Kulmala M, Bond TC, Boy M, Doherty SJ, Guenther A, Kanakidou M, Kawamura K, Kerminen V-M, Lohmann U, Russell LM, Pöschl U (2006) Critical assessment of the current state of scientific knowledge, terminology, and research needs concerning the role of organic aerosols in the atmosphere, climate, and global change. Atmos Chem Phys 6:2017–2038

Guo H, Penner JE, Herzog M, Pawlowska H (2007) Examination of the aerosol indirect effect under contrasting environments during the ACE-2 experiment. Atmos Chem Phys 7:535–548

Heard DE (ed) (2006) Analytical techniques for atmospheric measurement. Blackwell Oxford, (ISBN 1405123575)

Hering SV, Flagan RC, Friedlander SK (1978) Design and evaluation of a new type of low-pressure impactor. I. Environ Sci Technol 12:667–673

Herner JD, Ying Q, Aw J, Gao O, Chang DPY, Kleeman MJ (2006) Dominant mechanisms that shape the airborne particle size and composition distribution in central California. Aerosol Sci Technol 40:827–844

Jourdain B, Preunkert S, Cerri O, Castebrunet H, Udisti R, Legrand M (2008) Year-round record of size-segregated aerosol composition in central Antarctica (Concordia station): Implications for the degree of fractionation of sea-salt particles. J Geophys Res A:113. doi:10.1029/2007JD009584

Kaufman YJ, Koren I (2006) Smoke and pollution aerosol effects on cloud cover. Science 313: 655–658

Kulmala M, Vehkamäki H, Petäjä T, Dal Maso M, Lauri A, Kerminen V-M, Birmili W, McMurry PH (2004) Formation and growth rates of ultrafine atmospheric particles: A review of observations. J Aerosol Sci 35:143–176

Murphy DM (2007) The design of a single particle laser mass spectrometers. Mass Spectromet Rev 26:150–165

Orsini DA, Ma YL, Sullivan A, Sierau B, Baumann K, Weber RJ (2003) Refinements to the particle-into-liquid sampler (PILS) for ground and airborne measurements of water-soluble aerosol composition. Atmos Environ 37:1243–1259

Patashnick K, Rupprecht EG (1991) Continuous PM_{10} measurements using the tapered element oscillating microbalance. J Air Waste Manag Assoc 41:1079–1083

Putaud J-P, Van Dingenen R, Mangoni M, Virkkula A, Raes F, Maring H, Prospero JM, Swietlicki E, Berg OH, Hillamo R, Makela T (2000) Chemical mass closure and assessment of the origin of the submicron aerosol in the marine boundary layer and the free troposphere at Tenerife during ACE-2. Tellus B 52:141–168

Quinn PK, Bates TS (2005) Regional aerosol properties: comparisons of boundary layer measurements from ACE 1, ACE 2, Aerosols99, INDOEX, ACE Asia, TARFOX, and NEAQS. J Geophys Res A 110. doi:10.1029/2004JD004755

Quinn PK, Bates TS, Baynard T, Clarke AD, Onasch TB, Wang W, Rood MJ, Andrews E, Allan J, Carrico CM, Coffman D, Worsnop D (2005) Impact of particulate organic matter on the relative humidity dependence of light scattering: a simplified parameterization. Geophys Res Lett 32. doi:10.1029/2005GL024322

Ramanathan V, Crutzen PJ, Kiehl JT, Rosenfeld D (2001) Atmosphere – aerosols, climate and the hydrological cycle. Science 294:2219–2224

Van Dingenen R, Raes F, Putaud J-P, Baltensperger U, Charron A, Facchini M-C, Decesari S, Fuzzi S, Gehrig R, Hansson H-C, Harrison RM, Hüglin C, Jones AM, Laj P, Lorbeer G, Maenhaut

W, Palmgren F, Querol X, Rodriguez S, Schneider J, ten Brink H, Tunved P, Tørseth K, Wehner B, Weingartner E, Wiedensohler A, Wåhlin P (2004) A European aerosol phenomenology-1: physical characteristics of particulate matter at kerbside, urban, rural and background sites in Europe. Atmos Environ 38:2561–2577

Wozniak AS, Bauer JE, Sleighter RL, Dickhut RM, Hatcher PG (2008) Molecular characterization of aerosol-derived water soluble organic carbon using ultrahigh resolution electrospray ionization Fourier transform ion cyclotron resonance mass spectrometry. Atmos Chem Phys 8(Discussion):6539–6569

Chapter II.4
Weather Radar Remote Sensing of Volcanic Ash Clouds for Aviation Hazard and Civil Protection Applications

Frank S. Marzano

1 Introduction

The injection of large amounts of fine and coarse ash and rock fragments and corrosive gases into the troposphere and lower stratosphere is usually followed by a long lasting ashfall which can cause a variety of damages (Wilson, 1972). When volcanic ash accumulates on buildings, its weight can cause roofs to collapse. Because wet ash conducts electricity, it can cause short circuits and failure of electronic components, especially high-voltage circuits and transformers. Eruption clouds and ash fall commonly interrupt or prevent telephone and radio communications in several ways, including physical damage to equipment and frequent lightning due to electrically charged ash particles. Even more important, volcanic ash clouds are an increasing hazard to aviation safety because of growing air traffic volumes that use more efficient and susceptible jet engines (Miller and Casadevall, 2000). Several hundreds of commercial aircrafts have unexpectedly encountered volcanic ash in flight and at airports in the past 15 years. Tens of these encounters caused in-flight loss of jet engine power, which nearly resulted in the crash of the airplane. A range of damages may occur to airplanes that fly through an eruption cloud depending on the concentration of volcanic ash and gas aerosols in the cloud, the length of time the aircraft actually spends in the cloud, and the actions taken by the pilots to exit the cloud itself (Maki and Doviak, 2001). Fine ash can also be a health hazard as aerodynamically fine particles will be taken into the lungs during breathing.

Real-time and areal monitoring of a volcano eruption, in terms of its intensity and dynamics, is not always possible by conventional visual inspections, especially during worse visibility periods which are quite common during eruption activity. Remote sensing techniques both from ground and from space represent unique tools to be exploited (Rose and Schneider, 1996; Rose et al., 2000; Wen and Rose, 1994). Microwave weather radars can gather three-dimensional information of atmospheric scattering volumes up several hundreds of kilometers, in all weather conditions, at a

F.S. Marzano (✉)
Department of Electronic Engineering, Sapienza University of Rome, Rome, Italy;
Centre of Excellence CETEMPS, University of L'Aquila, L'Aquila, Italy
e-mail: marzano@die.uniroma1.it

D. Cimini et al. (eds.), *Integrated Ground-Based Observing Systems*,
DOI 10.1007/978-3-642-12968-1_11,

fairly high spatial resolution (less than a kilometer) and with a repetition cycle of few minutes (Harris and Rose, 1983; Rose et al., 1995; Maki and Doviak, 2001; Lacasse et al., 2004; Marzano et al., 2006a, b). Ground-based radar systems represent one of the best methods for determining the height and volume of volcanic eruption clouds. Single-polarization Doppler radars can measure horizontally polarized power echo and Doppler shift from which ash content and radial velocity can be, in principle, extracted.

In this work, in order to quantitatively evaluate the ash retrieval by weather radars, a prototype algorithm for volcanic ash radar retrieval (VARR) is formulated and discussed. Starting from measured single-polarization reflectivity, the estimation method has been based on two cascade steps: (i) a classification of eruption regime and volcanic ash category and (ii) estimation of ash concentration and fall rate. Finally, the VARR algorithm is applied to C-band radar data available during the eruption of the Grímsvötn volcano in Iceland during November 2004, discussing the obtained results.

2 Volcanic Ash Radar Retrieval

The retrieval of ash concentration C_a and fall rate R_a from measured radar reflectivity Z_{Hm} is a typical remote sensing inverse problem. As an inverse problem, it exhibits properties of non-uniqueness and instability of the solution. In order to circumvent this difficulty, the inverse problem can be stated as an estimation problem in a probabilistic framework. A crucial role in this approach is played by the a priori information which consists of all knowledge about the geophysical solution, possibly translated as constraints within the inverse problem. In our context this means to construct an effective model of ash cloud microphysics for remote sensing purposes.

The microwave weather radar response is mainly controlled by the atmospheric particle size distribution (PSD) within the range volume bin. In case of ash cloud formation processes within a humid environment, we may suppose to have two distinct phenomena within an observed range volume: (i) coexistence of ash particle and hydrometeors without mixing processes and (ii) aggregation of ash particles with hydrometeors to form a new mixed-phase particle.

2.1 Microwave Model

There is a fairly large consensus about the capability to model PSD through either a normalized Gamma or Weibull distribution (Marzano et al., 2006a). In case of a multi-mode size distribution, it is always possible to suppose more than one analytical PSD characterized different mean sizes and total number of particles. In this work, the size distribution $N_p(r)$ of an ensemble of particles p has been modeled by factorizing its analytical expression as follows:

$$N_p(r) = N_{tp} F_p(r), \tag{1}$$

where r is the particle radius and N_{tp} the total particle number. The generalized Gamma function F_{p} in Eq. (1) can be interpreted as the probability to find a particle within a radius bin and is given by,

$$F_{\mathrm{p}}(r) = \frac{1}{\Gamma(\nu_{\mathrm{p}})}\left(\frac{r}{r_{\mathrm{cp}}}\right)^{\nu_{\mathrm{p}}-1}\frac{1}{r_{\mathrm{cp}}}\exp\left(-\frac{r}{r_{\mathrm{cp}}}\right), \tag{2}$$

where ν_{p} is the PSD skewness parameter, r_{cp} is the PSD characteristic radius, and Γ is the complete Gamma function. The particle total number N_{tp} of particles, having a mixing ratio q_{p} and a density ρ_{p}, is expressed by

$$N_{\mathrm{tp}} = \left(\frac{q_{\mathrm{p}}}{r_{\mathrm{cp}}^3}\frac{3}{4\pi\rho_{\mathrm{p}}}\frac{\Gamma(\nu_{\mathrm{p}})}{\Gamma(\nu_{\mathrm{p}}+3)}\right). \tag{3}$$

Microwave scattering from ash particles and from cloud water and ice droplets satisfies the Rayleigh approximation. Under this condition, the radar reflectivity factor at horizontal polarization Z_{Hp} due to an ensemble of particles p is expressed as the sixth moment of PSD as follows:

$$Z_{\mathrm{Hp}} = \eta_{\mathrm{Hp}}\frac{\lambda^4}{\pi^5|K_{\mathrm{p}}|^2} = \int_0^\infty r^6 N_{\mathrm{p}}(r)dr = N_{\mathrm{tp}}r_{\mathrm{cp}}^6\frac{\Gamma(\nu+6)}{\Gamma(\nu)}, \tag{4}$$

where η_{Hp} is the radar volumetric reflectivity, λ the wavelength, and K_{p} the dielectric factor of the particle ensemble. The last term of Eq. (4) is obtained by substituting the analytical Gamma PSD given in Eq. (1). The advantage of using a generalized gamma function is that it can be obtained an analytical solution for any PSD moments.

2.2 Retrieval Algorithm

In the case of Plinian and sub-Plinian volcanic eruptions, we can exploit both experimental and modeling results to characterize ash particles (Marzano et al., 2006b). We have defined three classes (or modes) of ash sizes: fine ash, coarse ash, and lapilli. As a synthesis of available volcanic information, within each class we have supposed a Gaussian random distribution for: (i) D_n with average value m_{Dn} equal to 0.01, 0.1, and 1 mm for fine, coarse, and lapilli ash and a standard deviation $\sigma_{D_n} = 0.2m_{D_n}$ and (ii) C_{a} with mean value $m_{C\mathrm{a}}$ equal to 0.1, 1, and 5 g/m^3 for light, moderate, and intense concentration regimes and a standard deviation $\sigma_{c_a} = 0.5m_{c_a}$. In total we have a number $N_{\mathrm{c}} = 9$ of classes: fine ash, coarse ash, and lapilli each of them in low, moderate and intense concentration. By exploiting the previous microphysical model of pure ash, the physically based volcanic ash radar retrieval (VARR) algorithm can be structured as follows: (i) detection of the ash class from the measured reflectivity Z_{Hm} within each range bin by using a Bayesian identification

technique and (ii) retrieval of the ash amount and fall rate from the measured Z_{Hm} by applying a polynomial regression method.

For what concerns the classification step, its aim is related to the possibility to automatically discriminate between ash categories which were defined as fine, coarse, and lapilli sizes. In the overall retrieval scheme, classification may represent a first qualitative output before performing parameter estimation. Maximum *a posteriori* probability (MAP) criterion can be used to carry out cloud classification in a model-based supervised context. Using the Bayes theorem, if c is the ash class, then the conditional probability density function (PDF) of a class c given a measurement Z_{Hm} reduces to (Marzano et al., 2006b)

$$\hat{c} = \mathrm{Mode}\left[p(c\,|Z_{\mathrm{Hm}})\right], \tag{5}$$

where Mode is the modal value of the posterior PDF $p(c|Z_{\mathrm{Hm}})$. Assuming a Gaussian probability framework to describe $p(c|Z_{\mathrm{Hm}})$and exploiting the Bayes theorem, computing Eq. (5) means to know the reflectivity mean m_Z (also called class centroid) and standard deviation σ_Z of Z_{Hm} for each ash class c. The prior PDF can be used to subjectively weight each class as a function of other available information (such as coincident satellite and/or in situ data).

Once an ash class is detected, then an estimate of ash concentration and fall rate is possible. A way to approach the quantitative retrieval problem is to adopt a statistical parametric model to describe the relation P–Z_{Hm} where P stands for either C_{a} or R_{a}. Assuming a power-law model, we can write the estimated quantity for each class c as (Marzano et al., 2006b)

$$\begin{cases} \hat{C}_{\mathrm{a}}^{(c)} = \alpha \left[Z_{\mathrm{H_m}}\right]^{\beta} \\ \hat{R}_{\mathrm{a}}^{(c)} = \gamma \left[Z_{\mathrm{H_m}}\right]^{\delta} \end{cases}, \tag{6}$$

where $c = 1{:}N_{\mathrm{c}}$ and the "hat" indicates estimated quantity.

3 Case Study

An eruption started in Grímsvötn in the evening of November 1, 2004 and was observed by a C-band weather radar located in Keflavik, Iceland. The aim of this section is to show an application of VARR to experimental data, but the complete analysis of the volcanic eruption is beyond the scopes of this work. The Keflavik weather radar is an Ericsson C-band radar without a Doppler capability (Vogfjörd et al., 2005). It is located about 3 km north of the Keflavik international airport at 47 m above sea level in southwest Iceland. Its main operational characteristics are: transmitted peak power of 245.2 kW, antenna beam-width of 0.9°, pulse duration of 2.15 μm, pulse repetition frequency of 250 Hz, and antenna gain of 44.9 dB. The radar system at Keflavik is remotely operated by the Icelandic Meteorological Office (IMO) in Reykjavik and it has been recently updated. Currently, scanned

images are routinely acquired every 20 min for normal weather monitoring and every 5 min during volcanic eruptions. The lowest detectable height by weather radar is a function of the elevation angle of the radar beam, the distance of the target from the radar and the earth's curvature. Using the Keflavik radar characteristics, this relation can be used to infer the lower and upper radar detection limits above the Grímsvötn volcano.

3.1 Grímsvötn Volcano Eruption

Iceland seismic structure is of relevant importance for Icelandic volcanic plume evolution. On the morning of November 1, a jökulhlaup tremor was observed on the seismic records at the Grímsfjall station. In the early morning of Nov. 1, an earthquake swarm began beneath Grímsvötn and at 20:10 earthquake magnitudes increased and the swarm intensified. An eruption warning was sent to the Civil Defense at 20:10, November 1. During the next 2 h about 160 earthquakes were recorded with magnitudes up to 2.8. Volcanic tremor was first observed and after an earthquake with a magnitude of 2.7 occurred at 21:50. The frequency of the tremor energy was concentrated around 1 Hz. The intensity of the tremor increased in the next hours. The volcanic tremor was continuous throughout the night. An increase in power between 04:00 and 05:00 h on November 2, 2004 was observed.

Radar volume scans were continuously acquired and data have been made available from 23:00 on November 1, 2004 till 06:00 on November 2, 2004 every half an hour (Vogfjörd et al., 2005). Reflectivity data were radially averaged to 2 km. From the available radar imagery it was observed that the eruption plume increased in size around 04:00. Figure II.4.1 shows the plan-position indicator (PPI) radar image at 0.5° elevation angle of the measured reflectivity field at the same time. The image is zoomed, for clarity, around the volcano vent placed at a location around 255 km on x and 42 km on y.

The signal of volcanic cloud is quite evident from both PPI and RHI signatures with values up to 35 dBZ. Notice that the height of this signature avoids any misinterpretation as a rain cloud radar echo, whereas the minimum detectable reflectivity factor (MDZ) of the Keflavik radar at 260 km is about –5 dBZ. At the time of observation after about 5 h from the first radar ash echo, the volcanic plume has been already advected toward northwest and the reflectivity maximum contour results to be slightly misplaced with respect to the volcano vent (indicated by a triangle). The extension of the ash cloud area is about 1,000 km^2 with an average wind velocity of about 10 km/h.

3.2 Results

The measured reflectivity images can be then inverted to retrieve the ash concentration and ashfall rate by applying the VARR technique. If the VARR classification

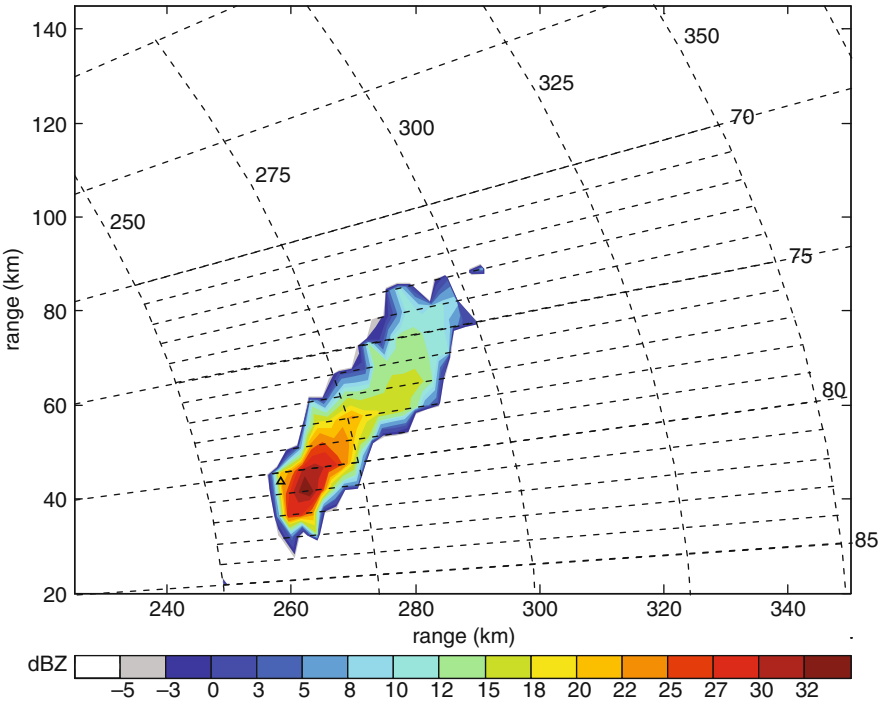

Fig. II.4.1 Plan-position indicator (PPI) at 0.5° elevation of the measured horizontally polarized reflectivity at 04:00 UTM during the Grímsvötn volcano eruption on November 2, 2004. The *triangle* indicates the volcano vent

algorithm is applied, from radar PPI data, we can detect the class index displayed in Fig. II.4.2. The code of the ash classes is listed in the caption of the figure itself. We note that the reflectivity peak is associated to a light concentration of lapilli which corresponds to an average reflectivity of 34 dBZ. Surrounding this area and closer to the volcano vent, we note the presence of an intense concentration of coarse ash whose average reflectivity is about 21 dBZ. Around this high-reflectivity plume along the northwest direction, there is a dispersion of moderate and light concentration of coarse corresponding to an average reflectivity of 14 and 4 dBZ, respectively. Fine ash is only weakly detected at the border of the PPI sector. This ash areal distribution is quite realistic as the eruption has started few hours before and there is an experimental evidence that lapilli can be suspended in air for some hours after the explosion. A sorting of ash particles is also typical during the evolution of the erupted volcanic cloud. Unfortunately, we do not have any chance to verify these results within the ash plume.

Figure II.4.3 shows the results in terms of estimated ash concentration C_a, obtained by applying the VARR technique given in Eq. (13) to the measured reflectivity PPI data. Values of C_a up 6 g·m^{-3} and of C_a up 31 kg·h^{-1}·m^{-2} are noted. It is worth underlining that the C_a estimated pattern does not resemble the measured

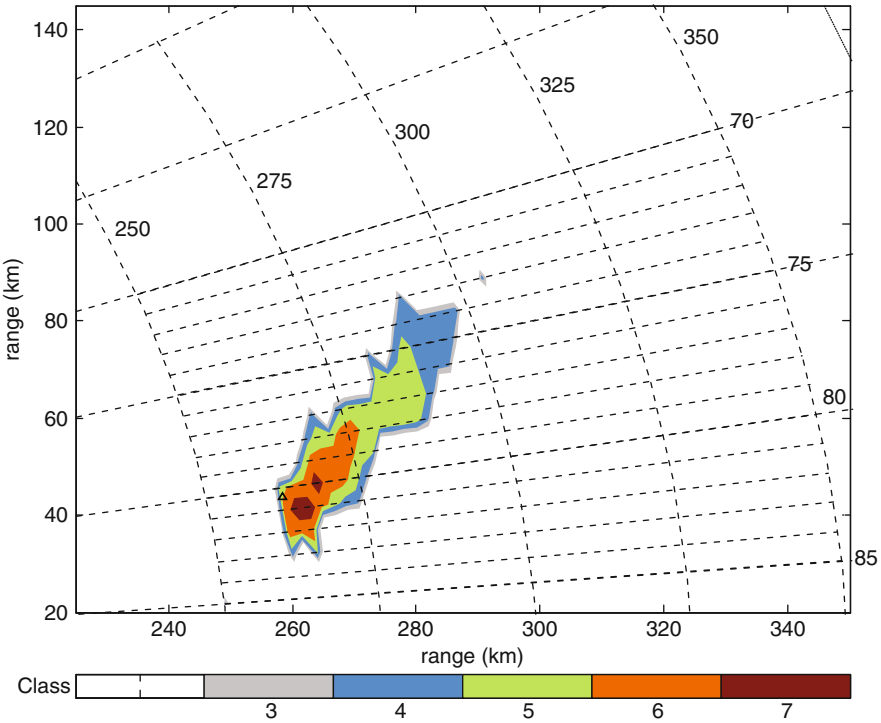

Fig. II.4.2 Plan-position indicator (PPI) at 0.5° elevation of the estimated class index c, derived from the PPI scan shown in Fig. II.4.1 by applying the VARR classification algorithm. Classes are enumerated as 3 = (intense concentration of fine ash), 4 = (light concentration of coarse ash), 5 = (moderate concentration of coarse ash), 6 = (Intense concentration of coarse ash), 7 = (light concentration of lapilli). The *triangle* indicates the volcano vent

Z_H PPI pattern in the sense that we would have expected the larger concentration in correspondence of higher reflectivity values. This difference may be explained by looking at Fig. II.4.1 taking into account the estimated ash class pattern of Fig. II.4.2. In fact, higher values of radar reflectivity are associated to a low concentration of lapilli. This means that, in order to give a comparable radar reflectivity, the concentration of coarse ash must be much larger than that of lapilli.

4 Concluding Remarks

The potential of using ground-based weather radar systems for volcanic ash cloud detection and quantitative retrieval has been evaluated. The relationship between radar reflectivity factor, ash concentration, and ashfall rate has been statistically derived for various eruption regimes and ash sizes by applying a radar reflectivity microphysical model previously developed. A prototype algorithm for volcanic

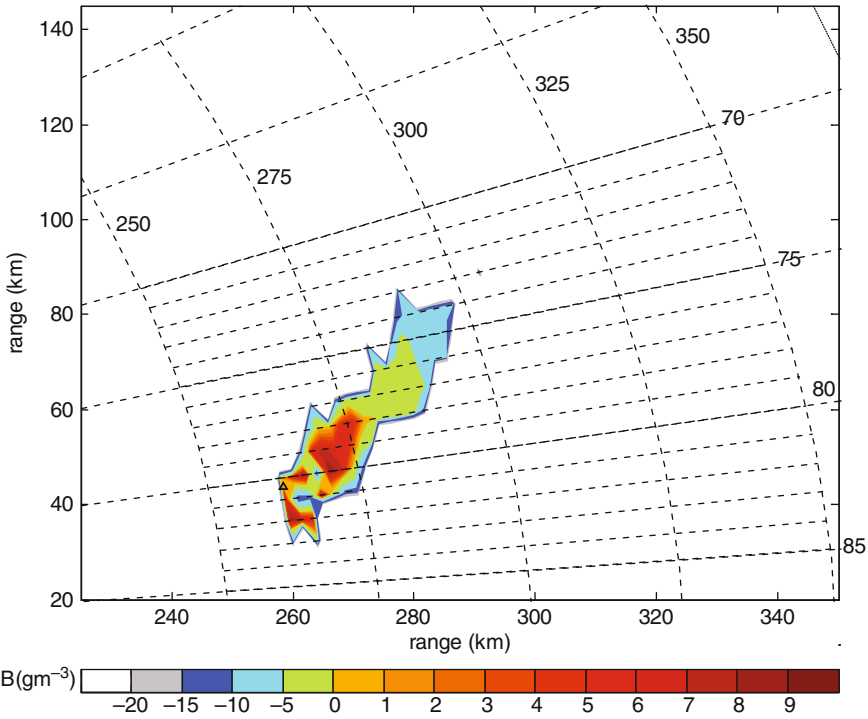

Fig. II.4.3 Plan-position indicator (PPI) at 0.5° elevation of the estimated ash concentration C_a [expressed in dB or 10 Log_{10}(g m^{-3})], derived from the PPI scan shown in Fig. II.4.1 by applying the VARR algorithm. The *triangle* indicates the volcano vent

ash radar retrieval (VARR) has been proposed and applied. Starting from measured single-polarization reflectivity, the inversion technique to retrieve ash concentration and fall rate has been based on two cascade steps: (i) a classification of eruption regime and volcanic ash category and (ii) estimation of ash concentration and fall rate.

An application of the VARR technique has been finally shown taking into consideration the eruption f the Grímsvötn volcano in Iceland on November 2004. Volume scan data from a Doppler C-band radar, located at 260 km from the volcano vent, have been processed by means of VARR. Examples of the achievable VARR products have been discussed.

References

Harris DM, Rose WI (1983) Estimating particle sizes, concentrations and total mass of ash in volcanic clouds using weather radar. J Geophys Res 88:10969–10983

Lacasse C, Karlsdóttir S, Larsen G, Soosalu H, Rose WI, Ernst GGJ (2004) Weather radar observations of the Hekla 2000 eruption cloud. Iceland Bull Volcanol 66:457–473

Maki M, Doviak RJ (2001) Volcanic ash size distribution determined by weather radar. In: Proceedings of international geoscience and remote sensing symposium 2001, New South Wales, Sydney, Australia, 9–13 July 2001

Marzano FS, Vulpiani G, Rose WI (2006a) Microphysical characterization of microwave radar reflectivity due to volcanic ash clouds. IEEE Trans Geosci Remote Sens 44:313–327

Marzano FS, Barbieri S, Vulpiani G, Rose WI (2006b) Volcanic cloud retrieval by ground-based microwave weather radar. IEEE Trans Geosci Remote Sens 44(11):3235–3246

Miller TP, Casadevall TJ (2000) Volcanic ash hazards to aviation. In: Sigurdsson H (ed) Encyclopaedia of volcanology. Academic Press, San Diego, CA, pp 915–930

Rose WI, Kostinski AB, Kelley L (1995) Real time C band radar observations of 1992 eruption clouds from Crater Peak/Spurr Volcano, Alaska. US Geol Surv Bull 2139:19–26 (Spurr eruption, Keith T (ed))

Rose WI, Schneider DJ (1996) Satellite images offer aircraft protection from volcanic ash clouds. EOS 77:529–532

Rose WI, Bluth GJS, Ernst GGJ (2000) Integrating retrievals of volcanic cloud characteristics from satellite remote sensors – a summary. Philos Trans R Soc A 358(1770):1585–1606

Vogfjörd KS, Jakobsdóttir SS, Gudmundsson GB, Roberts MJ, Ágústsson K, Arason T, Geirsson H, Karlsdóttir S, Hjaltadóttir S, Ólafsdóttir U, Thorbjarnardóttir B, Skaftadóttir T, Sturkell E, Jónasdóttir EB, Hafsteinsson G, Sveinbjörnsson H, Stefánsson R, Jónsson TV (2005) Forecasting and monitoring a subglacial eruption in Iceland. EOS 86(26):245–252

Wen S, Rose WI (1994) Retrieval of sizes and total masses of particles in volcanic clouds using AVHRR bands 4 and 5. J Geophys Res 99:5421–5431

Wilson L (1972) Explosive volcanic eruptions. J Geophys Res 30:381–392

Chapter II.5
An Integrated Observing System for Boundary Layer Monitoring at Concordia Station, Antarctica

S. Argentini and I. Pietroni

1 Introduction

Antarctica has a fundamental role in the global climate system; its ice sheet acts as a heat sink by extracting sensible heat flux from the atmosphere. Due to its remoteness and inaccessibility, yet relatively little is known about processes in the interior of the ice sheet. In the long Antarctic winter, when the shortwave radiation is not present, the surface is cooled continuously through negative net longwave radiation which is enabled by clear sky conditions and the very cold and dry overlying atmosphere. This energy loss is partially compensated by the turbulent and sub-surface heat fluxes which extract heat from both atmosphere and ice sheet, cooling the near surface air and snow. When a surface slope is present, the denser and colder mass of air adjacent to the surface is forced down-slope by a horizontal pressure gradient and deflected to the left by the Coriolis force. As a result the well-known katabatic winds take place. This situation can be occasionally interrupted by the horizontal advection of warm air masses or the presence of strong large-scale winds. On the other hand, during the Antarctic summer, the absorption of shortwave radiation introduces a diurnal cycle. The amount of solar radiation available to heat the surface is limited by the high surface albedo. However, the surface warming may cause a weak convection and the formation of a mixed layer can be observed on the plateau during daytime (Mastrantonio et al., 1999, Argentini et al., 2005).

A large atmospheric field experiment STABLEDC (study of the STABLE boundary layer at Dome C) was held at the Franch-Italian station of Concordia located on the Antarctic plateau at Dome C during 2004–2005. This was the first over wintering at Concordia. The aim of the field experiment was to test an observing system to study the processes occurring in the long-lived stable and the weak convective atmospheric boundary layers observed during winter and summer respectively, and to collect the parameters relevant for the atmospheric models.

S. Argentini (✉)
ISAC/CNR, via del Fosso del Cavaliere, 100, 00133 Roma, Italy
e-mail: s.argentini@isac.cnr.it

Submitted to ISSAOS 2007 Special Issue

D. Cimini et al. (eds.), *Integrated Ground-Based Observing Systems*,
DOI 10.1007/978-3-642-12968-1_12,

2 Site and Instrumentation

Dome C (75° 06' S, 123° 23' E) lies at 3,250 m a.s.l. on the East Antarctic plateau, approximately 1,000 km from the nearest coast on the top of a large dome, with no discernible slope, therefore it is not subjected to the typical katabatic winds observed in Antarctica (King and Turner, 1997). The annual mean wind speed is 3.4 m s^{-1} with extreme values up to 16 m s^{-1}. Monthly mean temperatures were −39°C in summer and –61°C in winter. Most of the time, strong surface inversions occur at Dome C, creating a large cold air source feeding the katabatic winds observed in some zones of confluence along the East Antarctic coast. In situ and ground-based remote sensing sensors were used to monitor the behaviour of the meteorological parameters. The instrumentation and the measurements done during the field experiment are listed in Table II.5.1.

Turbulence and radiation measurements were made in the period November 2004–February 2006. Turbulent fluxes of heat and momentum were measured using a Metek USA-1 thermo-anemometer (Sozzi and Favaron, 1996) installed on a 3.6 m mast above the snow surface; long- and shortwave radiation components were measured using Kipp & Zonen pyrgeometers and pyranometers installed 1 m above the snow surface. The heat flux within the snowpack was measured at a depth of 50 mm using a Campbell Scientific HFP01 heat flux plate. A mini-SODAR (SOund

Table II.5.1 Sensor and measured micrometeorological variable

Sensor	Measure
Radiometer mod.*CNR-1* (Kipp & Zonen) with two pyranometers (*CM3*) up and down and two pyrgeometers (*CG3*) up and down	*Radiative budget.* Incoming and outgoing shortwave and longwave radiation. – Net Radiation – Albedo
Conventional *HFP01* heat flux plates – 0, 5, 15, 30 and 50 cm	*Sub-surface energy fluxes, snow temperature profiles* – Snow heat fluxes
A sonic anemo-thermometer mod. *USA-1* (Metek) and a fast response LICOR *Lyman-alpha-hygrometer* (only summer)	*Energy budget*. – Turbulent fluxes (heat, water vapour, momentum)
13-m tower : thermometers, hygrometers and wind probes at 1.25, 2.5, 5, 10 and 13 m	*Surface layer profiles of mean variables*
A *triaxial Doppler mini-sodar* – range: 12–400 m, resolution: 13 m	*PBL measures.* Thermal structure of the ABL, boundary layer depth, and wind speed
Micro-lidar: 532-nm wavelength, range: 300 m	*PBL measures.* Aerosols content, aerosol phase (liquid water or ice cristal), particles size
Passive microwave radiometer MTP- 5P by Kipp & Zonen. Range: 0–600 m	*PBL measures.* Temperature, development and break down of atmospheric inversions
Radiosoundings	*Atmosphere.* Temperature, pressure, wind speed

Detection And Ranging) Doppler system (Mastrantonio et al., 1999) provided a continuous record of the structure of the atmospheric boundary layer along the year. A passive Meteorological Temperature Profiler (MTP-5P) (Kadygrov and Pick, 1998) was used for the remote measurement of the air temperature profile.

The instrumentation was placed approximately 500 m south of the main base buildings. Since the dominant wind direction is from the sector 150°–210° this ensured an unobstructed fetch over the measurement site.

In addition to the measurements described above, standard meteorological parameters – provided by the AWS (Automatic Weather Stations), and daily radiosonde profiles – were available from other projects.

For convenience, all subsequent results are presented with reference to local time. All time we use the term "night-time" or "nocturnal" we refer to the periods when the surface radiation balance is negative.

3 The Climatological Setting

Table II.5.2 shows the average values of the mean wind, temperature, and sensible heat flux for the period 14 December 2004–13 January 2006 and for the different seasons. The "seasons" have been defined as follows:

1° Summer: 14 December 2004 – 1 February 2005
Autumn: 1 February 2005 – 1 April 2005
Winter: 1 April 2005 – 15 September 2005
Spring: 15 September 2005 – 15 November 2005
2° Summer: 15 November 2005 – 13 January 2006

The annual mean wind speed is 4.4 m s^{-1} with extreme values (not shown in the table) up to 12 m s^{-1}. The annual mean temperature is –44°C. The lowest temperatures (–72°C) are observed during the winter while the highest temperatures (–29°C) are observed during the summer. Strong long-lived ground-based inversions occur most of the time at Dome C with the exception of the summer days during the hours of maximum insulation (and positive values of net radiation). These inversions

Table II.5.2 Mean values of the wind speed, temperature and sensible heat flux for the all measurement period

Period	All data	1° Summer	Autumn	Winter	Spring	2° Summer
Parameter						
Mean wind speed (ms^{-1})	4.4±2.0	3.5±1.6	4.2±1.7	4.9±2.0	4.8±2.2	4.0±2.0
Mean temperature (°C)	–44.8±12.2	–29.3±4.7	–47.2±7.8	–54.8±6.9	–46.8±7.6	–30.2±5.7
Mean sensible heat flux (Wm^{-2})	–4.5±10.4	3.2±8.9	–4.8±8.1	–10.6±8.8	–6.1±9.5	2.4±9.0

contribute to create a large cold air source producing and feeding the katabatic winds observed in most of the glaciers confluence zone along the East Antarctic coast. Few clouds are generally present in the sky above Dome C since cloud cover and precipitation decrease as one moves inland from the coast, and the frequency of occurrence of active weather systems is low (King and Turner, 1997). However Argentini et al. (2001) have shown that warming events are periodically observed at Dome C during the winter, during these periods the surface temperatures sometimes may reach the summer values. In correspondence of these warming events the wind direction changes from 180° (the most frequent wind direction) to 0° (which is from the coast), indicating that the warming events are correlated to phenomena originating along the coast (i.e. advection of warm air).

4 Measurements

4.1 Wind and Temperature Distributions, Time Behaviour of Some Meteorological Parameters

4.1.1 Wind Distribution

The frequency distribution of the wind for three velocity ranges (1 m $s^{-1} \leq v \leq 2$ m s^{-1}, 2 m $s^{-1} \leq v \leq 4$ m s^{-1}, $v \leq 4$ m s^{-1}) is shown in the polar graph of Fig. II.5.1. Most of the data fall in the angular sector 180°–210° that is from the continent. In this sector the strongest winds (greater than 4 m s^{-1}) are also observed.

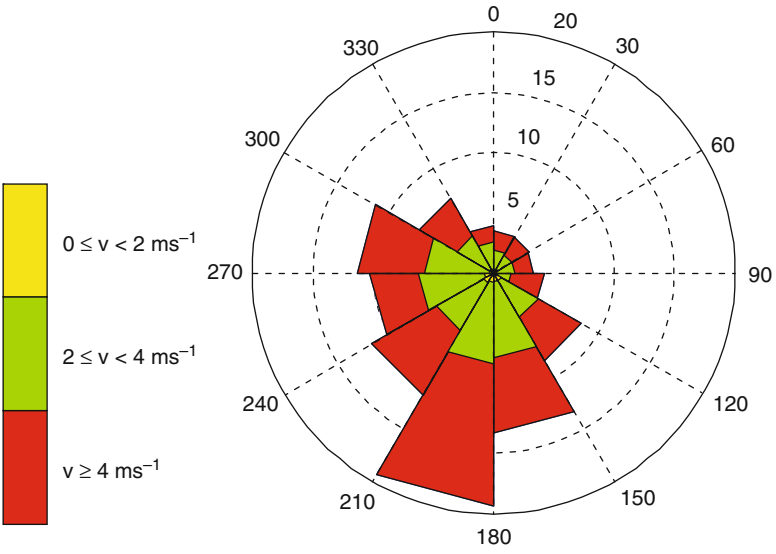

Fig. II.5.1 Wind rose for three different velocity ranges

4.1.2 Temperature

Figure II.5.2 shows the daily averages of the 3-m sonic temperature. The sonic temperature has a strong seasonal cycle with values varying between –25°C during the short summer and –70°C in the long and coreless winter. If warming events would not occur periodically between April and the end of October the average temperature variations during the winter would be contained within 10°C. These warming events are due to synoptic perturbations periodically penetrating the continent and reaching the Antarctic plateau (Argentini et al., 2001). As shown by Van As et al. (2005a, b) a similar phenomenon was also observed at the high Antarctic plateau station of Kohnen.

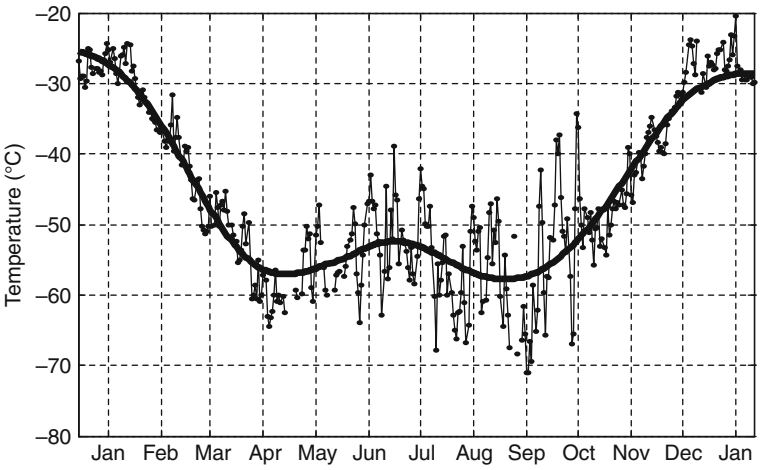

Fig. II.5.2 Temperature behaviour during the year

4.1.3 Sensible Heat Flux

The sensible heat flux on average is negative (Fig. II.5.3). Positive (approximately 5 Wm^{-2}) values occur in full summer (months of December and January) and in a few cases in correspondence of the winter warming events. The minimum of the sensible heat flux is observed at the end of June–beginning of July. Carefully analysing the high frequency data we realized that when the temperature drops below –50°C the sonic anemometer does not work properly and the fluxes could not be estimated.

4.1.4 Wind Speed

The wind (Fig. II.5.4) reaches the highest velocities that is around 11 m s^{-1} (average value over 1 h) during the winter warming events. For the rest of the time it periodically varies between 2 m s^{-1} and 7 m s^{-1}. The friction velocity, as expected, follows the behaviour of the wind speed although it varies between 0.075 m s^{-1} and

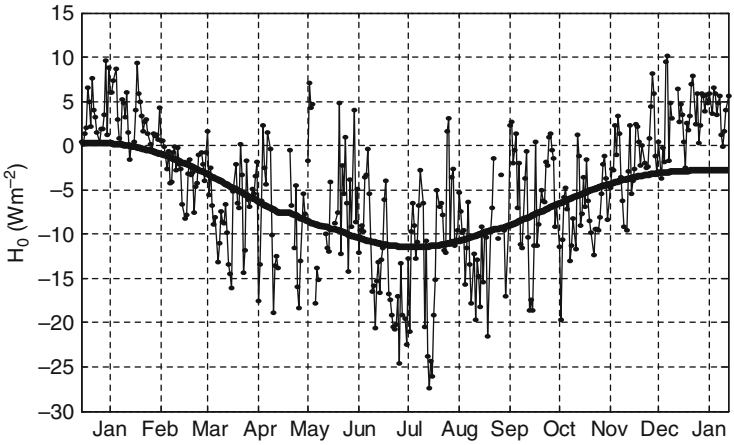

Fig. II.5.3 Sensible heat flux behaviour during the year

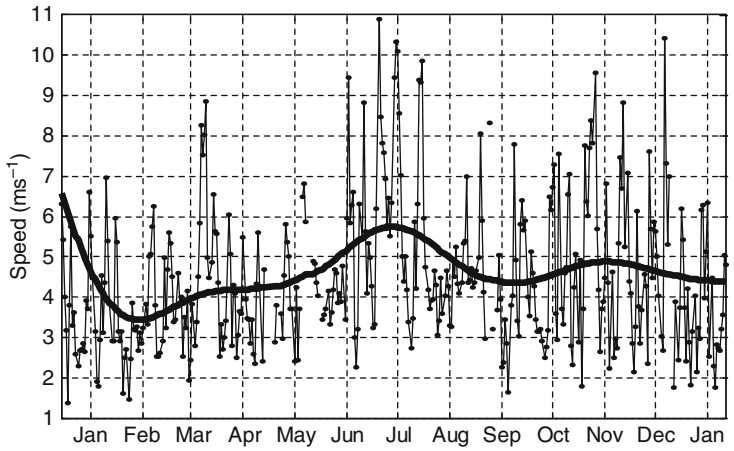

Fig. II.5.4 Wind velocity behaviour during the year

0.4 m s^{-1}, values which are 20 times smaller that the wind speed (at mid-latitudes a ratio of 10 is generally observed).

4.2 Thermal Structure of the Atmosphere and Temperature Profiles

As an example of the atmospheric thermal structure during the winter we show the sodar echogram for day 21 July 2005 (Fig. II.5.5a). Although the temperature decreases of about 25° in 200 m (Fig. II.5.5b) no echoes are shown in the echogram because the strongest fluctuations occur in a narrow layer close to the ground which is not resolved by the mini-SODAR.

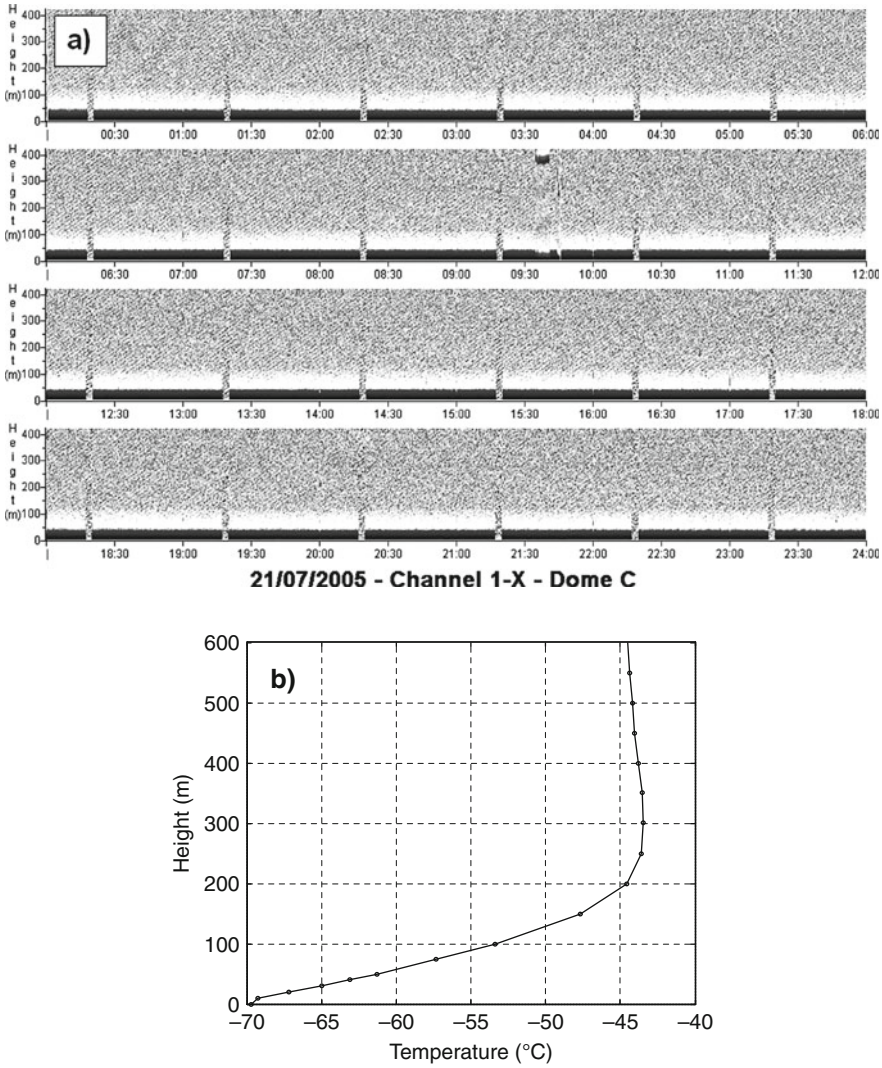

Fig. II.5.5 **a** Thermal structure of the atmosphere during winter as seen by a sodar for day 21 July 2005 and **b** temperature profile by MTP5 for the same day at 1400 LT

Figure II.5.6a gives instead the thermal structure during the summer for 7 January 2005. Figure II.5.6b shows for the same day, the temperature profile at 1400 LT (Fig. II.5.6b). In spite the small amount of sensible heat flux at the ground, a convective boundary layer develops during the warmest hours of the day. The height of the inversion capping the well-mixed layer reaches a maximum (about 200 m) at 1400 LT.

Figure II.5.7a–d shows the seasonally averaged temperature profiles for summer (a), autumn (b), winter (c) and spring (d) in the height range of 0–600 m. Each

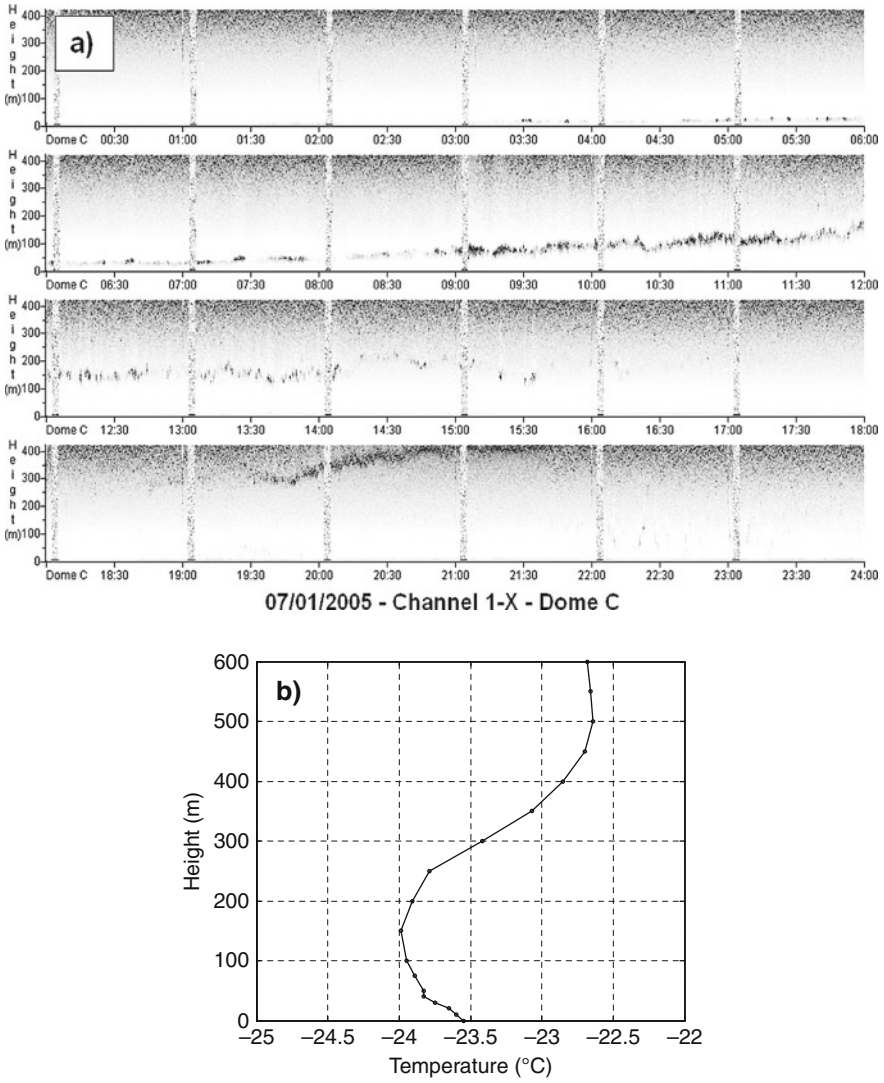

Fig. II.5.6 **a** Thermal structure of the atmosphere during summer as seen by sodar for day 7 January 2005 and **b** temperature profile by MTP5 for the same day at 1400 LT

figure contains three profiles corresponding at averages over different hours of the day. A "diurnal" profile (averages between 1000 and 1400 LT), an "all day" profile (averages over the 24 hours), and a "nocturnal" profile (averages between 2200 and 0200 LT). An unstable profile is observed only during the summer when the sun elevation reaches a peak. For all the other hours/seasons a stable boundary layer develops. The temperature increases of about 5°C in the first 100 meters during the summer and 20°C during the winter (if we do not include the days with the warming events).

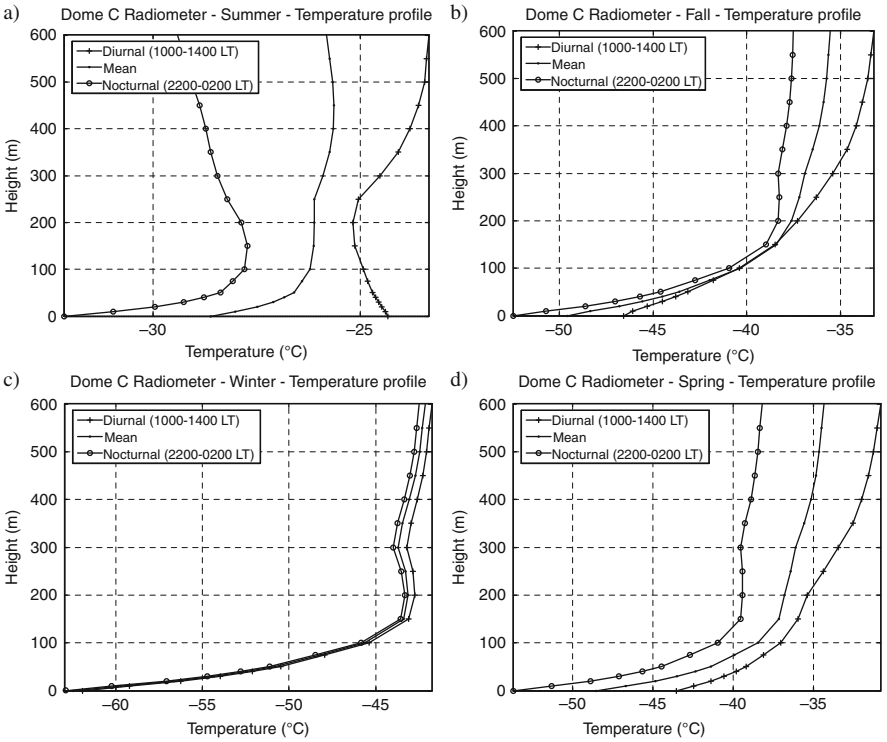

Fig. II.5.7 Temperature profiles diurnal (*crossed line*), averaged (*black dotted line*), nocturnal (*black dotted line*) during **a** summer, **b** autumn, **c** winter, and **d** spring

5 Summary and Future Work

A large PBL field experiment STABLEDC (study of the STABLE Boundary Layer Environmental at Dome C) was held at the French-Italian station of Concordia located on the Antarctic plateau at Dome C during 2004–2005. The aim of the field experiment was to test an automatic observing system to study the processes occurring during the year in this remote region of the world.

The measurements provided are fundamental to study the physical processes, to be used into numerical models and to support the activities related to the atmospheric site testing for astronomic purposes. This paper presents the experimental setup and the instrumentation and a few preliminary results related to the performances of the sensors and to the structure of the atmospheric boundary layer during the summer and winter. A long-lived stable and a weak convective atmospheric boundary layer were observed during winter and summer, respectively. The behaviour of the physical parameters and typical temperature profiles are shown. The thermal structure of the PBL has been investigated using a mini-SODAR.

In the future we want to study the shallow turbulent layer of about 30–40 m depth observed during the winter that up to now could not be studied with a certain detail

because it was below the first range gate of the sodar system. We plan to develop a new mini-sodar with higher frequencies and a larger antenna to investigate the turbulent structure of this very-stable PBL. In order to monitor the winter as well as the summer boundary layer structure we want to develop a system which can work in two modes:

- very high resolution (resolution 2.5 m, first range gate 5 m, maximum range 150 m) during the winter.
- high resolution (resolution 5m, first range gate 10 m, maximum range 300 m) during the summer.

Acknowledgments This research was supported by the Piano Nazionale Ricerche in Antartide (PNRA) in the frame of French-Italian "Dome C" project. The authors would like to thank the logistics staff at Concordia for their support during the experimental fieldwork. Ilaria Pietroni, PhD student in Polar Sciences, was supported by the PNRA and the University of Siena.

References

Argentini S, Petenko IV, Mastrantonio G, Bezverkhnii VA, Viola AP (2001) Spectral characteristics of East Antarctica meteorological parameters during 1994. J Geophys Res 106(D12): 12463–12476

Kadygrov EN, Pick DR (1998) The potential for temperature retrieval from an angular-scanning single-channel microwave radiometer and some comparison with in situ observations. Meteorol Appl 5:393–404

King JC, Turner J (1997) Antarctic meteorology and climatology. Cambridge University Press, Cambridge, 409 pp

Mastrantonio G, Malvestuto V, Argentini S, Georgiadis T, Viola A (1999) Evidence of a convective boundary layer developing on the Antarctic plateau during the summer. Meteorol Atmos Phys 71:127–132

Sozzi R., Favaron M (1996) Sonic anemometry and thermometry: theoretical basis and data-processing software. Elsevier Sci 11(4):259–270

Van As D, Van den Broeke M, Van De Wal R (2005a) Daily cycle of the surface layer and energy balance on the high Antarctic Plateau. Antarctic Sci 17(1):121–133

Van As D, Van den Broeke M, Reijmer C, Van de Wal R (2005b) The summer surface energy balance of the high Antarctic plateau. Boundary Layer Meteorol 114:289–317

Chapter II.6
Use of Remote Sensors in Air Quality Monitoring and Prediction

James M. Wilczak, Jian-Wen Bao, Irina Djalalova, Laura Bianco, Sara Michelson, Ola Persson, Christoph Senff, Bob Banta, and Lisa Darby

1 Introduction

Air quality is a highly interdisciplinary problem dependent on both chemical and meteorological processes. To be able to understand the causes of atmospheric pollution requires knowledge of the types of chemical compounds emitted into the atmosphere, the amounts or concentrations of those compounds, a knowledge of how those different chemical species interact with one another under different ambient meteorological conditions to form new chemical species, and finally a knowledge of how the atmosphere will transport and diffuse each of the chemical components.

Figure II.6.1 displays the effect of meteorology on air quality over the course of a diurnal cycle. During the nighttime hours a shallow stably stratified nocturnal boundary layer forms just above the Earth's surface, within which turbulence motions are weak and vertical mixing is slow. After sunrise, the convective boundary layer begins to form, with stronger turbulent motions that often span a layer several kilometers deep. Both natural and anthropogenic pollutants that are released at the Earth's surface are mixed through the nocturnal and convective boundary layers. Near sunset, turbulence within the deep convective boundary layer weakens or ceases altogether, leaving behind pollutants in the residual layer aloft. The prediction of air quality by numerical forecast models requires an ability to replicate the growth and decay of vertical mixing within both the stable and convective boundary layers, horizontal transport by the winds throughout these layers, and the amount of solar radiation that is available to drive photochemical reactions.

Because of the need to measure the strength of the vertical mixing and the depth through which it occurs, as well as the vertical profile of wind speed and direction throughout the lowest several kilometers of the atmosphere, remote sensors

J.M. Wilczak (✉)
NOAA/Earth Systems Research Laboratory, Boulder, CO, USA
e-mail: James.M.Wilczak@noaa.gov

Presented at International Summer School on Atmospheric and Oceanic Sciences, L'Aquila, Italy, September 3–7, 2007

D. Cimini et al. (eds.), *Integrated Ground-Based Observing Systems*,
DOI 10.1007/978-3-642-12968-1_13,

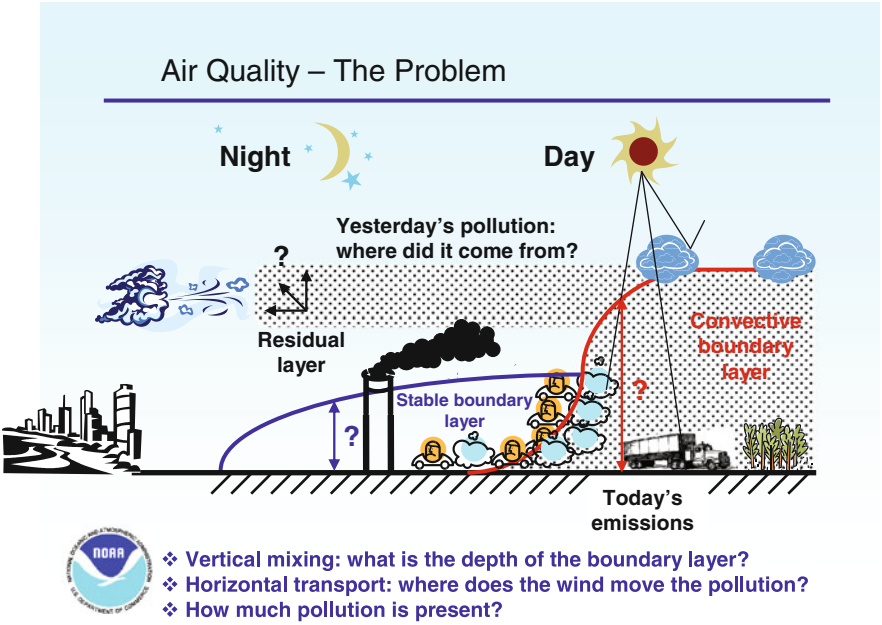

Fig. II.6.1 Overview of the key AQ processes

have proven to be extremely valuable for assessing air quality. In this presentation we focus on wind profiling radars, and ozone and Doppler lidars. When used in conjunction with surface ozone and aerosol (PM2.5) measurements and with standard surface meteorological instrumentation, these remote sensors can lead to new insights on how the local meteorology controls air pollutant concentrations.

2 Profiler Trajectory Tool

When high pollutant concentrations are observed at a location, one of the first questions asked is usually "Where did it come from?" This is especially true if the pollution is observed in what one would have thought should be a pristine environment, far from major sources of chemical emissions such as coal-burning power plants, petro-chemical processing facilities, cities, and metropolitan areas. To trace back the origins of the pollution and identify its sources is often the first step in being able to justify the costs of reducing the amounts of pollutants emitted. For this reason, estimates of parcel trajectories are a key component of almost all air quality field studies.

Trajectories can be calculated either from a numerical weather prediction model or directly from observations. Both techniques have their own limitations and advantages. Weather prediction models have the advantage that the wind fields exist on

gridded fields that are often high resolution in both space and time and have three-dimensional winds (both horizontal and vertical). They are limited, however, by the accuracy of the wind fields of the model, and this accuracy is often unknown. In contrast, trajectories based on observed winds potentially have a high and known accuracy, but depend on the number and quality of the observations available, and are constrained by the fact that often only horizontal winds are used, as the vertical motions of the atmosphere are too small to be able to accurately measure.

Examples of both types of trajectories will be compared using data collected during the summer 2004 New England Air Quality Study, which took place in the northeast portion of the United States. During this field campaign, a network of 915 MHz "boundary layer" wind profiling radars was deployed, as shown in Fig. II.6.2. The network consisted of both NOAA profilers deployed for the field campaign and pre-existing "cooperative agency" profilers that were already present. For deployments of networks of wind profiling radars such as that used in NEAQS, a profiler trajectory tool (White et al. 2006) was developed. This tool interpolates the observed hourly horizontal winds at a given level (using Cressman weighting of winds from all the profiler sites) to create horizontal trajectories.

The particular example that we present concerns an episode of high SO_2 concentrations that were observed at the Chebogue, Nova Scotia, Canada wind profiler sites. A time series of surface SO_2 measurements (Fig. II.6.3) shows high values occurring on Julian Days 223 and 224 (August 9–10, 2004). Since the Chebouge

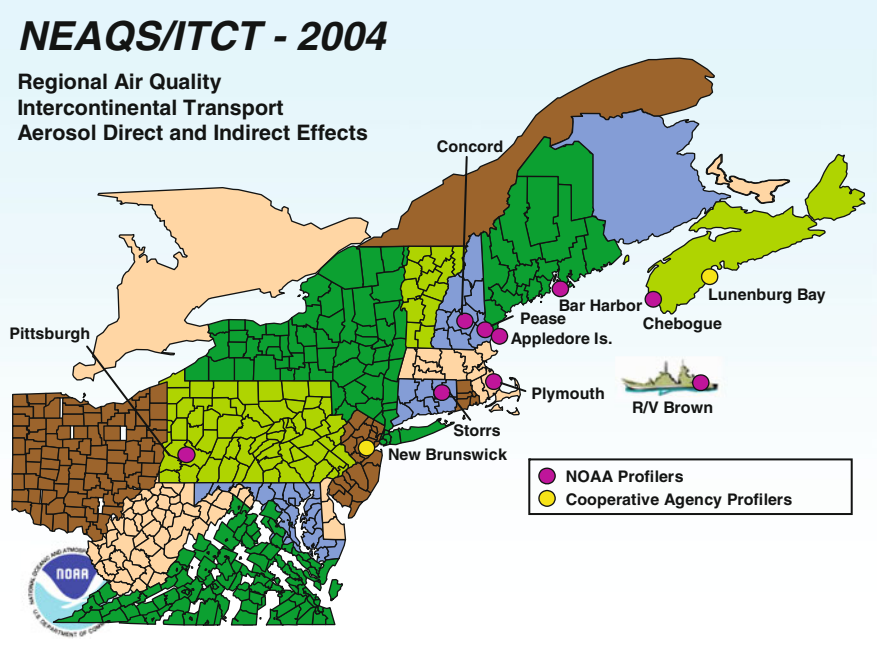

Fig. II.6.2 NEAQS wind profiler network

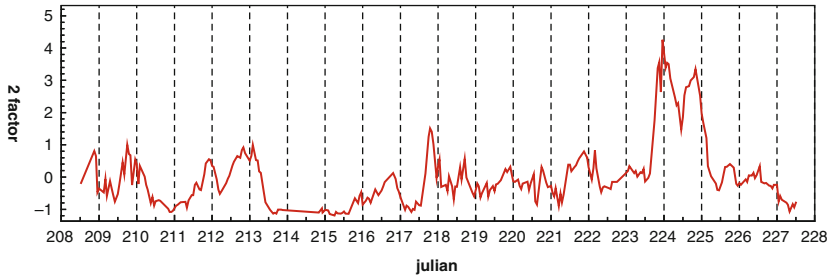

Fig. II.6.3 SO_2 index time series at Chebogue, Nova Scotia, Canada. Higher values indicate greater SO_2 concentrations

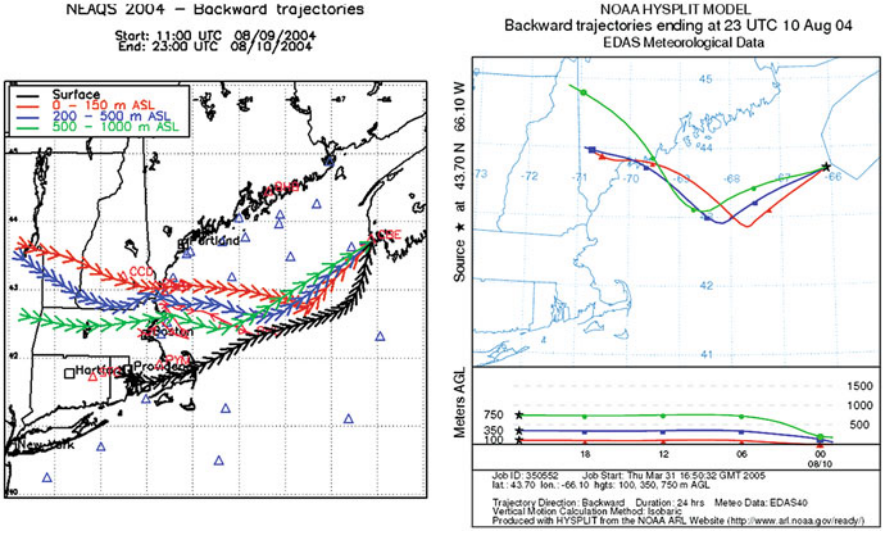

Fig. II.6.4 Back trajectories from Chebogue from the profiler tool and HYSPLIT

site is rural, and far from any major source of SO_2, trajectory analysis was necessary to understand the cause of this episode.

Backward trajectories from the Chebogue site were calculated using the profiler trajectory tool and from another common trajectory analysis tool, the HYSPLT program (Fig. II.6.4). HYSPLIT is a model-based trajectory, using winds archived every 3 h from the Eta model data assimilation system. Trajectories from HYSPLIT show that the parcels of polluted air at Chebogue would have previously crossed over southern Maine, which like Nova Scotia. is mostly forested with no major SO_2 sources. However, the profiler trajectory tool shows that the trajectories would instead have carried these air parcels much further south, over Massachusetts and southern New Hampshire. A map of the coal-fired power plants (the major sources

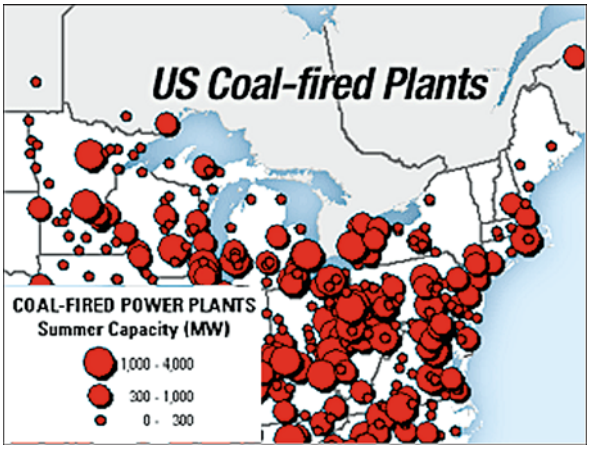

Fig. II.6.5 Coal-fired power plants in the northeastern United States

of SO_2) in New England (Fig. II.6.5) indicates that while there are no major SO_2 sources over Maine where the HYPLIT trajectories went, there are several large sources present to the south, where the profiler trajectories went. A further analysis of the data that went into the trajectories indicated that the reason for the more accurate profiler-based trajectories was because the model failed to get the timing of a frontal system accurately.

3 Ozone and Doppler Lidar

Ozone is one of the major atmospheric pollutants, which is of concern throughout the world because of its adverse effects on human health. Ozone is routinely monitored at surface sites, but its vertical profile is more rarely measured. These vertical profile measurements can be made using ozone sondes (similar to radiosondes) or with an instrumented aircraft. Because of the high cost of ozone sondes, most field programs use them sparingly, and very few are taken on a routine basis. Also, sondes give a "snapshot" in time measurement at a fixed point, while in situ aircraft measurements give time histories of ozone but only at the altitude of the aircraft. For these reasons remote sensing of ozone is an attractive alternative.

The NOAA Earth System Research Laboratory designed and built the Tunable Optical Profiler for Aerosol and oZone lidar (TOPAZ). TOPAZ is capable of measuring ozone concentration in the lower troposphere from an airborne platform with uncertainties of only a few ppbv at 90-m vertical and 600-m horizontal resolution. It also provides uncalibrated aerosol backscatter profiles. TOPAZ incorporates state-of-the-art technologies to make it compact and lightweight as well as having low power consumption. These features allow it to be deployed on smaller aircraft (Fig. II.6.6). This instrument has now been flown during several air quality field programs, and we show data from two of these.

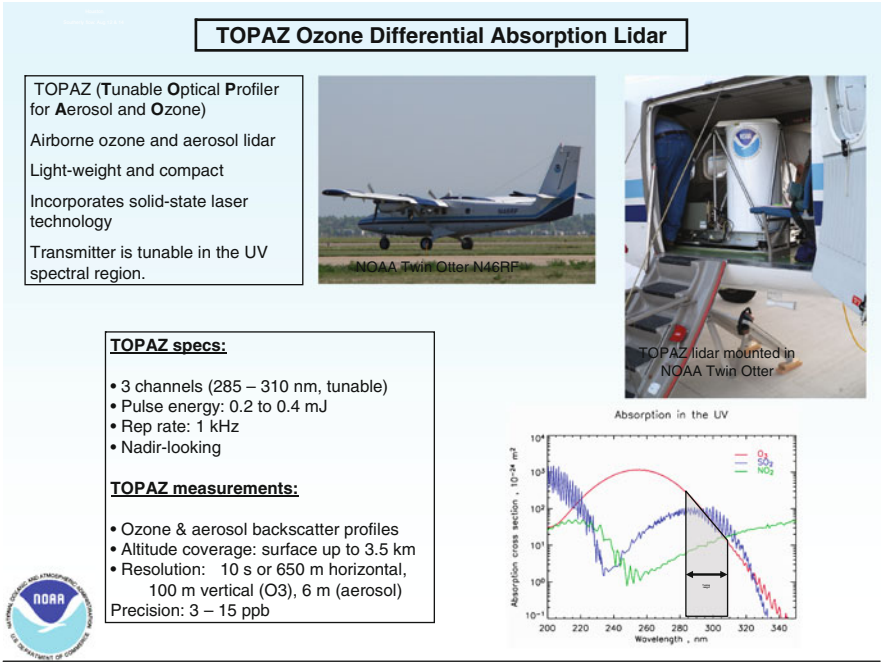

Fig. II.6.6 TOPAZ ozone lidar system

3.1 NEAQS 2004

During the New England Air Quality Study (NEAQS 2004) the TOPAZ ozone lidar system was flown on a small twin otter airplane. One goal of the NEAQS study was to understand the transformation of ozone in the marine boundary layer, as this ozone often times is transported back on shore. On July 21, 2004 the plane's flight track (Fig. II.6.7) took it over Boston, Massachusetts, and then out to sea where it tracked the evolution of an ozone plume. The time-height cross section of ozone concentrations from this flight is shown in Fig. II.6.8, and ozone concentrations as large as 120 ppbv are found.

Mean ozone concentrations aloft were calculated by computing the layer average ozone between 500 and 1,500 m, as indicated by the two black horizontal lines in Fig. II.6.8. The layer-averaged ozone is then plotted on a map, as shown in Fig. II.6.9. Here two major ozone plumes are seen, one over the Boston area, and a second one, approximately 200 km offshore (Fig. II.6.9). To understand the origins of the offshore plume, backward trajectories were then calculated using the network of wind profilers. These trajectories indicate that the offshore plume originated the previous day along the New York–Boston metropolitan corridor (Fig. II.6.10) and is distinct from the plume present on the current day over Boston.

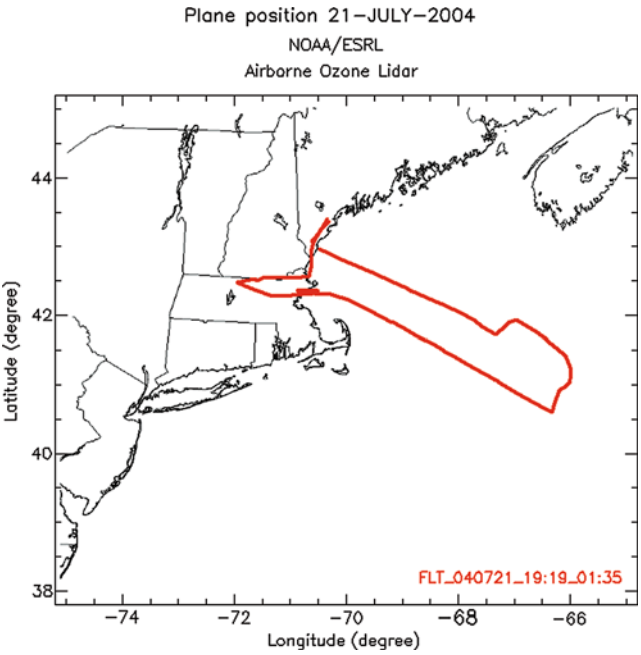

Fig. II.6.7 Flight track off New England on July 21, 2004

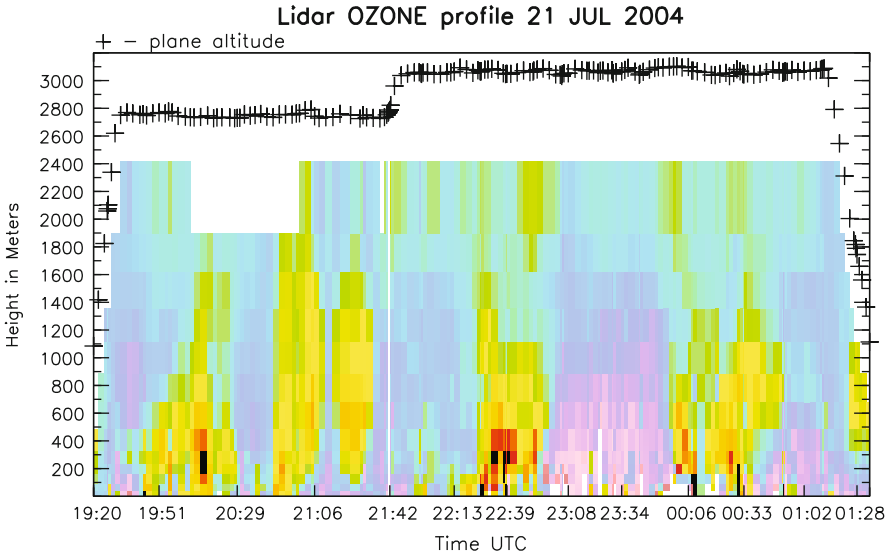

Fig. II.6.8 Ozone lidar time-height cross section during the July 21, 2004 flight. Ozone values are shown in ppbv in the scale on the right. *Black plus symbols* show the height of the aircraft. Two *solid black lines* show elevations of 500 and 1,500 m

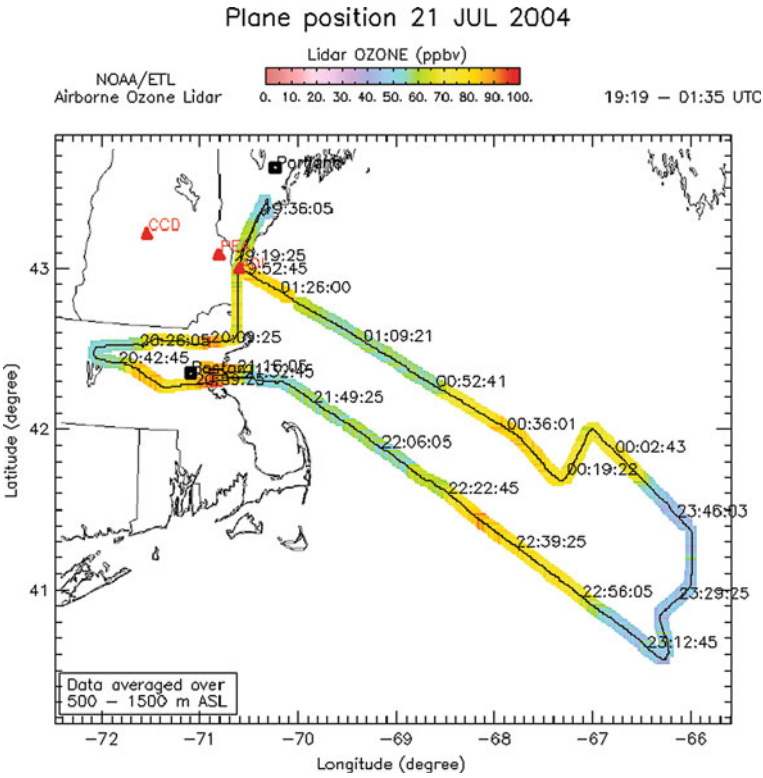

Fig. II.6.9 Map of vertically averaged ozone, with the averaging between 500 and 1,500 m agl

3.2 Texas Air Quality Study I (TexAQS 2000)

Houston, Texas is renowned for having some of the highest ozone levels in the United States in large part due to the many oil refineries and petro-chemical plants that are located there. Predicting high-zone concentrations in Houston is complicated by the fact that the area often has a rather complex meteorological conditions, due to the presence of a sea breeze as well as a "bay breeze" generated by Galveston Bay (Fig. II.6.11).

To study the effects of these mesoscale circulations on ozone, a Doppler lidar was located at point A in Fig. II.6.11, and overhead (RHI) scans were made of the radial wind velocity (Banta et al., 2005). Figure II.6.12 shows the radial velocities on the afternoon of August 16, 2000, when a well-developed sea breeze front was propagating onshore. The two panels in Fig. II.6.12 show the front just before and after it had passed the lidar site. Also visible in both panels is a layer of return (land to sea) flow aloft at a height near 1.5 km.

Surface meteorology and ozone data, shown in Fig. II.6.13, indicate that the front passed shortly after 16 CST, as indicated by the vertical solid line. At this time

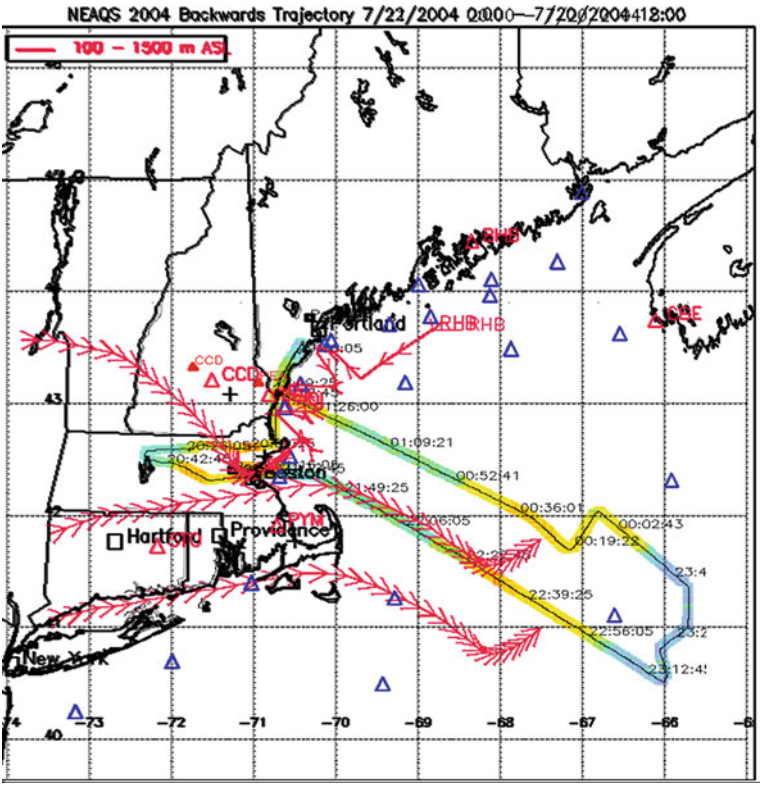

Fig. II.6.10 Ozone vertically averaged map with trajectories

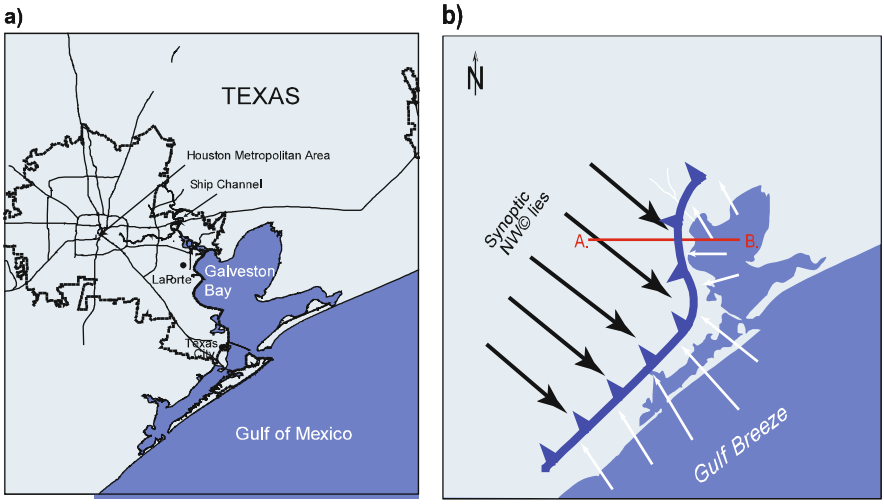

Fig. II.6.11 Houston sea breeze schematic. The Doppler lidar was positioned at point A

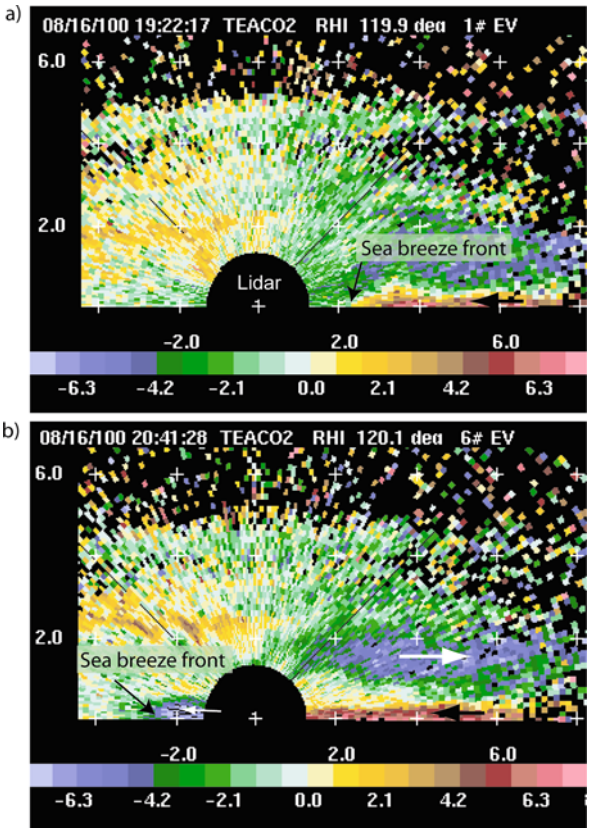

Fig. II.6.12 Doppler lidar radial winds taken from the lidar stationed at point A in Fig. II.6.11. Positive values are toward the lidar

the temperature dropped, the relative humidity jumped higher, and the wind speed increased. The highest ozone concentrations were observed shortly after the sea breeze front had passed.

To understand the horizontal and vertical spatial ozone structures, the TOPAZ airborne lidar was flown through the sea breeze front. Maps of the distribution of the vertically averaged ozone for a morning flight are shown in Fig. II.6.14 (left panel), together with "curtain" plots showing both the vertical and horizontal structure (right panel). In the left panel we also show boundary layer wind vectors for several hours, determined from wind profiling radars, displaced in space according to the local advection. The wind vectors clearly demonstrate that the evolving ozone layer in the morning is shallow and is being carried offshore by the dominant wind flow.

In contrast, the TOPAZ data from an afternoon flight that same day (Fig. II.6.15) show that the ozone plume has moved back on shore in the sea breeze flow. In addition, the ozone layer is considerably deeper and reaches its greatest altitude in the convergence zone along the sea breeze front.

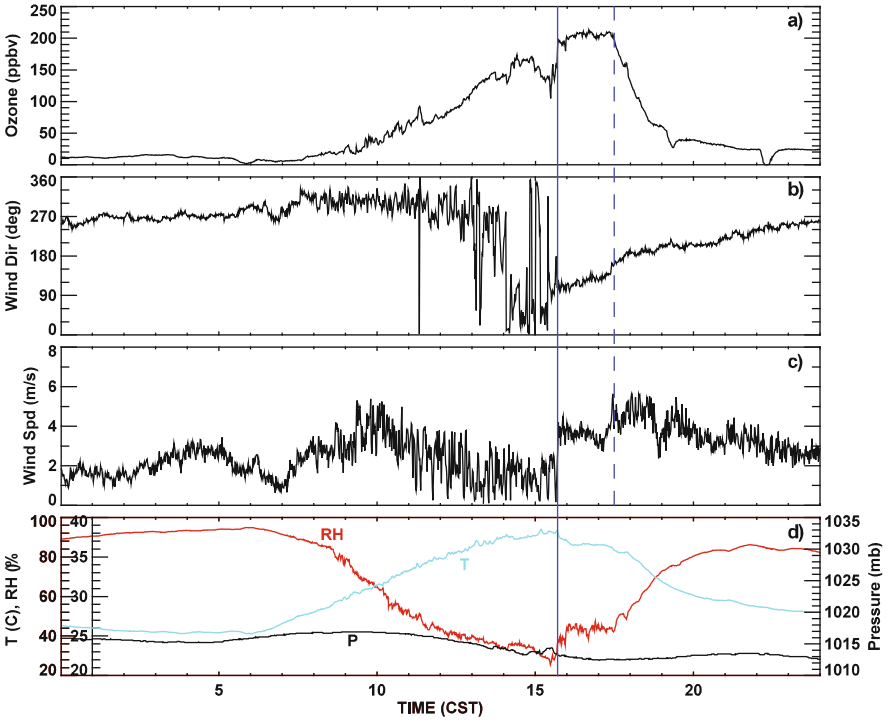

Fig. II.6.13 Surface met and ozone

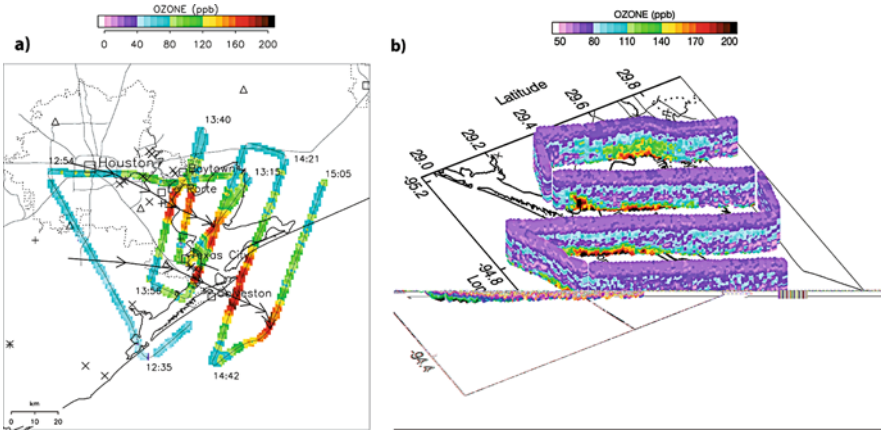

Fig. II.6.14 Ozone lidar morning flight. *Left panel* shows the vertically averaged ozone and *right panel* shows the vertical profiles of ozone as a curtain

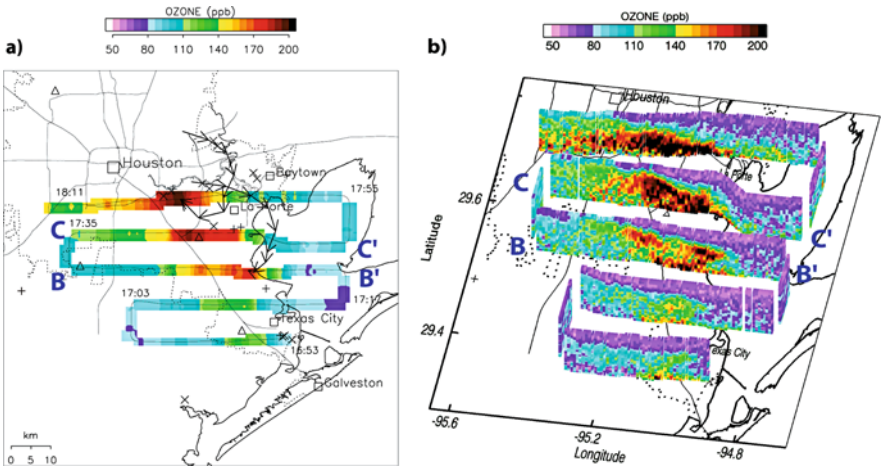

Fig. II.6.15 As in Fig. II.6.14, for an afternoon flight on the same day

4 Model Evaluation from Intensive Field Programs: TexAQS-2006

Another important use of remote sensing data is to evaluate air quality forecast models. In this study (Wilczak et al., 2009) we examined the meteorological conditions associated with regional surface ozone using data collected during the summer 2006 Texas Air Quality Experiment and the ability of the NMM-CMAQ and WRF-Chem models to simulate the observed meteorology and surface ozone. The surface ozone data consist of 118 sites that are part of the US EPA AIRNow network, while the meteorological data came from a network of 11 915 MHz wind profilers with RASS and supporting surface meteorological stations (Fig. II.6.16). For reasons that will become apparent later, the surface ozone data were placed into geographical groups, as indicated in Fig. II.6.17.

The depth of the atmospheric boundary layer, defined here as the layer of active turbulent mixing, is provided by the network of radar wind profilers. These radars provide vertical profiles approximately every 6 min of refractive index structure function C_n^2, vertical velocity, and spectral width (which is a measure of turbulent intensity within the radar pulse volume). An automatic algorithm (Bianco et al. 2008) uses these profiles to compute hourly values of the depth of the actively mixed, convective boundary layer. The depth of the boundary layer is very important for air quality as it determines the depth through which chemical species are mixed and diluted.

Composite diurnal variations of the observed PBL depth, averaged over the 47 days of the TexAQS II analysis period, are shown in Fig. II.6.18 for each of the 11 profiler sites (black curves). The panels of the figure are arranged such that those profilers sites located in the north of the study domain are at the top of the figure, and those in the south of the domain are at the bottom. Also shown are ± one

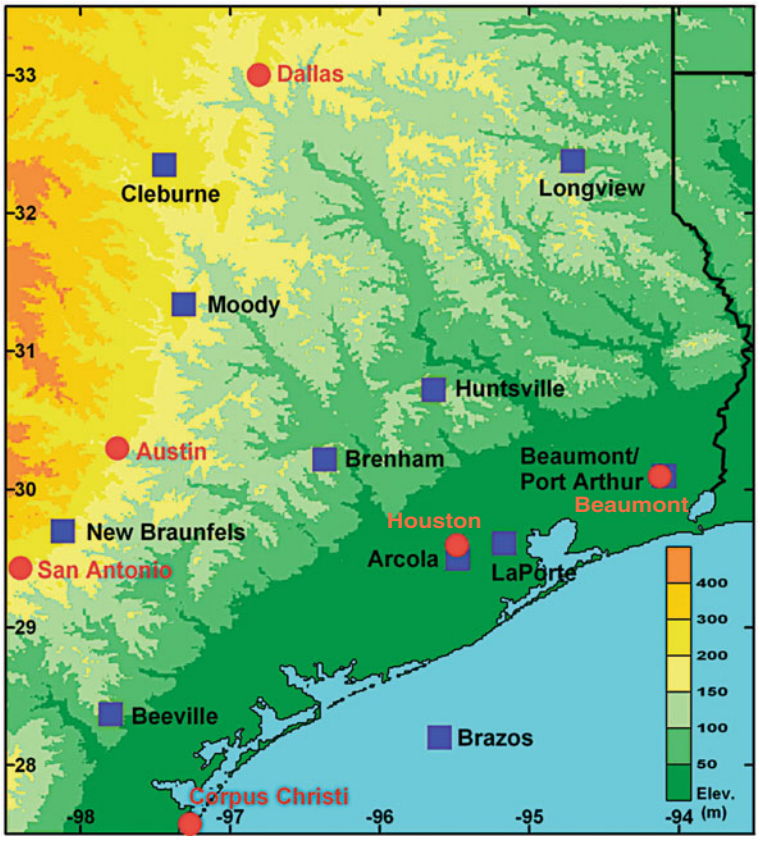

Fig. II.6.16 Wind profiler base map showing the locations of the 11 boundary layer (915 MHz) wind profilers used in this study (*squares*) and major city locations (*circles*). *Shading* shows terrain elevation

standard deviation of the observed PBL depth values. The observed values at nearly all sites reach their maximum value between 1500 and 1700 LST and then decrease afterward. The daily maximum mean values are approximately 1.3 km near the coast (Beeville, Arcola, La Porte) and increase to 2.1 km in the northern part of the domain.

Model values of PBL depths are also shown in Fig. II.6.18, using a green curve for the NMM-CMAQ model and a red curve for the WRF-Chem model. The skill of each model at reproducing the mean PBL depth varies considerably from site to site. The NMM/CMAQ has too deep of boundary layers for most hours of the day at many sites (CLE, MDY, BHM, LPT, BVL) leading to an overall positive bias. In contrast to the positive bias of the NMM-CMAQ model, at many sites the WRF-Chem model's PBL depths are considerably lower than the observations (HVE, BPA, BHM, BVL), with the worst performance at BHM, where the model value is only about 35% of the observed.

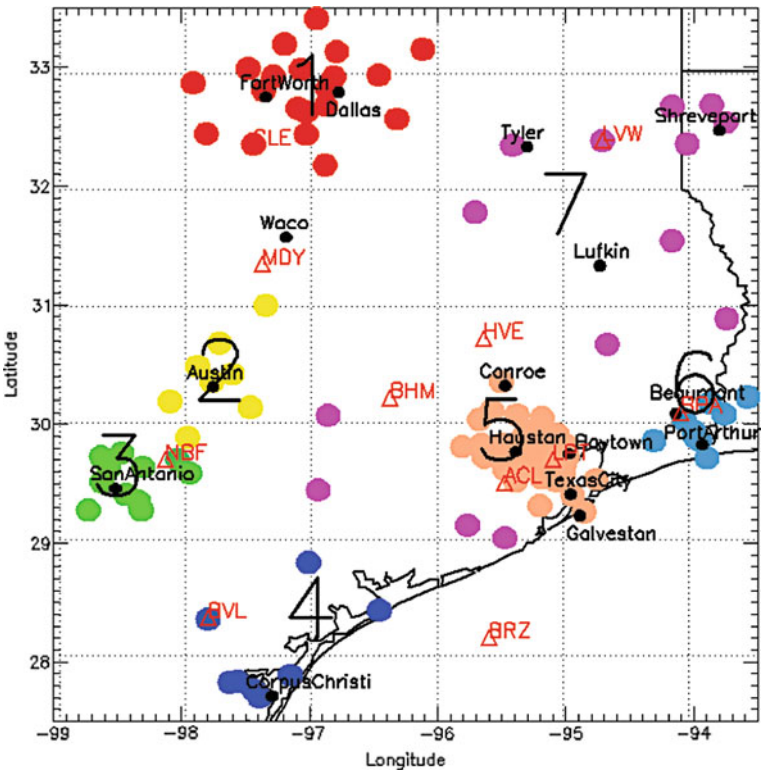

Fig. II.6.17 Classification of the 118 surface ozone sites into seven geographic sectors: (*1*) Dallas/Ft. Worth metro area; (*2*) Austin; (*3*) San Antonio; (*4*) Corpus Christi; (*5*) Houston/Galveston metro area; (*6*) Beaumont/Port Arthur; and (*7*) the remaining, mostly rural sites. Wind profiler sites are shown as *triangles*

Since the present analysis focuses on regional variations in ozone, we find it useful to combine the 118 surface ozone sites into a set of seven geographical sectors, as indicated in Fig. II.6.17. Next, we then graphically present the values of the seven geographical sectors as a function of time for the entire analysis period in Fig. II.6.19. In this diagram, similar to a Hovmoller diagram, the seven sectors are plotted on the abscissa, with the eighth column being the mean of all 118 sites; the days of the analysis are plotted on the ordinate axis, starting at August 12 at the top and ending at September 27 at the bottom of the each panel; and the magnitude of each days sector-averaged 8-h max ozone is indicated by the scale at the bottom. The left panel of Fig. II.6.19 presents the observed ozone values, the middle panel the NMM-CMAQ model, and the right panel the WRF-Chem model.

Figure II.6.19 allows us to graphically visualize the spatial and temporal variations of the observed and model ozone for the entire analysis domain and the entire analysis period. From this diagram one can immediately see that high-ozone

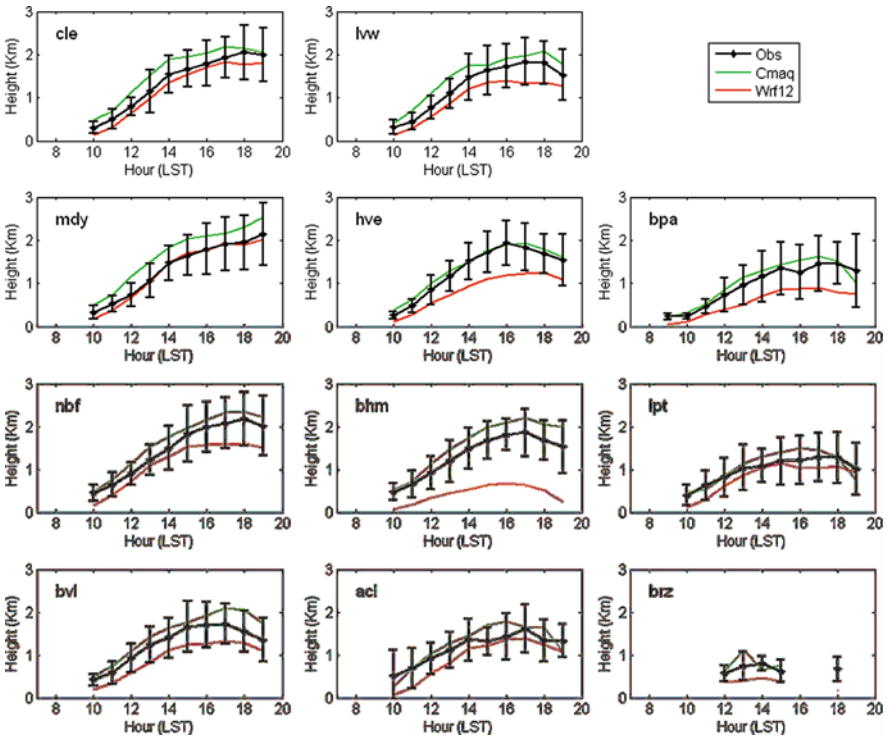

Fig. II.6.18 Diurnal variation of PBL depths (m agl) at each profiler site averaged for the entire 47-day analysis period as a function of time (LST): observed (including ±one standard deviation); NMM-CMAQ and WRF-Chem/12. The profiler sites are oriented according to geographic location, with Cleburne (cle) furthest to the northwest and Brazos (brz) furthest to the southeast

episodes tend to be regional events, with high ozone occurring simultaneously in almost all of the sectors. To assist in the meteorological analysis of high- and low-ozone events, we define high-ozone days to be when the mean 8-h max ozone for all 118 sites is greater than 50 ppbv, and low-ozone days when it is less than 40 ppbv. High-ozone days are then indicated in Fig. II.6.19 with a "+" sign, and low-ozone days with a "–" sign. With these definitions, there are 19 high-ozone days, a nearly equal number of 17 low-ozone days, and 11 "other" days, when the mean value falls between 40 and 50 ppbv. Using these definitions, it is apparent that high- and low-ozone events occur on roughly weekly timescales, with five high-ozone episodes separated in time by intervening low-ozone episodes, over the 47-day analysis period. This weekly timescale is associated with the synoptic timescale of the basic meteorological forcing conditions.

In comparison to the observations, the NMM-CMAQ values (middle panel) broadly follow the same temporal patterns as the observations. However, NMM-CMAQ clearly has less dynamic range than the observations, with higher minimums

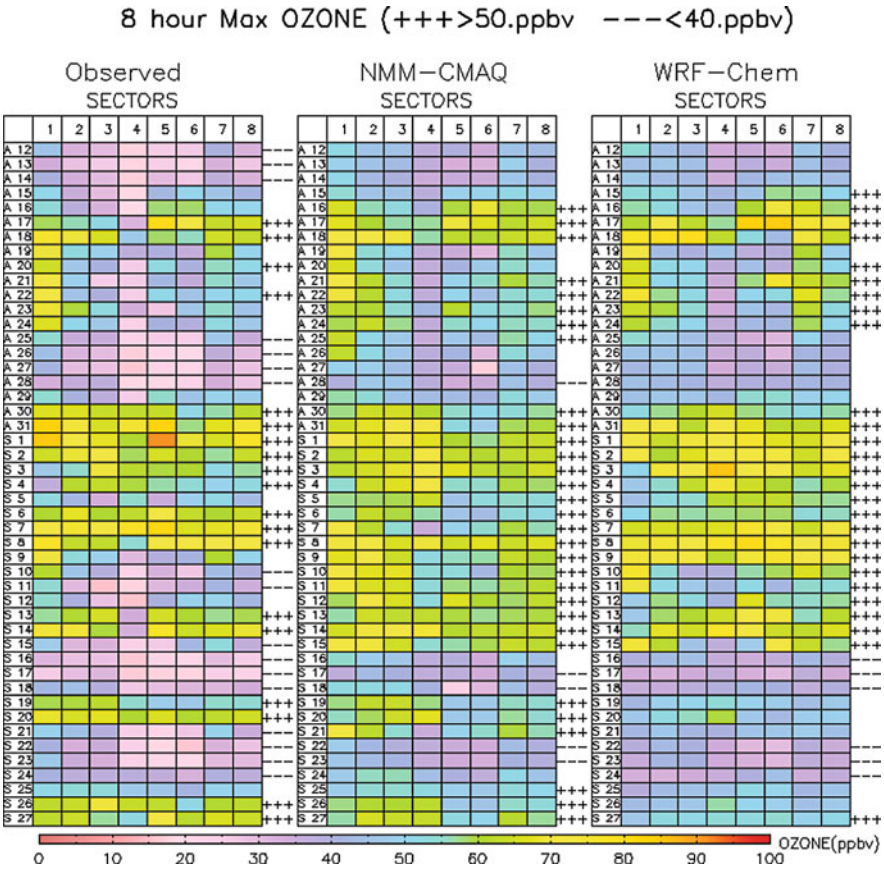

Fig. II.6.19 Time series daily 8-h max ozone spatially averaged into each of the seven geographical sectors shown in Fig. II.6.3, plus the average of all 118 sites (shown in column 8.) The *left panel* displays the observations, the *middle panel* the NMM-CMAQ model, and the *right panel* the WRF-Chem model. The time series runs from August 12 through September 27. Days with the all site average greater than 50 ppb are labeled with a "+++," and days with the all site average less than 40 ppb are labeled with a "——." The locations and number of sites averaged in each sector are : Sector 1 (Dallas/Ft. Worth, 20), Sector 2 (Austin, 8), Sector 3 (San Antonio, 11), Sector 4 (Corpus Christi, 8), Sector 5 (Houston, 40), Sector 6 (Beaumont/Pt. Arthur, 10), Sector 7 (Rural, 21), Sector 8 (All Sites, 118)

and slightly lower maximums. The WRF-Chem model behavior (right panel) is similar to NMM-CMAQ in that it too has a smaller dynamic range than the observations, a positive bias, and too many moderately high-ozone days.

Differences in the large-scale meteorological forcing between the 19 high-ozone days and the 17 low-ozone days (as determined from the observed surface ozone values in Fig. II.6.19) were investigated by calculating composites of 1,000 and 700 mb geopotential height (Fig. II.6.20). The 1,000 mb high-ozone day composite (top left panel) shows a ridge of high pressure that extends from the Gulf of Mexico

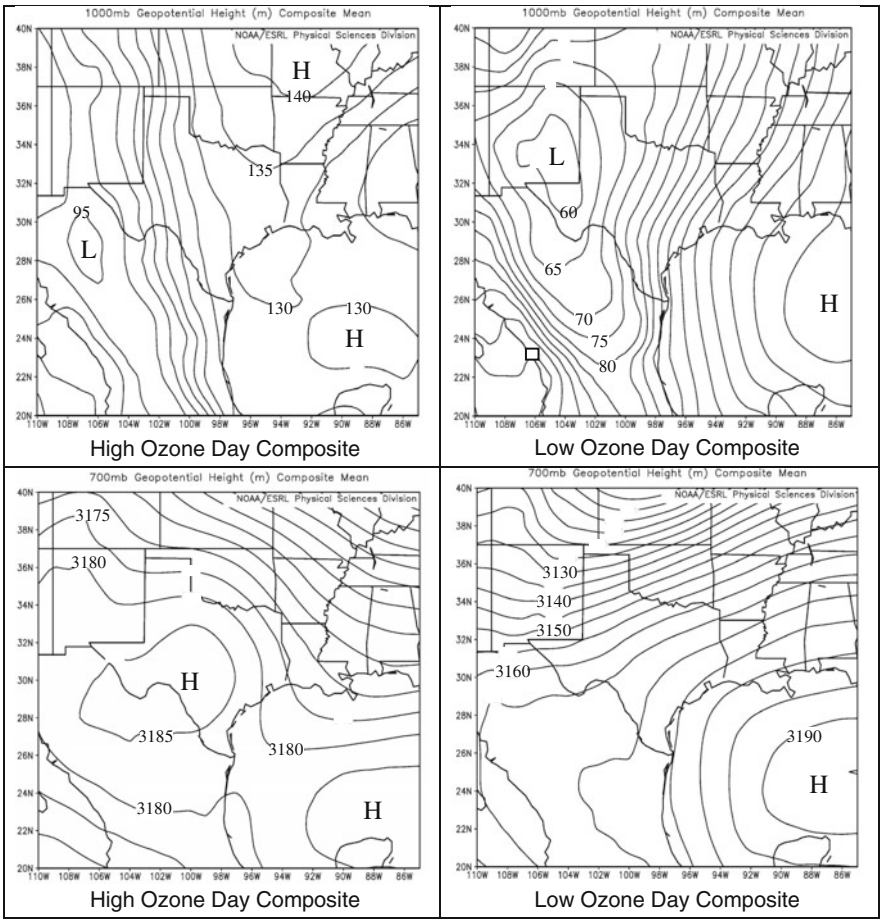

Fig. II.6.20 Composite analyses of geopotential height (m) at 0000 UTC for the 19 high-ozone days (*left panels*) and 17 low-ozone days (*right panels*) at 1,000 mb (*top panels*) and 700 mb (*bottom panels*)

through East Texas and up into Missouri. Over most of the TexAQS II study domain the pressure gradient is weak, with an easterly component to the geostrophic wind. In contrast, the low-ozone day 1,000 mb composite shows a very tight pressure gradient, with strong southerly flow across all of East Texas.

The spatial distribution of the 8-h max surface ozone and boundary layer meteorological parameters for the high-ozone days is shown in Fig. II.6.21 for the observations and the two models. The composite high-ozone day surface ozone is shown as circles; wind barbs represent a vertical average through the approximate depth of the boundary layer (0–1.2 km agl) and averaged for three afternoon hours near the time of peak ozone (2100-2359 UTC; 1500–1759 LST); lines show

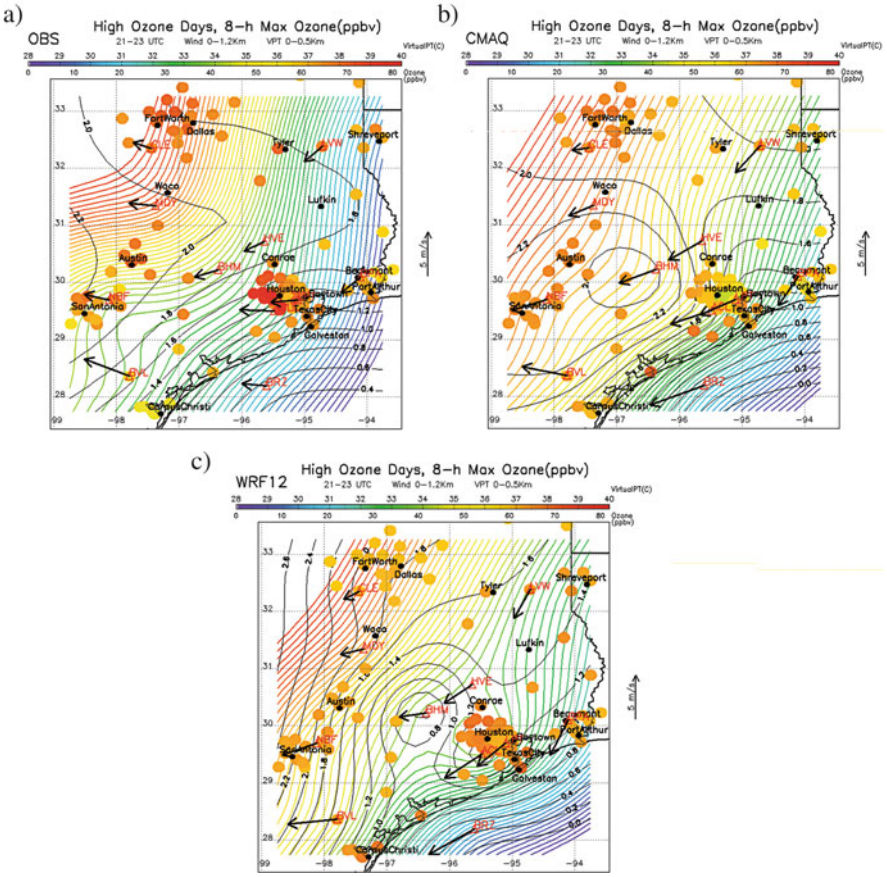

Fig. II.6.21 Surface ozone and meteorology for the 19-day high-ozone composite, from the **a** observations; **b** NMM-CMAQ model; and **c** WRF-Chem model. *Circles* show the average 8-h max surface ozone; *arrows* show the wind profiler velocities, averaged vertically up to 1.2 km agl and from 21 to 23 UTC; *contours* show RASS temperatures averaged vertically up to 0.5 km agl and from 21 to 23 UTC; and *black contours* show the boundary layer depth averaged between 19 and 23 UTC

contours of virtual potential temperature averaged vertically from 0 to 500 m and also averaged for the same afternoon 3-h interval; and black lines show contours of daytime maximum PBL depth. The spatial distribution in surface ozone for the high-ozone day composite is remarkably uniform across the domain in the observations, with values mostly between 60 and 65 ppbv. The only significant variations are an ∼10 ppbv increase in ozone to the west of Houston, an ∼5 ppbv increase to the northwest of Dallas/Ft. Worth, and a ∼10 ppbv decreases at Corpus Christi. Given the easterly flow, the two areas of increased ozone can be interpreted as downwind plumes emanating from the two large metropolitan areas. In comparison to

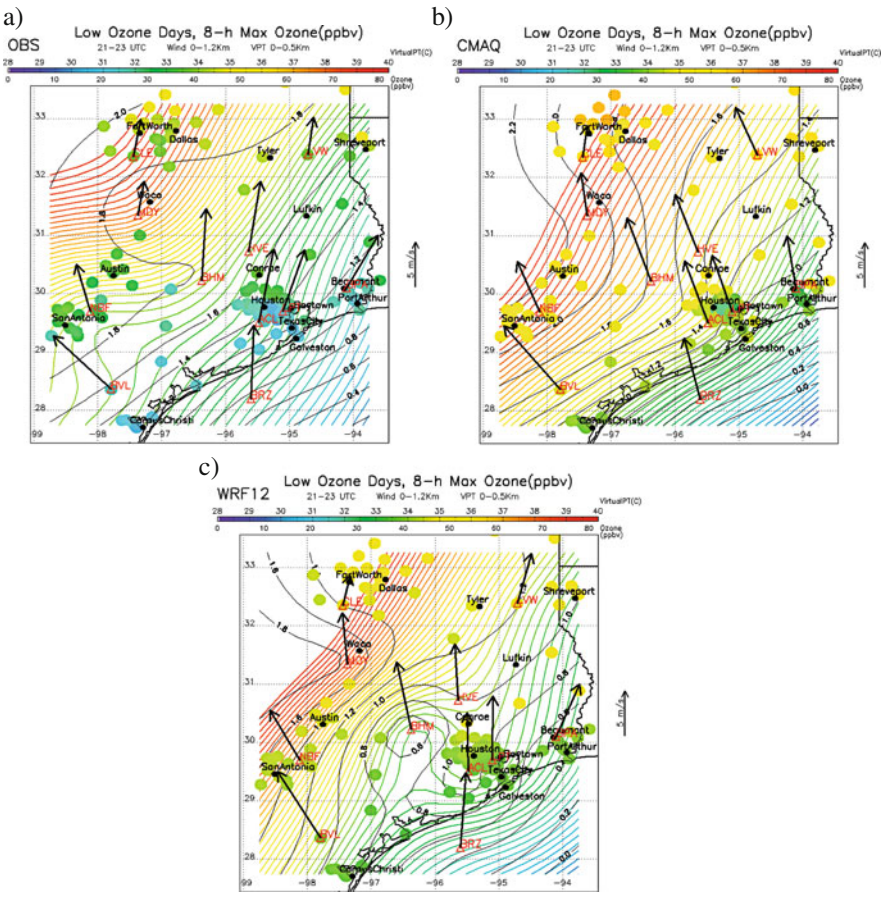

Fig. II.6.22 As in Fig. II.6.21, except for the 17-day low-ozone composite

the observations, the two models also replicate the overall uniformity of the ozone field. In fact, the ozone is too uniform in the models, as both NMM-CMAQ and WRF-Chem miss the Houston downwind plume enhancement, and for Dallas/Ft. Worth, NMM-CMAQ has a weaker gradient than observed to the northwest, and WRF-Chem has almost no enhancement at all.

The spatial distribution of the 8-h max surface ozone and boundary layer meteorological parameters for the low-ozone days is shown in Fig. II.6.22 for both the observations and the two models. Unlike the high-ozone days, the observed surface ozone pattern is far from uniform (Fig. II.6.22a), with a significant gradient in ozone concentration normal to the coastline, with low concentrations (15–20 ppbv) near the coast and higher concentrations inland, reaching ~50 ppbv in North Dallas. At every site the mean ozone concentration is lower than the equivalent mean value in the regional high-ozone day composite.

Mean 8-h max surface ozone concentrations in the NMM-CMAQ model (Fig. II.6.22) differ significantly from the observations. The model produces a gradient in ozone normal to the coast, but the gradient is only about half the observed value, and at all locations the model ozone has a positive bias. This bias is greatest near the coast (∼20 ppbv) and decreases in magnitude with distance inland (∼10 ppbv in North Dallas). The WRF-Chem behavior is quite similar to NMM-CMAQ, in that it also has a spatial gradient only half of that observed and that it has a positive bias that decreases with distance inland. However, the positive bias is smaller in WRF-Chem than in NMM-CMAQ and nearly goes to zero north of Dallas. The high-ozone biases for coastal locations found in both models strongly suggest that the inflow boundary conditions (35 ppbv for NNM-CMAQ and 30 ppbv for WRF-Chem) are too high. The data indicate that a more reasonable value would be ∼15–20 ppbv for inflow boundaries over the Gulf of Mexico.

In contrast to the weak easterly winds in the high-ozone composite, for the low-ozone days the composite observed boundary layer winds are strong and from the south. Maximum speeds are 6–8 ms^{-1} for profiler sites near the coast, where there is also a significant diffluent pattern in the flow, and decrease further inland to values of 3–4 ms^{-1} at Cleburne and Longview. NMM-CMAQ winds generally have the correct magnitude (the mean speed bias is only +0.05 ms^{-1}) and decrease inland as observed, but do not replicate the diffluent flow near the coast. As a result, sites on the east side of the domain have a distinct easterly bias, reaching as large as 30° at several sites, and the average bias at all sites is 22°. WRF-Chem boundary layer winds also accurately match the observed speeds (with a mean speed bias of +0.08 ms^{-1}), including their decrease inland, and the model also reproduces the observed wind directions quite well, including the diffluent flow pattern near the coast. The mean direction error for WRF-Chem is only 7° too easterly.

Next, ozone histograms are shown separately for each of the seven regional sectors and for high- and low-ozone days (Fig. II.6.23 and II.6.24). Since the high-ozone days have easterly flow across the domain, we expect that there should be less oceanic influence and a more normal distribution in the ozone histogram. In contrast, since the low-ozone days are characterized by strong onshore flow we would expect to see a greater oceanic influence. For the high-ozone days (Fig. II.6.10) normal distributions are found in the observations not only for the average of all sites, but also for most individual sectors as well, with peaks typically near 65 ppbv. High-ozone occurrences with ozone greater than 85 ppbv come almost entirely from the Houston area, with a few occurrences in the range of 90–100 ppbv from Dallas. The NMM-CMAQ model also has single-peaked distributions, although the peak often occurs at a lower value than observed (e.g., Dallas, Houston, and Austin). In addition, the model under-predicts the high end of the ozone distribution for these three sectors, suggesting a misrepresentation of urban emissions or chemistry in the model. In contrast, WRF-Chem has an unrealistic bimodal distribution at Dallas, Houston, others (rural), and to a lesser degree for Austin and San Antonio, with one

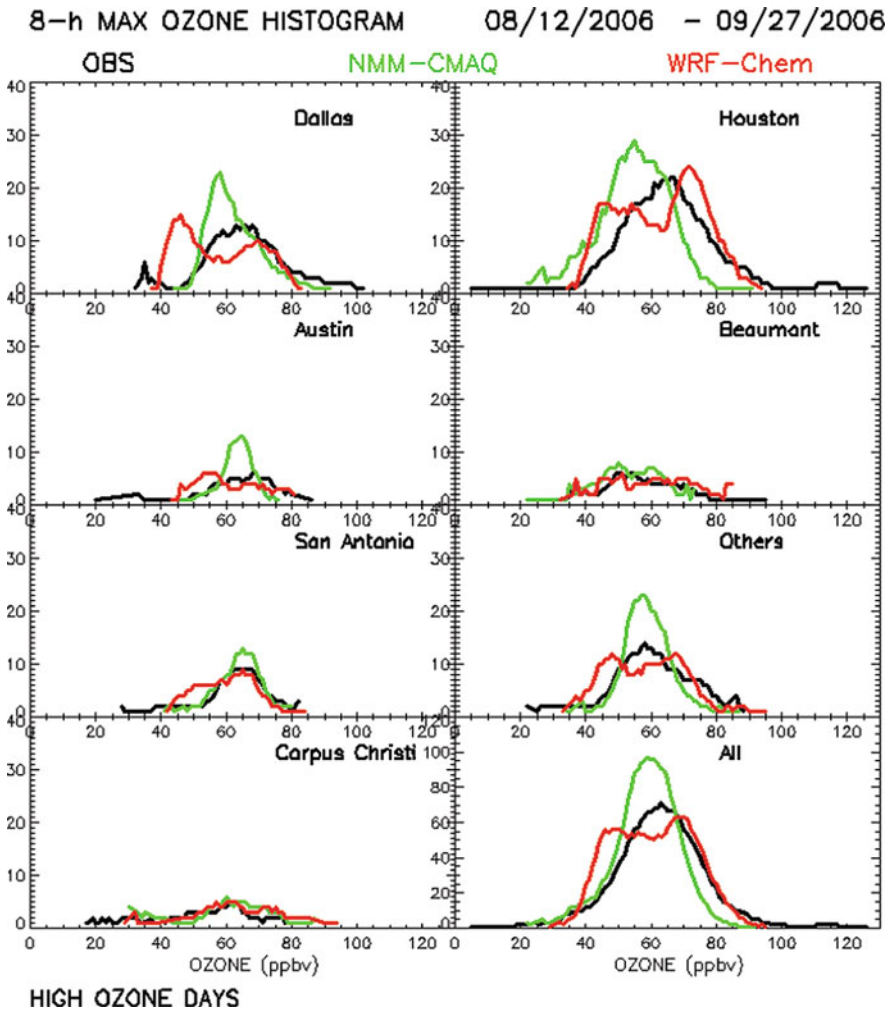

Fig. II.6.23 Histograms of 8-h max ozone for the 19 high-ozone category days, for each of the seven regional sectors and for all sites combined, after smoothing using a five-point box-car filter, for the observations, NMM-CMAQ model, and WRF-Chem model

peak at ~45 ppbv and a second peak at ~75 ppbv. The lower value peak in WRF-Chem is not seen in either of the observations or NMM-CMAQ. WRF-Chem well simulates higher ozone values at Houston in the range of 75–95 ppbv, although it too misses the long tail of values extending to 128 ppbv. However, this improved high-end performance is not replicated for Dallas, where WRF-Chem does not produce any 8-h max ozone in the range of 85–100 ppbv.

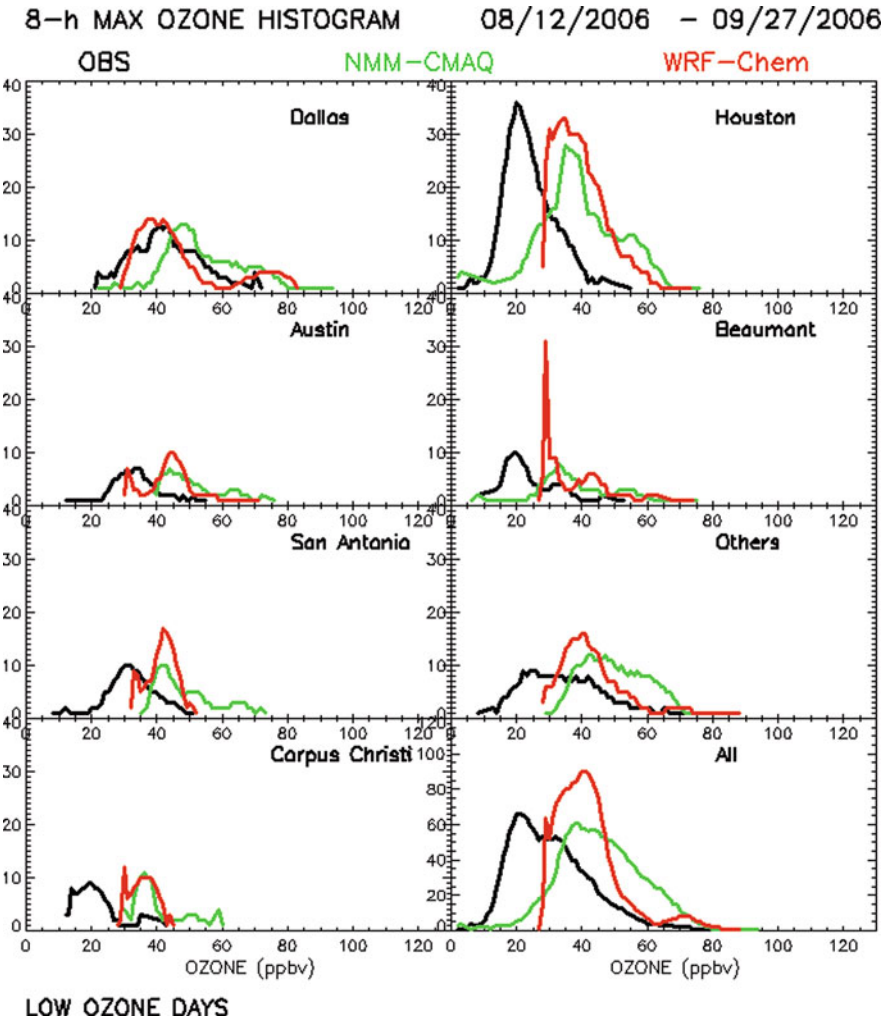

Fig. II.6.24 As in Fig. II.6.23 except for the 17 low-ozone category days

For low-ozone days (Fig. II.6.24) the observations again show a single-peaked distribution for all seven sectors, although the distributions tend to be skewed toward the low end. Peak values occur at 20 ppbv for coastal sectors (Houston, Beaumont, and Corpus Christi), increasing to 30 ppbv at moderate distances inland (San Antonio and Austin), and then increasing further to 40 ppbv Dallas. This increase represents the chemical transformation of the initially clean air on its northward trajectory from the Gulf of Mexico. Both the NMM-CMAQ and WRF-Chem models have low-ozone day peaks at too high of ozone values. This offset is the clearest for the coastal sectors (Houston, Beaumont, and Corpus Christi), where the offset is as large as 15–20 ppbv and decreases with distance inland, so that by Dallas

the offset in NMM-CMAQ is only 5 ppbv and in WRF-Chem it has disappeared entirely. Again, the positive bias of the models supports the earlier finding that the inflow boundary conditions of 35 ppbv in NMM-CMAQ and 30 ppbv in WRF-Chem are too high and that a more appropriate value would be closer to 20 ppbv.

5 Meteorological Data Assimilation in Air Quality Models: CCOS

In the final topic in our discussion on the use of remote sensors in air quality, we examine the utility of remote sensing data for assimilation into the meteorological components of air quality forecast models. Data assimilation is of great importance for studies that investigate the best ways to reduce air pollution through regulation of emissions. These control studies typically focus on a high-concentration episode and use the best possible meteorological fields as input to a chemical transport and transformation model. The emissions are then changed slightly over and over again, and simulations are run in each scenario to determine how the resulting ozone will be affected. Without accurate meteorology, it is possible that the response of the photochemistry model can lead to misleading results regarding the emissions dependency, and therefore meteorological data assimilation is required.

The CCOS 2000 observational field program was operated from June 1 through October 2, 2000. Extensive observations were collected in central California to document high-ozone episodes and the meteorology associated with them. In this study we focus on the five-day July 29–August 2 intensive operating period (IOP2), when the highest surface ozone was observed. During the field phase of CCOS, a network of 25 wind profilers was deployed across California, as shown in Fig. II.6.25.

The MM5 mesoscale model has been used to simulate the flows observed during CCOS, both with and without four-dimensional data assimilation (FDDA). The mesoscale model without the FDDA (simulation MNFD) is generally able to reproduce the main features (Fig. II.6.26), though there are obvious differences in wind magnitudes and directions. These features include the (a) sea breeze, which can bring cooler, moisture, and lower ozone concentration air as it propagates inland; (b) flow through the San Francisco Bay area, which is the principal inflow to the Central Valley, and the split of this flow, which determines the relative inflow into the Sacramento and San Joaquin Valleys; (c) nocturnal low-level jets (LLJs), which can rapidly transport boundary layer pollutants along the Central Valley; (d) the Sacramento (also known as the Schulz) and Fresno mesoscale eddies which can recirculate ozone and its precursors; (e) slope flows, which result in transport in or out of the valleys, support boundary layer venting along mountain crests, and produce subsidence or ascending motion over the valleys.

As was seen in Fig. II.6.26, the MM5 model was able to replicate the dominant flow features, even without FDDA. This means that the role of FDDA is to introduce relatively minor changes to the flow and that the flow with FDDA will still be in close dynamic equilibrium. The FDDA MM5 simulations are run using

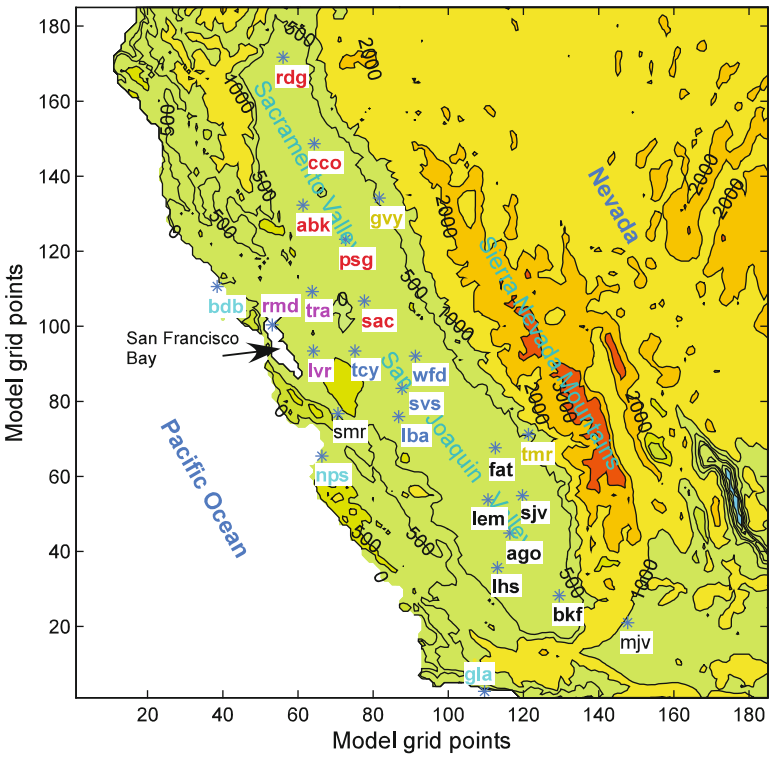

Fig. II.6.25 Map showing the 4-km model mesh and the array of CCOS 2000 wind profilers. The Sacramento Valley sites, the Central Valley inflow sites, the northern San Joaquin Valley sites, the southern San Joaquin Valley sites, the slope sites, and the coastal sites are shown. The terrain isopleths intervals are 0, 100, 200, 500, 1,000, 2,000, and 3,000 m

analysis nudging on the 36-km domain, observational nudging of the profiler, and surface winds on the 4-km domain. A radius of influence parameter for the nudging is set to 40 km, as a larger radius is not justified considering the complex terrain of the domain. Only nudging of the wind field is done in this study as previous studies have indicated that assimilation of temperature data near the surface and within the boundary layer can adversely affect the simulation.

To best show the effects of FDDA, time–height cross sections of winds from both the MM5 simulation without FDDA (MNFD) and with FDDA (MFDi) are juxtaposed with the observations in Figs. II.6.27 and II.6.28 for the Arbuckle wind profiler site in the northern portion of the valley. As can be seen, without FDDA, the model replicates many of the features of the flow. However, with FDDA (Fig. II.6.28) the winds are seen to follow the flow almost exactly. Again, the high accuracy of the winds using nudging is achieved because the non-FDDA simulation already replicates the main features of the flow, so that FDDA really applies a small amount of "nudging" to the flow.

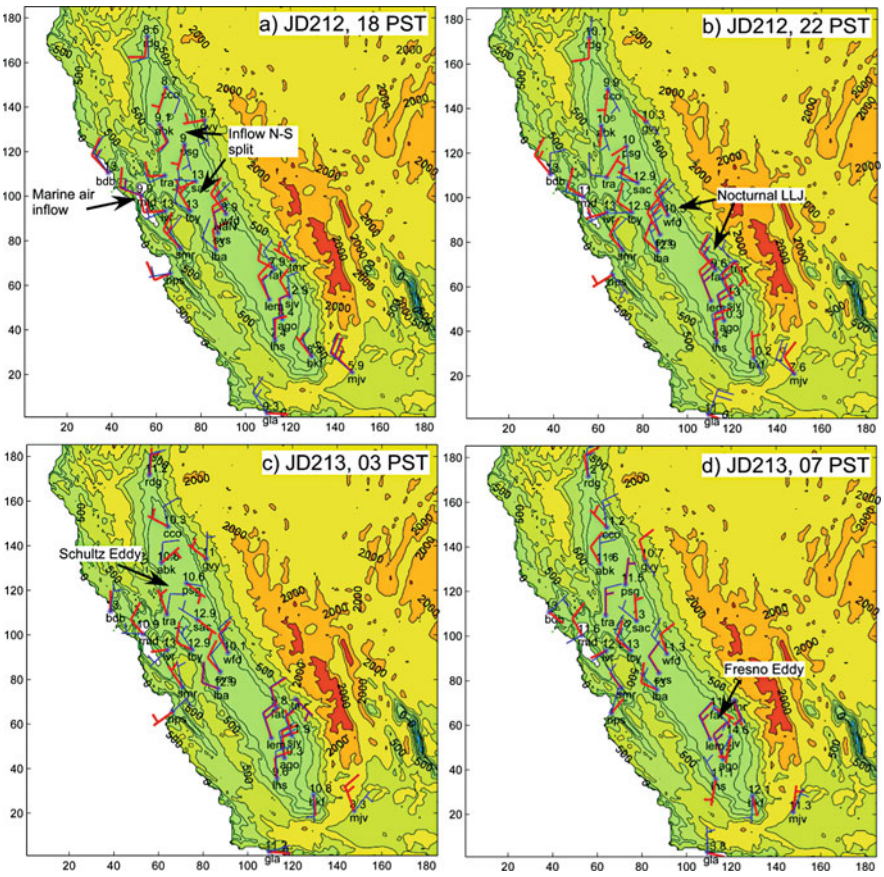

Fig. II.6.26 Observed and modeled wind barbs at 300 m at the CCOS wind profiler sites. Times shown are **a** 18 PST YD212, **b** 22 PST YD212, **c** 03 PST YD213, and **d** 07 PST YD213. Key meteorological features are highlighted

The degree of improvement to the flow with FDDA is examined statistically in Fig. II.6.29 for the scalar speed and vector wind speed, at three heights, all as a function of time for the 5-day simulated episode. Without FDDA, the model sometimes produces large scalar speed biases. At lower heights, these biases vary diurnally and are largest at night. Using FDDA, the scalar speed biases and vector RMS errors are much reduced and are uniform in time.

The non-FDDA simulated wind directions (Fig. II.6.30) have RMS errors of 30–130°, with the larger errors occurring during the night and morning hours when the winds speeds are generally weaker. Wind direction evaluations at higher levels are similar to the 20-m level. With FDDA the wind direction RMS errors are reduced to between 15° and 70°.

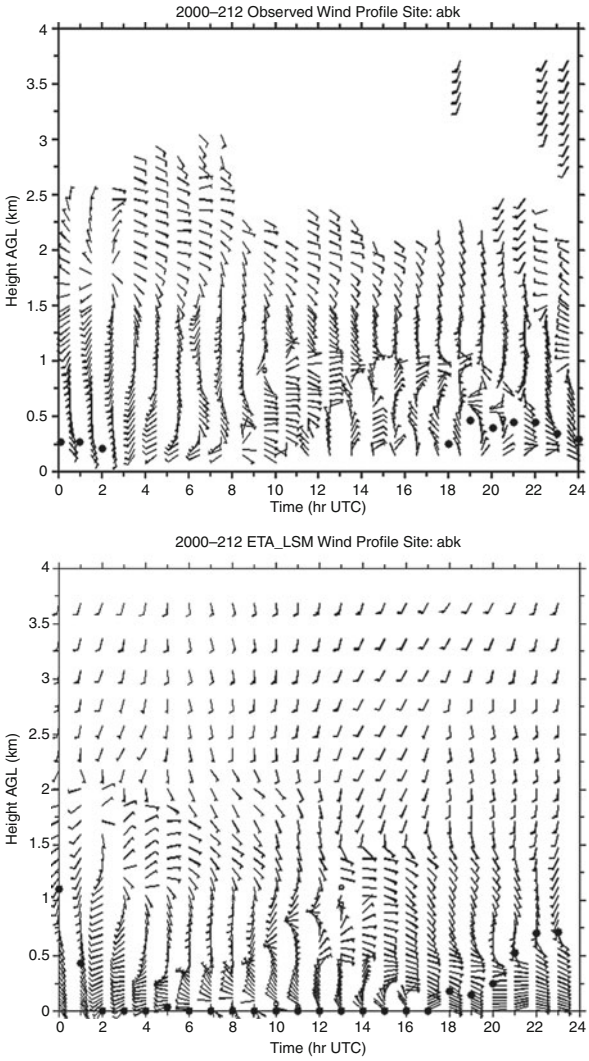

Fig. II.6.27 Arbuckle winds observed and MM5 without FDDA

The non-FDDA (MNFD) simulated near-surface temperatures are clearly too cold during the nighttime, and this negative bias becomes larger throughout the simulation (Fig. II.6.31a). The 19-site near-surface temperature bias is about –1°C during the first day and decreases to about –2.3°C at the end of the simulation. Assimilating the profiler winds not only improves the wind field but also improves the temperature bias, presumably through geostrophic adjustment of the mass field as suggested by the fact that this improvement only occurs after about 24–36 h of simulation. The assimilation of the winds could also be improving the horizontal temperature advection, though the delay in the temperature improvement shown by Fig. II.6.31a, b suggests a less direct dynamical

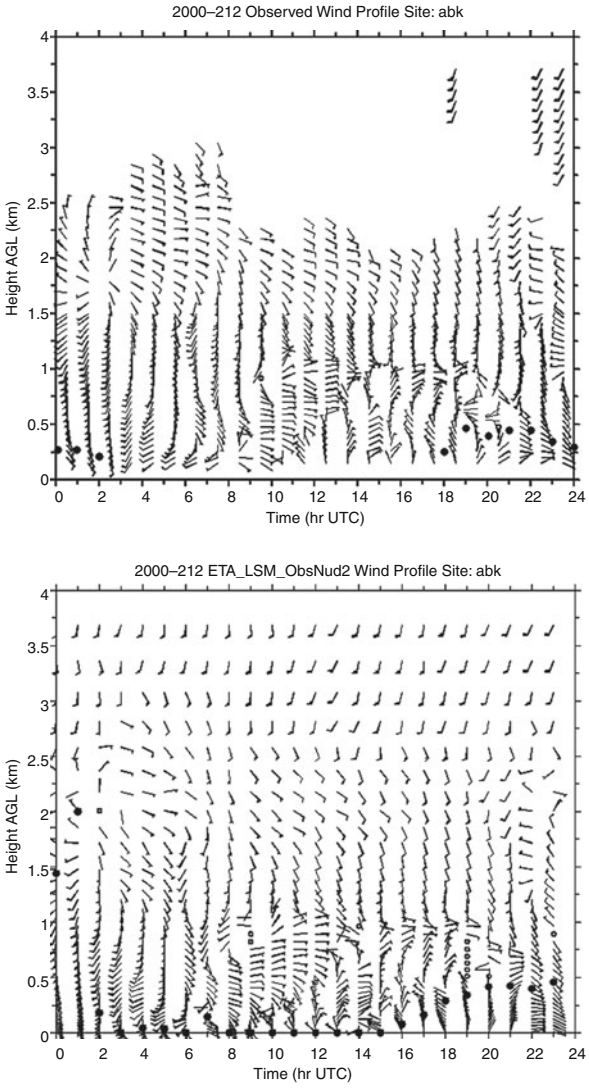

Fig. II.6.28 Arbuckle winds observed and MM5 with FDDA

feedback on the temperature field. The 1,000 m mean temperature in MFDi is within 0.5°C of the observed, and the near-surface nighttime cold biases are improved. Probably most significantly, the decreasing trend in the bias is no longer present.

Vertical profiles of the error statistics were computed for each validation site and then averaged for all of the validation sites. The profiles of wind statistics (Fig. II.6.32) show that the positive wind speed bias at low levels for the non-FDDA simulation (MNFD) changes sign near 500 m and that there is a peak in the vector RMSE profile near 200 m. The wind direction bias is small (2–4°) in the lowest

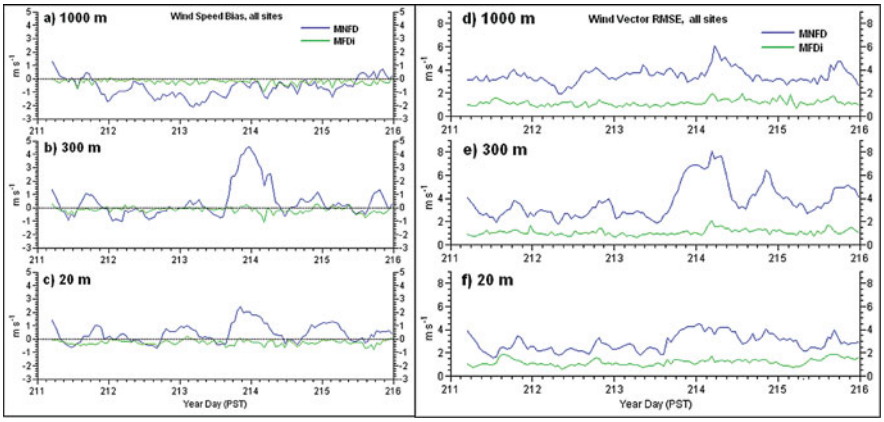

Fig. II.6.29 Wind validation of simulations MNFD and MFDi using data from all 25 wind profiler sites. The *left panels* show the scalar wind speed bias (mode – observation), the *right panels* the vector RMS error at 1,000 m (**a**, **d**), 300 m (**b**, **e**), and 20 m (**c**, **f**)

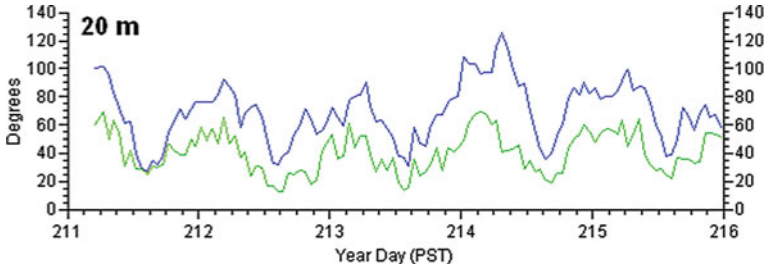

Fig. II.6.30 MM5 RMS error of wind direction at a height of 20 m, averaged over 25 wind profiler sites

1,000 m, but the model has a spurious directional shear of about 15° in the lowest 2,000 m which suggests that cold air advection is too strong in the model. This would be consistent with the noted increasing cold bias with time. The directional RMSE is slightly less below 1,000 m than above. In all cases assimilation of wind profiler data (MFDi) improves the statistics significantly.

Since the effects of the FDDA are evaluated with the same data that are used to nudge the model, it may not be surprising that FDDA greatly improves the simulation at these sites. To evaluate the improvement achieved at a distance away from the sites used in the FDDA, experiment MFDiwh4 was run. In this experiment, the observations at sites AGO, CCO, SAC, and SVS were not used in the FDDA (Fig. II.6.33). The impact of the FDDA was then evaluated at these four withheld sites.

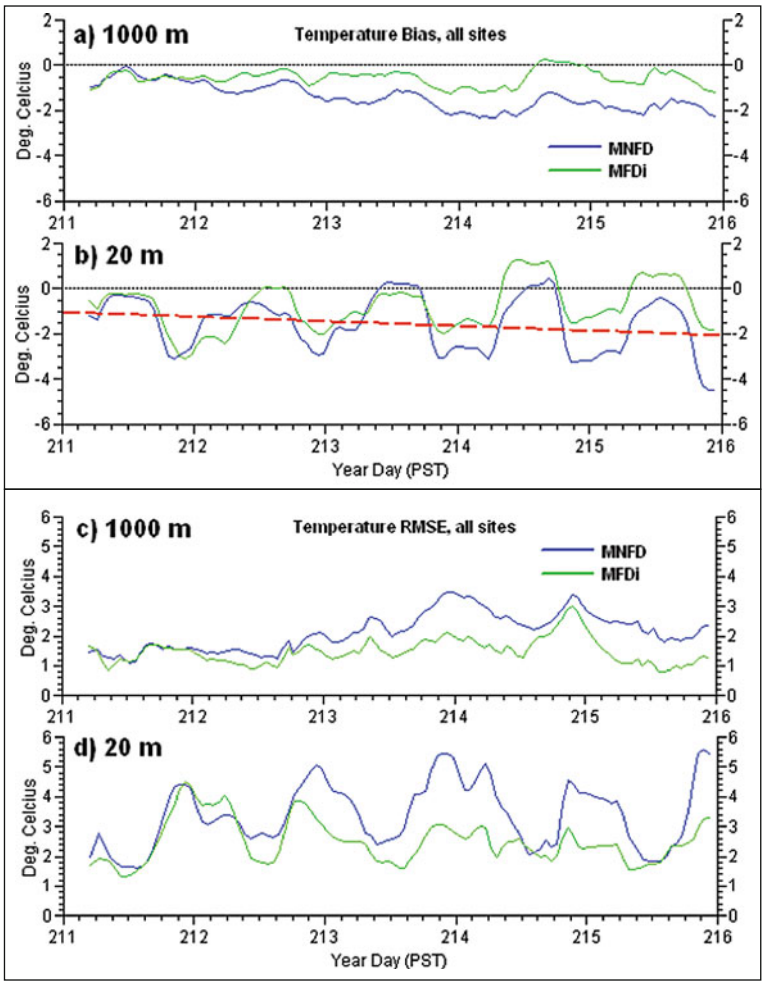

Fig. II.6.31 Virtual temperature validation of simulations MNFD and MFDi. The *panels* show bias and RMSE, respectively, at 1,000 m (**a**, **c**) and 20 m (**b**, **d**). All 25 profiler sites are used. The *dashed line* in (**b**) shows a linear fit to the MNFD bias curve

Figure II.6.34a, b shows that the mean wind speed and direction profiles at the four sites are significantly improved using FDDA in MFDiwh4 compared to the non-FDDA simulation (MNFD), but the error characteristics at these four sites were not as good in MFDiwh4 as when the data from the four sites were used in the FDDA (MFDi). Note also that the error characteristics of the temperature field improved dramatically at these four sites through the use of FDDA in MFDiwh4 and were very nearly as good as those obtained when the winds at these four sites were used in the full FDDA simulation (Fig. II.6.34c). This suggests that the radius of influence

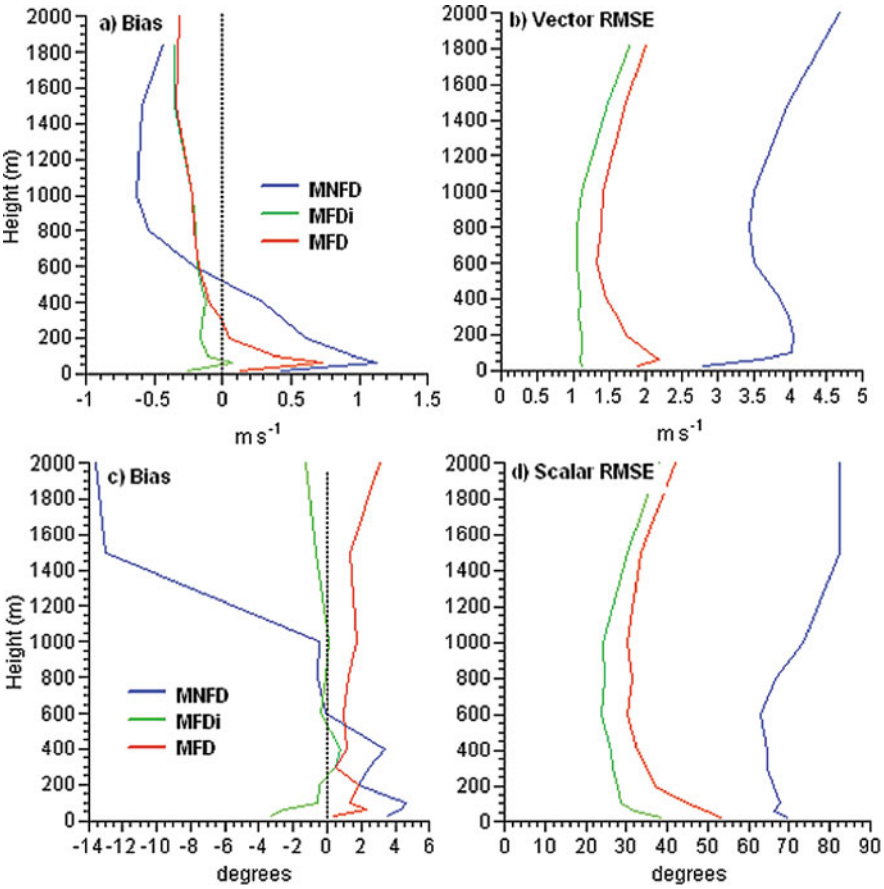

Fig. II.6.32 Vertical profiles of **a** wind speed bias, **b** wind vector RMSE, **c** wind direction bias, and **d** wind direction scalar RMSE for simulations MNFD, MFDi, and MFD. The values were averaged over the 25 wind profiler sites

for the assimilation of wind data on the temperature (mass) field is greater than the radius of influence on the wind field.

6 Summary

Remote sensing observations, both of meteorological and chemical parameters, are of great use in air quality research. Specifically, we have shown that wind profiler observations can be used for trajectory analysis, model evaluation, and data assimilation. For model evaluation, the separation of analysis days according to the observed meteorology can lead to insights into the model's chemistry that are

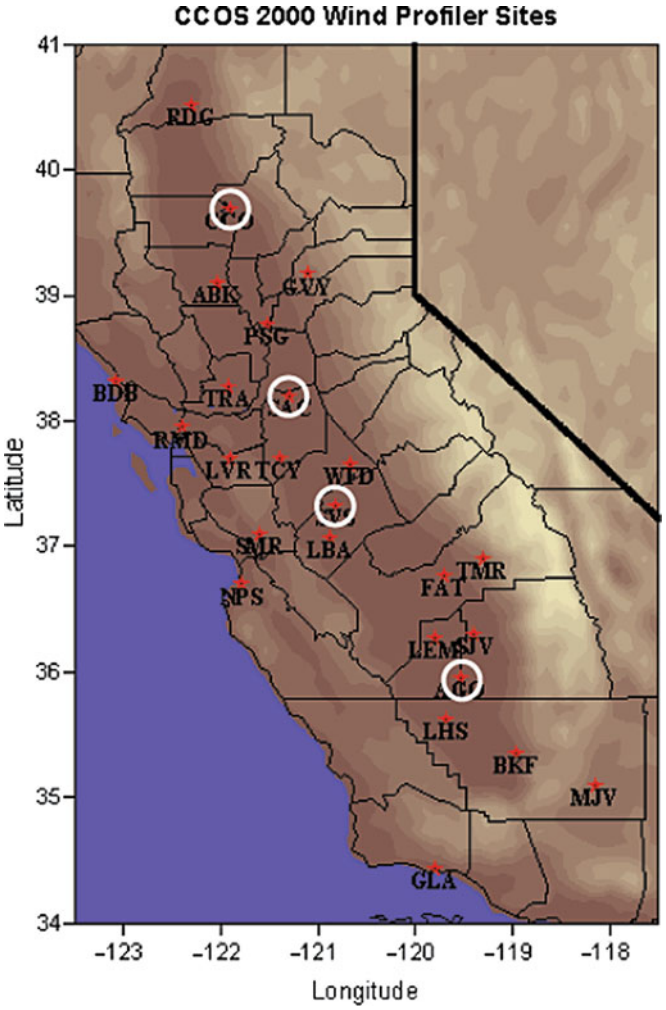

Fig. II.6.33 Wind profiler array, with four stations identified (CCO, SAC, SVS, and AGO) at which no FDDA took place

otherwise not possible to achieve. With data assimilation of dense profiler networks, meteorological models can reach a high degree of accuracy, increasing their utility for regulatory studies.

Doppler lidar can also be an effective tool for detailed studies of local meteorology and its impact on air quality. Although a much more recently developed instrument, ozone lidar is proving to be a great tool for studying regional air quality, especially when the lidar is operated from an aircraft, as it provides a three-dimensional depiction of the ozone concentrations. This tool is certain to become an essential component for future air quality field campaigns.

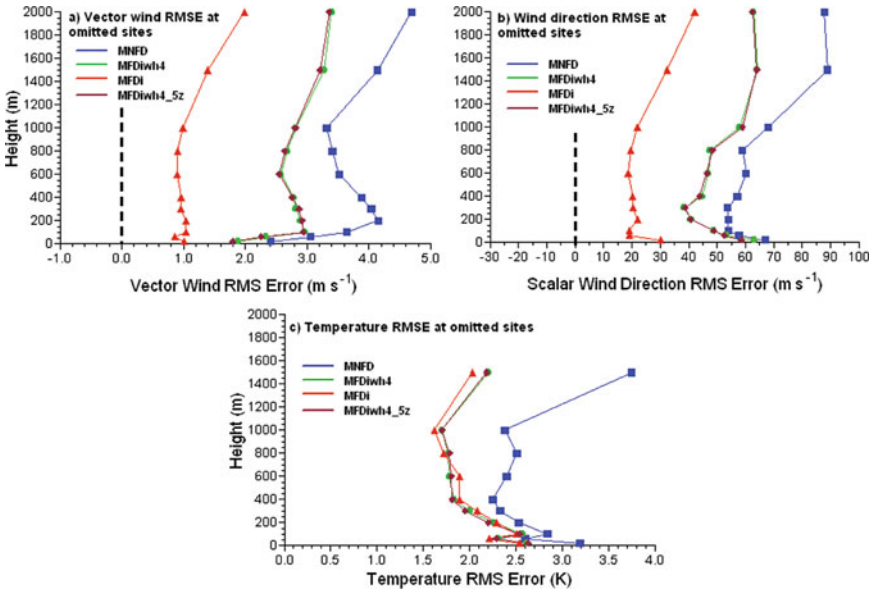

Fig. II.6.34 Vertical profiles of **a** vector wind RMS error, **b** wind direction RMSE, and **c** potential temperature RMSE at sites AGO, CCO, SAC, and SVS for MNFD (squares), MFDi (triangles), MFDiwh4 (dots), and MFDiwh4_5z (diamonds)

References

Banta RM, Senff CJ, Nielsen-Gammon J, Darby LS, Ryerson TB, Alvarez RJ, Sandberg SP, Williams EJ, Trainer M (2005) A bad air day in Houston. Bull Am Meteorol Soc 86. doi:10.1175/BAMS-86-5-657

Bianco L, Wilczak JM, White AB (2008) Convective boundary layer depth estimation from wind profilers: statistical comparison between an automated algorithm and expert estimations. J Atmos Ocean Technol 25:1397–1413

White AB, Senff C, Keane A, Darby L, Djalalova I, Ruffieux D, White D, Williams B, Goldstein A (2006) A wind profiler trajectory tool for air quality transport applications. J Geophys Res 111(D23S23). doi:10.1029/2006JD007475

Wilczak JM, Djalalova I, McKeen S, Bianco L, Bao J-W, Grell G, Peckham S, Mathur R, McQueen J, Lee P (2009) Analysis of regional meteorology and surface ozone during the TexAQS II field program and an evaluation of the NMM-CMAQ and WRF-Chem air quality models. J Geophys Res 114(D00F14). doi: 10.1029/2008JD011675

Chapter II.7
Validation of Satellite Rain Rate Estimation with Ground-Based Observing Systems

P. Antonelli, S. Puca, F. Zauli, R. Bennartz, L. de Leonibus, W. Feltz, and H. Woolf

1 Introduction

The goal of the described work is to present an experimental product for the estimation of convective precipitation rain rates (RR) from satellite observations and the procedure used to create and evaluate the new product. The algorithm, developed to estimate convective RR, combines an existing precipitation product based on AMSU data and developed under the Nowcasting Satellite Application Facility (SAF) (Bennartz 2005) with a convection detection algorithm based on SEVIRI data and developed at the Italian Centro Nazionale di Meteorologia e Climatologia Aeronautica (CNMCA). The convective precipitation derived by the combination of these two products is intended to be used by hydrologists for civil protection purposes. The described validation procedure was not only relevant to the overall product accuracy evaluation, but also represented a critical component for the development of the merging algorithm. The chapter is divided into sections which describe:

- the available in situ data and their consistency;
- the precipitation product from AMSU (theoretical basis for precipitation algorithm, product description, product validation and consequent error characterization, and algorithm improvements);
- the convection detection algorithm based on SEVIRI data (theoretical basis for the convection detection algorithm, product validation and consequent error characterization, and algorithm improvements);
- the convective precipitation product based on the merging of precipitation (AMSU) and convection (SEVIRI) products (methodology, product description, and product validation);
- the conclusions on:
  - validation issues related to the scientific hypothesis behind the merging algorithm;

P. Antonelli (✉)
CIMSS/University of Wisconsin, Madison, WI, USA
e-mail: paoloa@ssec.wisc.edu

D. Cimini et al. (eds.), *Integrated Ground-Based Observing Systems*,
DOI 10.1007/978-3-642-12968-1_14,

- the individual modules used to derive the convective precipitation product;
- the accuracy of available observations;
- the accuracy of the final derived product.

2 Available in Situ Data

This section describes the in situ observations used to develop and evaluate the convective precipitation product (RADAR RR and rain gauge values) and presents a qualitative comparison between them.

2.1 RADAR

The Italian Department of Civil Protection (DPC), through the network of the Regional Functional Centers, collects in real and near real-time RADAR data for the hydro-meteorological monitoring and management. Using these observations, the Meteorological Service of the Air Force (CNMCA) produces national mosaic of rainfall intensity on a grid of $1,400 \times 1,400\,\text{km}^2$ with a spatial resolution of 2.5 km^2 and a time sampling of 30 min. This product (Fig. II.7.1) covers mainly North and Center of Italy. It is worth emphasizing that the national surface rainfall intensity (SRI), used for this project, was not validated nor adjusted with rain gauges. The Italian SRI mosaic is composed of several RADARs managed directly by Regional Government, the Italian Air Force and some foreign countries such as France, Swiss,

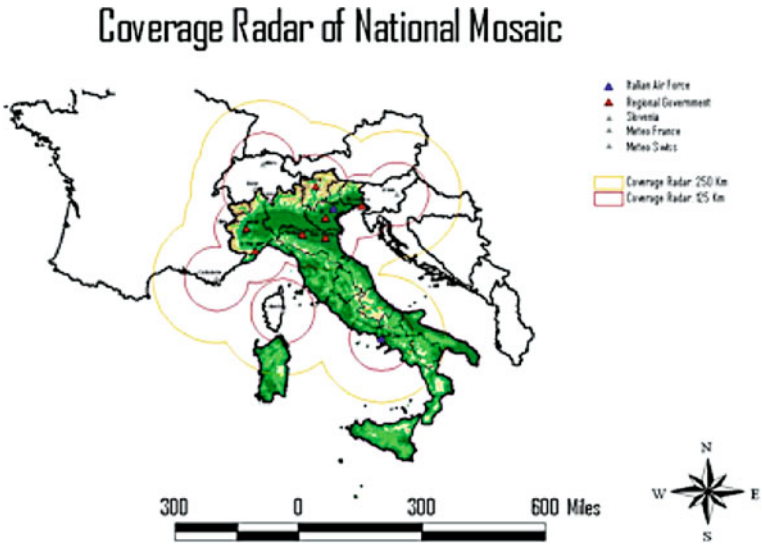

Fig. II.7.1 RADAR coverage

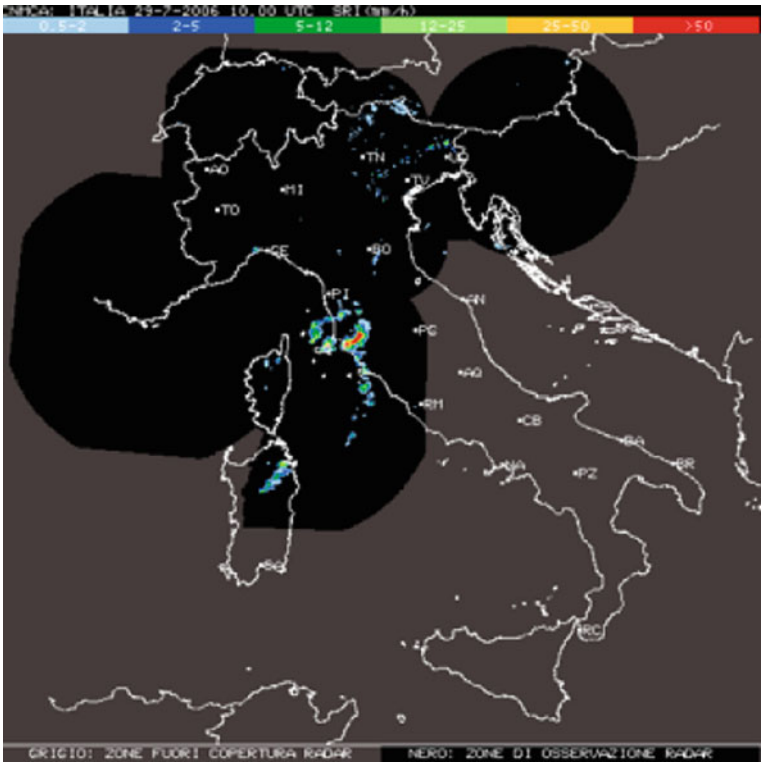

Fig. II.7.2 RADAR national mosaic (For color figure see online version)

and Slovenia (Fig. II.7.2). However for this study only Italian RADAR network was used. The most important technical features of the used RADAR systems are:

- C-band
  - Frequency: 3.900–5.750 GHz
  - Wavelength: 7.69–5.20 cm
- Doppler capacity up to 125 km;
- operation with polarimetric quantities (e.g., dual polarization);
- antenna with characteristics compatible with polarimetric observations;
- beam width = 1^{o};
- RADAR system remotely controlled with 24-h operability.

2.2 Rain Gauges

Rain gauge data acquisition and processing are performed at different temporal intervals ranging from 5 to 30 min. The observation collected by the National

Fig. II.7.3 Rain gauge distribution

Centers and Cumulate Maps of precipitation is made available within 45 min from the acquisition. Figure II.7.3 shows the distribution of the rain gauges over Italy and provides example of the available products.

2.3 Qualitative Comparison: RADAR–Rain Gauges

Since rain gauges and radars represent the main validation instruments for satellite-derived precipitation estimates, it was considered worth to evaluating how they compare to each other. This section describes the comparison of radar data aggregated on a SEVIRI grid (app. A) with individual rain gauges. Figures II.7.4 and II.7.5 show some of the inherent difficulties in using these kind of observations, especially for quantitative estimations. Some of the issues, described also in Sect. 3.4.1, are evident when comparing these two ground-based instruments. In particular:

- too many rain gauge observations are suspiciously reported to be 0 even where radar (as AMSU) sees precipitation;
- the rain gauge observations have not been convolved to the SEVIRI grid using the same convolving scheme used for radar data;
- often the radar temporal resolution (30 min) does not allow for a fair comparison with 10 min cumulated rain observed by the rain gauges;
- dependency of radar RR on observation radial distance from radar coordinates should be taken into account.

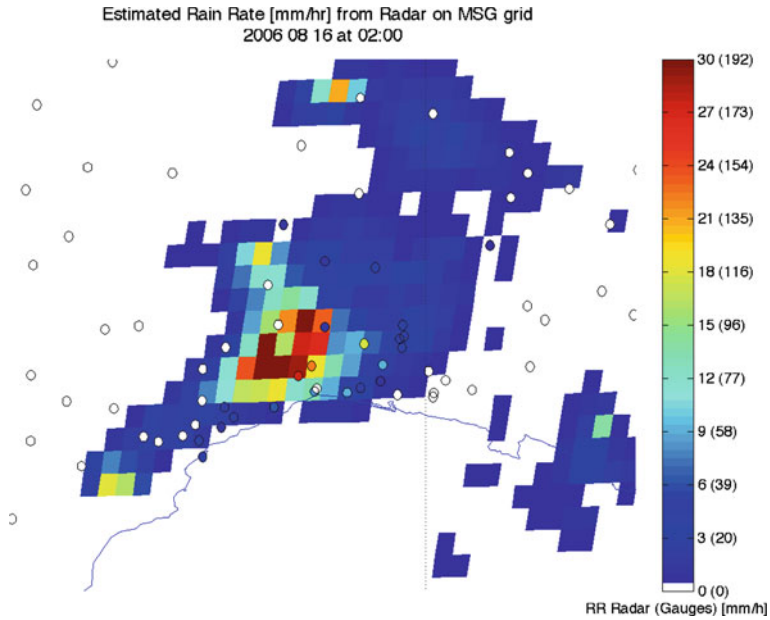

Fig. II.7.4 Radar-estimated RR on AMSU native grid between 02:00 and 02:30 UTC over the Gulf of Genova. RR-derived precipitation is described by the values next to the *colorbar*. The *colored circles* represent rain gauge observations. RR intensity estimated from 10 min cumulate precipitation measured by the gauges at 02:20 UTC is described by the values in parenthesis next to the colorbar (For color figure see online version)

3 Precipitation Retrieval from Microwave (AMSU) Data

3.1 AMSU Data

The advanced microwave scanning unit (AMSU) is a cross-track scanning microwave radiometer consisting of two separate modules: AMSU-A and AMSU-B. The first one has sounding channels in the water vapor (23.8 GHz) and oxygen absorption band complex (50 GHz) plus some window channels (at 31.4 and 89 GHz) and is dedicated mainly to the retrieval of temperature and water vapor profiles. AMSU-B has two window channels (at 89 and 157 GHz) and three channels in the water vapor absorption band at 183 GHz and is dedicated to the retrieval of ice cloud and precipitation (Grody et al., 2004). Being a sounding instrument, AMSU-A has a lower spatial resolution than AMSU-B. Channels and spatial resolutions are detailed in Table II.7.1. AMSU data used for this study were obtained from five platforms (NOAA 15, 16, 17, 18, and METOP-A) over the H-SAF domain (Europe), for a total of 10 overpasses per day, starting from February 1, 2006 (AMSU data from METOP-A were added after the platform launch). Examples of AMSU-B data at 89 and 157 GHz are shown in Figs. II.7.6 and II.7.7.

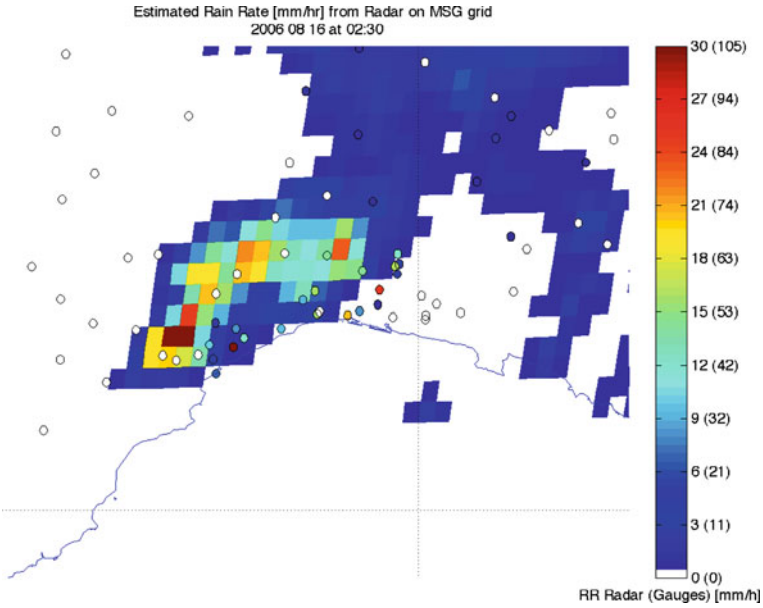

Fig. II.7.5 Radar-estimated RR on AMSU native grid between 02:30 and 03:00 UTC over the Gulf of Genova. RR-derived precipitation is described by the values next to the *colorbar*. The *colored circles* represent rain gauges observations. RR intensity estimated from 10 min cumulate precipitation measured by the gauges at 02:50 UTC is described by the values in parenthesis next to the colorbar (For color figure see online version)

Table II.7.1 AMSU-A and AMSU-B/MHS instrument characteristics

Satellite characteristics	AMSU-A	AMSU-B
Spatial resolution	3.3°	1.1
Nadir effective FOV	$50 \times 50\ \text{km}^2$	$20 \times 16\ \text{km}^2$
Scan edge effective FOV	$150 \times 80\ \text{km}^2$	$64 \times 52\ \text{km}^2$
Channels	23.8, 31.4, 50 GHz O_2 complex, 89.0 GHz	89.0, 150.0, 183 (WV absorption and) GHz

3.2 Precipitation Algorithm Theoretical Basis

The algorithm, hereafter referred to as precipitating clouds (PC) algorithm, uses two channels from AMSU-B. The main principle is that rainfall can be derived from the brightness temperature (BT) difference depression with respect to the background BT difference obtained in the absence of precipitation. In other words, the radiative cooling due to the scattering of the radiation by the ice particles overshooting precipitating convective clouds is taken as a rain indicator, and AMSU-B window channels (89 and 157 GHz) are used for deriving a so-called *Scattering Index* (*SI*):

$$s_{I1} = (T_{89} - T_{150}) - \Delta T_{bk\,(89-150)}$$

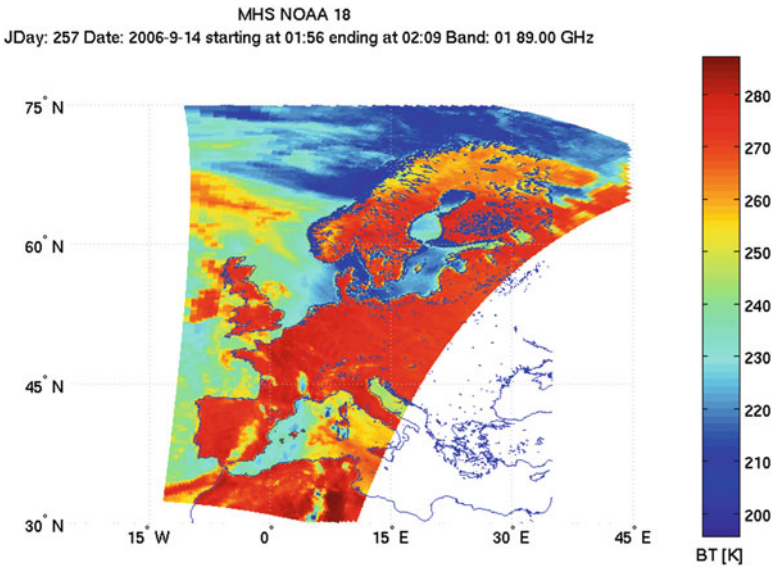

Fig. II.7.6 Example of AMSU-B at data 89 GHz

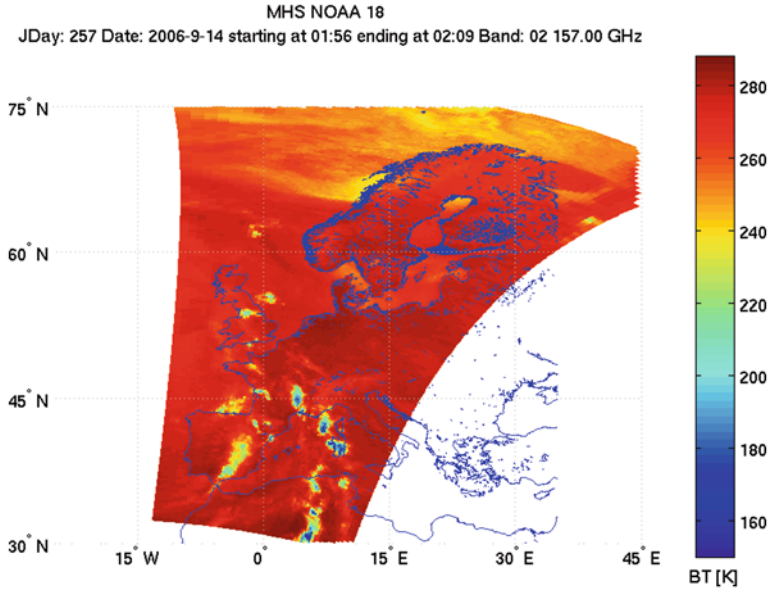

Fig. II.7.7 Example of AMSU-B at data 157 GHz

where T_{89}, T_{150}, for a specific field of view, are BTs at 89 and 150 GHz and $\Delta T_{bk\,(89-150)}$ is the corresponding difference of the BTs at 89 and 150 GHz in absence of precipitation. Detailed description of the algorithm can be found in Bennartz et al. (2002). Final product, obtained at AMSU-B resolution (Bennartz, 2000) is the likelihoods of rainfall classes (i.e., the probability that the rainfall falls within predefined ranges of RRs). Table II.7.2 shows the different classes used. Therefore, a given pixel will not be assigned a certain value but rather a set of probabilities for each of the four RR classes. The algorithm's approach is empirical. The relationships between the precipitation classes and the AMSU-derived scattering indexes and derived from the use of co-located, radar data, convolved at AMSU resolution. This approach allows to overcome the large systematic deviations that the current lack of knowledge about the microwave response to cloud/precipitation microphysics would introduce in case a detailed inverse modeling approach was chosen. This is especially true where surface characteristics are highly heterogeneous. The *precip-radiation database*, created by convolving rain gauge adjusted radar estimates, was used to calibrate the algorithm. The database is composed of thousands of couples of AMSU observations and related radar-derived precipitation classes. These data were collected during 8 months (April–November 1999) at Swedish Hydrological and Meteorological Institute (SHMI) and cover the Baltic Sea region. Due to the limited representativeness of this data set, the algorithm sensitivity, in the current implementation, does not allow for the discrimination of more classes.

It is worth emphasizing that the algorithm was tuned to perform optimally over northern Europe and it may not be exported to other regions straightforwardly. In fact, an adjustment to other climate regions is deemed necessary to re-define algorithm characteristic thresholds. It is also important to recognize that the database used to tune the algorithm must be statistically significant, and all the meteorological and climatological situations of interest must be conveniently represented. In fact, the problem of the representativeness of the database is a well-known problem in rainfall retrievals and may hamper the validity of the retrieval if not properly handled (Panegrossi et al., 1998; Bauer, 2001; Di Michele et al., 2003; Kummerow and Giglio, 1994). Finally, when using the *precip-radiation database*, one must be conscious that several errors are intrinsically taken on-board like the spatial and temporal collocation errors between radar data and satellite observations (due, for example, to temporal misalignments, to satellite navigation errors, to the different geometries of the observations).

Table II.7.2 Classes of different precipitation intensities used in this investigation (Bennartz, 2002)

Class	Type of precipitation	Minimum RR (mm/h)	Maximum RR (mm/h)
1	No precipitation	0.0	0.1
2	Risk of light precipitation	0.1	0.5
3	Light/moderate precipitation	0.5	5.0
4	Intensive precipitation	5.0	

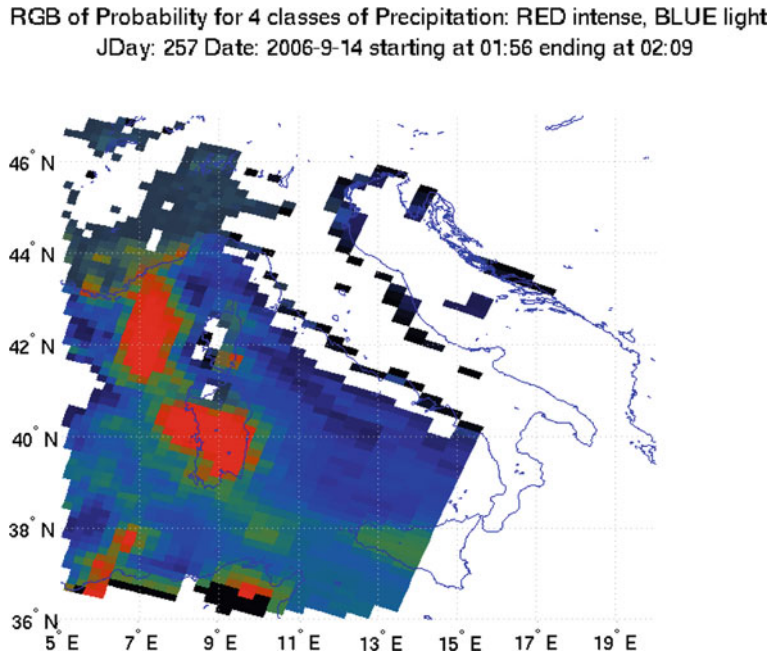

Fig. II.7.8 Example of PC standard RGB composite. The RGB is obtained mapping the probability of each pixel belonging to class 1 to *blue*, class 2 to *green*, and class 3 to *red*. The RGB obtained in this way shows high precipitation in *red* and low precipitation in *blue*. No precipitation is shown in *white*. The RGB conveys the full information about the likelihood of each pixel belonging to any of the four classes, however, it does not provide a single value per pixel and therefore can be used only for qualitative comparisons with radar or rain gauges (For color figure see online version)

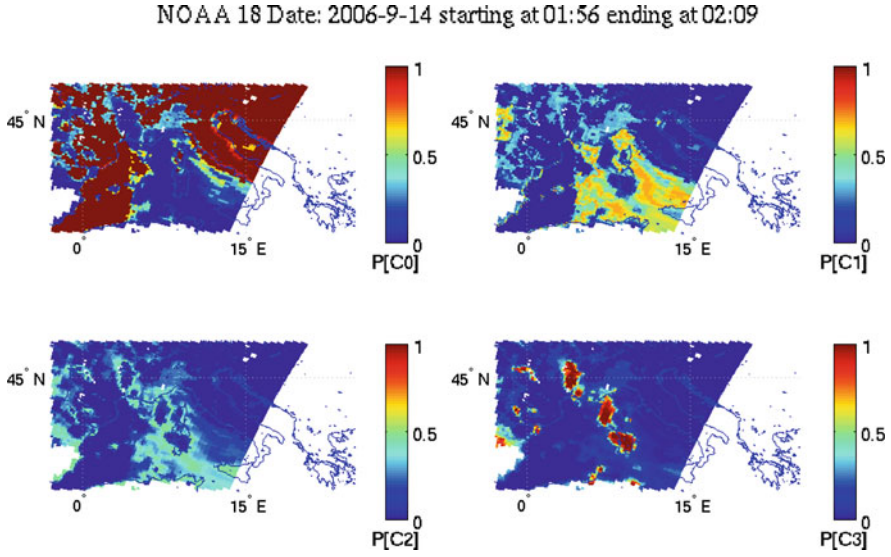

Fig. II.7.9 Example of likelihood for each individual class of precipitation as described in Table II.7.2

3.3 PC Products

From the PC output two products generated on the AMSU native grid are:

- likelihoods for four different intensity classes of precipitation;
- PC standard RGB composite (Fig. II.7.8). The RGB is obtained mapping the probability of each pixel belonging to class 1 to BLUE, class 2 to GREEN, and class 3 to RED. The RGB obtained in this way shows high precipitation in RED and low precipitation in BLUE. Absence of precipitation is shown in white. The RGB conveys the full information about the likelihood of each pixel belonging to any of the four classes, however, it does not provide a single value per pixel and therefore can be used only for qualitative comparisons with radar or rain gauges. Individual classed of probability are shown in (Fig. II.7.9).

In order to obtain point values of precipitation, the first PC product was further manipulated in two different ways:

- *Maximum probability approach* (Fig. II.7.10). The class with the highest probability is chosen. It is a straightforward approach, however it can be misleading: for

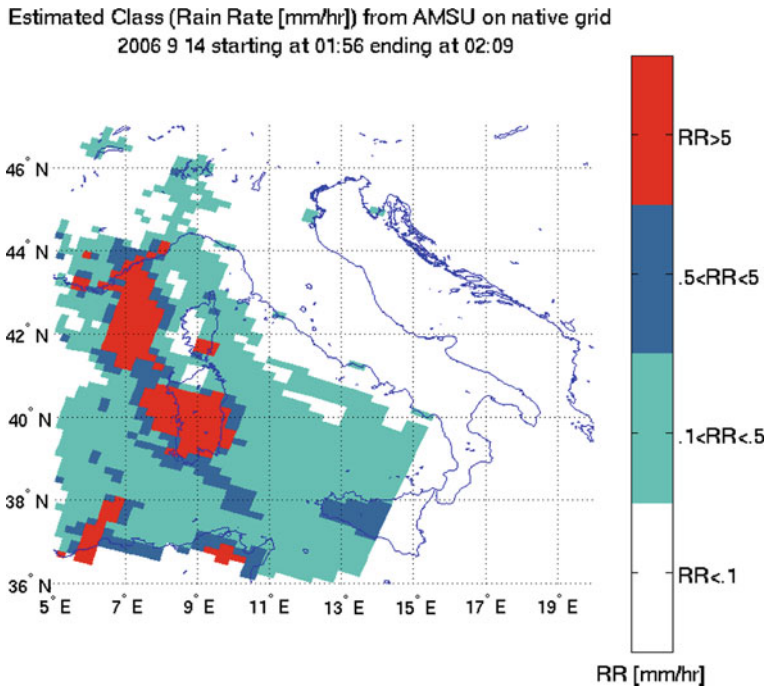

Fig. II.7.10 Example of original PC product: classification using the maximum probability approach. Classifying each pixel according to the maximum probability among the different classes provides a unique value (class), however, this value can be misleading when, for example, the probability, for a given pixel, is spread across two or more different classes. In this case the algorithm would still assign the pixel to one class and of the information regarding the probability distribution is lost

example if, for a given pixel, the probability across two or more different classes was uniform, the algorithm would still assigning one class only, and the information regarding the actual probability distribution among the different classes would be lost;

- *Weighted average RR approach* (Fig. II.7.11). The weighted average approach provides *an arbitrary* estimate of the RR according to the following equation: $\overline{RR} = \sum_{i=1}^{4} p_i \overline{rr}_i$ where p_i is the likelihood, and $\overline{rr}_i$ the mean RR value for class i. This quantity conveys the full information about the likelihood of each pixel belonging to any of the four classes, but the actual $\overline{RR}$ values are arbitrary as the mean value for each class (especially class four, intense precipitation) is set to a given value in an arbitrary way. In spite of this limitation, under specific circumstances, the representation is still useful for qualitative and quantitative comparisons.

Further developments of the PC algorithm, occurred after the realization of this study, introduced a new PC product for the instantaneous RR. However, the new product not used for the presented work is not discussed in this chapter.

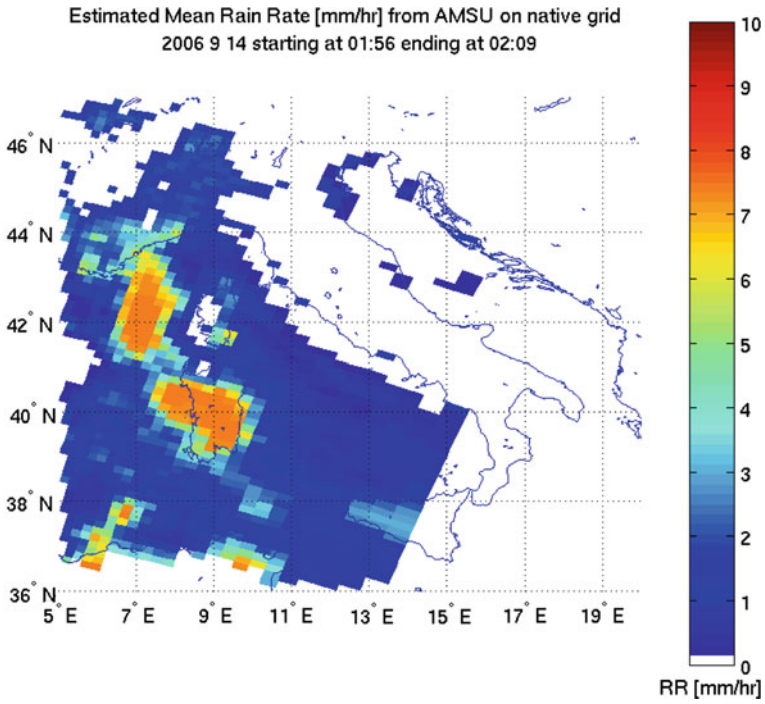

Fig. II.7.11 Example of original PC product: classification using the weighted average RR. The weighted average conveys the full information about the likelihood of each pixel belonging to any of the four classes, but the values above 5 mm/h are arbitrary as the mean value for class 4 (intense precipitation) was set to 10 mm/h in an arbitrary way. In spite of this, the representation is still useful for qualitative and quantitative comparisons

3.4 PC Validation

3.4.1 Qualitative Validation: PC-GAUGES

Figure II.7.12 and II.7.13 shows that a simple comparison, between PC-weighted average RR and the rain gauge observations, does not provide conclusive evidence useful for the estimation of the PC accuracy. This might be explained by the following considerations:

- too many rain gauge observations are *suspiciously* reported to be 0 even where AMSU (as radar) sees precipitation;
- rain gauge observations were not convolved at AMSU resolution; and
- the impact AMSU geolocation uncertainty should be carefully estimated.

In spite of these difficulties the 10 min (cumulated rain) temporal resolution of the rain gauge observations and their dense spatial distribution make them potentially useful for qualitative and quantitative estimate of the PC accuracy.

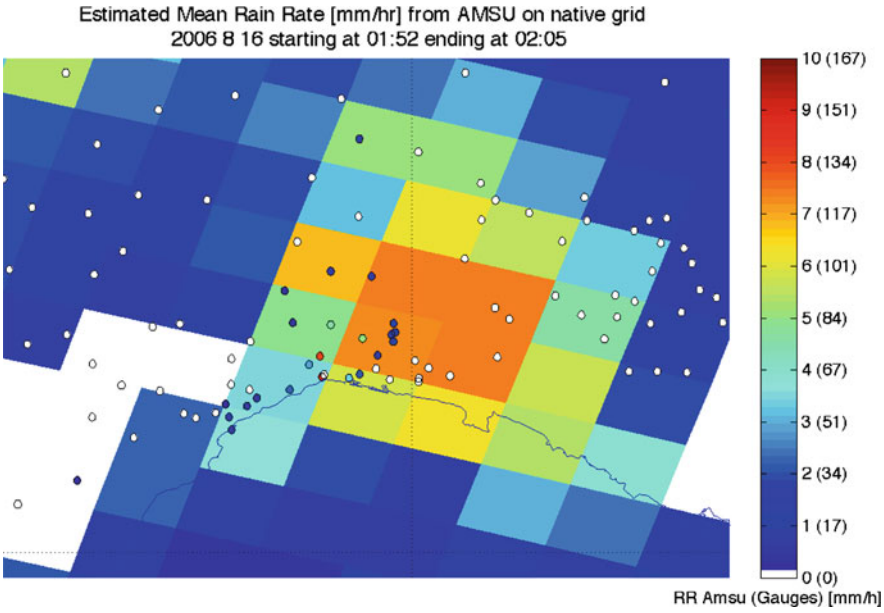

Fig. II.7.12 PC-weighted average on AMSU native grid at 01:52 UTC over the Gulf of Genova. AMSU-derived precipitation is described by the values next to the *colorbar*. The *colored circles* represent rain gauges observations. RR intensity estimated from 10-min cumulate precipitation measured by the gauges at 02:00 UTC, is described by the values in parenthesis next to the *colorbar* (For color figure see online version)

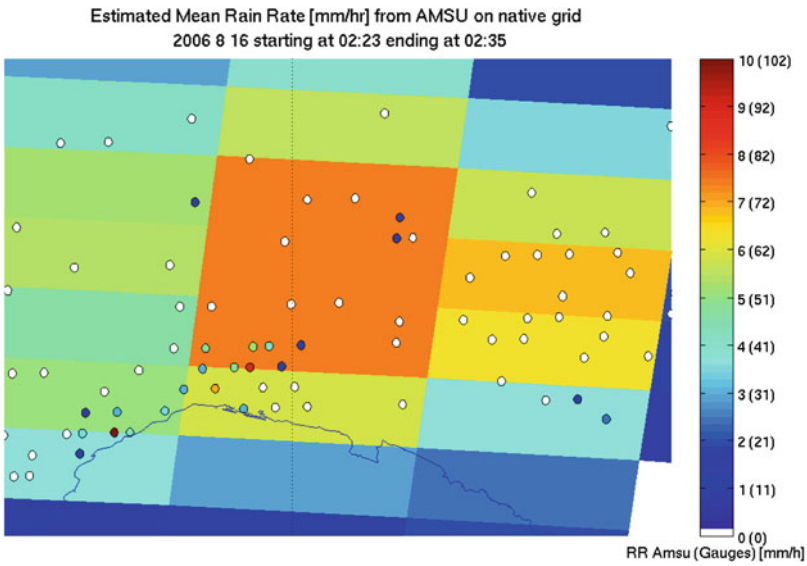

Fig. II.7.13 PC-weighted average on AMSU native grid at 02:35 UTC over the Gulf of Genova. AMSU-derived precipitation is described by the values next to the *colorbar*. The *colored circles* represent rain gauges observations. RR intensity estimated from 10 min cumulate precipitation measured by the gauges at 02:30 UTC is described by the values in parenthesis next to the *colorbar* (For color figure see online version)

3.4.2 Quantitative Validation of PC with Radar Data on AMSU Grid

The quantitative validation of the original PC algorithm, applied to Southern Europe, was done for about 43,000 observations taken in 7 different days by the NOAA 16 and 18 satellites. It was performed using radar data convolved on the AMSU grid as shown in Fig. II.7.14. The results were compared in two ways:

1. AMSU precipitation classes (max probability approach) were compared to radar-derived classes of precipitation, pixel by pixel on AMSU native grid.
2. AMSU re-calculated classes (weighted average approach) were compared to radar-derived classes of precipitation, pixel by pixel on AMSU native grid, according to the following procedure:

   (a) AMSU-derived RR was calculated using the weighted average of the likelihoods. A mean RR value was assigned to each class (as described by third point of Sect. 3.3) and
   (b) weighted averages of RR were classified again according to Table II.7.2.

This methodology was required because the weighted average is an arbitrary estimate (in particular, the mean value of the intense precipitation class is arbitrary), and the one based on the maximum likelihood does not take into account

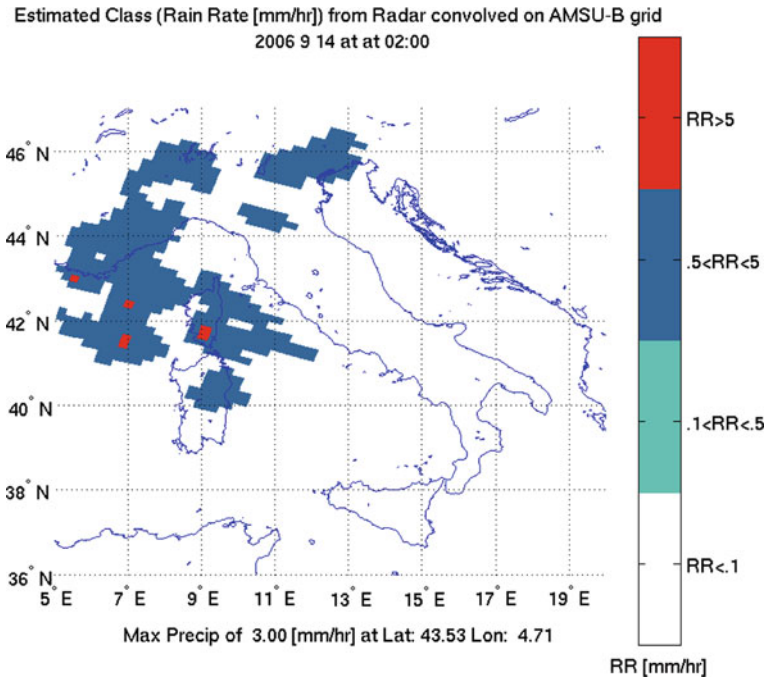

Fig. II.7.14 Example of radar data convolved at AMSU-B spatial resolution and binned using the same classification thresholds used by the PC algorithm

the probability distribution among the different classes but only the maximum probability.

Radar data were convolved on AMSU grid and classified according to Table II.7.2 and the contingency tables were then calculated for all the selected overpasses. These procedures do not take in account several of the issues discussed in the previous sections but still provide some useful information on the performances of the PC algorithm over the Mediterranean area. The results presented in Tables II.7.3, II.7.4, and II.7.5 indicate that:

- In both cases (max probability and weighed average) PC misclassified several pixel assigning them to class 2 and 3 ($0.1 < RR < 5$ [mm/h]) while according to the radar the pixels were belonging to class 1 (no precipitation) as showed in Table II.7.5. This misclassification issue appeared to be more evident for daytime passes (Table II.7.3) than for nighttime ones (Table II.7.4);
- Several pixels were classified as class 4 ($RR > 5$ [mm/h]) by PC while according to the radar they were belonging to class 3 ($0.5 < RR < 5$ [mm/h]). The issue is due to the fact that radar, with increasing distance, tends in general to underestimate RR intensity. The problem is also due to the arbitrary mean value associated to class 4 in the intermediate step for the PC product when the weighted average RR was calculated.

Table II.7.3 Contingency table for daytime only for the max probability approach and for the weighted average approach (in parenthesis). PC classification are on the rows while radar estimations are on the columns

PC/RADAR	*R*1	*R*2	*R*3	*R*4
C1	93.69 (95.02)	4.74 (3.86)	1.52 (1.10)	0.05 (0.01)
C2	66.05 (93.66)	21.21 (4.03)	12.15 (2.11)	0.73 (0.20)
C3	23.66 (63.33)	36.62 (19.79)	37.22 (16.03)	1.85 (0.84)
C4	3.40 (0)	16.54 (5.81)	68.98 (71.32)	5.82 (22.86)

Table II.7.4 Contingency table for nighttime only for the max probability approach and for the weighted average approach (in parenthesis). PC classification are on the rows while radar estimations are on the columns.

PC/RADAR	*R*1	*R*2	*R*3	*R*4
C1	92.47 (93.52)	5.34 (4.70)	2.17 (1.76)	0.01 (0.01)
C2	53.50 (82.75)	28.78 (13.55)	16.99 (3.70)	0.73 (0.00)
C3	21.69 (50.87)	37.03 (26.24)	39.41 (21.70)	1.85 (1.18)
C4	13.60 (12.10)	17.67 (12.81)	62.91 (69.39)	5.82 (5.69)

Table II.7.5 Contingency table for day- and nighttime for the max probability approach and for the weighted average approach (in parenthesis). PC classifications are on the rows while radar estimations are on the columns. Overall the radars detected 37,044 FOVs with no precipitation (*C*1), 3,427 of *C*2, 2,464 of *C*3, and 171 of *C*4; PC detected 36,740 FOVs with no precipitation (*C*1), 3,955 of *C*2, 1,219 of *C*3, and 1,192 of *C*4

PC/RADAR	*R*1	*R*2	*R*3	*R*4
C1	93.11 (94.28)	5.01 (4.28)	1.82 (1.42)	0.03 (0.01)
C2	62.14 (88.89)	23.56 (8.20)	13.65 (2.8)	0.63 (0.10)
C3	23.05 (59.79)	36.75 (21.62)	37.90 (17.63)	2.29 (0.94)
C4	7.80 (6.03)	17.03 (9.46)	66.35 (70.31)	8.81 (13.91)

Both issues are well understood and they were expected in the application of the PC algorithm to Italian areas. For the described validation exercise the results obtained were, on average, 18% worse, with a peak of 58% for class 4, with respect to those obtained by Bennartz (2005). The discrepancies can be furher explained considering that:

- the radar data used in the validation were not gauge adjusted, underestimation of precipitation from radar data was, therefore, expected;
- the algorithm was trained only with North European radars and for high latitude climate regimes;
- in his validation Bennartz discriminated between land and water pixels and excluded coastal regions, which were less relevant over northern Europe, than for the Italian case;

- over coastal (and in general heterogeneous) and non-vegetated pixels the current scheme for background temperature estimation does not provide optimal results, this issue appears to be more evident over Italy;
- class 4 pixels over northern Europe are much less frequent than over southern Europe, therefore the data set used to calibrate the algorithm might not be, at this stage, enough representative for the Italian cases.

It is worth mentioning that overall the radars detected 37044 FOVs with no precipitation ($C1$), 3427 of $C2$, 2464 of $C3$, and 171 of $C4$; PC detected 36740 FOVs with no precipitation ($C1$), 3955 of $C2$, 1219 of $C3$, and 1192 of $C4$.

3.5 Improvements to the PC Algorithm

As described in Sect. 3.2, and as shown in Sect. 3.4.2, the performances of the PC algorithm largely rely on the computation of a realistic radiative background. In fact, the rainfall estimation is based on the deviation of the measured BT differences, at 89 and 150 GHz, with respect to the background BT differences (i.e., the ones that would be measured in non-precipitating conditions). In its original implementation, the background BT was computed dynamically over a wide region surrounding the pixel of interest (2 degrees by 2 degrees). This technique is simple and efficient but has several drawbacks, since the possibility that the resulting BT is contaminated by precipitation and/or by heterogeneous backgrounds is extremely high. As a consequence, an effort was devoted to developing a new technique for deriving background BTs: a grid of clear sky pixels was built by making use of a certain number of AMSU overpasses. For a given time interval preceding the one of interest, AMSU data were projected onto a fixed regular grid (the SEVIRI one was used). This projection was done by using the remapping process described in Appendix A. The warmest AMSU clear sky BTs at 89 and 157 GHz, among all the overpasses within a certain time window (4 days in this study), were retained and mapped onto the the higher resolution SEVIRI fixed grid.

This approach provides good results but is not optimal. In fact, over the (radiatively) hot land surfaces, scattering cooling from precipitation causes BTs to decrease. Thus, hot backgrounds easily mark clear sky pixels. However, the same reasoning cannot be applied over ocean surfaces. In fact, since sea surface emissivity at 89 and 157 GHz varies between 0.6 and 0.7, ocean backgrounds are always radiatively cold. Convective events still cause radiative cooling by scattering, however, water vapor and light precipitation can warm the measured BTs with respect to the clear sky signatures. Therefore, hottest pixels might not necessarily correspond to clear sky ones. However, since the warming varies with the wavelength (the 89 GHz being more sensitive to water vapor), the differential signal should in theory be kept as an indicator of clear sky pixels. The SI should be maximum at clear sky (due to the differences in SSE) and minimum during convective precipitation (due to the enhanced scattering at 157 GHz than at 89 GHz). The differential

discrimination was attempted but caused significant errors by detecting light precipitation over clear sky ocean regions, therefore, was not adopted for this study as deeper investigation is needed for its use.

The time window of 4 days used for the computation was proved to be large enough to allow for clear sky conditions to be found for every scene pixel and short enough to remain within background conditions that are representative of the overpass under examination.

In this regard, it is worth noting that a considerable impact was observed from night/day variations (implying deviations as large as 30 K on the background BTs), a fact which suggested to restrict the computation of the background temperatures to overpasses within a few (6 in this study) hours from the time of interest. In order to avoid problems linked to the instrument calibration, separate background calculations were also done for the different satellites.

The described approach resulted in a considerable improvement on the computed clear sky BTs, and this had a significant impact on the derived precipitation estimates as shown in Figs. II.7.15 and II.7.16. The improvements are visible especially over coastal regions (North Africa) and over non-vegetated land (Sicily and Sardinia) where with original scheme, false precipitation was detected in clear sky

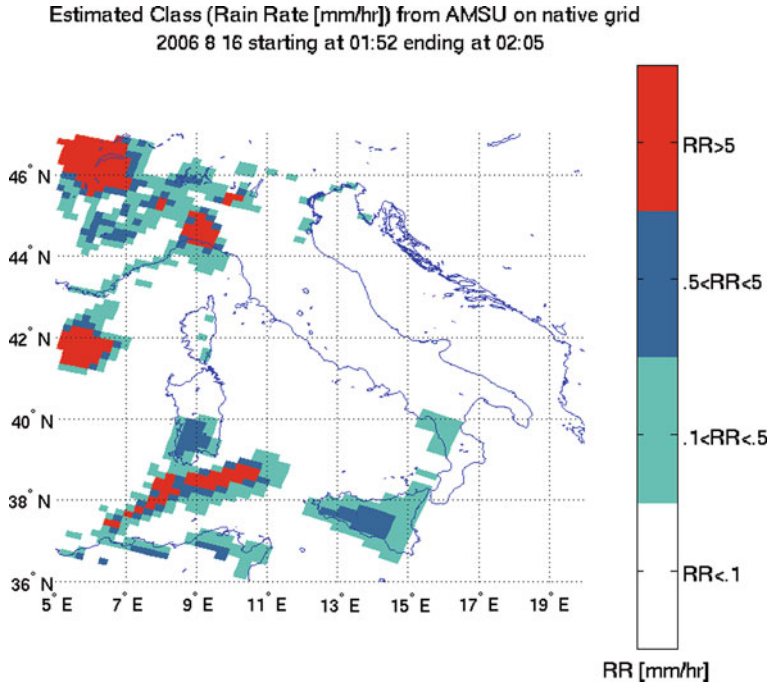

Fig. II.7.15 NOAA 18 16-08-2006 at 01:52 UTC: PC retrieval obtained with original estimation of background BTs. Light precipitation is erroneously detected in clear sky regions (over Sicily, Sardinia, and North Africa), Fig. II.7.21

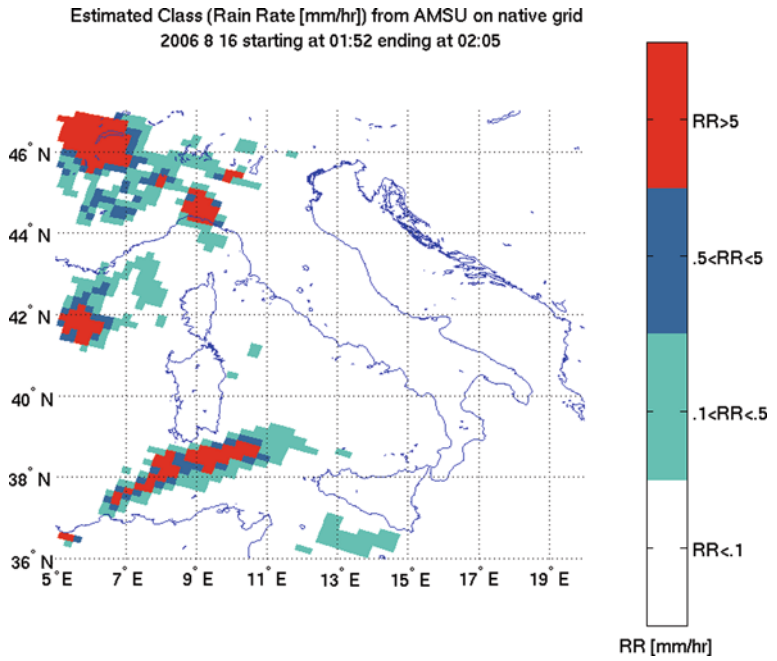

Fig. II.7.16 NOAA-18 August 16, 2006 at 01:52 UTC: PC retrieval obtained with the estimation of background BTs derived from previous time-coincident, same-platform overpasses. No precipitation is detected in the clear sky regions over Sicily, Sardinia, and North Africa

regions (Fig. II.7.21), whereas with the new scheme, the misclassification tends to disappear. SEVIRI data in Fig. II.7.22 show the improvements of the new approach even over ocean (Fig. II.7.17) with respect to the original version of the PC algorithm for a different NOAA 18 overpass (September 14, 2006 at 01:56 UTC) as shown in Fig. II.7.10. For the sake of clarity, Figs. II.7.6, II.7.8, II.7.9, and II.7.10, show examples obtained with the original version of the PC algorithm.

The new implementation also allowed for an improvement in the estimation of precipitation over very heterogeneous surfaces (namely over coastal areas): the fact that the background BT selection was done by considering several overpasses and on a fixed, high-resolution grid (the SEVIRI one is used), the heterogeneity of the background BTs was better retained, thus allowing a mitigation of the estimation errors.

A further possible improvement for this algorithm could consist of a smoothing of the computed background BTs before ingesting them in the retrieval scheme. In fact, being computed over different overpasses (and therefore even from different observation angles) the radiative backgrounds may present some important discontinuities among adjacent pixels (e.g., differences as large as 10% could derive from the different scan angles of the retained clear sky pixel) that could impact on the final rain estimation.

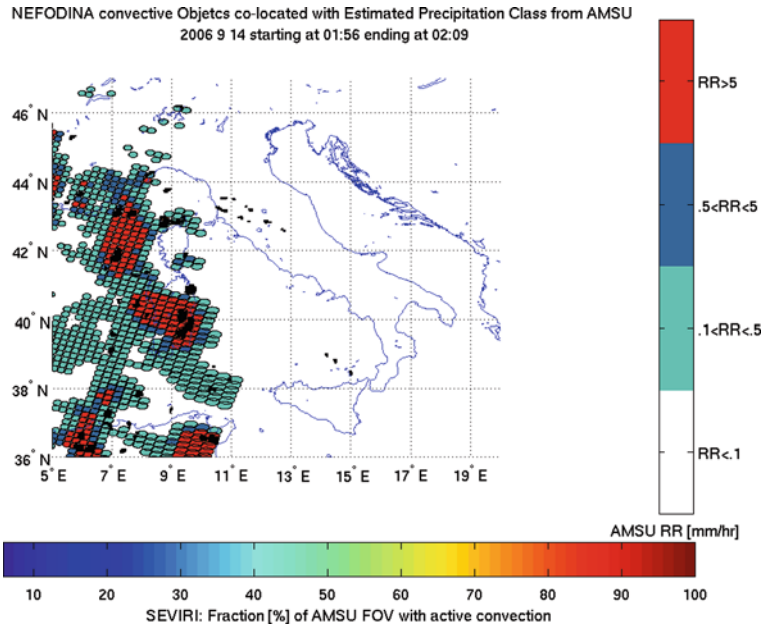

Fig. II.7.17 NOAA-18 September 14, 2006 at 01:56 UTC: PC retrieval obtained with improved estimation of background BTs derived from previous time-coincident, same-platform overpasses. No precipitation is detected in the clear sky regions over Sicily and over ocean. In this figure PC values are mapped onto actual AMSU effective FOVs (EFOVs) calculated according to Bennartz (2000)

3.6 Errors and Uncertainties

The validation procedure described in Sect. 3.4.2 highlighted some issues specific to the PC product. These issues, discussed in the following subsections, were accounted for the implementation of the merging algorithm described in Sect. 5.1.

3.6.1 AMSU Geolocation Uncertainties

AMSU data suffer from considerable geolocation errors, depending on the platform. NOAA scientists have evaluated these errors by analyzing the discontinuity in correspondence of coastline in clear sky conditions. Errors were found in both the along and the cross-track direction. The displacement was quantified as large as 4.2 and 5.5 km (cross-track and along-track respectively) for NOAA-17 and 3.2 km and −16.4 km for NOAA-18. As for NOAA-18, an example of the considerable displacement (two pixels) that was evidenced on the Red Sea with such a technique is clearly visible in Fig. II.7.18.

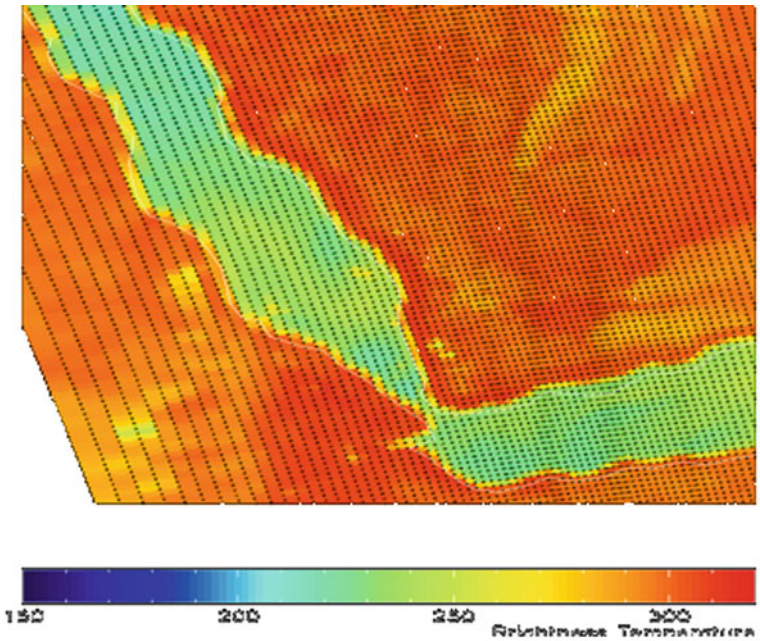

Fig. II.7.18 NOAA-18 AMSU-B image at 89 GHz over the Red Sea (figure exerted from http://www.orbit.nesdis.noaa.gov/smcd/spb/n18calval/calval/mhs.html#mhsgeo)

3.6.2 Scan-Dependent Uncertainties

The fact that AMSU is a cross-track scanning instrument has a major impact on the relative quality of the resulting rainfall estimations, due to several reasons. Different viewing geometries correspond to different sensed areas and different radiative properties. The effect of atmospheric optical thickness, surface emissivity, and hydrometeor particle emissivity, on observed BTs, all depend, to different extent, on the viewing geometry. Even purely geometrical effects related to the change in the equivalent area of the sensed portion of the cloud play an important role in this respect. In addition, off-nadir slanted observing geometries may introduce important geometrical distortions in the rain cell localization at surface level, as schematically sketched in Fig. II.7.19. At the frequencies of interest, the source of the (scattering) signal is not the surface rainfall layers, but the ice layers aloft. At nadir, the surface rainfall can be assumed co-located with the BT scattering signal.[1] However, when observing through slanted views, significant displacements may exist between the location of the scattering source location and the effective

[1] This is true only in the hypothesis that the convective towers extend vertically under the sensor field of view. However, horizontal shears may introduce possible shifts and generate tilted events (see for instance Hong et al., (2000) about a tilted convective event observed from the TRMM precipitation radar)

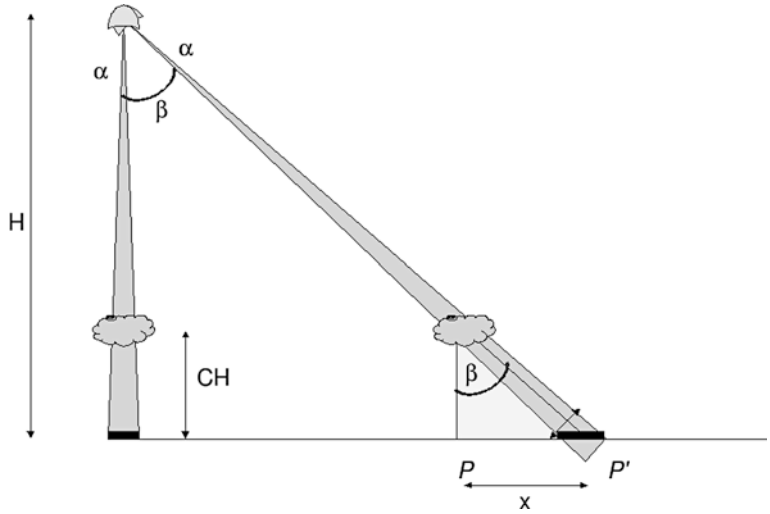

Fig. II.7.19 Schematic representation of the localization error for surface rainfall rate position. At slant angle β, rainfall is located in correspondence of position P, whereas the current location should be P'. The corresponding shift x is referred to as the *parallax error*

location of the convective rain at surface level. This displacement is often referred to as the *parallax error*, and it increases proportionally with the altitude of the cloud and with the observation angle. Theoretically, a graupel cloud situated at 10 km height could be located almost 10 km away from the real surface RR location, if sensed at maximum scan edge.

A straightforward correction could be therefore attempted once the corresponding cloud top height is supposed to be known. However, from using AMSU brightness temperatures, there is no mean to derive this piece of information.[2] Therefore an automatic correction for such a displacement is not deemed possible: estimating the height of the main source of the scattering signal (i.e., the center of gravity of the *generalized weighting function*) seems not reasonable due to the complexity and the uncertainties related to the characterization of the micro and macro-physical properties of the precipitating cloud.

Another scan-dependent source of error is due to the calibration of the instrument itself: NOAA scientists have observed an asymmetric behavior of the sensed radiances across the scan lines which amounts to more than 5 K

- http://www.orbit.nesdis.noaa.gov/smcd/spb/n18calval/calval/mhs.html#mhsgeo
- http://www.orbit.nesdis.noaa.gov/smcd/spb/mirs/validation/characterization.html

[2]Or in any case without introducing significant errors. As an example, the possibility to use SEVIRI-derived cloud top heights was discarded due to the fact that the cloud top height sensed by the IR channels might in general be much higher than the source of scattering signature characterizing the microwave frequencies and also to the time-shift that in any case would exist between the two observations.

The main impact, however, is due to the fact that the dimensions of the sensed area vary by more than 200% from nadir to scan edges. According to Bennartz (2000), the relationship between EFOV and scan angle, both in cross-track and along-track direction, can be modeled through the following interpolating formula:

$$\begin{aligned} \mathrm{EFOV(across-track)} &= 79.08 + 2.84\, m - 14.78\, m^{0.66} \\ \mathrm{EFOV(along-track)} &= 28.72 - 0.9\, m + 0.094\, m^{1.5}, \end{aligned}$$

where m is the scanning position. The cross-track EFOV passes from 15 km at nadir to more than 50 km at scan edge. Within such a variation, the heterogeneity of the sensed scene (and the possibility that the observed precipitation event "fills" the EFOV homogeneously–the so called beam filling problem, see for instance Kummerow (1998)) augments considerably. Everything that falls inside the sensed area is integrated and filtered in the sensor view, but the significance of the resulting information decreases with the heterogeneity of the observed scene. At scan edges, the probability to filter out and even loose narrow isolated sub-pixel convective cells increases considerably.

From all the considerations mentioned above, it should be clear that a different degree of uncertainty should be associated to AMSU measurements, proportionally depending on the scan angle: as a consequence, rainfall estimations at nadir are more reliable than the ones located along scan edges. Instead of attempting risky (and, at this stage, subjective) corrections to the estimates, we propose, as future work, that a scan-dependent confidence index should be associated to AMSU measurements, being maximum at nadir, and decreasing with the scanning angle. The confidence index should be taken into account when evaluating the performances of AMSU-derived rainfall rates.

4 Convection Detection from SEVIRI Data (Nefodina)

4.1 Data Description

SEVIRI is a scanning radiometer which operates on Meteosat Second Generation (MSG). It provides data in visible, near infrared, and infrared channels. Full spatial resolution in 12 spectral channels. *Nominal Coverage* includes Europe, Africa and locations with satellite elevation greater than or equal to 10°. The IR channels are designed with three narrow band detector elements per channel to scan the Earth every 3 km at the sub-satellite point. The high-resolution visible (HRV) channel provides measurements with resolution of 1 km.

The full Earth disc image is obtained after 1,250 scan line steps (south–north direction) of 9 km SSP per line step. The satellite spins at 100 rpm allowing to complete (east–west direction) a full image in about 12.5 min. The Earth observation repeat cycle is of 15 min. These real-time data are processed to Level 1.5, i.e., are

corrected for radiometric and geometric non-linearity, before onward distribution to the user. All SEVIRI data are available through EUMETCast.

4.2 Algorithm Description

Nefodina (Puca et al., 2005, 2009) is an automated tool, developed at the Italian Meteorological Service, which uses SEVIRI data to detect convective cloud systems to monitor their life cycle and to forecast their development. The derived product, using a varying threshold method in infrared window 10.8 μm and absorption channels 6.2 and 7.3 μm, allows for the identification of the convective object (CO) with a top BT lower than a temperature threshold of 236 K.

The detection method relies on the following basic assumptions:

- the temporal and spatial satellite data sampling is compatible with the corresponding scales of the phenomena;
- the evolution of the cloud top temperature joined with the water vapor amount in the medium and high troposphere represent a good tracer of convective cells;
- it is possible to represent the life cycle of the convective cell with a linear combination of cloud top temperature and the water vapor amount in the high troposphere.

The nefodina algorithm flow chart is reported in Fig. II.7.20.

4.3 Product Description

The nefodina product consists of a portable network graphic (PNG) image of the last available SEVIRI infrared (10.8 μm) image where the detected cells, their development, and their tracking are color coded to give a quick overview to the forecaster (Figs. II.7.21 and II.7.22). This output image is associated to an ASCII file where the minimum, medium, and modal BT of the 10.8, 6.2, and 7.3 μm channel is reported with shape, slope area, and other information relative to the detected COs.

4.4 Nefodina Validation

4.4.1 Qualitative Comparison of Nefodina CO with Radar Data

As previously done for radar and rain gauge data, the nefodina-detected COs superimposed to radar-derived RR are showed in Fig. II.7.23. The grey diamonds represent the centers of the SEVIRI FOVs labeled as convective by nefodina, while the black circle represent the positions of the COs after a rigid shift which maximize

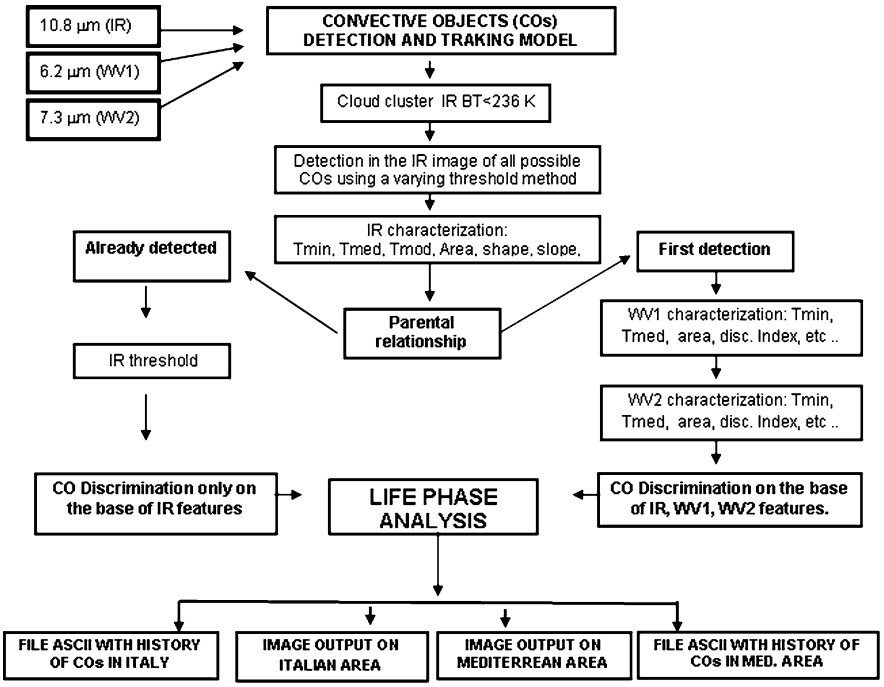

Fig. II.7.20 Nefodina flow diagram

the radar-detected precipitation within each CO. The misalignment of the original CO positions with respect to the radar map looks consistent for the different COs. Misalignments are mostly due parallax and geolocation errors. While Sect. 4.5.1 introduces a methodology to properly correct for parallax errors, the actual approach selected to mitigate the misalignment between AMSU, SEVIRI, and radar data was based on a rigid shift which maximizes the precipitation within each object and it is described in Sect. 5.1.

4.4.2 Quantitative Validation

Validation on the detection efficiency of nefodina was performed, following the idea that a CO during its life has an electric activity. Often this happens during the mature stage. The validation was based indeed on the observation of lightning measured by the lightening network (LN) of the International Association of Forensic and Security Meteorology (IAFMS) during the life of the CO and it was conducted on a set of 12,000 data uniformly selected along 1 year of MSG data. Probability of detection (POD) and false alarm rate (FAR) were obtained, respectively, equal 0.84 and 0.17. Sixty percent of the CO were detected and classified as convective by nefodina 30–45 min (2–3 MSG slot) before any electric activity was measure by LN.

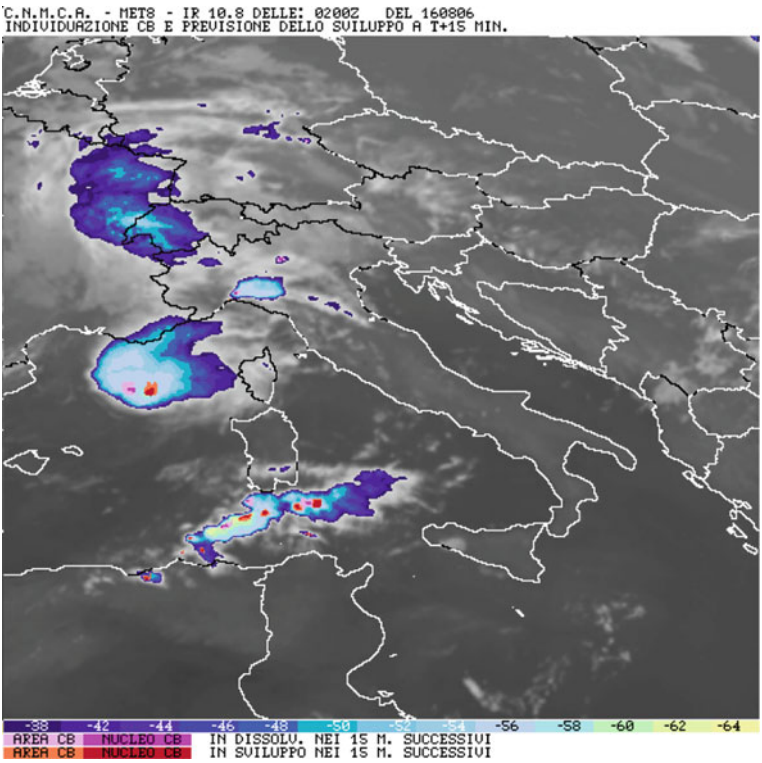

Fig. II.7.21 Example of nefodina product at 02:00 UTC on August 16, 2006. The colorbar shows the cloud top temperature. The red pixels show increasing CB, while the pink pixels show the decreasing CB (For color figure see online version)

4.5 Errors and Uncertainties

In this section the only source of uncertainty described refers to the parallax errors because a full validation of nefodina is beyond the scope of work presented in this chapter.

4.5.1 Parallax Error

The concept of parallax error (i.e., the mislocation, on the Earth surface, of rain cells due to slanted satellite observations) was already introduced in Sect. 3.6.2 for AMSU. However, even SEVIRI rain products may be affected by such a problem, as already noticed by Davenport et al. (2007). In fact, the SEVIRI camera is observing the Earth with a spherical geometry centered in the Gulf of Guinea (approximately at 0° latitude and longitude). The sensor viewing angle increases with the radial distance from the nadir point. The viewing angle increases as function of the geographical location, introducing potential distortions and pixel enlargement (the

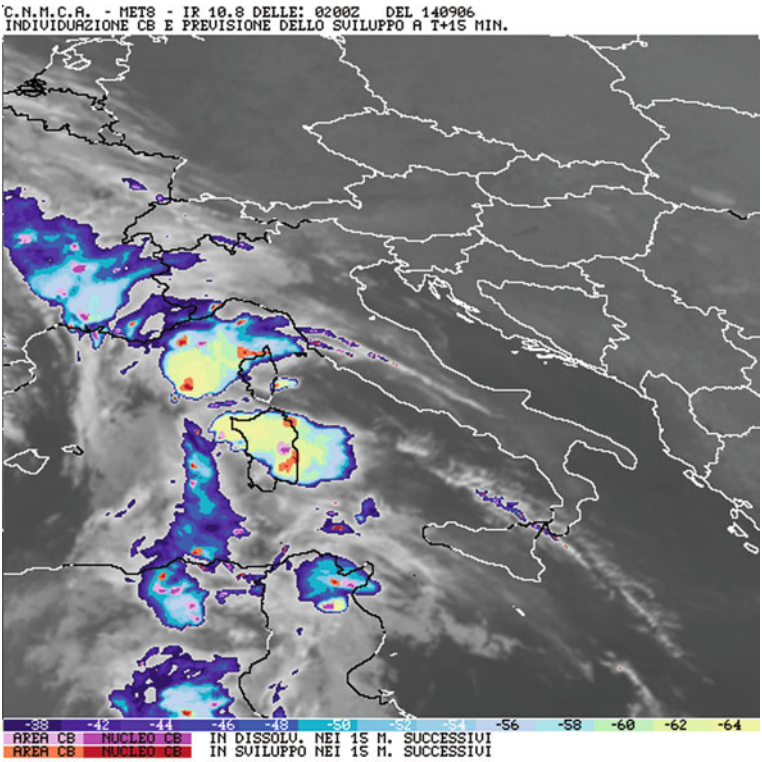

Fig. II.7.22 Nefodina September 14, 2006 at 02:00 UTC (For color figure see online version)

effective pixel size increases radially from the nadir point). Complete details about SEVIRI are provided by Wolf et al. (1999).

For the purposes of this study, the SEVIRI slanted observing geometry may have an impact in that the location of the observed signal source (cold pixels associated to convective events and possibly to the largest cloud top heights) may be shifted by several kilometers with respect to the effective location of the precipitation at the surface. Therefore, the convective pixels are relocated so that are in correspondence with the effective location of the surface rain. From Wolf (1999), we computed such a displacement as function of the latitude and longitude of the observation (radial distance from nadir sub-satellite pixel). As an example, for a 10 km height cloud top in the Mediterranean, we obtain a displacement as large as 7 km in the radial direction. It must be highlighted, though, that this calculation relies on the assumption that the observed event is perfectly vertical and that horizontal shears are minimal. Correcting SEVIRI precipitation products for the parallax did not account for the whole misplacement of the convective cell location with respect to the region of high radar precipitation. However, the correction did lead to improved geolocation with respect to radar data (Fig. II.7.24)

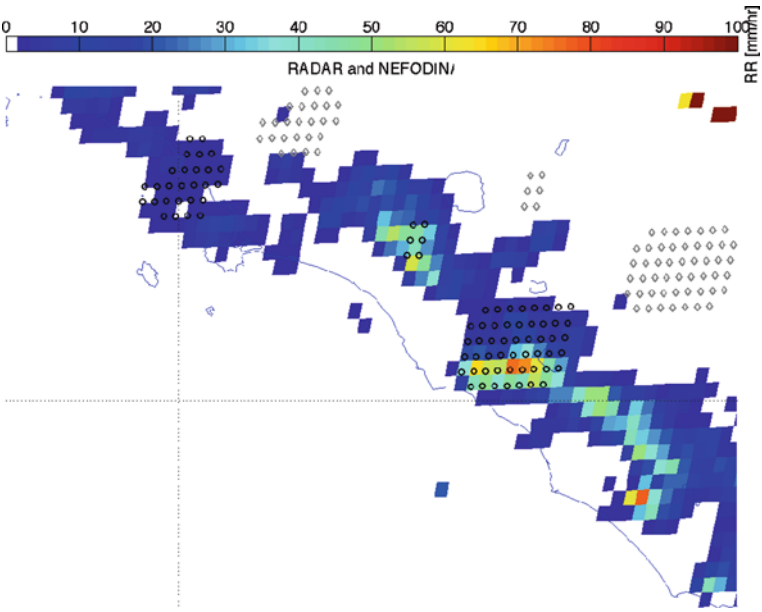

Fig. II.7.23 Comparison of nefodina-detected CO and radar RR for April 24, 2008 at 15.30 UTC. *Grey diamonds* represent the original COs detected by nefodina, the *color-map* represent the radar rain rate and the *black circles* indicate the optimal position of the COs after re-colocating them according to the procedure described in Sect. 5.3. (For color figure see online version)

5 Convective Precipitation Retrieval from Combined AMSU and SEVIRI Data

5.1 Algorithm Description

In the proposed approach AMSU PC data were co-located with nefodina-detected COs. The basic ideas were:

- to identify, for each CO detected in the closest SEVIRI time slot, the AMSU FOVs affected by convection and use the corresponding AMSU precipitation rates to calculate the mean precipitation associate to the CO and
- to apply a rigid shift to AMSU-derived precipitation of ± 3 FOVs in every directions and select the one which maximizes the amount of precipitation for each individual CO;

The estimated mean co-precipitation (MCP), Φ, was then computed as follows:

$$\Phi = \frac{\sum_{i=1}^{N} \mathrm{RR}_i * A_i}{\sum_{j=1}^{M} a_j},$$

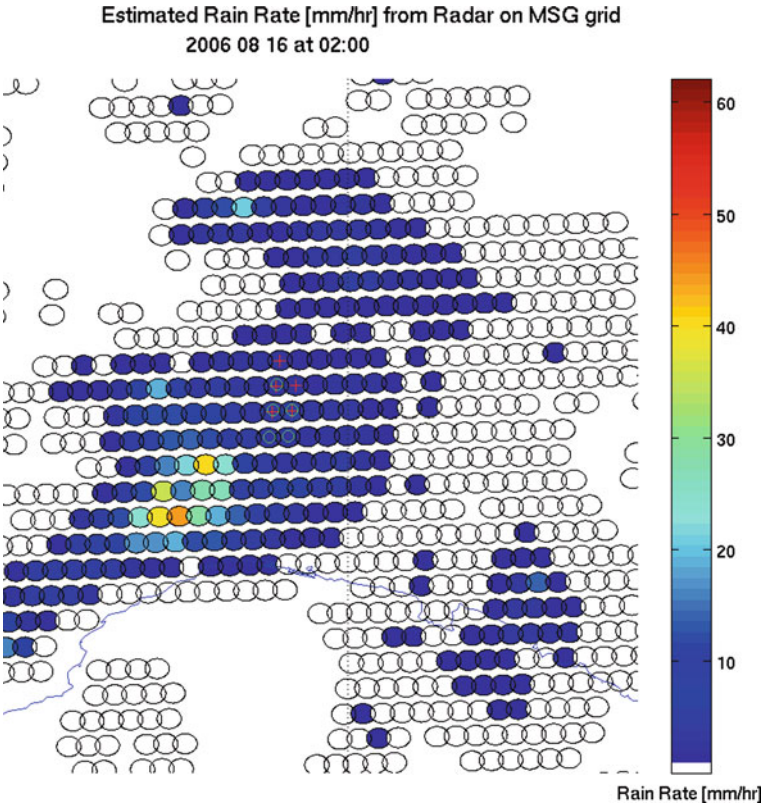

Fig. II.7.24 Parallax correction: the *colored circles* represent radar data interpolated and reprojected on the fixed SEVIRI grid, the *red crosses* are SEVIRI FOV characterized by convection before parallax correction, and the *green circles* are the same SEVIRI FOVs after parallax correction (For color figure see online version)

where RR_i is the AMSU-derived RR for the *j*th; A_i the area of the *i*th AMSU FOV; *i* goes from 1 to *N* with *N* being the number of AMSU FOVs affected by the convective object; a_j the area of the *j*th SEVIRI FOV; and *j* goes from 1 to *M*, with *M* being the number of SEVIRI FOVs within the convective object.

In summary, Φ represents the precipitation that would characterize the CO if all the precipitation observed in the corresponding AMSU FOVs was confined to the convective region only. This assumption represents an approximation, and it is intended to provide an upper bound to the precipitation associated to the CO. In its current implementation the algorithm calculates the AMSU IFOVs according to Bennartz (2000) and it accounts for the parallax error on the SEVIRI FOVs (Sect. 4.5.1), it also corrects for AMSU geolocation errors (Sect. 3.6.1) using a rigid shift scheme as previously described. In addition to the mean precipitation the algorithm generates also RR values for each SEVIRI pixel, identified as convective by nefodina, according to the following expression:

$$\phi_{i,j} = \frac{\mathrm{RR}_{i,j} * A_{i,j}}{\sum_{k=1}^{L} a_k},$$

where $\mathrm{RR}_{i,j}$ is the RR for the AMSU FOV in the ith row and jth column of the satellite swath; $A_{i,j}$ the area of the AMSU FOV in the ith row and jth column of the satellite swath; and a_k is the area of the kth SEVIRI convective FOV within the AMSU $A_{i,j}$ FOV, with k going from 1 to the total number of convective pixels, L, within the AMSU FOV.

The single pixel estimate ϕ is in general prone to geolocation and co-location errors. If fact if, due to a small geolocation error, a single SEVIRI pixel belonging to a broad CO which densely populate an AMSU FOV was erroneously located within a different AMSU FOV, its RR would have been much higher with respect to the average of the CO. Since even small errors in the AMSU geolocation can determine whether a SEVIRI FOVs belongs to one (less densely populated) or another (more densely populated) AMSU FOVs, this estimate might vary significantly within the same CO, and it is to be used in a careful way.

5.2 Product Description

The co-location products were differentiated into: MCP (Φ) values which define the mean RR for a nefodina CO; estimates ($\phi_{i,j}$) of RR for individual SEVIRI FOVs belonging to a nefodina CO. Since the first product, MCP, was more robust to geolocation and parallax errors, while the second product was generally prone to these errors and provided highly variable estimates even within the same CO, hereafter only results on MCP are discussed.

5.3 Qualitative Validation of Nefodina/AMSU Combined Products

Proper co-location of PC and nefodina had a central role in the development of the the MCP product. It represented the basis for merging geostationary and polar orbiting products which allowed for the identification of highly precipitating regions at SEVIRI spatial resolution (3–8 times finer than the native AMSU resolution), and under well-defined approximations it provided an upper bound estimates of the RR, within the convective regions. To describe the validation procedure established to evaluate MCP, the following example in Fig. II.7.25 is provided. The example shows the co-location of CO, as detected by nefodina, on the AMSU PC product. The selected data for this comparison were related to the NOAA-15 overpass on April 24, 2008 at 15:30 UTC. The figure shows the PC-weighted average for the AMSU along with different convective systems which were active in the scene (for sake of clarity only three systems over central Italy are shown to demonstrate the concept). The PC-weighted average RR for the AMSU overpass is represented by the color of the large FOVs, while the smaller SEVIRI FOVs indicate the location

Fig. II.7.25 PC-weighted average on AMSU native grid at 15:30 UTC and on SEVIRI FOVs

of the nefodina-detected COs. The COs co-locate nicely with the highly probable ($P \simeq 1$) class 4 (RR $>$ 5 mm/h) FOVs characterized by a weighted average RR of about 7 mm/h. Under the assumption that most of the precipitation occurred in the highly convective region, nefodina was shown to provide relevant information about the distribution of precipitation within the AMSU FOVs. Figure II.7.26 shows the same convective objects showed in Fig. II.7.25 but co-located with radar precipitation: the objects identified by nefodina properly matched the regions of highest radar precipitation, providing encouraging evidence that the hypothesis made on the precipitation distribution (highest where the convection is active) is solid. Quantitative comparisons for all the COs detected for this overpass and for the NOAA-16 overpass at 16:03 UTC are presented in Tables II.7.6 and II.7.7. The first raw of the tables

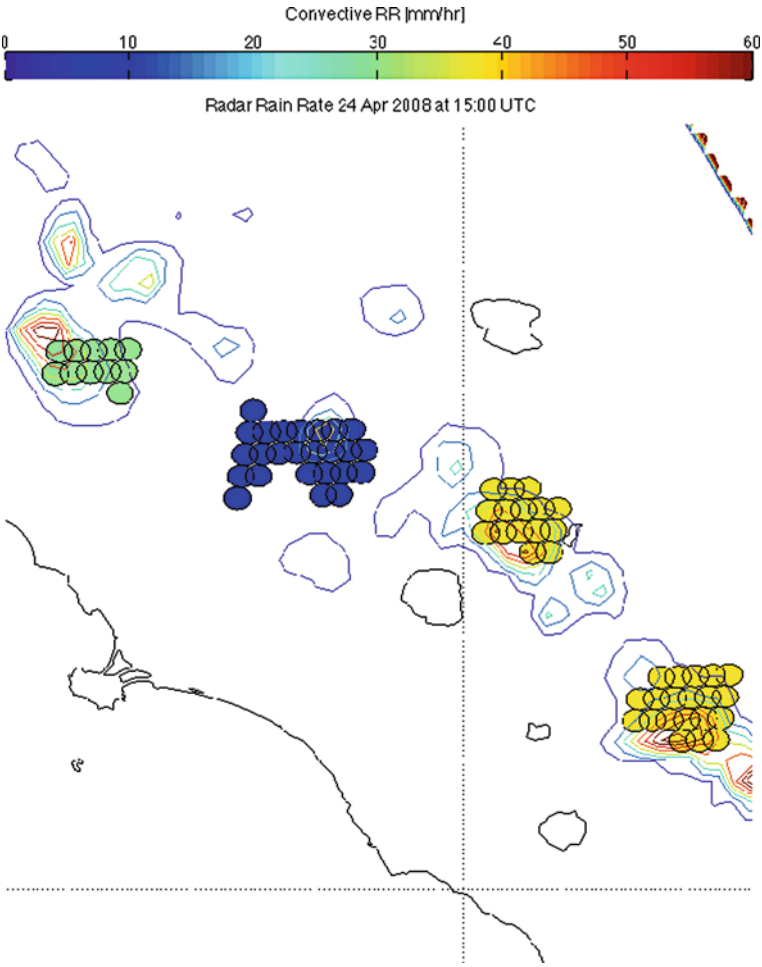

Fig. II.7.26 Radar RR compared to convective RR on SEVIRI grid 15:30 UTC (For color figure see online version)

Table II.7.6 Comparison of MCP and CO radar-derived convective RR for NOAA-15 overpass at 15:30 UTC

RR in mm/h	CO_1	CO_2	CO_3	CO_4	CO_5
RADAR 15:30 UTC	39	42	23	3	22
MCP 15:20 UTC	38	27	17	13	11

shows the radar RR averaged on the nefodina-detected COs, while the second raw shows the values of MCP for the same COs. The values of RR for MCP and radar exhibit a correlation $\rho = 0.66$ which, given the very limited size of the sample, is a purely indicative, but also encouraging, number.

Table II.7.7 Comparison of MCP and CO radar-derived convective RR for NOAA-16 overpass at 16:00 UTC

RR in mm/h	CO_1	CO_2	CO_3	CO_4
RADAR 16:00 UTC	27	25	21	16
MCP 15:55 UTC	36	41	46	18

6 Conclusions

This chapter described how in situ observations were used to show an important relation between the precipitation estimates derived by the PC algorithm at AMSU resolution and COs detected by nefodina at SEVIRI resolution. This relation opens the way to a potentially fruitful merging of geostationary and polar orbiting products which could improve the accuracy and the usefulness of the AMSU-derived precipitation products to hydrological and QPF activities. The case studies presented showed the good accordance between heavy rainfall (Class 4: RR > 5 mm/h) deduced by PC and convection detected by nefodina. They also showed encouraging results for the basic assumption on which the proposed merging strategy is based. For this study, the PC algorithm (Bennartz et al., 2002) developed within NWC-SAF was selected as the most suitable AMSU-based precipitation retrieval algorithm for the development of a convective precipitation product (MCP). The selection was based on pre-operational software availability, knowledge of performance characteristics over a large part of H-saf area (Northern Europe), use of AMSU channels more sensitive to heavy rainfall. The PC algorithm outputs were extended to the whole H-saf area allowing for testing and validation in the Mediterranean regions (Italy). Improvements in the performances of the algorithm were obtained through a refinement of the estimation of the radiative background field. AMSU data from NOAA 15, 16, 17, and 18 (and METOP after launch) were routinly processed, but lack of daily availability of radar data limited the validation activity. The precipitation observations from radar and rain gauges were collected only for a few Italian convective cases and upscaling and downscaling algorithms were developed to compare precipitation ground-based observations with PC algorithm retrievals and SEVIRI products. The validation procedure described in this chapter allowed:

- For improvements of the individual products. For the PC algorithm example, more than 43,000 RR retrievals taken in 7 different days from NOAA 16 and 18 data were compared to radar data convolved on the AMSU grid. The results obtained were on average 18%, with a peak of 58% for class 4, worse than those obtained by Bennartz (2005). This was explained by the fact that the background brightness temperature tuning that was originally developed for northern Europe frequently produces spurious rainfall signatures, especially in arid regions during daytime. On this basis a new approach for the estimation of the background BT in the PC algorithm was implemented to mitigate, and in most cases eliminate, the problem of spurious rainfall signatures.

- For tuning of a merging algorithm capable of taking into account geolocation and parallax errors which represented the most serious issues in combining SEVIRI-derived products with AMSU RRs.
- For verification that most of the precipitation does indeed occur in the detected convective portion of the cloud, hypothesis which represents the foundation of the MCP algorithm.
- For an initial evaluation of the MCP product with radar data.

Future work includes a more extensive validation with radar data and also a more accurate use of rain gauge data, only partially used in the described effort.

Appendix A Implementation Details on Data Projections

This appendix is included simply to clarify the methodology used for the inter-comparisons of the various products. In order to compare values derived at different resolutions, several procedures were implemented to remap products:

- from AMSU to SEVIRI grid;
- from radar to AMSU grid;
- from radar to SEVIRI grid;
- from gauges to SEVIRI grid.

In particular the SEVIRI grid was chosen as reference, since it provides a fixed grid at a convenient resolution.

A.1 The AMSU-to-SEVIRI Remapping Process

This process was designed to allow the comparison of current PC products with SEVIRI-derived rainfall products and with radar and rain gauge data on a fixed grid. However, it was also used to compute the background BTs for the PC algorithm (as described in Sect. 3.2). An example of the AMSU-SEVIRI remapping is shown in Fig. II.7.27.

The basic concepts of the implementation are hereafter described.

Given the location of a SEVIRI pixel, the bounds of the corresponding AMSU pixel are found. Routine begins by determining if it lies within the bounds of the AMSU grid, and if so, then searches for the closest AMSU observation. Having found the nearest AMSU, the routine then looks to the left and right (on the same AMSU row) to find which of these two is closer to the SEVIRI, and then the closest and its neighbor to the left or right are chosen as two of the four AMSUs surrounding the SEVIRI pixel. A check is performed to make sure the selected pixel is not on the lateral edge of the AMSU array, so that it makes sense to look left or right. If the pixel is on the edge, then the algorithm simply uses the two points on the row

nearest the edge. A weight is assigned to these two based on their distance from the SEVIRI pixel. The distances are determined by computing the angle between the SEVIRI position vector and either of the two chosen AMSU position vectors. This part of the algorithm, using vector algebra, is quite efficient.

Once the distances are calculated there are two different strategies to derive the BT on the SEVIRI grid. The first one makes simply use of the nearest neighbors, while the second interpolates (weighted average) among the four closest AMSU FOVs according to the following procedure: returning to the previously found nearest AMSU, the routine looks at the two AMSU points above and below, in adjacent rows, to find which of these two is closer to the SEVIRI point. The chosen row (above or below the row in which the closest AMSU lies) is then used, and the four points used for interpolation are the two found in the first row, and the two in the next-best row.

An interpolated estimated is made in each row (W_i) between the two chosen points on that row, using weights

$$\begin{aligned} W_{i1} &= 1 - s_1/(s_1 + s_2) \\ W_{i2} &= 1 - W_{i1} \end{aligned} \tag{3}$$

where s_1 and s_2 are the distances (in latitude degrees) between SEVIRI and the first and second closest AMSU points on that row. In the above case, if $s_1 = 0$ (i.e., an AMSU coincides with SEVIRI), then that AMSU has weight 1 and its neighbor has weight 0. A similar weighting scheme is then used vertically (W_j) along the AMSU column containing the closest AMSU to arrive at the weights which are used to interpolate as many of the AMSU channels as are needed to the SEVIRI location.

$$\begin{aligned} W_{j1} &= 1 - d_1/(d_1 + d_2) \\ W_{j2} &= 1 - W_{j1} \end{aligned} \tag{4}$$

where d_1 and d_2 are distances of two AMSUs along the minimal column from SEVIRI.

The horizontal weights and the vertical weights are then used to average the AMSU BTs (or any other quantity defined on the AMSU grid) on the two rows (e_1 and e_2):

$$\begin{aligned} e_1 &= W_{i1} * \mathrm{BT}(1,1) + W_{i2} * \mathrm{BT}(2,1) \\ e_2 &= W_{i1} * \mathrm{BT}(1,2) + W_{i2} * \mathrm{BT}(2,2) \\ e &= W_{j1} * e_1 + W_{j2} * e_2 \end{aligned} \tag{5}$$

to get the final estimate e of the BT.

The co-location scheme based on the nearest neighbors was used for the derivation of background BTs (as described in Section 3.5), while the second one (based on weighted averages) was used for validation purposes.

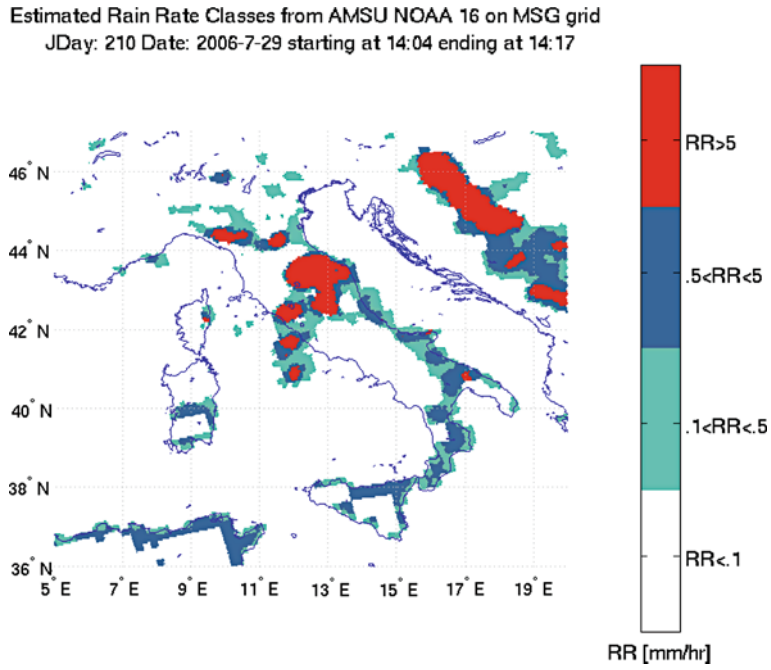

Fig. II.7.27 Example of PC remapping onto SEVIRI grid

A.2 The RADAR-to-AMSU Remapping Process

Radar data were convolved to the AMSU footprint using the methods described in Bennartz (1999), Bennartz and Michelson (2003), and Bennartz et al. (2002). The methods used in this study were initially derived for Baltex radar Data Center (BRDC) composites but were adjusted to account for the radar composites provided by CNMCA. The convolution takes into account the actual spatial sensitivity of AMSU-A and AMSU-B as outlined in Bennartz (2000). A fixed Z–R relation of $Z = 200R^{1.6}$ was used in this study. Due to missing information about the actual position of the radar in the composite imagery, a parallax correction could not be performed. Also, the radar data used in this study were not gauge adjusted.

A.3 The RADAR-to-SEVIRI Remapping Process

The observations available for surface rain intensity (SRI) were on a different scale (spatial resolution and projection) compared to satellite grids and since the variability of precipitation fields strongly depends on the scale at which the fields were considered a meaningful comparison was not trivial. The upscaling technique (fine to course resolution) used to remap radar data onto MSG grid, here described, is very

simple but numerically effective. National mosaic of SRI generated by radars and MSG product were composed of two static grids, each radar cell was linked to the SEVIRI pixel which contains the center of radar pixel. Therefore, radar data were remapped onto geostationary grid through the mean value of SRI calculated on radar cells linked to each satellite grid (Fig. II.7.28). An example of the RADAR-SEVIRI remapping is shown in Figs. II.7.29 and II.7.30.

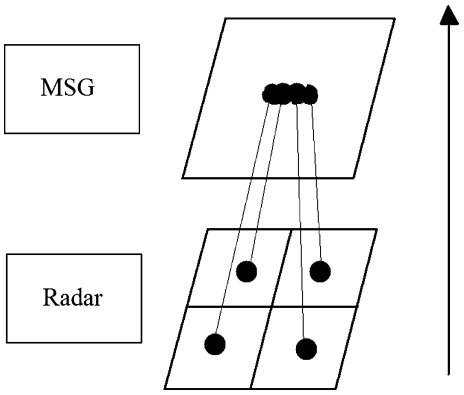

Fig. II.7.28 Radar-to-SEVIRI remapping scheme

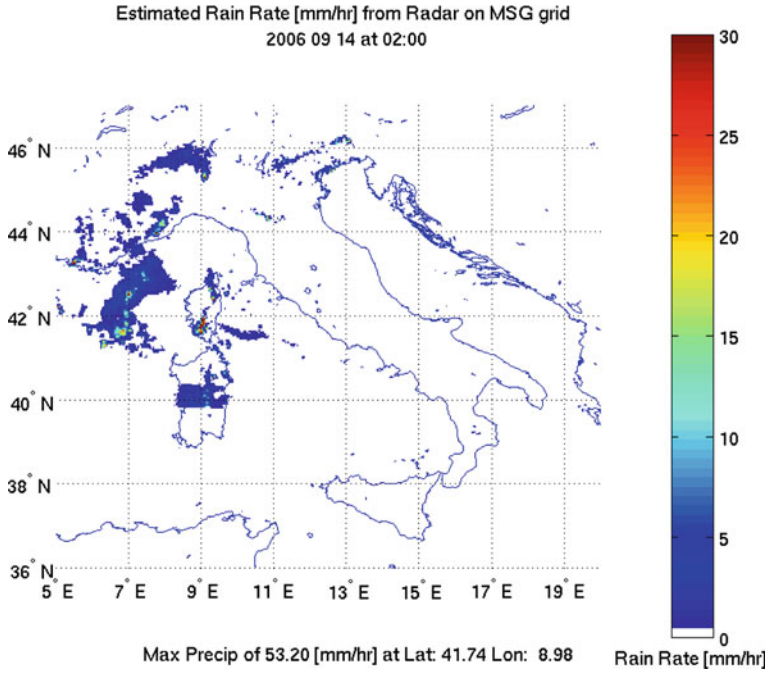

Fig. II.7.29 Example of radar-derived RR on SEVIRI grid

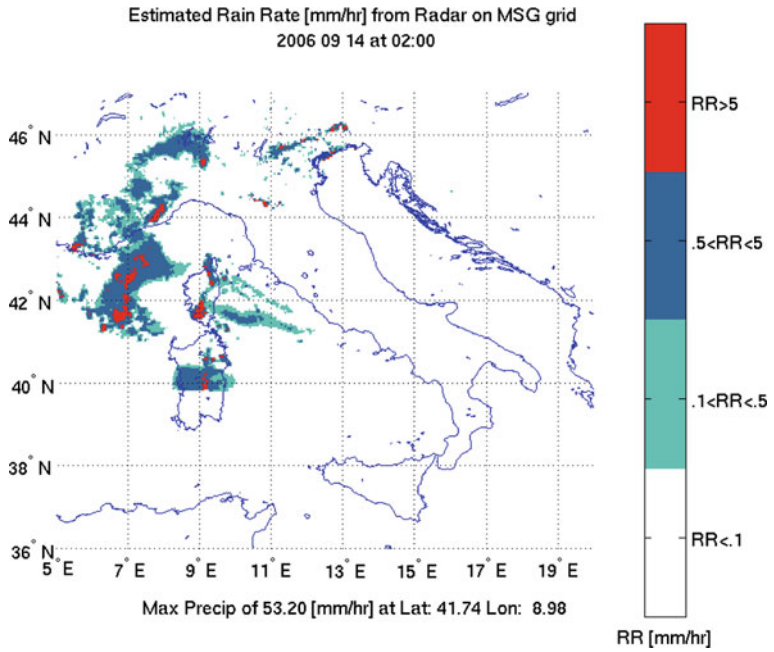

Fig. II.7.30 Example of radar-derived precipitation classes on SEVIRI grid

References

Bauer P (2001) Over-ocean rainfall retrieval from multisensor data of the tropical rainfall measuring mission. Part I: design and evaluation of inversion databases. J Atmos Ocean Technol 18(8):1315–1330

Bennartz R (1999) On the use of ssm/i measurements in coastal regions. J Atmos Ocean Technol 16:417–431

Bennartz R (2000) Optimal convolution of amsu-b to amsu-a. J Atmos Ocean Technol 17:1215–1225

Bennartz R (2005) Integration of Nowcasting SAF scattering indes into AAPP. EUMETSAT SAFNWC, Visiting Scientists Report, pp 1–4

Bennartz R, Michelson DB (2003) Correlation of precipitation estimates from spaceborne passive microwave sensors and weather radar imagery for baltex pidcap. Int J Remote Sens 24:723–739

Bennartz R, Thoss A, Dybbroe A, Michelson DB (2002) Precipitation analysis using the advanced microwave sounder unit in support of nowcasting applications. Meteorol Appl 9(2):177–189

Davenport JC, Vicente GA, Scofield RA (2007) The role of orographic and parallax corrections on real time high resolution rainfall rate distribution. Int J Remote Sens 23(2):221–230

Di Michele S, Mugnai A, Marzano FS, Poiares Baptista Tassa JPV (2003) A cloud model-based Bayesian technique for precipitation profile retrieval from the tropical rainfall measuring mission microwave imager. Radio Sci 38:8074

Grody NC, Zhao L, Meng H, Kongoli C, Pellegrino P, Qiu S, Ferraro RR, Weng F, Dean C (2004) Noaa operational hydrological products derived from the advanced microwave sounding unit (AMSU). IEEE Trans Geosci Remote Sens 43(5):1036–1049

Hong Y, Hafermann J, Olson WS, Kummerow C (2000). Microwave brightness temperatures from tilted convective systems. J Appl Meteorol 39:983–998

Kummerow C (1998) Beam-filling errors in passive microwave rainfall retrievals. J Appl Meteorol 37:356–370

Kummerow C, Giglio L (1994) A passive microwave technique for estimating rainfall and vertical structure information from space, part I: algorithm description. J Appl Meteorol 33(3):18

Panegrossi G, Dietrich S, Marzano FS, Mugnai A, Smith EA, Xiang X, Tripoli GJ, Wang PK, Poiares Baptista JPV (1998) Use of cloud model microphysics for passive microwave-based precipitation retrieval: significance of consistancy between model and measurement manifolds. J Atmos Sci 54:1644, 1673

Puca S, Biron D, De Leonibus L, Rosci P, Zauli F (2005) Improvements on numerical "objects" detection and nowcasting of convective cell with the use of seviri data (ir and wv channels) and numerical techniques. In: The international symposium on nowcasting and very short range forecasting (WSN05)

Puca S, Zauli F, De Leonibus L, Rosci P, Antonelli P (2009) Automatic detection and monitoring of convective cloud systems based on geostationary infrared observations. Meteorol Appl (Submitted)

Wolf R (1999) Lrit/hrit global specification coordination group for meteorological satellites. Technical Report 2.6. EUMETSAT, August 1999

Chapter II.8
Observations of the Lower Atmosphere Over West Africa Using Ground-Based Remote Sensing Instruments

Bernhard Pospichal and Susanne Crewell

1 Introduction

Weather and climate over tropical West Africa are determined by the annual cycle of the West African monsoon, which is an annual reversal of the lower tropospheric flow pattern between the moist southwesterly monsoon flow and the dry northeasterly Harmattan flow (Hastenrath 1985). At the beginning of the monsoon season in March/April, the inter-tropical convergence zone (ITCZ) moves inland, reaching its northernmost point in July and August. The ITCZ marks the upward branch of the Hadley cell and the maximum of tropospheric water vapor convergence. It is situated at the equator (Gulf of Guinea) in January and moves north to about 11°N in August. The ITCZ is not to be confused with the inter-tropical discontinuity (ITD) which marks the convergence zone between the low level flows. The ITD is always situated north of the ITCZ (at about 7°N in December/January and 20°N in July/August). The ECMWF analysis of April 10, 2006 (Fig. II.8.1) presents the sharp meridional moisture contrasts along the ITD which was at about 10°N at that time. At the same time, the integrated water vapor (IWV) maximum at about 5°N marks the ITCZ. It was most pronounced over the Atlantic Ocean. Rainfall also shows an annual cycle with a very pronounced rainy season becoming shorter and less regular when moving north.

The mechanisms that influence the observed inter-annual variability of the West African Monsoon are still not well understood. The African Monsoon Multidisciplinary Analysis (AMMA) project has been launched to gain a deeper insight into this question by combining a wide variety of ground-based, maritime, airborne, and satellite measurements (Redelsperger et al., 2006). Atmospheric humidity plays a key role in those processes that determine the strength of the monsoon. A very significant part of the atmospheric water – whether liquid or as water

B. Pospichal (✉)
University of Cologne, Cologne, Germany
e-mail: pospichal@meteo.uni-koeln.de

D. Cimini et al. (eds.), *Integrated Ground-Based Observing Systems*,
DOI 10.1007/978-3-642-12968-1_15,

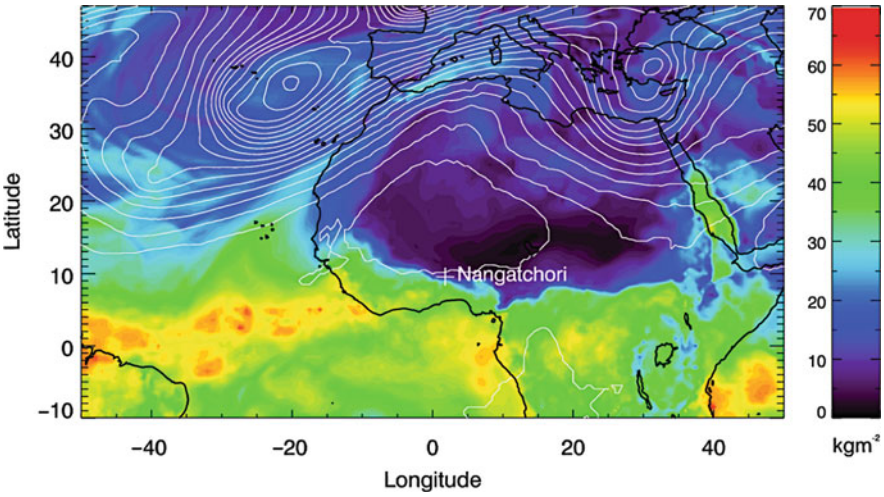

Fig. II.8.1 Synoptic situation on April 10, 2006, 00 UTC from ECMWF analysis. Integrated water vapor (*shaded*) and 500 hPa geopotential height (*contour lines* with 20 gpm distance) are shown

vapor – is located in the atmospheric boundary layer (ABL). For this reason, the observation of the lowest part of the atmosphere is essential to get a comprehensive view of the monsoon.

Observations are rather sparse in West Africa. In the past some campaigns, e.g., HAPEX-Sahel in 1992 (Dolman et al., 1997) and Jet 2000 (Thorncroft et al., 2003) have provided more detailed observations by aircraft, enhanced radiosoundings, pilot balloons, and in situ surface stations. Since all these data are confined to limited time intervals, Parker et al. (2005) note the complete lack of measurements with high temporal resolution in that region. This deficit can also not be closed through satellite observations as those measurements do not resolve the ABL adequately. Within AMMA a wealth of observations was gathered during special observation periods of a few months and longer term observations for a period of 1 year or more were installed. One example is the radiosounding network which has been extended as part of AMMA, but even then, most of the stations performed soundings only 2–4 times a day at the main synoptic hours with a spacing of about 500 km between the stations.

2 Instrumentation

In order to fill the gap of detailed observations in West Africa AMMA initiated – amongst others – the setup of the Djougou/Nangatchori site where a variety of remote sensing and in situ instruments were installed (Pospichal and Crewell, 2007). Nangatchori is situated in northwestern Benin (9.6°N, 1.8°E, 435 m MSL,

Fig. II.8.1). The rainy season typically starts there in late April and lasts until mid-October. The month with the highest amount of rain is August.

Continuous thermodynamic monitoring of the lower troposphere was performed in 2006 by a novel ground-based microwave radiometer the Humidity And Temperature PROfiler HATPRO (Rose et al. 2005) with high temporal resolution. Compared to other microwave radiometers HATPRO is able to observe temperature profiles with high vertical resolution in the atmospheric boundary layer through scanning (Löhnert and Crewell, 2003) in addition to the standard products, e.g., IWV, LWP (cloud liquid water path), and full troposphere temperature and humidity profiles. To our knowledge, this has been the first time that such a microwave radiometer was used in West Africa for monitoring the lower troposphere. Additional instruments at Nangatchori include a lidar ceilometer, vertical pointing Doppler rain radar, measurements of temperature, humidity, and wind on a tower at five levels up to 6 m height, a rain gauge network, detailed in situ and remote sensing aerosol observations (Pelon et al., 2008), wind profiler, and ozone lidar.

The instrument setup was very well suited to describe the lower atmosphere in much detail, both temporally and vertically. The operations were conducted over a full year's cycle (January 12, 2006–January 22, 2007), with a data availability of 82% (HATPRO) to 92% (ceilometer) during this period. The downtime of HATPRO is due to power breaks, a mirror failure, and water contamination of the radome. A brief description of the instruments and the measurement parameters is given in Table II.8.1. HATPRO and ceilometer were tilted to the north in order to avoid

Table II.8.1 Instruments in Nangatchori in 2006 used for this study

Instruments	Frequencies	Measured parameters	Resolution/accuracies
Microwave radiometer RPG-HATPRO	Seven channels at H_20 absorption line (22.24–31.4 GHz) Seven channels at O_2 absorption complex (51.26–58.0 GHz)	• Fourteen channels microwave brightness temperatures (zenith obs., every 15 min elevation scanning) Derived parameters: • IWV (total column atmospheric water vapor content) • LWP (atmospheric liquid water path) • Temperature (T)and humidity (q) profiles	Temporal resolution: 2 s for zenith obs.,15 min for elevation scans Accuracies: • IWV: < 1 kg m^{-2} • LWP: 20–30 gm^{-2} • T-Profiles: 0.5 K at 500 m, decreasing to 2 K at 5 km (Crewell and Löhnert, 2007) • q-Profiles: not more than two independent layers can be detected
Lidar ceilometer Vaisala CT25 K	$\lambda = 905$ nm	• Vertical backscatter profiles up to 7.5 km AGL • Cloud base height (up to three layers can be detected)	Temporal resolution: 15 s Vertical resolution: 30 m

Table II.8.1 (continued)

Instruments	Frequencies	Measured parameters	Resolution/accuracies
Micro Rain Radar Metek	24.1 GHz	Vertical Doppler spectra (up to 4.8 km AGL) Derived parameters: • Drop size distribution • Fall velocity • Rain rate	Temporal resolution: 10 s Vertical resolution: 160–200 m (depending on measurement mode)
GPS receiver in Djougou (10 km west of Nangatchori)		Zenith tropospheric wet delay Derived parameter: • Integrated water vapor	Temporal resolution: 15 min. Accuracy 0.5 kg m^{-2} (Bock et al., 2008)

pointing directly into the sun during the course of the year. Although these measurements were performed under an elevation angle of 70°, we will later refer to them as "zenith."

In order to derive meteorological quantities from HATPRO brightness temperature measurements, statistical retrievals for IWV, LWP, temperature, and humidity profiles have been developed from radiosonde data. Due to a lack of sufficient high-quality soundings in West Africa, it was necessary to use radiosonde data from a region with similar climatic conditions. We chose to take northern Australia (Darwin, Gove) where nearly 15,000 sondes between 1990 and 2005 were available. Comparisons of Darwin climatology with soundings from Parakou in 2006 (100 km east of Nangatchori) confirm that the atmospheric states are quite similar.

3 Overview over Atmospheric Parameters in 2006 in Central Benin

3.1 Integrated Water Vapor (IWV)

The IWV during 2006 as derived by HATPRO and complemented by GPS measurements from Djougou (10 km east of Nangatchori; Bock et al., 2008) shows the strong variations between 10 and 50 kg m^{-2} (Fig. II.8.2). The dry season in early 2006 was characterized by several outbreaks of humid air from the south which resulted in large inter-diurnal variations of the atmospheric water vapor content and on average much moister conditions than normal. The diurnal mean of IWV varied between 15 and 43 kg m^{-2} before 15 April. During this period, two major rainfall events were observed (15 February and 23 March). In late April, the southerly monsoon flow became dominant in the area, resulting in IWV daily mean values of 40−50 kg m^{-2}, combined with more frequent rainfall events during this period. In

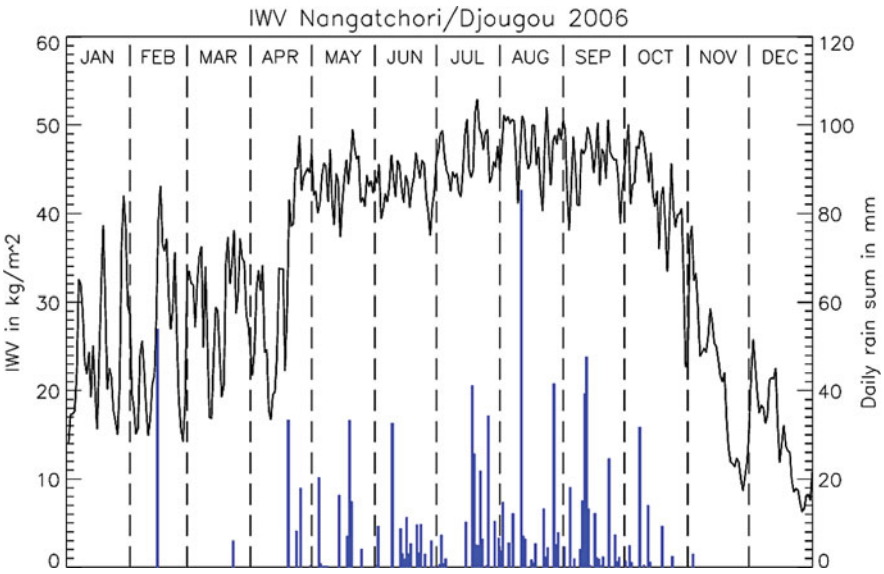

Fig. II.8.2 *Solid line*: Mean daily values of integrated water vapor (aggregate from HATPRO and GPS measurements). *Bars*: Daily rain amount in millimeter from Nangatchori

June 2006, there were only unusually few rain events. Finally, by mid-July heavy monsoon precipitation sets in. This occurred in conjunction with a slight increase in IWV values. By the end of September, precipitation started to diminish, associated with a decrease in IWV. After the last rain of the season on 2 November, the water vapor content continued to fall considerably from nearly 40 to less than 10 kg m^{-2} by the end of November. December was quite dry with IWV values between 7 and 25 kg m^{-2}, much in contrast to the dry season in January 2006. Measurements in January 2007 revealed much drier and cooler conditions also during that month compared to 2006 (not shown).

The high water vapor variability during the dry season is also presented in Fig. II.8.3. During the wet season (May–October 2006) 90% of the IWV observations range between 35 and 50 kg m^{-2}, whereas in the dry season (January–April and November–December 2006), the variation is much larger (90% of the observed values lie between 8 and 41 kg m^{-2}).

3.2 Clouds

To further investigate water cycle variables, the daily amount of cloud cover is plotted in Fig. II.8.4. The annual cycle of cloud cover follows the IWV cycle quite well with a maximum between July and September (Fig. II.8.2). However, even during dry season between January and March 2006, several days with 20–50% cloud cover can be identified. These days are connected with higher IWV values and also with a

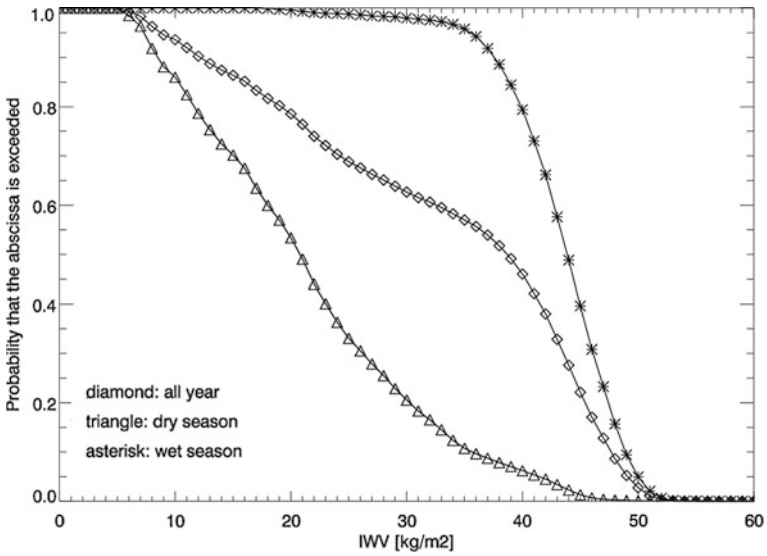

Fig. II.8.3 Cumulative frequency distribution of IWV from HATPRO measurements. Dry season: January–April and November–December 2006. Wet season: May–October 2006

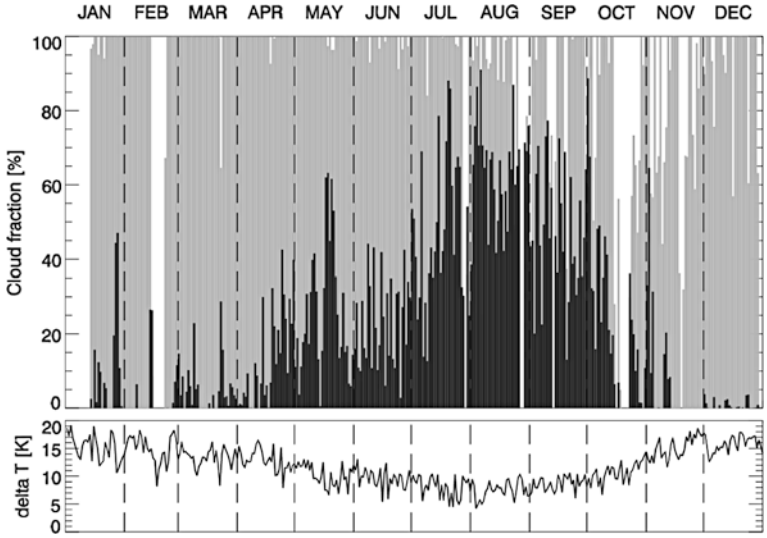

Fig. II.8.4 Fraction of the day (in percent) with cloud cover <7,500 m AGL (*black*), clear sky (*grey*), no data (*white*). *Lower part* shows the diurnal temperature range (T_{max}–T_{min})

lower diurnal temperature range (Fig. II.8.4, bottom). These periods are characterized by moist air from the south over the area. With the beginning of the wet season in late April, cloud cover rises significantly. A further increase of cloudy periods toward the end of July marks the beginning of the peak monsoon time. This is in good agreement with the higher rainfall amounts during that period (Fig. II.8.2). Until mid-October cloud cover remains fairly high, followed by a rapid decrease of clouds and moisture toward November. After 15 November, virtually no clouds have been detected. At that time, also the driest air masses for the whole year 2006 were observed over Nangatchori (Fig. II.8.2).

In order to demonstrate the impacts of clouds, Fig. II.8.5 presents the dependency of the diurnal temperature range with respect to the fraction of the day with clouds. Nearly all cloud-free days have a temperature range higher than 12 K, whereas on cloudy days with more than 50% clouds the difference between maximum and minimum temperature is mostly between only 5 and 10 K. These days are characteristic for the wet season when maximum temperatures are lower than during the dry season.

Cloud observations by ceilometer can also shed light on ABL development because ABL depth is often connected with the base of developing cumulus clouds. The mean diurnal cycle of cloud base height (Fig. II.8.6) is characterized throughout the whole year by a vertically developing ABL after the sun rises at around 6 UTC (Sunrise varies only between 5:31 and 6:15 UTC throughout the year). However, there are some significant differences between the seasons concerning the ABL depth. Before the onset of the monsoon (March/April) when cloud cover is sparse and the soil is dry, the large sensible heat flux over the whole day leads to strong ABL development with highest cloud bases (about 2,500 m) in the afternoon. The ABL becomes less deep in May/June (1,500 m) and reaches only up to about 1,000 m during July–October (peak of wet season). In addition, the amount of low night-time clouds (fog) is much larger at that time. In the end of the year hardly any

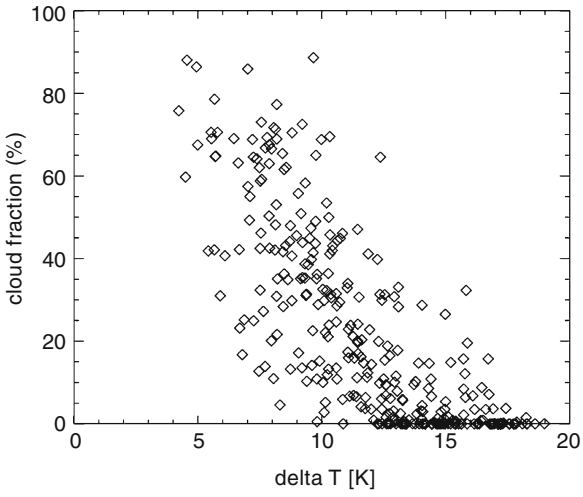

Fig. II.8.5 Scatterplot of diurnal 2-m temperature range (T_{max} minus T_{min}) and cloud cover for all days of 2006

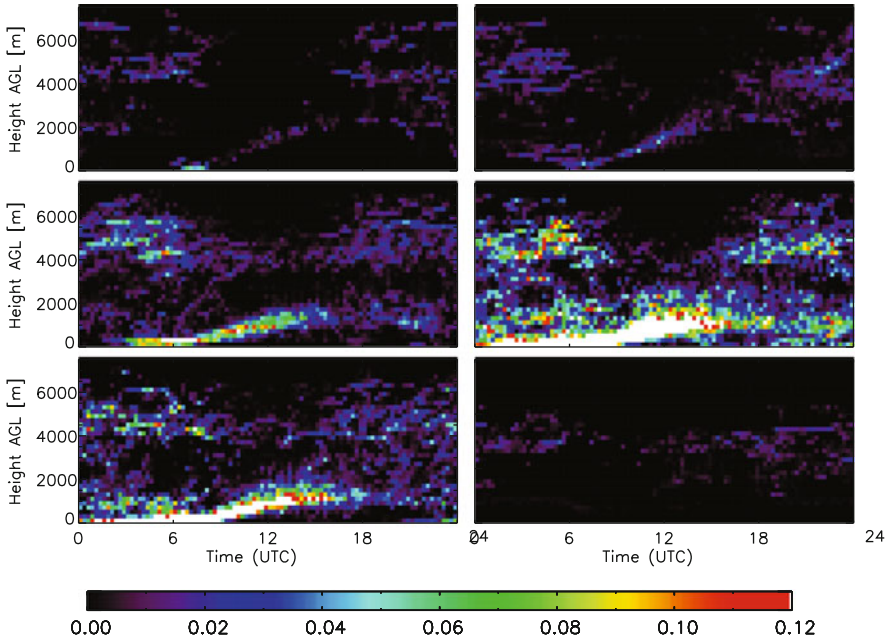

Fig. II.8.6 Diurnal cycle of cloud base heights in 2006 for six periods of 2 months each. Shading indicates the relative frequency of cloud base occurrence

clouds occur which is in no comparison with the dry season at the beginning of the year.

Another evident feature is a second cloud maximum in 4–6 km above ground which can be detected throughout all seasons. These clouds are presumably connected with the African Easterly Jet which has its maximum in about 4 km above ground and are mainly present during night as shown in Fig. II.8.6. However, this might be artificial since the distribution of medium to high clouds is somewhat influenced by the presence of opaque low clouds which cannot be penetrated by the ceilometer, making the detection of higher clouds impossible.

3.3 Cloud Liquid Water Path (LWP)

Microwave radiometry is by far the most accurate method to remotely sense the amount of cloud liquid water and therefore provides a unique opportunity to view the statistical distribution of cloud liquid water for all 2006 (Fig. II.8.7). LWP values above 1,000 gm^{-2} are very rare, but nevertheless, during rainy season some clouds with an LWP of up to 2,000 gm^{-2} were present over Nangatchori. Here it is important to note that only non-precipitating clouds are considered and that some high LWP events occurring after a rain event might be excluded due to a wet radome. In Table II.8.2, the percentage of HATPRO measurements with LWP values greater

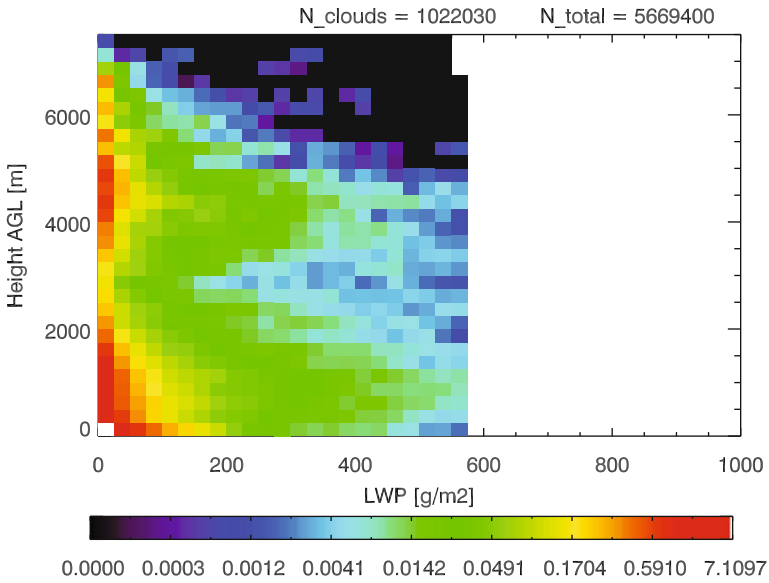

Fig. II.8.7 Frequency distribution of LWP (HATPRO) vs. cloud-base heights (ceilometer). The number of cloudy observations ($N_{\_clouds}$) as well as the total number of observations where both HATPRO and ceilometer operated (N_{total}) are shown at the top. Shading indicates the percentage of detected clouds relative to N_{clouds} for each particular bin (the maximum value being in lowest left bin)

than 10 gm^{-2} is indicated. This distribution is – as one should expect – well correlated with the cloud observations from the ceilometer (Fig. II.8.2). The highest monthly mean LWP was observed in August (75 gm^{-2}). The higher values of cloudy times between July and September are mainly due to HATPRO data gaps when the radome was wet.

The vertical distribution of LWP cannot be derived by microwave radiometry only. With the co-located ceilometer observations, it is possible to allocate a cloud-base height to each LWP measurement. Figure II.8.7 gives an overview of the distribution of cloud-base heights with respect to the corresponding LWP measurement. For this plot, all measurements in 2006 were used where LWP was greater than 0 gm^{-2} and clouds were detected by the ceilometer at the same time. Again two distinct cloud types are visible: boundary layer clouds and mid-tropospheric ones.

Table II.8.2 First line: Percentage of HATPRO measurements in 2006 with LWP > 10 gm^{-2}. Second line: Percentage of cloudy times, detected by the ceilometer

	Jan	Feb	Mar	Apr	May	Jun	Jul	Aug	Sep	Oct	Nov	Dec
LWP (%)	11	–	9	10	21	18	34	44	30	18	8	8
Clouds (%)	10	4	5	13	26	23	47	64	48	26	7	1

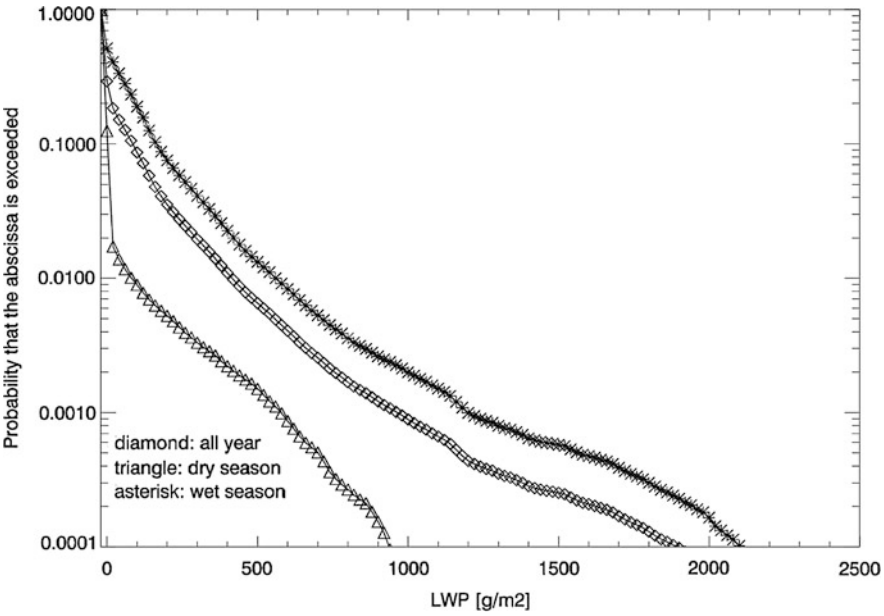

Fig. II.8.8 Frequency distribution of LWP from HATPRO measurements. Dry season: January–April and November–December 2006. Wet season: May–October 2006

Similar to water vapor a strong difference between dry and wet seasons is visible in LWP (Fig. II.8.8). During the dry months only 1% of the HATPRO measurements exceeded LWP values of 100 gm^{-2}, whereas in the wet season 20% of the time LWP was higher than 100 gm^{-2}. During wet season 1% of the values lay even beyond 550 gm^{-2}.

3.4 Temperature Profiles

From HATPRO measurements throughout the year, tropospheric temperature profiles with high temporal resolution could be derived, using a statistical retrieval algorithm which includes also elevation scans for the opaque frequencies close to the oxygen line. Generally, temperatures in the tropics do not change much in the course of the year, but there were some interesting features which could be observed here. The main differences between dry and wet season are captured by the profiles of potential temperature (theta) (Fig. II.8.9). During dry season (January–April and November–December), well-mixed conditions with adiabatic lapse rate (constant theta) prevailed in the afternoon, and a strong nocturnal temperature inversion (highly stable atmosphere) due to efficient radiative cooling is present. The depth of the well-mixed ABL (January–April > 2,000 m, July–September only about 700 m) is consistent with Fig. II.8.6.

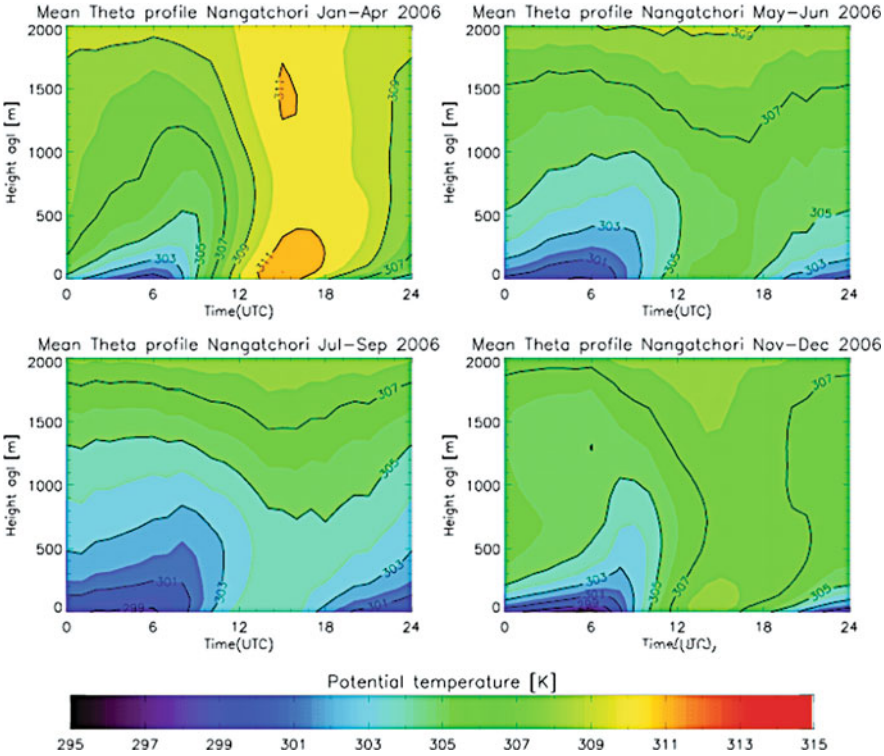

Fig. II.8.9 Mean potential temperature profiles for four different periods in 2006

In order to illustrate the diurnal cycle in more detail the mean diurnal cycle of potential temperature in 50 m above ground is shown for every month (Fig. II.8.10a). The largest diurnal temperature differences are present in dry season months when surface heating is strongest. This diurnal cycle is strongly reduced at 700 m above ground (Fig. II.8.10b) due to mixing processes. The differences between the warmest and the coldest months in 2006 are about 5 K. Fig. II.8.11 gives an overview over the inversion strength in the lowest 700 m of the atmosphere. During wet season the mean monthly theta difference does not exceed 5 K, being relatively constant throughout the night. In contrast, the dry season inversion strength increases until sunrise (6 UTC), the largest values being in November up to 9 K in monthly mean. This is due to the lower water vapor load which leads to less downwelling thermal radiation. In the afternoon, these values are reversed. During wet season the atmosphere is well mixed with basically no gradient in potential temperature between 0 and 700 m above ground. In dry season, for the lowest layers, superadiabatic conditions were observed due to the strong surface heating during daytime.

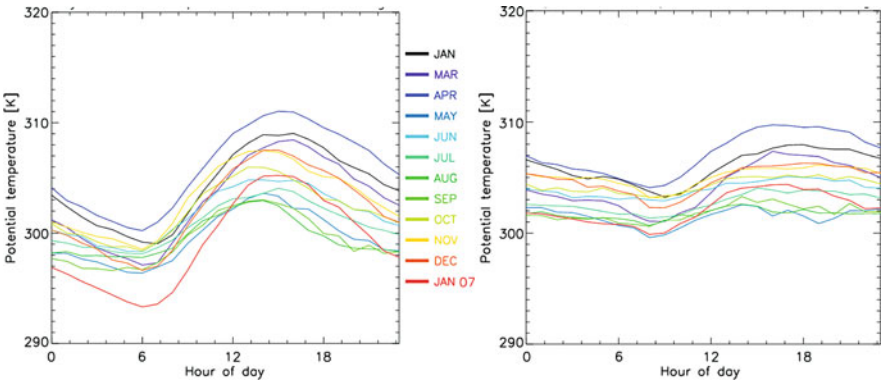

Fig. II.8.10 **a** (*left*): Diurnal cycle of potential temperature in 50 m above ground **b** (*right*): Same for 700 m above ground

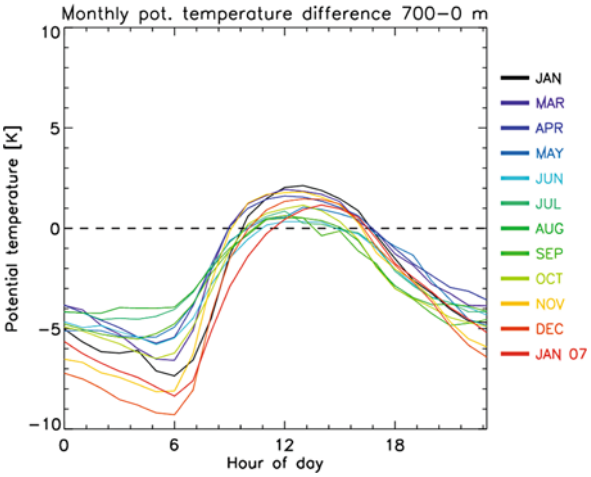

Fig. II.8.11 Diurnal cycle of potential temperature difference between 700 m above ground and the surface for different months of 2006

4 Diurnal Cycle of the Inter-Tropical Discontinuity (ITD)

The diurnal cycle of atmospheric processes around the ITD is recognized to be a key factor for the meridional transport of humidity in West Africa. A detailed overview of previous research is given by Parker et al. (2005) which is briefly summarized in the following: During daytime a heat low develops over the Sahara with a pressure minimum in the afternoon. As the convective boundary layer grows during the day, vertical mixing prevails and the horizontal flow is rather weak. In the late afternoon when sensible heating diminishes, turbulence stops rapidly and the flow is able to respond to the heat-low pressure gradient force. The low-level southerly flow intensifies over night and its edge moves northward. This nocturnal meridional flow is responsible for the advection of moist air in low levels further inland and

forms the main moisture source for summertime convection in the Sahel. In higher regions around 700 hPa there is a dry return flow. By day the low-level humidity falls, as dry air from above is mixed down in the developing convective boundary layer. When the ITD moved northward over Nangatchori, a distinct diurnal cycle of the ITD could be observed during 16 nights between April 1 and April 18, 2006 (Pospichal and Crewell, 2007). The meridional extent of this diurnal cycle is 100–200 km. During the night, the front between the moist monsoon air and the dry Harmattan air moves northward.

The continuous measurements of the HATPRO microwave profiler turned out to be a very good means to describe these processes with a high temporal as well as vertical resolution. In Fig. II.8.12, profiles of temperature, relative humidity, potential temperature, and equivalent potential temperature for the night of April 9/10, 2006 are presented. During the afternoon (12–18 UTC), a well-mixed layer with relatively low humidity values is present. After sunset at 1803 UTC, when the vertical turbulent mixing has stopped, dry air is advected from the northeast by the Harmattan flow, resulting in a decrease of relative humidity and equivalent potential temperature. On the contrary the temperature remains constant, except for a shallow layer close to the ground where an inversion has formed. Shortly after 00 UTC, the moist monsoon air arrives at Nangatchori. The temperature in the lowest 500 m diminishes by about 5 K, whereas humidity increases nearly instantaneously. Until sunrise (at 0545 UTC), the moist layer becomes deeper. After sunrise, vertical mixing starts

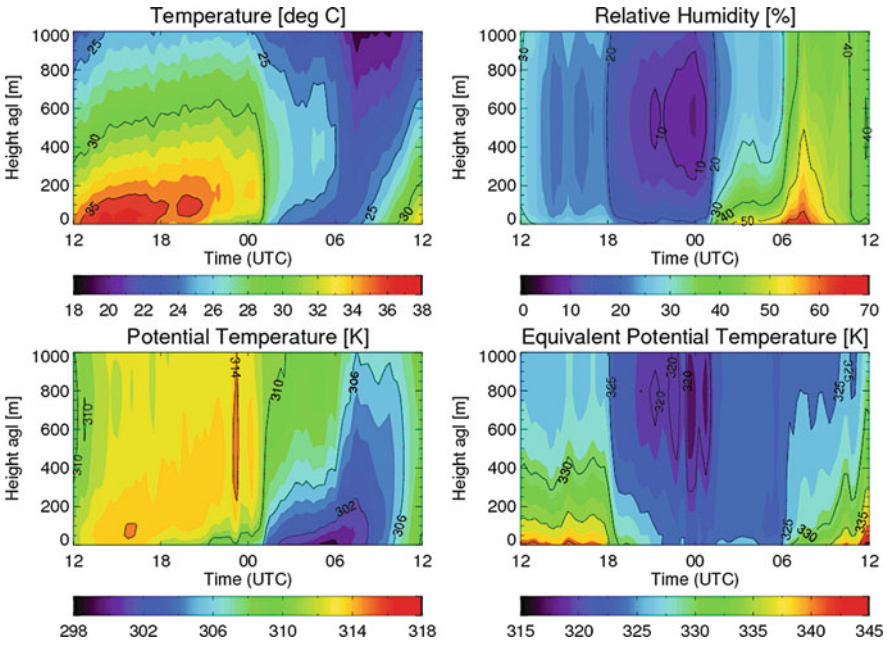

Fig. II.8.12 24-h cross sections of temperature, relative humidity, potential temperature, and equivalent potential temperature over Nangatchori on April 9/10, 2006. All measurements are derived from HATPRO measurements

and the moist and cool air is distributed vertically and at 12 UTC, the conditions are again nearly the same as 24 h before.

5 Conclusions and Outlook

During the whole year 2006, several ground-based remote sensing instruments were operated at Nangatchori (Benin) to study the conditions in the lower atmospheric levels with respect to the West African monsoon cycle. For the first time, continuous measurements with a microwave profiler and a ceilometer have been performed in this region. The instrument setup turned out to be a very good means to describe the atmospheric boundary layer with high temporal resolution. The deployment for one whole year made it possible to describe the complete annual cycle of cloud cover, IWV, LWP, and temperature profiles. Furthermore, a distinct diurnal cycle, connected with the northward move of the ITD before the onset of the wet season, was observed and could be used to evaluate a mesoscale model (Pospichal et al., 2010).

In the framework of AMMA, a similar data set of ground-based remote sensing observations has been collected at Niamey (Niger, 13.5°N, 2.1°E) which is located 400 km north of Nangatchori. At that location the mobile facility of the Atmospheric Radiation Measurement (ARM) Program was deployed (Miller and Slingo, 2007). A similar examination of these data is planned to get information on the meridional differences over West Africa, as Niamey represents a drier region with a much shorter rainy season and more dominant Harmattan winds throughout the year.

The 2006 measurements in Nangatchori continued until January 22, 2007. The first month of 2007 showed special conditions which were rather different to 2006. Dry air masses and a strong Harmattan flux were dominant in this month, resulting in unusually dry conditions even further south (3 weeks of dry air in Cotonou at the Guinean coast from December 31, 2006–January 22, 2007). In Nangatchori, this month was considerably cooler and drier than January 2006. This indicates that only continuous observations over a longer time period can provide information over inter-annual fluctuations. Evaluation of long-term monitoring would be necessary to understand more deeply the mechanisms that are responsible for inter-annual variability of the West African Monsoon.

Acknowledgments Based on a French initiative, AMMA was built by an international scientific group and is currently funded by a large number of agencies, especially from France, the UK, the USA, and Africa. It has been the beneficiary of a major financial contribution from the European Community's Sixth Framework Research Programme. Detailed information on scientific coordination and funding is available on the AMMA International Web site http://www.amma-international.org.

References

Bock O, Bouin MN, Doerflinger E, Collard P, Masson F, Meynadier R, Nahmani S, Koité M, Gaptia Lawan Balawan K, Didé F, Ouedraogo D, Pokperlaar S, Ngamini JB, Lafore JP, Janicot S, Guichard F, Nuret M (2008) The West African monsoon observed with ground-based GPS receivers during AMMA. J Geophys Res. doi:2008JD010327

Crewell S, Löhnert U (2007) Accuracy of boundary layer temperature profiles retrieved with multi-frequency, multi-angle microwave radiometry. IEEE Trans Geosci Remote Sens 45(7): 2195–2201. doi:10.1109/TGRS.2006.888434

Dolman AJ, Culf AD, Bessemoulin P (1997) Observations of boundary layer development during the HAPEX-Sahel intensive observation period. J Hydrol 189:998–1016

Hastenrath S (1985) Climate and circulation of the tropics. D. Reidel Publishing Company. Dordrecht, Boston. 455 pp

Löhnert U, Crewell S (2003) Accuracy of cloud liquid water path from ground-based microwave radiometry. Part I: dependency on cloud model statistics and precipitation. Radio Sci 38:8041. doi:10.1029/2002RS002654

Miller MA, Slingo A (2007) The arm mobile facility and its first international deployment: measuring radiative flux divergence in West Africa. Bull Am Meteorol Soc 88:1229–1244

Parker DJ, Burton RR, Diongue-Niang A, Ellis RJ, Felton M, Taylor CM, Thorncroft CD, Bessemoulin P, Tompkins AM (2005) The diurnal cycle of the West African monsoon circulation. Q J R Meteorol Soc 131:2839–2860

Pelon J, Mallet M, Mariscal A, Goloub P, Tanré D, Bou Karam D, Flamant C, Haywood J, Pospichal B, Victori S (2008) icrolidar observations of biomass burning aerosol over Djougou (Benin) during African monsoon multidisciplinary analysis special observation period 0: dust and biomass-burning experiment. J Geophys Res 113(D00C18). doi:10.1029/2008JD009976

Pospichal B, Crewell S (2007) Boundary layer observations in West Africa using a novel microwave radiometer. Meteorol Z 16:513–523

Pospichal B, Bou Karam D, Crewell S, Flamant C, Hünerbein A, Bock O, Said F (2010) Diurnal cycle of the inter-tropical discontinuity over West Africa analysed by remote sensing and mesoscale modelling. Q J R Meteorol Soc 136(S1):92–106. doi: 10.1002/qj.435

Redelsperger JL, Thorncroft CD, Diedhiou A, Lebel T, Parker DJ, Polcher J (2006) African monsoon multidisciplinary analysis: an international research project and field campaign. Bull Am Meteorol Soc 87:1739–1746

Rose T, Crewell S, Löhnert U, Simmer C (2005) A network suitable microwave radiometer for operational monitoring of the cloudy atmosphere. Atmos Res 75:183–200

Thorncroft CD, Parker DJ, Burton RR, Diop M, Ayers JH, Barjat H, Devereau S, Diongue A, Dumelow R, Kindred DR, Price NM, Saloum M, Taylor CM, Tompkins AM (2003) The JET2000 project: aircraft observations of the African easterly jet and African easterly waves. Bull Am Meteorol Soc 84:337–351

Chapter II.9
Technology Transfer to Business and Industry

The Roles of Government, Academia, and the Private Sector

George L. Frederick

1 Introduction

Transition of research to operations has taken many forms over the years. Some have referred to this process as "crossing the valley of death" (Dumont, 2001) since it is fraught with stumbling blocks and often is not successful for one reason or the other. Not all research is even considered for transition to operations and this situation is sometimes referred to as "crossing the valley of lost opportunities" (Anthes, 2003). This chapter will discuss these processes and present several examples of transition activities. Some conclusions will be drawn and some challenges will be offered.

2 Transition Pathways

Figure II.9.1 shows the transition pathways that exist in transitioning research to operations. This diagram was related to the US environmental satellite system by a committee of the National Research Council (NRC) that reflects the respective roles of the National Aeronautics and Space Administration (NASA) and the National Oceanic and Atmospheric Administration (NOAA) and the Department of Defense (DoD) and end-users (National Research Council, 2003). NASA has a primary research responsibility, while NOAA and DoD are the operational entities that apply satellite information for user requirements. At the research end are the NASA researchers that are either responding to requirements of users or are expanding the research based on new technology. At the other end are the users who either apply the data directly or create products that are provided to the ultimate users. In the middle are the satellite data providers who operationalize the research of NASA. Along the way some NASA research never sees the operational light of day – the valley of death. Other research makes the transition to the operational providers but

G.L. Frederick (✉)
Falcon Consultants LLC, Georgetown, TX, USA
e-mail: falconsultants@aol.com

D. Cimini et al. (eds.), *Integrated Ground-Based Observing Systems*,
DOI 10.1007/978-3-642-12968-1_16,

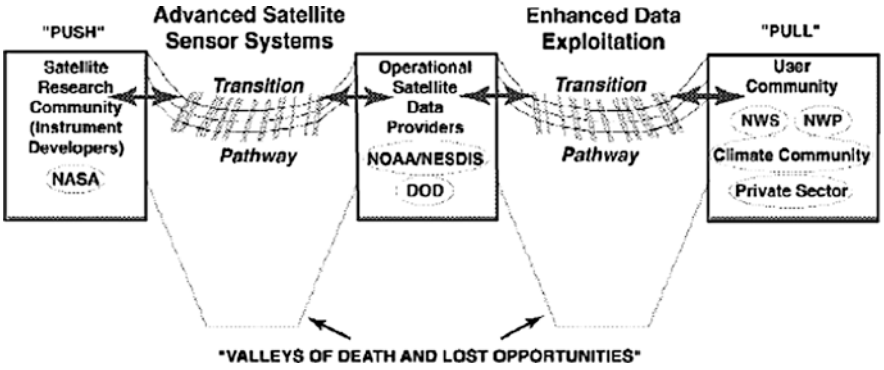

Fig. II.9.1 Transition pathways in transitioning research to operations

never makes it to the users – valley of lost opportunities. Finally, some research makes the transition and is applied by users – a successful transition.

In order to solidify the transition process a number of steps are necessary. They are depicted in Fig. II.9.2 which was the final recommendation of the NRC committee. To avoid the valley of death, clearly defined requirements which lead to proper allocation of resources by the research and operational communities – all

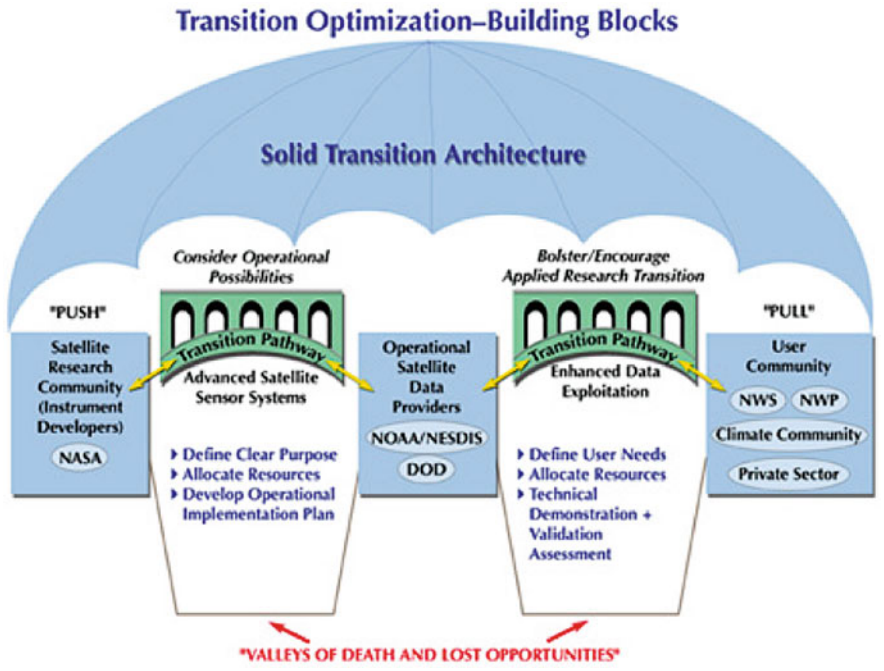

Fig. II.9.2 Transition optimization-building blocks

highlighted with a detailed operational implementation plan – are mandatory to ensure that relevant research is performed and ultimately implemented by the operators.

Technology Transfer Paradigms. There are a number of ways to foster the transfer of technology.

Government Funds Support R&D. The most common way is for government funds to support research and development. In some cases academia does the research, publishes it in open literature, and industry adopts, often by licensing from academia. Sometimes small business research stipends are available from the government and industry then commercializes the results. Finally, federal laboratories may conduct the research and make it available to industry through several different avenues.

Private Sector Funds Support R&D. Less common is either private not-for-profit associations or individual companies developing and commercializing technology development. This usually requires the technology be either sufficiently mature to guarantee return on investment or be of sufficiently high payoff potential to warrant the risk.

Government, Academia, and Private Sector Establish Partnerships. This is an emerging phenomenon where the various sectors form relationships that build on the strengths of each for the common good. This is essential in a period of diminished public resources and allows all sectors to thrive through cooperation and mutual benefit. The American Meteorological Society has established a Commission dedicated to this premise and positive results have occurred since its inception in 2005.

Examples of Transition of Research to Operations. There are a whole host of examples of successful transition of research to operations. The examples range from dropwindsondes to weather radar, to wind profilers, to numerical weather prediction models, to lightning detection systems, to weather satellites – to name just a few. This chapter will focus on two examples—dropwindsondes and wind profilers.

Dropwindsondes. Hurricane reconnaissance is the backbone of the US tropical storm warning system. US Air Force and NOAA aircraft penetrate these dangerous storms and take measurements that are critical to estimating the strength, trend, and forecast track of these destructive forces. One of the most important sources of data is an instrumented device called a dropwindsonde or dropsonde that is ejected by the aircraft at significant points within the storm to collect data on the vertical structure of the storm and most significantly the character of the central pressure and the maximum winds in the eyewall. The current version of the dropwindsonde was developed with government funding by the National Center for Atmospheric Research (NCAR) and licensed to Vaisala for commercial production. A model of the device appears as Fig. II.9.3. The use of this new GPS-based dropsonde has been credited with improving the hurricane track forecasts by 20%. This was important as one famous storm – Katrina – bore down on the US Gulf Coast in 2005 (Extreme

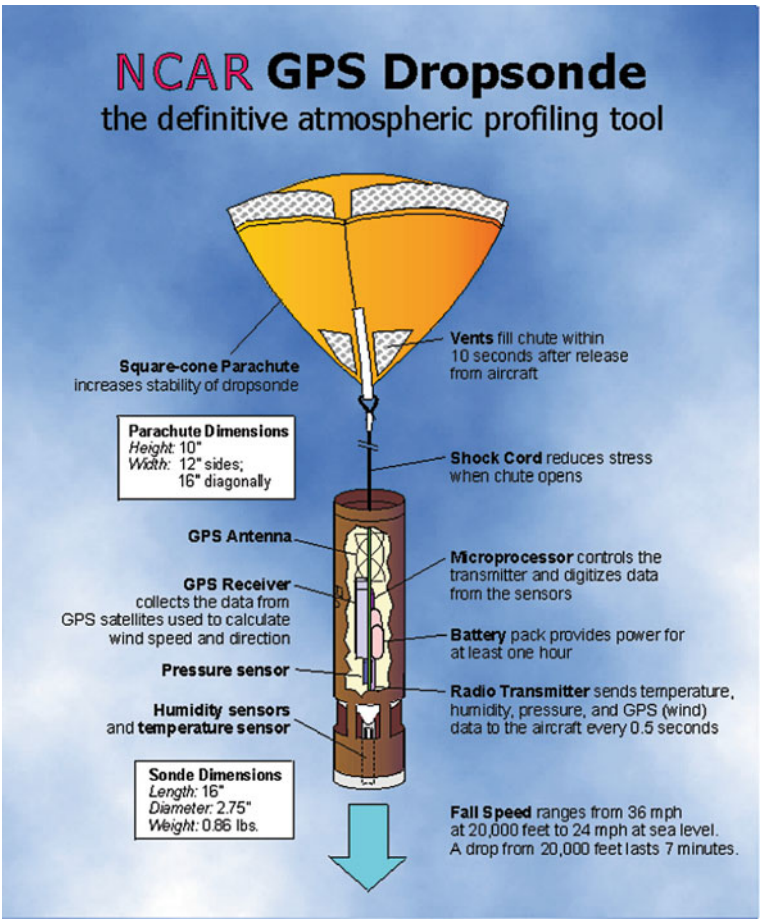

Fig. II.9.3 NCAR-developed GPS dropsonde

Weather Sourcebook). Figure II.9.4 shows the forecast track with and without the dropsonde data. Without it the track would have brought it ashore along the central Louisiana coast. With the data the track brought it ashore in the vicinity of New Orleans. The latter was spot on and allowed the weather service to provide many hours of warning to the citizens and officials of the Crescent City. Damage and loss of life were significant even with these near perfect warnings but would certainly have been more severe without them.

To summarize the dropsonde research to operations process, airborne reconnaissance needed an improved wind finding sensor. Federal funds enabled NCAR to develop a prototype GPS wind finding dropsonde. Partnership with Vaisala evolved into a license agreement to commercially produce GPS dropsondes. As a result, reconnaissance units now routinely employ GPS dropsondes during operational missions providing critical data for accurate storm forecasting.

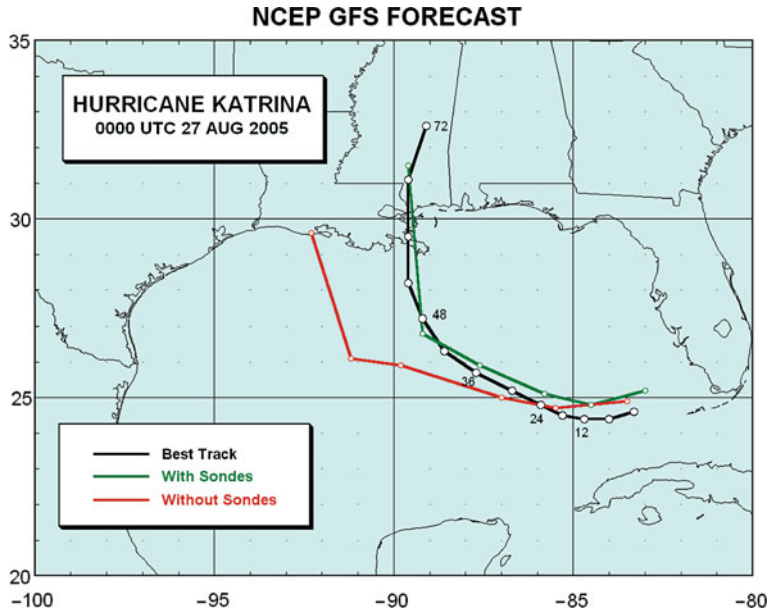

Fig. II.9.4 Katrina forecast track with and without dropsonde data (Figure courtesy of James Franklin, National Hurricane Center, USA)

Radar Wind Profilers. NOAA research laboratories were noted for world leadership in radar technology in the 1970s–1980s. A product of their advanced research was a boundary layer radar wind profiler that had potential for commercialization to support air quality forecasting and other weather forecasting needs. In 1991 NOAA competitively awarded a Cooperative Research and Development Agreement (CRADA) to Radian Corporation, Austin TX, to mutually develop and prepare the boundary layer profiler for the commercial market. The terms of the agreement provided for NOAA to continue advanced signal processing development while Radian would focus on advancing the hardware to the point where it could be mass produced. As the agreement progressed, each party did a little and mutually produced a final hardware and software package that emerged on the market in 1992–1993. Since that time, over 135 systems have been fielded in such applications as air quality, aviation, and mesoscale forecasting. A picture of the profiler appears as Fig. II.9.5 (Vaisala).

To summarize the wind profiler transition process, there was a community requirement for continuous monitoring of the winds and temperatures aloft in the boundary layer. Federal research funds led to the development of a family of radar wind profilers by NOAA. The government awarded a CRADA to Radian (subsequently acquired by Vaisala) in 1991 to marry the requirements with the product. The CRADA has been renewed three times since 1991 and has returned stipends to NOAA in excess of $1 million to benefit continued research and development. Vaisala now has evolved the capability into a complete line of wind profilers that meet a full range of atmospheric needs.

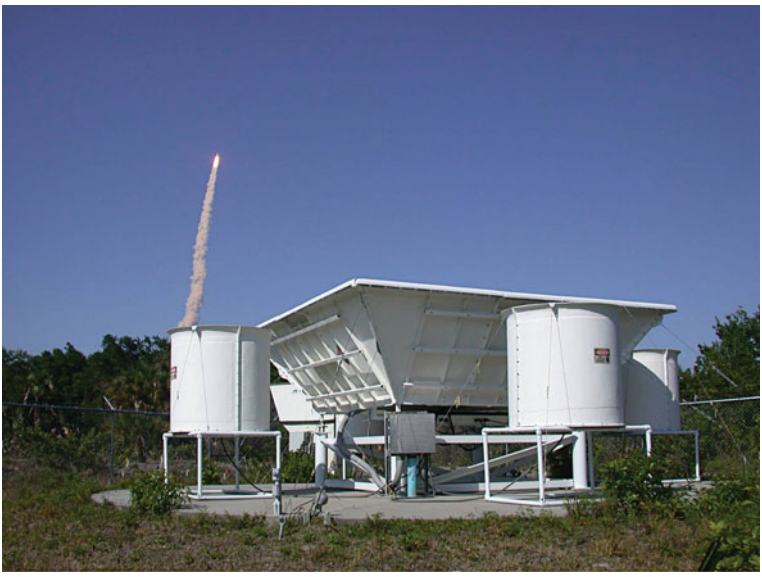

Fig. II.9.5 NOAA developed and Radian fielded boundary layer wind profiler at Cape Canaveral FL during the launch of the Space Shuttle

3 The Future – Partnerships

The question is Can government, academia, and the private sector establish true and effective partnerships to meet the needs of the entire community for technology transition in the future? What is needed is a relationship that resembles a legal partnership that involves close cooperation between parties having specified joint rights and responsibilities. The government, academia, and industry have different yet complimentary needs but if resources are pooled and risks shared the costs can be managed. How to do this is the big question – testbeds may be the answer. Testbeds provide infrastructure for transitioning from research to operations. The testbed needs the flexibility to test many new ideas, the expertise to judge which of them are viable, and the infrastructure to harden the sensors, algorithms, and models that will generate new products for operations (Ruffieux and Furger, 2006). Figure II.9.6 provides a model of how a testbed could work.

For the meteorological community a testbed could be defined as "a working relationship in a quasi-operational framework among forecasters, researchers, private sector, and government agencies aimed at solving operational and practical regional problems with a strong connection to end-users." The testbed concept has been put into action in Helsinki Finland with the Helsinki Testbed depicted in Fig. II.9.7 (Dabberdt et al., 2005). The partners include

- Finnish Meteorological Institute (FMI)
- Vaisala Oyj

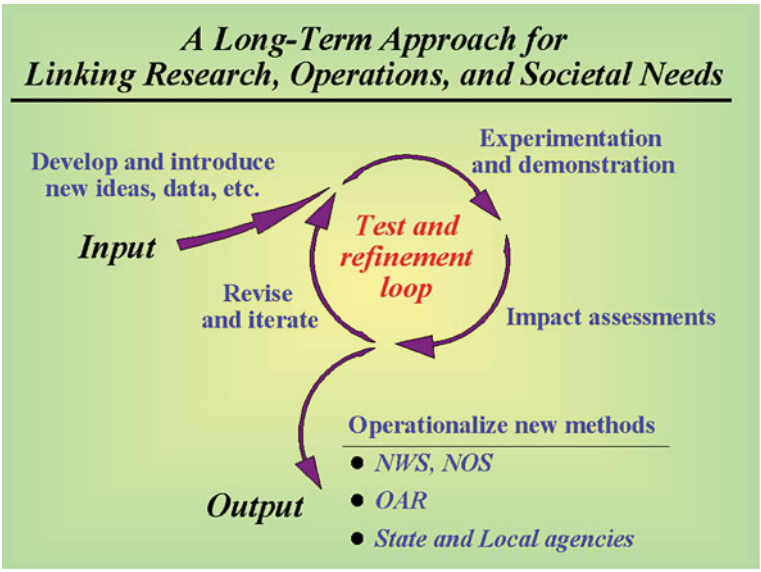

Fig. II.9.6 Testbed model

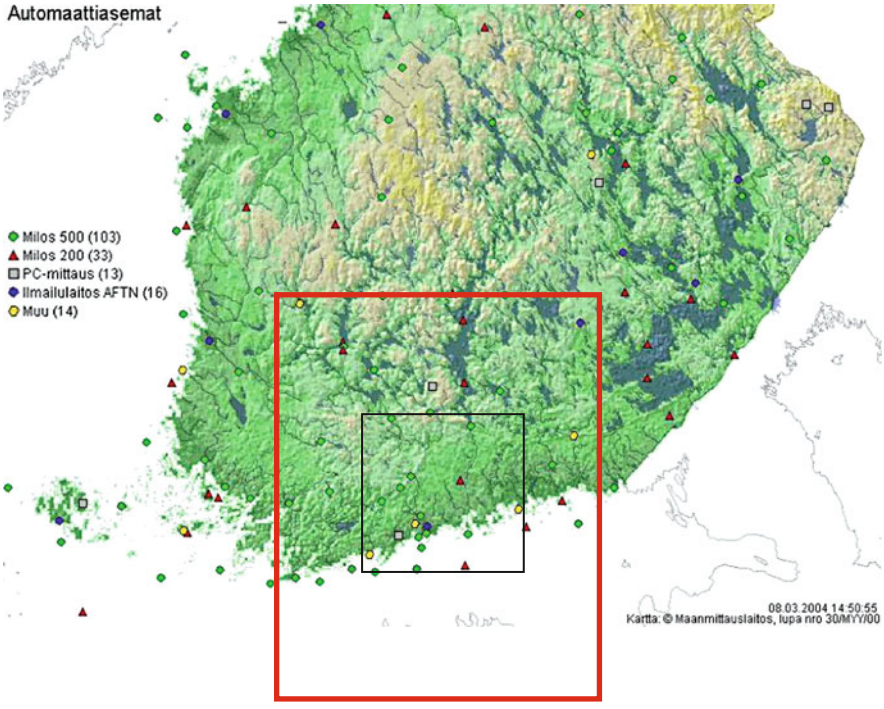

Fig. II.9.7 Helsinki Testbed (larger square) is the outer limit for model work and the smaller square is the intensive region for high density observations

- Nokia
- TVO Power company
- Radiation and Nuclear Safety Authority STUK
- Road administration, Road enterprise
- Helsinki Metropolitan Area Council – Air Quality
- World Championships in Athletics 2005

The Helsinki Testbed has experienced multiple uses as follows:
May 2005 – test of communications
August 2005

- nowcasting by extrapolation; convection
- world championships in Athletics
- no database yet, limited remote sensing instrumentation

November 2005

- snow/rain

January–February 2006

- Inversions

May 2006

- Sea breeze, fog

August 2006

- Convection

The research plan for the Helsinki Testbed includes

- water phase: rain/snow/mixed
- visibility
  - fog and
  - precipitation phase and intensity
- inversion height and strength
- urban-mesoscale model
- air quality model
- sea breeze
- sensitivity tests with LAM
- road surface radiation balance model

So the Helsinki Testbed provides a database for measurements, numerical weather prediction fields with access over the internet for all users. It provides infrastructure for research to operation activities with an extensive measurement capability.

4 Summary

The challenge of transitioning research to operations is crossing both the valley of death and the valley of lost opportunities. The research to operations transition can take many forms: government investment, government licenses, CRADAs, and corporate investment. Testbeds can be a bridge for research to operations transition. They provide for multi-sector partnerships and cooperation where bugs in the system can be worked out before the system is made fully operational – saving money and resources.

References

Anthes R (2003) Crossing the valleys of death and lost opportunities: toward an earth information system, UCAR Quarterly, Summer 2003. Online: http://www.ucar.edu/communications/quarterly/summer03/president.html. Accessed on May 2009

Dabberdt WF, Koistinen J, Poutiainen J, Saltikoff E, Turtiainen H (2005) The Helsinki Mesoscale Testbed, An invitation to use a new 3-D observation network. Bull Am Meteorol Soc 86(7):906–907, July 2005

Dumont R Bridging the valley of death, the Federal plan for meteorological services and supporting research, office of the federal coordinator for meteorological services and supporting research, FCM-P1-2001. Online: http://www.ofcm.gov/fp-fy02/pdf/sec1.pdf. Accessed on May 2009

Extreme Weather Sourcebook. Online: http://www.sip.ucar.edu/sourcebook/. Accessed on April 2009

National Research Council (2003) Satellite observations of the earth's environment: accelerating the transition of research to operations, National Academies Press, Washington, DC, ISBN-10: 0-309-08749-X

Ruffieux D, Furger M (2006) Special Issue COST 720 TUC. Meteorol Zeitschrift 15(1):97 pp. doi: 10.1127/0941-2948/2006/0103

Vaisala Weather Sensors Brochures. Online: http://www.vaisala.com/weather.html. Accessed on April 2009

Index

Note: The letters ‘f’ and ‘t’ followed by the locators refers to figures and tables cited in the text.

D. Cimini et al. (eds.), *Integrated Ground-Based Observing Systems*,
DOI 10.1007/978-3-642-12968-1, © Springer-Verlag Berlin Heidelberg 2010